The University of Nottingham

UNITED KINGDOM · CHINA · MALAYSIA

Faculty of Engineering

Department of Chemical and Environmental Engineering

Numerical Simulation of Heavy Oil and Bitumen Recovery and Upgrading Techniques

By

Muhammad Rabiu Ado (BEng, AMIChemE)

Thesis submitted to the University of Nottingham for the degree of Doctor of Philosophy

January 2017

Abstract

As a result of the increasing energy demand but a heavy dependence on easy-to-produce conventional oil, vast reserves of recoverable heavy oil have been left untapped. According to the International Energy Agency, IEA, fossil fuels – oil, coal, natural gas – will still predominate, despite a decline in their overall share, towards meeting the increasing world energy demand. While heavy oil has been predicted to account for an increasing share, contributions from conventional light oil have been predicted to drop from 80% to 53% in the next two decades (IEA, 2013b). Therefore, the large reserves of the under-utilised heavy oil, if extracted cost-effectively and in an environmentally friendly manner, will facilitate the meeting of both the short and long term energy demands.

In this work, different thermal heavy oil recovery processes were reviewed with particular attention given to the air injection processes. In-situ combustion, ISC, has been identified as the most efficient and environmentally friendly technique used to recover heavy oil. Until the last decade, there was only a small interest in the conventional ISC. This is due to the complex nature of the processes taking place during ISC and the lack of success recorded over the years. The successful pilot scale testing of the Toe-to-Heel Air Injection, THAI, by Petrobank has revived interest both industrially and in the academic environment. Experimentally, THAI has been consistently proven to exhibit robust and stable combustion front propagation. Among the advantages of THAI is the ability to incorporate the in-situ catalytic upgrading process, THAI-CAPRI, such that further catalytic upgrading is achieved inside the reservoir.

To realise the theoretical promise offered by THAI-CAPRI, there is a need to develop a reliable numerical simulation model that can be used to scale laboratory experiments to full field scale. Even for 3D combustion cell experiments, only one such model exists and it is incapable of predicting the most critical parameters affecting the THAI process. Therefore, the subject of this work was the development and identification of an accurate and reliable laboratory scale model that can then be used to develop field scale studies and investigate the effect of reservoir geology on the THAI process. However, because of the significant uncertainty introduced by the kind of kinetics scheme used and the fact that the main mechanism through which fuel deposition takes place is still a contentious issue, three different kinetics schemes, based on Athabasca bitumen, have been tested for the model of the 3D combustion cell experiment.

All the models offered an insight into the mechanism through which oxygen production begins. They revealed that oxygen production was as a result of the combustion front propagating along the horizontal producer (HP). They also showed that the presence of coke inside the horizontal producer is an essential requirement for stable combustion front propagation. It was also observed that LTO is not the main mechanism through which fuel is deposited as oxygen does not bypass the combustion front. The models also showed that the temperature around the mobile oil zone (MOZ), where catalytic reaction in the CAPRI^{TM} is envisaged to be located, will not be sufficient to make the hydro-treating catalysts effective. Therefore, it is concluded that some form of external heating must be used in order to raise the temperature of the catalyst bed.

Two out of the three different Arrhenius kinetics schemes that were successfully used to history-match the 3D combustion cell experiment were adjusted and implemented in field scale simulations. This is because the kinetics parameters obtained from the laboratory scale model cannot be used directly for the field scale simulation as they led to excessive coke deposition. A comparative study, between the two kinetics schemes, showed that the adjusted direct conversion kinetics predicts higher oil rate, and higher air rate can be injected right from the initiation of the combustion compared to in the case of the split conversion kinetics.

The direct conversion kinetics was then used to study the field performance because it provided a more realistic representation of the physicochemical processes than the split conversion kinetics. The study revealed that even if the combustion front swept the whole reservoir length, it has to propagate along the horizontal producer for oxygen production to take place. It was observed that the combustion zone does not only have to cover the whole reservoir length but also has to expand laterally in order to produce the whole reservoir.

For heterogeneous reservoirs, the THAI process was found to have larger air-oil ratio (AOR) in reservoir containing a discontinuous distribution of shale lenses compared to the homogeneous model. However, overall, the THAI process is only marginally affected in terms of cumulative oil recovery. The combustion front was found to propagate in a stable manner just like in the homogeneous model. However, further study is needed to investigate the effect of different permeability distributions would have on the THAI process. This should allow the optimum location of the wells to be determined.

Studies of the effect of bottom water (BW) on the THAI process have shown that the oil recovery is heavily affected depending on the thickness of BW zone. It was found that the location of the HP well relative to the oil-water interface significantly affects the oil production rate and hence the cumulative oil produced. More oil is recovered when the HP well is located inside the BW zone. It was found that a 'basal gas layer', just below the oil-water interface, is formed when the HP well is located in the BW zone. The study has shown that there is a limit to BW thickness above which the THAI process cannot be applied to a BW reservoir. However, future work is needed to determine this BW thickness.

The reservoir cap rock, depending on it is permeability and porosity, only marginally affects the oil recovery in the THAI process. It was found that the cap rock aids in heat distribution to the extent that most of the upper oil layer is mobilised. However, the effect is observed to be less pronounced with increased permeability and porosity. Future work should look into whether longer operation period has an adverse effect on the stability of the combustion front, and thus on the overall performance of the THAI process.

Acknowledgments

I wish to express my deepest and sincere gratitude to my supervisor, Professor Sean Rigby, for his encouragement, guidance, advice, and consistent support throughout my doctoral study period. This thesis would not have been possible without his immense knowledge and experience on the field of heavy oil and bitumen recovery. It is truly a privilege and indeed a great honour to work under his supervision.

I would like to sincerely acknowledge my second supervisor, Dr Buddhika Hewakandamby, for his support, guidance, and advice during this project. I am also deeply indebted to Professor Malcolm Greaves for his keen interest, support, and critically constructive comments over the last three years of this work. He was never tired of getting back to me whenever I requested his feedback.

I would like to gratefully acknowledge Deans of Engineering for the funding of this project. I am thankful to the Computer Modelling Group (CMG) for supplying the licence to access their thermal reservoir simulator (STARS) and for their technical support. I would also like to extend my appreciation to Dr Huw Williams and Dr Juliano Katrib for their helps in running NMR and Microwave experiments respectively.

I want to specially thank all the academic staffs, particularly Prof. Glenn, Dr Anca, Dr Paul, Dr Buddhi, Dr Iain, Dr Frank, and Dr John for giving me the opportunity to work as an undergraduate tutor. I cannot express my gratitude for this. I also would like to express my appreciation for the kind support I have

received from Kerry, Ellie, Farrah, Dean, Mack, Janet, Tracey, and Sue whilst carrying out this research project.

I owe many thanks to friends and colleagues for being readily collaborative and, thus, tremendously supportive. Last but surely not least, I am grateful to all my family members, most especially my caring parents and my lovely siblings, for their unconditional and boundless love, kind and constant support, and encouragement. Over the last two decades, my Mum and Dad have devoted so much of their time and energy to bring me up and educate me. To them, I can only say this: thank you very much indeed for you are truly all the world to me.

Table of Contents

List of Figures

List of Tables

Nomenclature

Acronym	Meaning
3D	Three Dimensional
AOR	Air-Oil Ratio
BPD	Barrel Per Day
BW	Bottom Water
CAPRI	Catalytic Upgrading Process In-Situ
CSS	Cyclic Steam Stimulation
CWE	Cold Water Equivalent
DLD	Direct Line Drive
EOR	Enhanced Oil Recovery
GB	Grid Block
HDS	Hydro-Desulphurisation
HDN	Hydro-Denitrogenation
HP	Horizontal Producer
HTO	High Temperature Oxidation
HUO	Heavy Upgraded Oil
IC	Immobile Pseudo-Component
ICP	In-Situ Conversion Process
IEA	International Energy Agency
ISC	In-Situ Combustion
K_h	Absolute Horizontal Permeability
K_v	Absolute Vertical Permeability
LC	Light Pseudo-Component

LTO	Low Temperature Oxidation
LUO	Light Upgraded Oil
MC	Mobile Pseudo-Component
OL	Oil Layer
PIHC	Pre-Ignition Heating Cycle
SAGD	Steam Assisted Gravity Drainage
SLD	Staggered Line Drive
THAI	Toe-to-Heel Air Injection
VI	Vertical Injection

List of Publications

- RABIU ADO, M., GREAVES, M. & RIGBY, S. P. 2017. Dynamic Simulation of the Toe-to-Heel Air Injection Heavy Oil Recovery Process. *Energy & Fuels*.
- RABIU ADO, M., GREAVES, M. & RIGBY, S. P. 2017. Scale-up of the THAI Heavy Oil Recovery Process. *To be submitted for publication.*
- At least two more journal papers out of this thesis are being prepared for submission.

1. Chapter One: Introduction

1.1 General Overview

Fossil fuels – Oil, Coal, Natural gas – have been and will continue to be the main source of energy for decades. According to IEA (2013a; 2013b) estimates, overall energy demand will increase by 33% from 2011 to 2035. It is predicted that there will be a decline in the share of fossil fuels, toward meeting the demand, from 82% to 76% over the same period. Despite the decline, fossil fuel still predominates. However, in order to cater for the increasing energy demand, attention has been heavily focused on the easy-to-produce conventional crude oil thereby leaving out the vast reserves of recoverable non-conventional oil. Heavy oil has been predicted to be supplied at a rate of 10^7 BPD by 2035, while the contribution from conventional oil has been predicted to drop from 80% to 53% in the next two decades (IEA, 2013b). Going by these predictions, it can be determined that the vast reserves of untapped heavy oil, if extracted cost effectively and in an environmentally friendly manner, will facilitate in meeting both the short and long term demand.

Geologically, conventional oil (i.e. light oil) is formed over temperatures of 65 to 150 ^{o}C (Hyne, 2001). It is formed when a mixture of organic matter and inorganic minerals is rapidly buried by sediments. It can also be formed when the mixture is deposited on the sea floor where there is no oxygen presence. The formation of non-conventional oil is thought to be as a result of bacterial as well as physicochemical degradation of conventional oil. After oil migration from the main point of generation (i.e. the oil window), it is usually trapped and separated according to density. Gas and water are respectively underlain and

overlain by oil layer as can be seen in Fig. 1.1a. Saturated reservoir is formed when gas cap is found overlaying oil layer. A free gas cap is trapped by cap rock which prevents the gas from migrating to the surface. May River heavy oil reservoir with oil layer thickness of around 40 m is an example of reservoir containing a gas cap (Sands, 2014). Reservoirs that do not contain free gas cap are called unsaturated reservoirs as more gas can be dissolved, at the reservoir temperature and pressure, to saturate the oil (Fig. 1.1b). A water layer overlain by oil layer is called bottom water (BW). Many heavy oil fields e.g. Kearl Lake oil field, Alberta Canada; N. Tisdale, Wyo, USA; Cado Pine, Is, La, USA etc. (Turta et al., 2009) have reservoirs underlain by BW. BW thickness varies from one reservoir to another.

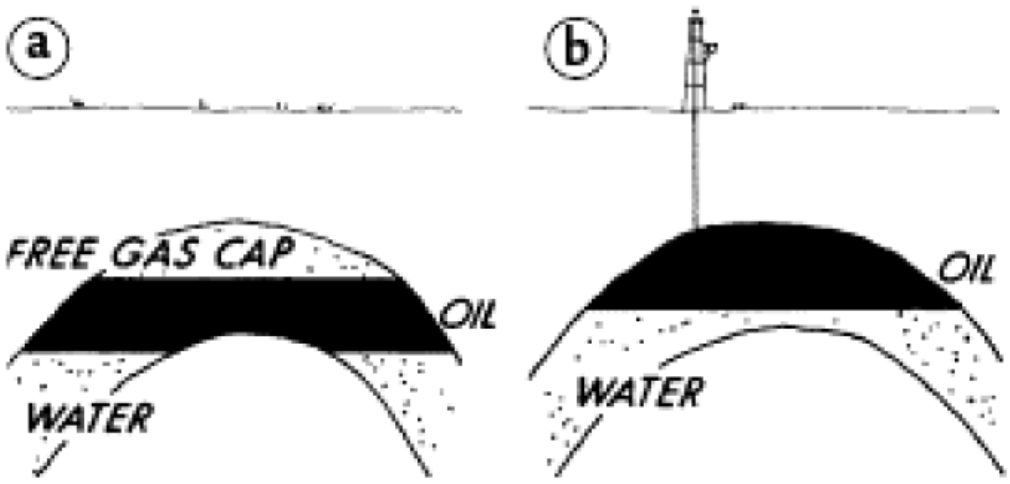

Fig. 1.1: (a) Saturated Reservoir and (b) Unsaturated Reservoir (Hyne, 2001)

Non-conventional oil (i.e. heavy oil) is very sticky with viscosities, in cP, of several orders of magnitude and low API gravity. Example is the Athabasca bitumen which has viscosity of around 5×10^5 cP and API gravity ranging from 6.5 to 10.7 ^{o}API at the temperature of 15 ^{o}C (Prowse et al., 1983). Loydminster reservoirs contain medium to heavy oil with viscosity ranging from 50 to 50,000

cP and API gravity of 10 to 25 ^{o}API at 20 to 30 ^{o}C (Gutierrez et al., 2011). At the reservoir conditions, heavy oil is virtually immobile and hence density as well as viscosity must be lowered substantially in order to mobilise it to the surface. For these reasons, heavy oil is costlier to produce.

Several commercial processes have been, and are being developed to ensure economical, environmentally friendly, and safe production. The production method applied depends on, among other things, reservoir geology, heavy oil properties, etc. A primary production technique in the form of surface mining has been used to recover some of Canada's shallow oil sand deposits. Despite the high recovery efficiency, the cost of mining, extraction, and upgrading is astronomically high when compared to in-situ recovery techniques (National-Energy-Board, 2013). It has been reported that as a result of the surface mining operations, a land area of 715 km^2 has been disturbed (Alberta-Energy, 2013). Mining has additional disadvantage of having detrimental environmental impact e.g. deforestation. On the other hand, deeper deposits require an impractical pressure gradient to mobilise and pump the heavy oil/bitumen to the surface. Therefore in-situ techniques such as: fluid flooding e.g. Cyclic Steam Stimulation (CSS), Steam Assisted Gravity Drainage (SAGD), polymer injection, CO_2 injection etc.; and in-situ combustion e.g. conventional in-situ combustion (ISC), Toe-to-Heel Air Injection (THAI) etc.; are used to upgrade and mobilise the heavy oil to the surface. Other recovery techniques such as Electrical heating e.g. Shell's In-Situ Conversion Process (ICP) for oil shale, and Electromagnetic heating using Microwave, are being tested for heavy oil upgrading and mobilisation.

The production techniques can be broadly divided into thermal and non-thermal displacement processes. Among the many available in-situ recovery techniques, thermal recovery processes have higher efficiency. This is as a result of efficient energy utilisation and the rapid decrease in oil viscosity with temperature. The main subject of this work is on thermal recovery processes. As a result, a critical review of the thermal techniques and the different area of their applicability revealed that THAI is the least understood technique. This was however partly as a result of the failures recorded over the years which resulted in substantial decrease in interest on air injection recovery processes. It is also due to the complex nature of the multiphase processes during the combustion and the significant uncertainty introduced by the kind of kinetics scheme used during design. However, the review indicated that THAI is potentially the most economical and environmentally friendly technique that operates over large range of reservoir conditions. It also uses the most inexpensive and readily available injection fluid – air.

1.2 Aims and Objectives

From the literature reviewed, the aims and objectives of this thesis are outlined as follows:

- Highlight the advantages of the THAI process over the other thermal heavy oil recovery techniques.
- To develop and validate a 3D combustion cell numerical model against experimental results.
- To scale up the experimental model to field scale under ideal geological conditions (i.e. homogeneous, bottomwater-free, and cap rock-free reservoir).

- To investigate combustion propagation, using numerical reservoir simulator, in a geologically realistic reservoir (i.e. under non-ideal geological reservoir conditions) and it is effect on the THAI process.
- To carry out preliminary simulation of the CAPRI process and provide suggestions for the future research directions.

1.3 Thesis Outline

This thesis is structured into the following chapters:

Chapter one gives a general overview of the oil recovery techniques and the reasons why there is need to carry out the current work. It also outlines the aims and objectives of this project.

Chapter two presents a review on the different thermal methods for enhanced heavy oil recovery. It also provides a comprehensive detail on the kinetics used to model air injection enhanced oil recovery techniques such as conventional in-situ combustion, THAI, etc. A critical analysis of what has been done by the previous authors and the gap that needs to be filled by the current study are also reviewed.

Chapter three summarises the governing equations required to model the multiphase reactive transport system present in the air injection enhanced oil recovery process. It also provides a brief description of the methodology employ in solving these equations.

Chapter four provides a comprehensive details of the kinetics scheme used to model the THAI process. It also presents the results of the validated kinetics scheme against a 3-D combustion cell experiments. Then, quantitative predictions on the effect of viscosity, air injection flux, and pre-ignition heating

cycle (PIHC) method respectively on the THAI process are also discussed under this chapter.

Chapter five involves presentation of a comparative study of the field scale predictions by each of the two validated kinetics schemes that best matched the experimental results. Conclusion is drawn on which of the kinetics schemes that provides the best representation with less uncertainty. The model is then chosen to study the difference between the direct line drive (DLD) and staggered line drive (SLD) well arrangements. The chapter closes by investigating the nature of fluid production along the HP well.

Chapter six investigates the applicability of THAI in the presence of bottom water. Due to the density difference among gas, oil, and water, most oil reservoirs contain bottom water which is overlain by oil layer. Previously, many failures have been recorded during many field trials. Also, injected air channelling through gas cap has been thought to be one of the main reasons causing heat transportation out of the reservoir. A field pilot study by Petrobank recorded an increase in temperature on an overlaying gas reserve. Therefore, how effective cap rock is, on serving as gas seal, is studied and the findings are presented in this chapter. Reservoir heterogeneities have been observed to cause significant problems during oil recovery. This chapter also investigates and presents how regions of zero porosity and or permeability affect the stability and advancement of the combustion front.

Chapter seven draws the conclusion on the research findings as well as provides suggestions on what should be done to further develop the THAI, and it is catalytic add-on, the CAPRI^{TM} processes.

2. Chapter Two: Literature Review

2.1 Introduction

The first section of this chapter presents a critical review of the different thermal heavy oil recovery (EOR) techniques. Their merits and demerits are also identified and discussed. The aim of the review is to identify the superiority of Toe-to-Heel Air Injection (THAI) over the other thermal recovery techniques. The following are identified to be among the realisable advantages of THAI over the other processes:

i. It generates its own fuel in the reservoir to fully sustain the process
ii. It does not require any natural gas or water during normal operation
iii. It can be made essentially self-sustaining, so that no net energy input is required
iv. It is carbon capture ready for EOR or sequestration
v. It has very high oil recovery potential
vi. It creates an underground 'reactor' for in-situ upgrading
vii. It has the potential for one-step 'heavy to light oil' upgrading in-situ
viii. improved economics for heavy oil recovery
ix. It has the benefit of reducing sulphur, nitrogen, and heavy metals inside the reservoir
x. It has a small surface-footprint
xi. In-situ catalysis as in CAPRI^{TM} can easily be coupled to THAI to achieve catalytic upgrading inside the reservoir.

The review of the thermal EOR technique was then followed by a comprehensive review of the kinetics schemes used to model THAI. The aim of

this is to identify different kinetics schemes to be validated against three-dimensional combustion cell experiment. This should then allow the best history match to be made.

2.2 The Thermal Recovery Processes

Thermal oil recovery techniques involve the injection of surface generated heat-carrying fluids (such as steam or hot water), in-situ generation of heat, or in-situ electrical heating of oil formations, in order to lower the viscosity of the heavy oil, or bitumen, and thus render it mobile. The thermal techniques take advantage of the exponential decrease in heavy oil or tar sand viscosity with increase in temperature of an oil formation. Unlike in the case of injecting heat-carrying fluids from the surface, in-situ heat-generating techniques do not suffer from the wellbore heat losses and therefore have higher thermal efficiency.

2.2.1 In-Situ Combustion (ISC)

In-Situ Combustion (ISC) has been used as a recovery process for over six decades since the first pilot test in 1951 (Greaves et al., 2008). Before the development of Toe-to-Heel Air Injection (THAI) in 1992, all the projects employed conventional ISC process. Conventional ISC process is a ‘‘long distance displacement’’ recovery technique that uses a combination of chemical reaction, and heat, mass and momentum transfer to mobilise the highly viscous oil for production. Air is injected through vertical injection well which is usually located hundreds of meters away from vertical production well (Fig. 2.1). The injected air is used to oxidise part of the oil to supply the heat required to lower viscosity and upgrade the heavy oil (Moore et al., 1995). One of the distinct features of in-situ combustion is the utilisation of highly viscous, immobile, and

unproducible part of the oil to fuel the process. The highly viscous residue produced due to, mainly, thermal cracking is termed coke, and is oxidised at temperatures of more than 400 ^{o}C (Burger et al., 1985). Propagation of combustion is sustained by continuous air injection into the formation. All the displaced oil has to travel over long distances, banking on the thick cold oil layer downstream of combustion zone, before reaching the production well. A comprehensive review has been carried out by Turta and Singhal, (2004) with attention specifically paid on the merits and demerits of the different short and long distance displacement processes in terms of gas override, channelling, and mobility ratio. In conventional ISC, there is always the possibility of gas override due to buoyancy effect. This could lead to premature termination of the process as the combustion efficiency would significantly be affected by oxygen breakthrough (Xia et al., 2005; Greaves et al., 2008).

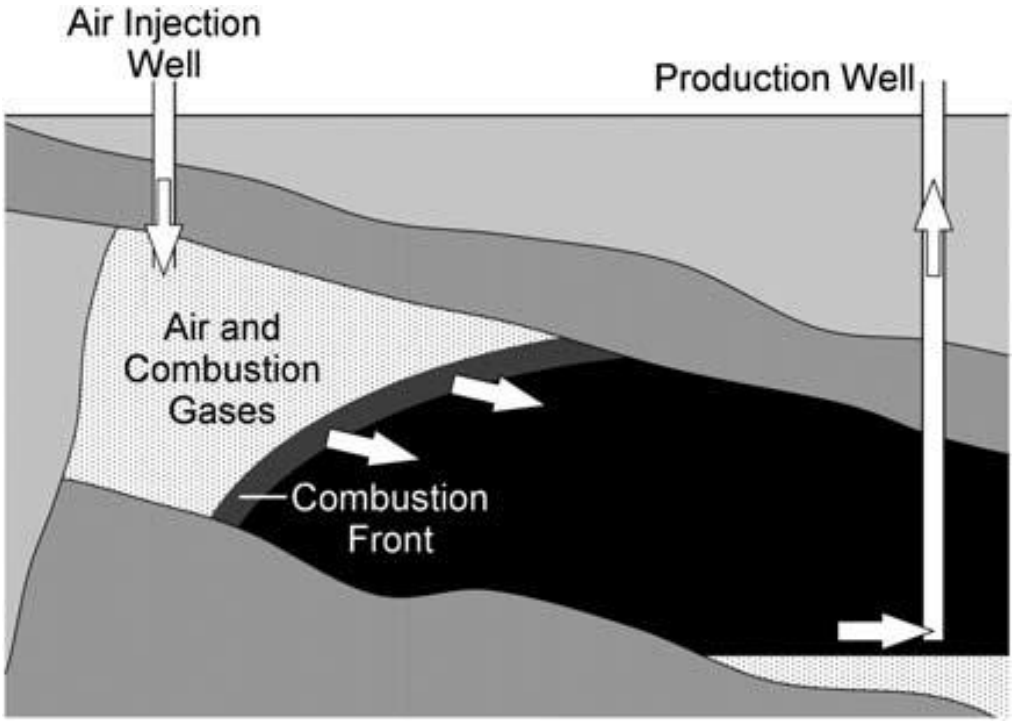

Fig. 2.1: Typical arrangement in forward conventional in-situ combustion (Shah et al., 2010)

Conventional ISC can either be forward or reverse ISC. The former involves the flow of injected air and advancement of combustion front in the same direction (i.e. towards the producer) while the latter has air flow counter-current to combustion front's advancing direction. However, according to Turta, (2014), only forward ISC has been applied at commercial scale. Among the many ISC projects over the last six decades, those in Suplacu de Barcau, in Romania, Balol and Santhal, in India, and Bellevue, Lu, in the USA, are the most successful. However, conventional ISC has proved to be difficult to control despite the considerable experience obtained over the length of time for which it has been operated. The lack of success recorded over the years has been discouraging. This leads to a substantial decrease in interest in ISC processes despite it having considerable theoretical promise. This is partly due to inadequate understanding of the nature of the process (Greaves et al., 2008).

Conducting conventional ISC in reservoirs with bottom water (BW) presents additional challenges. Few laboratory studies of ISC in the presence of BW have been performed. A review carried out by Turta et al. (2009) reported 12% oil recovery when BW thickness was 20% of oil layer thickness. Gravity override was observed once one third of the distance separating the two wells (i.e. injector and producer) had been swept by the combustion front. The bottom water, depending on it is thickness compared to the oil layer thickness, could act as a strong heat sink that consumes most of the generated heat. As a result, the low oil recovery could be due to vaporisation of water to steam as a result of significant energy consumption by the BW. Another laboratory scale study showed that a water cut of up to 80% was recorded during the test. Continuous decrease in peak temperature, with corresponding increase in oxygen

production, was observed. Maximum CO_2 production was limited to 6 mole% and continuously decreased with increasing oxygen production. The review concluded that combustion propagation in the presence of BW was unstable and could eventually die out. This showed that the excessive water cut indicates that a producer could easily become watered-out as a result of the BW zone acting as a strong source of water, and as a result of the high mobility of the water compared to that of heavy oil. Results from many field scale projects have also not been encouraging. Recovery ranges from 0 to 25% depending on the formation and BW thickness. A numerical modelling of basal combustion performed by Lau, (2001) showed that almost all the mobilised oil close to the oil/water transition zone drained into the bottom water zone. The oil production was observed to be very small because the producer was located above the oil-water interface. However, he observed an increase in oil production when the horizontal well was drilled at the oil-water contact zone. This study showed that the BW zone acts as a strong oil thief zone unless if the producer is located near the BW zone. Therefore, other techniques need to be explored in order to unlock the vast reserves of untapped heavy oil from reservoirs with BW. One of the techniques with such potential is toe-to-heel air injection (THAI) which is discussed in section 2.2.2. However, the effect of BW on THAI has not been investigated. As a result, it is one of the aims of this work to present the results of effect of BW on the THAI process in Chapter 6.

2.2.2 Toe-to-Heel Air Injection (THAI)

Toe-to-Heel Air Injection (THAI) is a variation of conventional ISC that uses horizontal well technology for heavy oil production (Fig. 2.2). In THAI, a combination of an coke combustion reaction, heat-, mass-, and gas- momentum

transfer, and gravity drainage is used to mobilise the heavy oil to the surface (Xia and Greaves, 2002; Turta and Singhal, 2004; Xia et al., 2005; Greaves et al., 2008). It is a ‘‘short distance displacement’’ process that uses horizontal wells for both injection and production (i.e. HIHP configuration). In some cases, vertical injector(s) is/are used with horizontal producer(s) (i.e. VIHP configuration). Different well arrangements were investigated through numerical simulation to explore the feasibility of THAI variants (Lim et al., 2008; Fatemi et al., 2009; Rojas et al., 2010; Anaya et al., 2010). In THAI, prior to air injection, the zone around the horizontal/vertical injection well is heated to create communication between the injector and the producer. This is also to leave behind some of the fuel needed for successful combustion front initiation and propagation (Coates et al., 1995). Once the region around the injector is conditioned and communication established, ignition is achieved, and sustained, by continuous air injection. As a result, a large temperature gradient is created leading to the development of different zones ahead of the combustion front, each with distinct features (Fig. 2.2). The heat released by the advancing combustion front is transported, via conduction and combustion gases, downstream to the mobile oil zone which is located upstream of the cold oil layer. The mobile oil zone, which is preceded by the cracking zone, is the region where the mobilised oil drains to the horizontal producing well. The highly viscous and carbonaceous material which fuels the process is deposited in the cracking zone. The coke is continuously oxidised at temperatures of more than 400 ^{o}C by the advancing combustion front. Because of the well arrangement, the mobile oil does not have to travel over a long distance as is the case in the conventional ISC; the oil is continuously produced as the robust and stable

combustion front propagates. The significant distance between the combustion front and the mobile oil zone is part of what makes THAI a highly safe and stable heavy oil recovery technique.

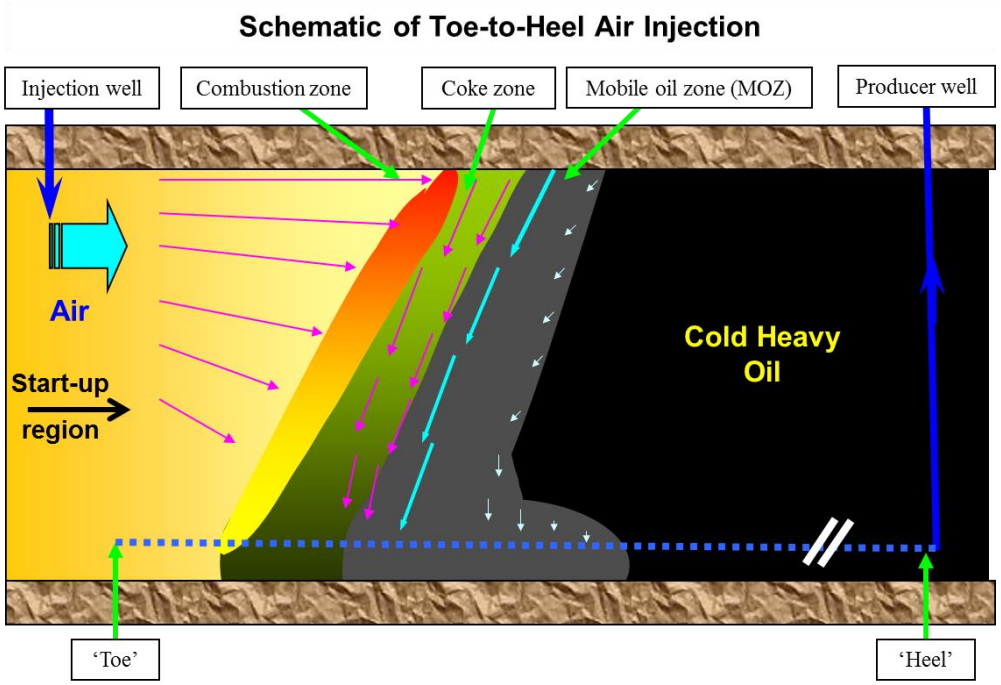

Fig. 2.2: Schematic arrangement in THAI (Xia and Greaves, 2002)

THAI was consistently proven to overcome the problems associated with conventional ISC from more than fifty experiments carried out at University of Bath (Xia et al., 2005). It also has the added advantage of providing significant in-situ upgrading with the possibility of further upgrading via an addition of catalytic upgrading process in-situ (CAPRI^{TM}). The full description of the experimental work on the CAPRI can be found in Xia and Greaves, (2002) and it is review is presented in section 2.2.3. THAI process was shown to be highly efficient as more than 80% of oil originally in place (OOIP) is usually recovered. Many variables, such as optimum fuel laydown ahead of the combustion front, optimum pre-heating prior to air injection, continuous air injection, etc., have been identified as affecting the stability of combustion front

propagation and sustenance. The main advantages of THAI and the conditions for process stability are summarised elsewhere (Turta and Singhal, 2004; Xia et al., 2005; Greaves et al., 2008; Gutierrez et al., 2009).

Apart from the many laboratory scale experiments, the first field scale THAI project was carried out in 2006. The project was in Conklin, in the Athabasca oil sand, one of Canada's large oil sand deposits. Nine months after the initiation of the process, combustion front peak temperatures were around 700 to 800^{o}C. The rate of advancement of the combustion front was around one-quarter of a metre per day. The oil production rate, after two years, was up to 2000 barrels/day with partial upgrading by 8 ^{o}API (Greaves et al., 2008). Since then, many THAI field pilot projects have been developed. Examples include the two Petrobank projects, namely: Kerrobert project, which has been on production since 2011; and the Dawson demonstration project, which was on cold production (i.e. primary oil production as the oil is mobile and can flow at the reservoir conditions) in late 2012. In the case of the latter, production was found to be uneconomical as the combined cold production rate averaged at 10 barrels of oil per day (bopd) in the second quarter of 2013. Petrobank has filed application for approval to initiate Cyclic Steam Stimulation (CSS) to better condition the reservoir for THAI operation (Petrobank, 2013). The Dawson project has been on CSS operation since December of 2013 and production was expected to start in the second quarter of 2014. However, after the takeover of Petrobank by Touchstone in the first quarter of 2014 (Petrobank, 2014a; Petrobank, 2014c), the company terminated the Dawson CSS project (Touchstone, 2014) before disposing it of in the second quarter of 2015 (Touchstone, 2015b). In contrast, the upgraded oil production from Kerrobert

THAI project, as at the first quarter of 2014, averaged at 335 barrels of oil per day (bopd) (Petrobank, 2014b). However, despite the high production rates, combustion propagation was not optimally achieved. The failure to establish a well-structured combustion front was thought to be due to inadequate pre-heating prior to air injection. Petrobank announced that they intended to suspend Kerrobert THAI operations in the event that proper combustion propagation was not established in the second quarter of 2014 (Petrobank, 2014b). However, as at the third quarter of 2015, the project was still going on with average daily production of 100 bopd (Touchstone, 2015a). By the first quarter of 2016, the Kerrobert project was disposed of due to operating losses (Touchstone, 2016). Despite the fact that THAI was proven to effectively solve many problems associated with conventional ISC, and offer many advantages over other recovery techniques, a lot has to be done to fully realise its theoretical promise. Many numerical models have been validated using laboratory scale combustion experiments. The models allow inference to be made that the likely mechanism of fuel deposition and consumption taking place at small laboratory scale would be taking place at full field scale. Anaya et al. (2010) have carried out simulation studies for pilot plant design. They developed a 'workflow' model in which combustion tube results were applied to a field scale model, and important parameters, such as well configurations, injection rates etc., were identified. The model was to be used at one of Venezuela's largest heavy oil deposits in the Orinoco Belt for pilot testing by the Venezuelan National Oil Company. The level to which the project has reached is not clear as information about its progress was not found.

Numerical simulations, which were validated against a 3D combustion cell experiment, were reported by Greaves et al. (2012a; 2012b). Important parameters, such as oil production rate, cumulative oil production, peak temperature variation, API gravity of the produced oil, produced oxygen concentration, etc., required to adequately scale the experiment up were monitored and compared with model predictions. Some good matches were obtained though the peak temperature and cumulative oil production rates were over-predicted. However, the model did not closely match the time at which oxygen production began. The concentration of deposited fuel, which is essential to the success of THAI operation, was not accurately predicted. Using the validated model, a field scale simulation was performed in which production limits to THAI were identified (Greaves et al., 2012c). Factors affecting the safety (i.e. oxygen breakthrough) as well as the economy (i.e. cumulative oil recovery, air to oil ratio, etc.) of the process were evaluated and the duration at which the process should be terminated determined. However, reservoir heterogeneity and bottom water were not considered, and the velocity of the combustion front, which was scaled linearly, was used to evaluate the various parameters, such as oil recovery, produced oxygen concentration etc. This would introduce significant error in the predictions as combustion front expands not only in one but in all the three directions. It implies that distance traversed, along the horizontal producer, by the combustion front would not allow the total combustion time to be determined with certainty.

Another ‘workflow’ model, which involves performing a series of screening to determine the possibility of successful combustion front propagation, and hence kinetic parameters was developed by Kovscek et al. (2013). A numerical

simulation model was then developed and validated against combustion tube experiment. However, only a qualitative match was observed since the model was not rigorous enough to match the experimentally determined parameters (i.e. the peak temperature, & gas composition). Predicted peak temperature overshoots the experimental value by up to 330 ^{o}C and different events, e.g. the peak temperature reaching maximum value at a given location, were predicted to happen at different times (i.e. model prediction of the events lagged the experimental). The fuel concentration predicted by the model was extracted, predefined, and then used as basis for non-Arrhenius upscaling. However, the real mechanism of fuel deposition at fields was not captured since the fuel is deposited as the process takes place rather than before it starts to take place. Also important parameters such as heating rate, air flux, reservoir geology, which are critical to successful in-situ combustion, were not considered during the model upscaling.

The success, or otherwise, of field scale in-situ combustion is solely dependent on accurate predictions of air injection rates, fuel deposition rate, oil production rates, and the combustion propagation rate. This has become quite difficult because of the significant uncertainty associated with kinetics of the process. Due to the complex nature of hydrocarbons, it is impractical to use kinetics explicitly based on the full number of compounds. Therefore, pseudo-components, based on boiling point range, are used. However, further uncertainty is introduced by the fact that different kinetics schemes lead to different predictions. This leads to the question as to which kinetics can reliably predict the critical parameters needed to upscale laboratory experiments to field scale. The reliable kinetics will allow the sensitivity of the predicted parameters,

such as oil rate, peak temperature, produced oxygen concentration, etc., to changes to initial reservoir viscosity, relative permeability, method of pre-heating (i.e. electrical or steam injection), and to the grid size to be investigated. The main objective of this work is partly to try to answer the posed questions.

2.2.3 Catalytic Upgrading Process In-Situ (CAPRI™)

Many laboratory studies have been, and are being, performed towards understanding down-hole catalytic upgrading of heavy oil or tar sands (Weissman et al., 1996; Cavallaro et al., 2008; Shah et al., 2011; Hart et al., 2013; Hart et al., 2014b; Abu et al., 2015; Hart et al., 2015; Dim et al., 2015). THAI's catalytic add-on process in-situ, known as CAPRI™, involves packing, around the horizontal production well, an industrial hydroprocessing catalysts to remove impurities (such as Sulphur, Nitrogen, Heavy Metals) and achieve further upgrading in-situ. A typical CAPRI arrangement is shown in Fig. 2.3. The partially upgraded THAI oil, formed due to heat from combustion (thermal cracking), serves as the reactant that must contact the catalyst bed for catalytic upgrading to take place. This is very important as it has the advantages, among others, of lowering surface upgrading requirement, providing easily transportable oil, environmentally friendly operations etc. A comprehensive review about downhole catalytic upgrading and the many challenges needed to be overcome before it can be fully implemented at field scale was given by Weissman, (1997).

Many laboratory studies have been conducted to study the performance of in-situ catalytic upgrading during either combustion tube, or 3D combustion cell, experiments. Xia and Greaves, (2001) studied downhole catalytic upgrading of

Wolf Lake heavy oil. Apart from 10 ^{o}API increase due to thermal upgrading, they achieved a further upgrading by 4 to 7 ^{o}API using Nickel-Molybdenum (NiMo) or Cobalt-Molybdenum (CoMo) HDS catalysts. Substantial viscosity reduction from the partially upgraded THAI oil was observed. Application of CAPRI to Lloydminster heavy oil resulted in an overall upgrading by 11.6 ^{o}API (Xia et al., 2002b). The highest upgrading was obtained with regenerated CoMo HDS catalyst. Similarly, the reduction in viscosity was also very substantial. An analysis of the extent of upgrading, and the properties of the upgraded oil from 3D combustion cell experiment was carried out by Greaves et al. (2004). Quantitatively, they showed that the sulphur, nitrogen, and metals content of the produced oil were significantly reduced compared to what was in the original oil. The overall oil quality in terms of API gravity and viscosity was substantially improved. However, the fate of the removed sulphur, nitrogen and the heavy metals has not been determined. Moreover, the effect of catalyst on the fluid flow and coke deposition around the horizontal producer was not studied. On the other hand, it was noted that the amount of residual solid carbon was increased by 3 to 6 times during the CAPRI process. The reaction temperature around the catalyst needs to be at least 300 ^{o}C for effective catalytic reaction to take place with HDS catalyst (Weissman, 1997). Specifically, Shah et al. (2011) has determined that the optimum temperature to maximise the catalyst life, and achieve appreciable upgrading is 420 ^{o}C. From the reported results, it is unclear whether the temperature range was reached due to heat generation from in-situ combustion or due to application of heat from an external source during the experiments.

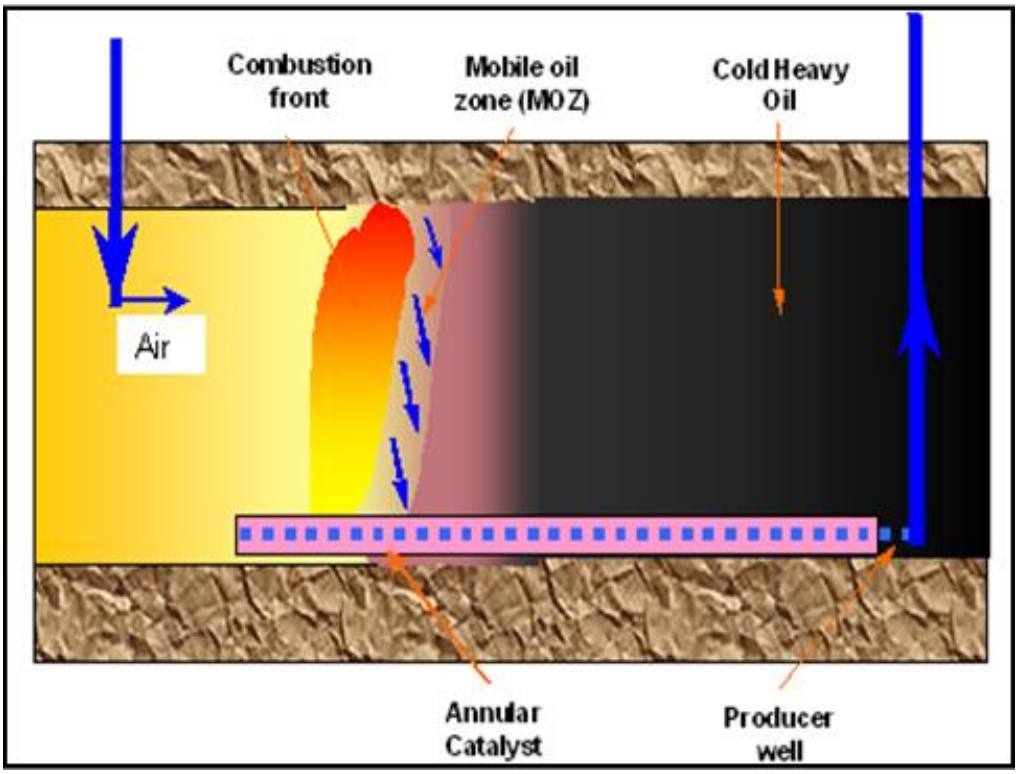

Fig. 2.3: Schematic arrangement in THAI-CAPRI process (Turta, 2014)

Another experiment conducted by Cavallaro et al. (2008) installed a heated bed of catalyst downstream of a combustion tube. Delayed oil production was observed as a result of catalyst packing downstream of combustion front. Once oil production was started, and the combustion front approached the catalyst bed, the bed was heated to a temperature of 330 ^{o}C, from external heaters, over a specific time period. An increased oil production rate was observed which was the result of the external heating. After the bed became effective, a reduction in heteroatoms in the produced oil was observed. As in the case of the 3D combustion cell experiments reviewed above, substantial viscosity reduction and increase in API gravity were achieved with the NiMo catalyst. One major source of concern during this experiment was the excessive pressure drop observed. This could be due to pore blockage as a result of increased coke deposition, as reflected in the reported fuel concentrations for combustion tube

experiments with and without catalyst bed. It, therefore, became difficult to conclude whether the substantial upgrading is solely due to catalytic action or the low oil mobility and high temperature combustion resulting in significant thermal cracking.

In further experimental studies, carried out by Shah et al. (2011), on the optimisation of in-situ catalytic process (CAPRI), severe limitations to the life of catalyst were observed as a result of coke deposition on the catalyst surface. The experiment was run in a catalytic reactor operated at pressure of 20 to 60 barg and temperature of 380 to 500 ^{o}C in the presence of hydrogen gas. Partially upgraded heavy oil from THAI pilot testing with API gravity of 13 was used. At optimum temperature of 420^{o}C, only a maximum of 3 ^{o}API upgrading was obtained with catalyst life of roughly 3.25 days. They concluded that coking, which leads to catalyst pore blockage, occurred at very early stage while the upgrading was taking place. However, the observed degree of upgrading could be as a result of thermal cracking which increased with increase in the system temperature. As observed from the experiment, substantial pressure drop occurs with increase in reaction temperature as a result of severe coking.

In all the CAPRI studies, catalyst pore blockage has been identified as one of the major problems affecting its performance. Numerical simulation needs to be performed to investigate how THAI is affected by the installation of a catalyst bed around the horizontal producer. Catalytic reaction must then be included to investigate by how much the THAI oil can be upgraded due to the catalyst emplacement around the producer. However, the above identified issues can only be investigated numerically if robust heteroatom removal kinetic is available. As during surface catalytic cracking, the presence of hydrogen is a

necessary requirement for in-situ catalytic cracking. In the case of in-situ combustion, hydrogen is thought to be generated as a result of thermal cracking and water-gas shift reaction (Weissman, 1997; Shah et al., 2010; Kapadia et al., 2013; Abu et al., 2015). Therefore, kinetic studies solely from in-situ combustion which incorporate hydrogen gas generation would be of use. Another major area of concern is the fact that numerical simulations have shown that the temperature around the mobile oil zone ranges from 100 to 200 ^{o}C (Greaves et al., 2012b). This is lower than the temperature at which the HDS catalysts are effective (Weissman, 1997). Since the mobile oil zone is where further catalytic upgrading is envisaged to occur, it is also the aim of this work to investigate how to increase the catalyst bed temperature around the mobile oil zone.

In addition to catalytic downhole upgrading during in-situ combustion, Ovalles and Rodriguez, (2008) conducted experimental, as well as numerical, studies on the use of hydrogen donor additive for in-situ catalytic upgrading during cyclic steam stimulation (CSS). During the experiment, a mixture of a hydrogen carrier called ‘tetralin’, heavy oil, and methane was injected into a heated sand-containing reactor and a delay time allowed before analysing the results. Based on measured quantities and the experimental observations, a kinetic scheme describing the mechanism of hydrogen addition was developed. The kinetic scheme was then used to numerically simulate CSS and the upgrading effect of hydrogen donor addition. Results showed that, in the presence of methane and mineral formations, a 3 API gravity increase was observed. It was further observed that the asphaltene content, and hence the oil viscosity, decreased with increase in tetralin conversion which also increase with temperature. This shows

the possibility of using liquid hydrogen carriers to deliver the needed hydrogen for CAPRI process.

2.2.4 Electric Inductive and Resistive Heating

Extensive studies on the use of electrical heating to upgrade and produce heavy oil have been carried out. Vermeulen and coworkers, (1983; 2000) studied, through numerical simulation, the temperature distribution in electrically heated heavy oil reservoirs. They observed that the distance into the reservoir that heat had penetrated depends on the kind of electrical heating method (i.e. either inductive or resistive heating) employed. Inductive electric heating involves heat generation as a result of induced current flowing through electric cables placed in a wellbore. In this method of heating, conduction is the main mechanism through which heat is distributed within the reservoir. The main disadvantage of this method is the fact that heat is distributed over a very small distance compared to in the case of resistive heating.

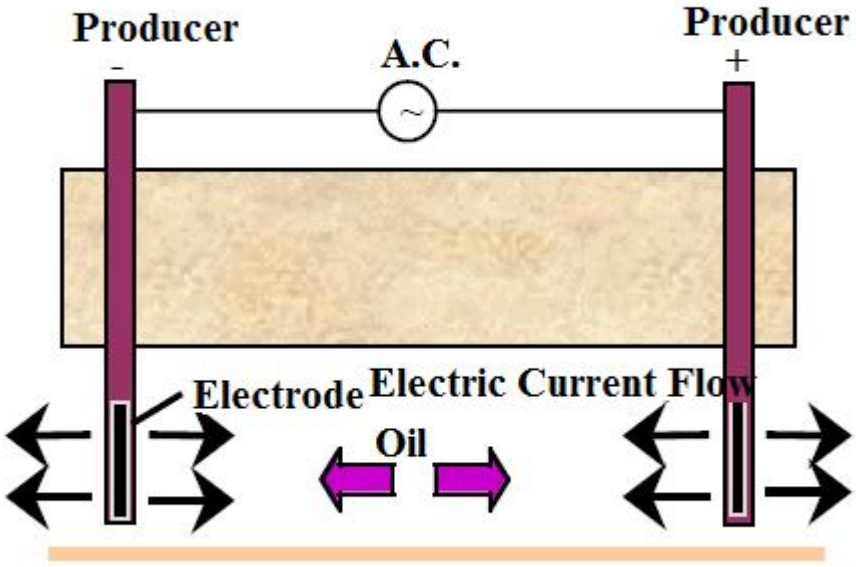

Fig. 2.4: Typical Arrangement for In-Situ Electric Resistive Heating for Heavy Oil Recovery adapted from Sahni et al. (2000)

Electric resistive heating takes place when a low frequency alternating current is forced to flow between two electrodes installed in the reservoir. The heat generation is due to ionic conduction through the continuous water-saturated part of the reservoir. A typical arrangement used in electrical resistive heating is shown in Fig. 2.4 in which two vertical producers act as cathode and anode electrodes respectively. Application of potential difference across the two electrodes resulted in a creation of electrical path via the reservoir water. However, water vaporisation in the vicinity of the electrodes as a result of high temperature is one of the major disadvantages of this method. The heating ceases once the water path is broken. Another drawback of the electric resistive heating, which Vermeulen and McGee, (2000) did not consider in their simulation, is it is dependence of the homogeneity of the water saturation across the reservoir. This means that presence of shale, where the water saturation is unity, could result in uneven temperature distribution, and this could in turn disrupt the flow of current to certain part of the formation. Sahni et al. (2000) showed that presence of shale resulted in an elongated heated zone, and consequently, the location of the wells, in reference to that of high water-saturation zones, must be optimise when implementing this recovery technique. Comparing the effectiveness of heat penetration into the reservoir, Vermeulen and McGee, (2000) defined a ‘‘heated radius’’ as the distance, further away from the electrodes, at which the temperature has increased by 10 ^{o}C after five years of heating. The simulation study showed that the heated radius when resistive heating was employed is more than five times compared to if inductive heating was implemented.

Rangel-German et al. (2004) carried out simulation studies on the use of electric heaters in the form of mineral insulated cables to upgrade and produce heavy oil. As conduction is the main mechanism through which heat distribution takes place and therefore heat transportation is highly influenced by the reservoir, as well as, the fluid, thermal conductivities. As the heating is highly localised, they explored various heater/injector/producer arrangements to ensure optimum recovery. Though it depends on reservoir properties, part of the heat supplied by the electric heaters was 'convected' out by the immediately produced oil when the heater was located inside, or too close to, the producer. Hascakir et al. (2010) performed an experiment to investigate the use of iron powder, in combination to electrical heating, to increase thermal conductivity of heavy oil. A decrease in the viscosity of the heavy oil, which has been thought to be the result of exothermic reaction between the iron powder and the oil impurities, was observed. The reduction in the heavy oil viscosity was also observed to be the result of reduction in the fraction of the polar components, which caused a decrease in hydrogen bonding, of the heavy oil. However, the mechanism by which the iron powder is introduced into the reservoir at field scale has not been studied. They also performed field scale numerical simulation to study the effectiveness of the electrical heating enhanced oil recovery. They observed that, as conduction being the main mechanism of heat distribution, there was a period beyond which no increase in oil production occurs. At that point, increasing heating rate does not lead to increase in oil production either.

Zhu et al. (2013) studied, using numerical simulation, a hybrid system in which electrical resistive heating was used in combination with solvent injection to recover heavy oil. They showed that the hybrid process resulted in more oil

recovery compared to when either of the processes was used alone. This is because the injected solvent reaches, and lowers the viscosity of the unaffected, and thus unheated, oil zone, where the resistive heating could not reach. More so, the heater/injector arrangement with producer placed close to the base of the reservoir resulted in higher recovery. Also, Rangel-German et al. (2004) has made the same observation about the fact that placing the heater inside or close to the producer results in low recovery as part of the heat is transported out of the reservoir. However, one possible advantage of placing the heater close to or around the producer will be when a bed of catalyst is wrapped around the horizontal producer as in the case of in situ catalytic upgrading (CAPRI^{TM}). The heater cables can be wrapped around, or embedded in, the hydro-treating catalyst bed. Electrically conducting catalyst that could serve as the 'cable', through which the flow of induced current results in heat generation, could be used as self-heating bed for the CAPRI^{TM}.

2.2.5 Electromagnetic Heating

Electromagnetic (EM) heating involves the use of high frequency in the form of microwave energy to decrease heavy oil viscosity and mobilise it to the surface. Many lab-based, as well as field pilot scale experiments, were performed to investigate the mechanism and applicability of microwave heating technology in heavy oil recovery. Vermeiden and Chute, (1983) performed measurements of thermal as well as electrical properties of Athabasca bitumen to explore the various conditions under which in-situ electromagnetic heating is effective. The main parameters identified as playing a decisive role in the selection of electromagnetic heating are depth of penetration, wavelength, and loss tangent, which is the ratio of electrical conductivity to the product of dielectric constant

and angular frequency. At a particular frequency, depth of penetration of an EM wave in oil sand and the wavelength of the wave give an indication of how uniformly a reservoir can be heated in a given antennal arrangement. On the other hand, the loss tangent gives a measure of whether a given antennal arrangement would result in EM wave propagation or not. At a particular frequency and a given antennal arrangement, loss tangent also allows determination of whether the distance at which the electromagnetic wave is fully attenuated is comparable to or less than a wavelength. For significant EM wave propagation to take place, the loss tangent should be less than unity implying that the dielectric constant is dominant compared to electrical conductivity. This is often the case when the moisture content of the formation is low and hence the electrical conduction becomes low.

As the penetration depth of an EM wave into the formation is quite small compared to that of electrical resistive heating at high frequency (Vermeulen and Chute, 1983; Vermeulen and McGee, 2000), the common arrangement is to place the microwave antenna close to the producer. A typical arrangement is shown in Fig. 2.5 where the microwave antenna is located close to the producer so that the fluids are continuously heated as they are being produced. Simulation studies carried out by Sahni et al. (2000) investigated the temperature distribution, as well as oil recovery, as a result of microwave heating with frequency of 0.915 GHz and at a power of 60 kW. An increase in temperature by 150 ^{o}C was observed around the antenna within a year of heating. At a distance of 18.3 m, the temperature increased by 38 ^{o}C after five years of heating. However, the localisation of heat around the antenna can cause serious damage to the encasing material. It also means poor energy distribution since

part of the heat will be conducted, as opposed to electromagnetically transported as a wave. In a critical review carried out by Chhetri and Islam, (2008), it was pointed out that a study on heavy oil recovery from thin pay zones by Jha and Chakma, (1999) showed that presence of water is desirable for uninterrupted wave propagation. This could be due to its high dielectric constant compared to that of oil. Therefore, heat localisation around the antenna could result in steam formation due to vaporisation of the surrounding water.

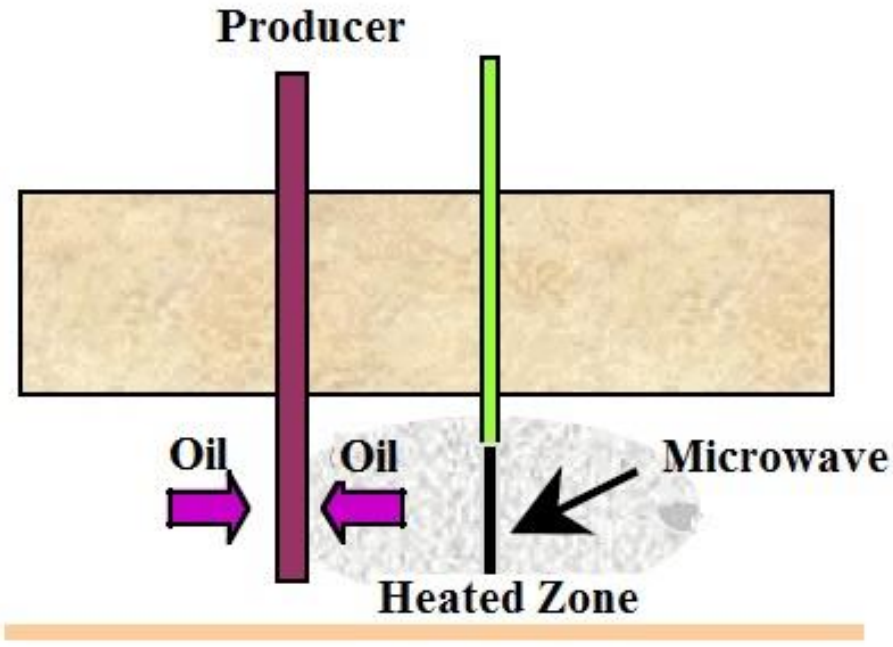

Fig. 2.5: Typical arrangement in Microwave In-Situ Heating adapted from Sahni et al. (2000)

The problem of high temperature localisation around microwave antenna was studied by Bientinesi et al. (2013). They conducted a large scale experiment over two weeks period to study temperature distribution, oil displacement and effectiveness of ‘‘low lossy’’ quartz sand in limiting extreme temperatures around the casing. Results from the experiment performed at a frequency of 2.45 GHz and power of 1 to 2 kW showed that the quartz shale is effective in

limiting the increase in temperature around the antenna. The temperature of the shale was observed to be always lower than the maximum temperature realised in the oil sand. On installing insulating rock-wool around the metallic walls, the temperature in the whole system increased as a result of substantial decrease in heat loss to the surroundings. The oil displacement observed was not significant. However, the study did not consider oil production and hence how the flow out of the system affects the temperature distribution as well as the effectiveness of the shale material in limiting the rise in temperature around the antenna.

Microwave heating has the advantages of being independent of thermal conductivity of heavy oil and the reservoir permeability. It can be used for selective heating – heating a specific region to minimise heat loss. It can be used for start-up in fluid injection recovery techniques. However, microwave heating has the disadvantage of having very low global efficiency (i.e. overall efficiency considering electricity generation up to conversion to high frequency electromagnetic wave) (Chhetri and Islam, 2008).

The high temperature localisation around microwave antenna can be beneficial if a bed of catalyst is wrapped around a horizontal producer, as is the case for CAPRI^{TM}. The microwave antenna can be placed very close to, or embedded in, the catalyst bed wrapped around the horizontal producer. This will help in raising the temperature of the catalyst bed to 350 to 420 ^{o}C so that it becomes effective.

2.2.6 In-Situ Conversion Process (ICP)

ICP is owned by Shell as an alternative technology used to enhance natural maturation of kerogen contained in oil shale. The company has been working

on ICP since 1980 and over 70 US patents have been granted. In-situ electric resistive heating is used to convert kerogen into lighter hydrocarbons that require less surface processing to be converted to transportation fuels such as gasoline, jet fuel etc. A so-called 'freeze wall' is installed by circulating chilled fluid at -43 ^{o}C in a closed loop piping system to prevent flow of ground water into the heated zone. This could be to ensure that there is no excessive heat loss to the flowing ground water, the ground water is not polluted, and to prevent displacement of the mobilised oil by the water. Trapped ground water in the freeze wall is removed via newly drilled producer holes (Shell, 2006; Lee et al., 2007; Brandt, 2008). Holes are then drilled around the targeted formation to install electric heaters. The formation is then heated for many years, depending on the rate of heating, to temperatures of 288 to 400 ^{o}C. At Oil Shale Test (OST) project site, a rate of heating of ≈ 0.5 ^{o}C per day was used, implying that the complete conversion at ≈ 350 ^{o}C will occur in two years (Brandt, 2008). Over the years, kerogen is thermally cracked into high API gravity hydrocarbon via in-situ hydrogenation. Geological as well as thermodynamic parameters were monitored over many years. Upgraded oil and gas is produced through the already drilled producers and processed in surface facilities.

A small field-scale test was carried out to demonstrate the feasibility of the process (Shell, 2014). Around 1700 barrels of high quality oil was recovered from an area of 1,200 ft^2 showing that it works at small scale. Shell aims to continue to develop the technology up to the point when it could be deployed at full field scale (Shell, 2014). The advantages of ICP include production of high quality products due to slow heating and limitation of temperature to that of the boiling point of diesels, elimination of surface or underground mining, creation

of no leftover piles of mine tailings, and it has low water requirement. The disadvantages include an excessive electricity requirement, which would lead to substantial greenhouse gas (GHG) emissions (Brandt, 2008), taking long period of time before production starts, and hence requires long term investment, the possibility of ground water pollution at field scale, and that substantial work is needed to prove its operability at large scale.

2.2.7 Steam Assisted Gravity Drainage (SAGD)

Steam Assisted Gravity Drainage (SAGD) is a fluid injection in-situ recovery technique which uses thermal energy from injected steam to mobilise heavy oil for production. The typical SAGD arrangement is shown in Fig. 2.6. Steam is injected through a horizontal injector well which is usually located 5 m above a parallel horizontal producer so that the mobilised heavy oil is gravity-drained to the producer (Mojarab et al., 2011; Liu et al., 2014). SAGD has been used to recover heavy oil at field pilot as well as full commercial scale with varying degree of successes. In some of the field pilot cases, SAGD was shown to not be a net energy producer (Gates and Larter, 2014). Cenovus Energy (2014) has two SAGD projects located at Foster Creek and Christina Lake respectively. The company claimed that the two projects have a combined Steam to Oil Ratio (SOR) of 2.1 as at 2012. In the case of Athabasca oil sand, laboratory tests showed overall recovery of 50% of oil initially in place. The SOR lies in the range of 1 to 3 cm^3 steam per cm^3 of recovered oil at standard condition (Turta and Singhal, 2004). Despite the apparent high recovery, a lot of oil was still left unrecovered due to the process becoming uneconomical during the steam spreading phase. This is the phase when significant portion of the injected steam is lost to, heating the depleted reservoir rock or channelling into an already fully

developed steam chamber thereby resulting in very low rate of oil production per m^3 of injected steam. There are also many factors that heavily affect the performance of the process e.g. reservoir thickness, permeability, heterogeneity, steam chamber growth rate etc. This ultimately results in restricted application to selected reservoirs (Paitakhti Oskouei et al., 2011; Shah et al., 2010; Turta and Singhal, 2004). In addition to these factors, the SAGD process is quite energy intensive and a large quantity of greenhouse gas is emitted to the atmosphere during the surface steam generation. It also requires significant quantity of water which could be detrimental to the nearby environment.

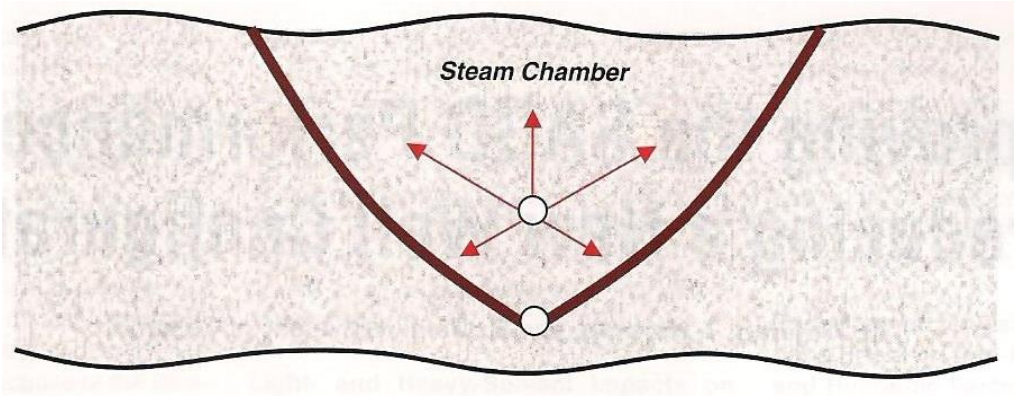

Fig. 2.6: Typical injector/producer well pair arrangement in SAGD process (Mojarab et al., 2011)

A laboratory scale study on the applicability of SAGD to reservoirs with bottom water was carried out by Saskoil and Butler, (1990). When no BW was present, a cumulative oil recovery of 87% OOIP was observed, compared to a recovery of 48% OOIP for a model with a BW thickness that was 41% of the total (i.e. BW and oil layer). From the temperature of the produced fluid, it can be deduced that a significant part of the injected steam was lost to the BW. This is so because the increase in produced oil temperature was delayed by more than twice the time that it took for the produced oil temperature to start to rise in the situation where no BW was present. Also, from the recovery curves, it can be

observed that an uneconomical SOR was reached at an earlier stage compared to when no BW was present. A numerical simulation performed by Liu et al. (2014), to study the feasibility of SAGD process in offshore reservoirs with BW, also showed a decrease in ultimate recovery by up to 10% OOIP.

Reservoir heterogeneity and other operational restrictions have been observed to cause an unequal growth rate in the steam chambers for SAGD pattern. The process efficiency is significantly reduced once injected steam from the developing chamber starts to leak into a fully developed chamber. Therefore, there is a need to develop a solution that could not only prevent steam dissipation but also lead to increased recovery. In-situ combustion was considered by Paitakhti Oskouei et al. (2011) as one of the possible remedies that would create low permeability zone around the fully developed chamber. Conducting in-situ combustion in a depleted SAGD steam chamber was observed to result in an increase in oil recovery by ≈ 30% of that produced from during the SAGD operation. It is important to note that the combustion operation lasted over a time period that is 14% of the total time over which the experiment was run. A post-mortem examination of the model revealed that a coke layer was formed around the edges of the steam chamber. However, it has not been shown whether the coke and asphaltene rings, formed around the perimeter of the fully developed steam chamber, are effective in providing the necessary sealing to prevent steam breakthrough.

Overall, to ensure smooth heavy oil supply and high recovery rates, a more generally applicable and energy efficient recovery process must be used. This is so when the fact that certain reservoirs are not suitable for SAGD process is

considered and that around 50% of the oil in reservoirs accessible to SAGD process remained unrecovered.

2.2.8 Cyclic Steam Stimulation

Cyclic Steam Stimulation (CSS) involves injection of high pressure steam into reservoir formations for heavy oil mobilisation and production. The injected steam is allowed to soak over period of 1 to 9 months (Ali and Meldau, 1979; Ali, 2003; Petrobank, 2014b) in order for the heat released by the condensing steam to be distributed within the reservoir. Once the oil becomes mobile, the well is then put on production as can be seen in Fig. 2.7.

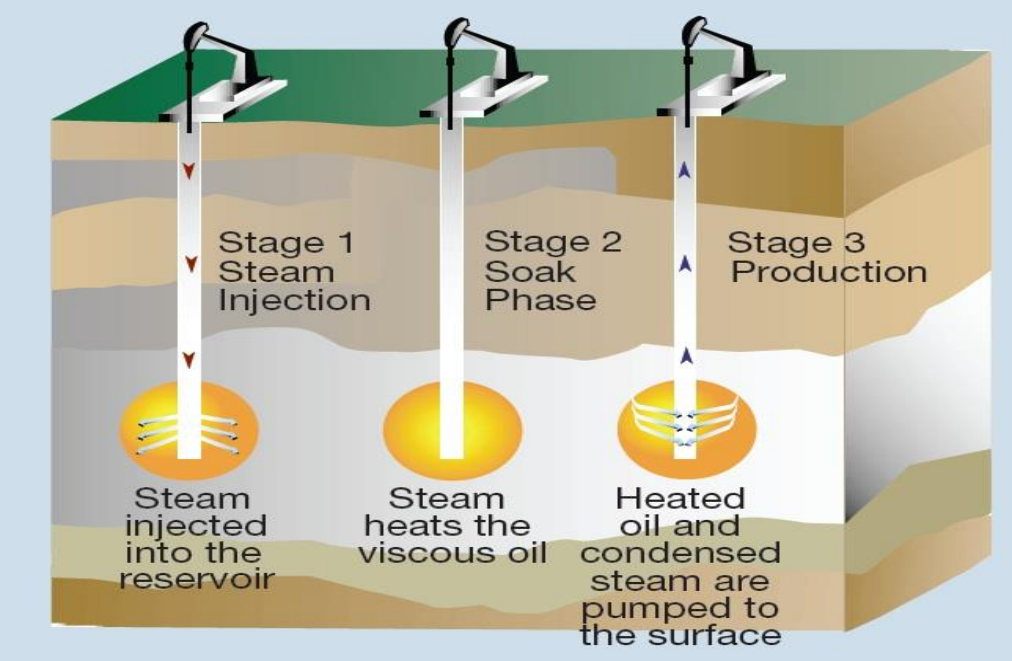

Fig. 2.7: Typical Cyclic Steam Stimulation Process (CAPP, 2015)

The producer can also be an injector well used during the injection of the high pressure steam (Gates and Larter, 2014), or a separate producer in an injector/producer well pair (Shah et al., 2010). The oil production rate usually becomes uneconomical after several months of production. The cycle is then

repeated with steam injection, soaking, and then production until steam to oil ratio ranges over 3:1 to 4:1 during the process (Shah et al., 2010). As a result of high steam pressure, very thick overburden rock layer is typically required for CSS to be implemented. Also, the CSS process is sensitive to reservoir geology. Heat distribution is mainly restricted to the vicinity of the steam induced fractures. Recovery factors are in the range of 10 to 40% compared to in-situ combustion which has recovery of up to 80%.

2.2.9 Analysis

Overall, considering the merits and demerits of the different thermal recovery processes, it can be concluded that THAI and its catalytic add-on process, CAPRI, hold substantial promise. If they are adequately understood, and, hence, fully developed, they will help in efficiently meeting the increasing energy demand with low overall greenhouse gas emissions. A model that accurately predicts the actual processes will not only help save time during scale up but will also substantially lower design costs. However, what has been one of the greatest challenges is the development of a reliable simulation models from both laboratory experiments and pilot plant tests that will lead to comprehensive understanding of the processes. The significant uncertainty associated with the type of kinetics scheme used in the model is also partly responsible for the lack of understanding. With a reliable model, all the parameters that could affect the performance of THAI such as reservoir bottom water, gas cap, and heterogeneities can be investigated. The reliable model could also allow the feasibility of implementing electrical or microwave heating around the catalyst bed, during CAPRI, to be studied.

2.3 Kinetics of Toe-to-Heel Air Injection (THAI)

The study of air injection enhanced oil recovery is mostly carried out at laboratory scale. This is usually performed by the use of either combustion tube (Martin et al., 1958; Alexander et al., 1962; Lin et al., 1984; Coates et al., 1995; Bagci and Kok, 2004; Razzaghi et al., 2008; Yang and Gates, 2009; Kovscek et al., 2013) or 3D combustion cell (Xia and Greaves, 2002; Xia et al., 2002a; Liang et al., 2012). The experiment helps in understanding the likely mechanism of the processes at field scale. However, even at laboratory scale, the full physics of the processes taking place must be fully understood in order to develop a rigorous model that can be used for scaling up to field scale.

The complexity of the air injection enhanced oil recovery process, as well as the multiphase nature of the flow within the reservoir, makes modelling THAI quite challenging. The kinetics of fuel deposition as well as coke combustion is the main source of uncertainty in modelling THAI. The complex nature of hydrocarbons makes it impractical to develop a 'reliable' kinetics based on the total number of the individual compounds. This necessitates the use of pseudo-components based on the range of boiling points. Many fuel deposition, as well as combustion, kinetics have been proposed for implementation during in-situ combustion modelling (Lin et al., 1984; Adegbesan et al., 1987; Millour et al., 1987; Belgrave et al., 1993; Cinar et al., 2011; Greaves et al., 2012a; Kovscek et al., 2013). Thermal cracking kinetics models on Athabasca bitumen have also been proposed (Phillips et al., 1985; Radmanesh et al., 2008; Kapadia et al., 2013).

2.3.1 Fuel Availability

The main fuel for the sustenance of in-situ combustion, referred to as coke, is the carbonaceous immobile fraction of the bitumen or heavy oil in place. It contains mainly carbon and hydrogen in the ratio of approximately 1:1 per unit (i.e. with relative molecular mass (RMM) of the unit at 13 g/mol). The amount of coke deposited per unit volume of reservoir was shown to be one of the most critical parameters that determines both stability and effective propagation of the combustion front (Greaves et al., 2008). Alexander et al. (1962) conducted a fire flood-pot experiment which showed that the concentration of fuel available during in-situ combustion is not a constant value but varies. It depends on, among others, heavy oil properties, oil saturation, air flux, reservoir properties, sand grain size, time and temperature relationship, etc. Figs 5, 6, & 7 in Alexander et al. (1962) showed the variation of fuel availability with API gravity, Viscosity at 50 ^{o}C, and atomic Hydrogen to Carbon (H/C) ratio respectively. Generally, the fuel availability increases with increase in bitumen viscosity, which in turn is due to increase in the fraction of a coke precursor. However, as the oil becomes lighter due to increase in API gravity or H/C ratio or both, the fuel availability becomes lower. Typically, for Athabasca bitumen, (which has H/C atomic ratio, viscosity at 50 ^{o}C, and an API at 25^{o}C of 1.53, 6200 cP, and 9 points respectively), the fuel availability ranges from 50 to 57 kg m^{-3}. However, it should be noted that the points on Alexander's plots are quite scattered and should, therefore, be used with caution.

Lin et al. (1984) carried out a numerical simulation study of combustion tube experiments, and they showed that the fuel availability depends on the catalytic nature of the reservoir minerals. Oil properties, most especially the phase

equilibrium constant of components, significantly influence the amount of coke deposited per unit volume of a reservoir. During their experiment, they observed coke to be the sole source of fuel. The fuel consumption observed was up to 39 kg m^{-3} of reservoir. Yang and Gates, (2009) validated a numerical simulation model, based on Belgrave et al. (1993) kinetics, against a one-dimensional combustion tube experiment. They claimed to observe that a maximum of 30 kg m^{-3} fuel is deposited from low temperature oxidation (LTO) compared to maximum of 3 kg m^{-3} deposited due to thermal cracking. Belgrave et al. (1993) also concluded, after validating their model against combustion tube experiments, that LTO is the main mechanism controlling fuel availability. However, by critically observing the result presented in Fig. 9 of Yang and Gates, (2009), it can be seen that the location at which coke concentration, from LTO, peaked is the same as that when oxygen mole fraction in the gas phase is zero. Looking further downstream, more coke is deposited when oxygen concentration has already dropped to zero. This implies that the high coke concentration is not as a result of oxygen consumption. In contrast, Alexander et al. (1962) observed that LTO plays a role in coke deposition mainly prior to coke combustion (i.e. during the start-up phase).

Xia et al. (2002a) conducted 3D combustion cell experiments, using Wolf Lake oil, to investigate the effect of oil layer thickness on the performance of THAI. They reported that the fuel consumption is in the range of 13 to 27 kg m^{-3}. However, the amount of residual coke has not been reported. Chen et al. (2012) reported fuel availability of 87 kg m^{-3} after conducting combustion tube experiment. The experiment was designed to investigate the feasibility of in-situ combustion as a follow up to primary cold oil production (CHOPS). Coates

et al. (1995) reported fuel availability of up to 108 kg m^{-3} from their top-down combustion tube experiment using Athabasca bitumen. However, they stated that the excessive coke deposition was due to inefficient drainage of the mobilised oil ahead of the combustion front. Another study performed by Kovscek et al. (2013) used two different kinds of coke to predict the overall fuel available during in-situ combustion. They considered the formation of the coke to be as a result of thermal cracking. From this review, it can be determined that the main mechanism through which the most critical parameter affecting the performance of in-situ combustion (i.e. coke) is deposited is still a contentious issue that needs resolving. Therefore, each claim will be investigated through the development of numerical models. This will allow to ascertain under which set of conditions (i.e. start-up, or when the system is already running) each claim highlighted earlier above is valid.

2.3.2 Cracking and Combustion Kinetics

One of the main sources of uncertainty in modelling in-situ combustion is the accuracy of the fuel deposition, as well as combustion kinetics. Most thermal cracking reactions showed that coke formation is mainly due to either primary conversion of asphaltene or secondary reactions taking place among the cracking products. Solid coke does not form immediately heat is supplied to the heavy oil but after a certain induction period (Levinter et al., 1966; Wiehe, 1993; Cinar et al., 2011). The existence of the induction period depends on the initial asphaltene content of the heavy oil implying that the amount of coke produced is a function of the asphaltene content. The higher the asphaltene content, the more solid coke is formed. A thermal cracking study, on Athabasca bitumen, was carried out by Phillips et al. (1985). They showed that when 'pure'

asphaltene was used as the starting material, a very large amount of coke was produced in comparison to when heavy oil was the starting material. A quite similar observation was made by Zhao et al. (2015)

Jia et al. (2006) developed a kinetic model of thermal cracking and low temperature oxidation reactions using different experimental data. Their model quite accurately predicted the cracking products obtained by Hayashitani el al. (1978). The induction period before coke formation took place was also closely predicted. However, reaction number four (equation 23) was omitted from the reaction scheme in the prediction of experimental product distribution data. No justification for the cause of the omission has been given. It was stated that the experimental data was generated over a long time. This implies that the accuracy of the proposed kinetics scheme is limited to experimental data generated over few hours. Also, there was a significant difference between the experimental and model prediction of oxygen uptake.

An experimental study of LTO of Athabasca bitumen, which was performed by Millour et al. (1987), showed that more coke was deposited when bitumen was used as the starting material instead of any of the bitumen pseudo-components. The coke formation was observed to take place after some induction period. They also observed that at temperatures of more than 175 ^{o}C, the reaction order with respect to oxygen concentration tended to zero. It implies that once a certain high temperature is reached, LTO is insignificant and, hence, has no effect on the process. In another study carried out by Adegbesan et al. (1987) on LTO of Athabasca bitumen, overall oxygen consumption kinetics together with four different cracking reactions were developed. The first kinetics scheme showed that bitumen combined with oxygen in the LTO region to produce

products. However, no information about what the products were has been given. A good match was observed when one of the cracking kinetics schemes was validated against the experimental results. It should be noted that the mechanism through which LTO lead to coke formation was not taken into account in the formulation of the cracking kinetics.

The conclusion that can be deduced from these different studies is that formation of coke, either due to thermal cracking or as a result of LTO, is not an instantaneous process. It requires conversion of part of the heavy oil to asphaltene and upon reaching the maximum asphaltene conversion, coke formation starts. The duration of the induction period depends on the initial asphaltene content of the heavy oil. In addition, in the case of LTO studies, high oxygen uptake is reported when the whole bitumen is used as the starting material. It means that LTO would only be significant if the heavy oil is present upstream of the combustion zone. It also can only be significant at a considerable distance downstream of the combustion zone. This would be possible if oxygen passes through, or by-passes, the combustion zone and reaches low temperature bitumen zone.

2.2.3.1 Direct Conversion Cracking Kinetics

Several thermal cracking reaction kinetics schemes, which are very similar in terms of general representation, were developed (Phillips et al., 1985; Adegbesan et al., 1987; Belgrave et al., 1993; Wiehe, 1993; Gray et al., 2004; Radmanesh et al., 2008). In all the models, solid coke was considered to be formed from asphaltene cracking. In addition to formation from asphaltene, the coke was also considered by Gray et al. (2004) to be formed from cracking of

the maltene pseudo-component. In the case of Radmanesh et al. (2008), cracking of both the light and heavy pseudo-components was also considered to result in coke formation as can be seen in Fig. 2.8 and Tab. 2.1. The number of pseudo-components considered by Radmanesh et al. (2008) has been reduced by lumping the ‘‘Distillates’’ & ‘‘Gas Oil’’ pseudo-components to form ‘‘Light Oil’’. These types of cracking kinetics can be described as direct conversion kinetics because formation of any component has a different set of kinetics parameters and the stoichiometry of any reaction is readily determinable.

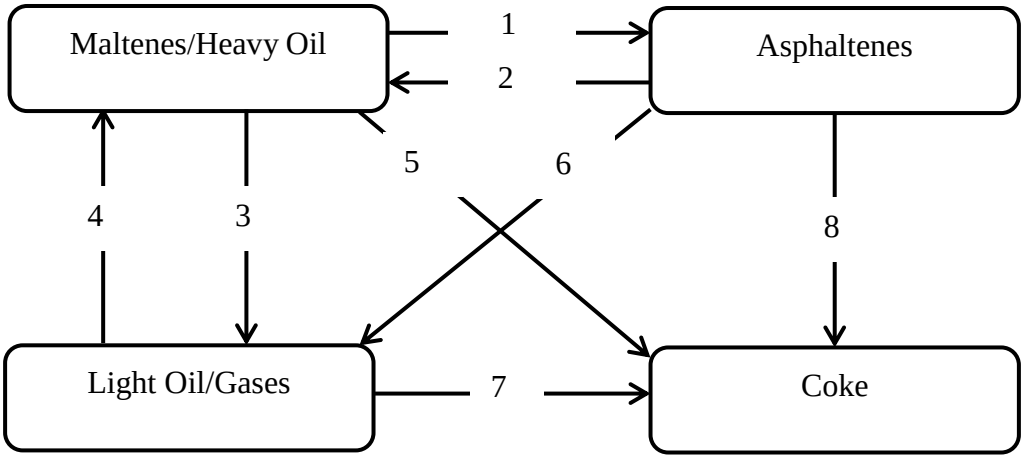

Fig. 2.8: General cracking kinetics scheme

Tab. 2.1: Reaction schemes as depicted in Fig. 2.8.

Authors	Kinetics scheme	Comment
Phillips et al. (1985)	1,2,3,4,8	‘Model A’ as defined by the authors
Adegbesan et al. (1987)	1,8	‘Resins’ and ‘Asphaltene’ are lumped
Belgrave et al. (1993)	1,6,8	LTO reactions have not been included

Wiehe, (1993)	1,2,3,6,8	'Aspaltene' & 'Asphaltene core' are lumped
Gray et al. (2004)	2,5,6,8,	Only liquid phase cracking considered
Radmanesh et al. (2008)	2,3,5,7,8	Reaction No. 6 has zero stoichiometry

The choice of reaction for each kinetics scheme is different. In the case of Wiehe, (1993) in which cracking kinetics of Cold Lake vacuum residue was developed, solid coke generation was considered to be the result of formation of supersaturated solution of ''asphaltene core''. The ''asphaltene core'' is formed directly from heavy oil. He suggested that solid coke formed only when the solubility limit of the ''asphaltene core'' was reached. However, the issue that has not been considered was the continuous decrease in ''asphaltene core'' despite the fact that solubility limit was attained. If the solid coke is as a result of precipitation of ''asphaltene core'', then the concentration of the latter should remain constant as only the excess should be converted to coke.

The kinetics of Athabasca bitumen developed by Belgrave et al. (1993) considered coke formation to be due to both thermal cracking and LTO reactions. Their LTO reactions is such that ''Maltenes'' combined with oxygen to form ''Asphaltenes'' and ''Asphaltenes'' in turn reacts with oxygen to form coke. A typical LTO reaction is shown in Fig. 2.10b. For the model to be accurately accounting for the oxygen atoms that combined with partially oxidised ''Asphaltenes'' to form solid coke ($CH_{1.3}$), gaseous products must be produced directly from the ''Asphaltenes''. This is represented by the thermal

cracking reaction 1 shown in Fig. 2.8. The other two cracking reactions are respectively represented by reactions 6 and 8 (Fig. 2.8).

On the other hand, Phillips et al. (1985) validated two set of cracking kinetics models for the thermal cracking of Athabasca bitumen-sand mixture based on four and six oil pseudo-components respectively. In one of the models, (i.e. ‘‘model A’’ which has four oil pseudo-components), formation of light components from asphaltene was considered insignificant based on the assumption that light oil is formed from cracking of heavy oil. The change in the weight fraction of each pseudo-component, at different reaction temperatures, was modelled as first order. Overall, the cracking kinetics data fitted excellently in ‘‘model A’’ compared to the fit obtained in ‘‘model B’’, which has six oil pseudo-components. The study also showed that as the cracking temperature is increased, concentration of produced coke increases. However, the oil pseudo-components have not been adequately defined making it difficult to apply kinetics parameters as in the study.

2.2.3.2 Split Conversion Cracking Kinetics

Split kinetics can be described as those schemes that consider coke formation to be the result of direct conversion of the heavier component into coke and light pseudo-components. A single frequency factor, as well as activation energy, for the formation of the two components is associated with this kind of scheme. The induction period before coke formation is neglected. A significant number of simulation studies have used this kind of cracking reactions (Lin et al., 1984; Rojas et al., 2010; Anaya et al., 2010; Cinar et al., 2011; Greaves et al., 2012a; Greaves et al., 2012b; Kovscek et al., 2013; Nissen et al., 2015) . A typical

general representation is shown in Fig. 2.9. A mix of matches between the experimental and the simulated oil rates, cumulative oil productions, peak temperatures, produced oxygen concentrations, etc., were obtained using this scheme. However, the main disadvantage with such a representation is the fact that the stoichiometric coefficients of the products are highly indefinite. Apart from the activation energy and the frequency factor, the stoichiometric coefficients must be determined by trial and error, which further introduces a significant uncertainty in the model.

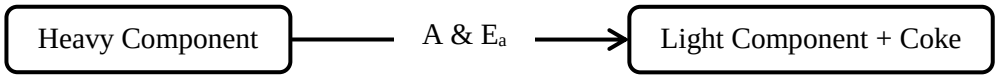

Fig. 2.9: General cracking scheme showing Coke & Light oil formation from Heavy oil

The kinetics parameters used by each author vary due to differences in boiling point range of the oil pseudo-components. Cinar et al. (2011) and Kovscek et al. (2013) model used a composition that is not typical of heavy oil. From the oxygen addition reaction in which ‘‘coke1’’ and ‘‘H_2O’’ were considered to be formed, the elemental composition of the whole bitumen can be estimated. It has been found that oxygen atom contributes 44.8 wt% to the total weight of the bitumen. This is far higher than the typical oxygen concentration in bitumen/heavy oil which can be found in Prowse et al. (1983) and Mahinpey et al. (2007).

2.2.3.3 Combustion Kinetics

Generally, hydrocarbon oxidation has been divided into two, namely; High, and Low, Temperature Oxidations (HTO and LTO). In HTO, coke is combusted in the presence of oxygen to produce carbon dioxide, carbon monoxide, and water. LTO is an oxygen addition reaction which results in an increase in asphaltene

content of heavy oil. The increase in asphaltene content results in an increase in overall oil viscosity. Operating in an LTO mode has been reported to result in poor combustion propagation due to restricted gas distribution (Moore et al., 1995; Xia et al., 2005). That is why adequate air injection rate must be maintained during ISC operation in order not to allow the system to switch from HTO to LTO mode. It usually takes place in temperature region of less than 300 to 380 ^{o}C (Millour et al., 1987; Greaves and Bentaher, 2007; Khansari et al., 2012). A detailed review about in-situ combustion reactions has been given elsewhere (Mahinpey et al., 2007; Kapadia et al., 2015). Typical HTO and LTO representations are shown in Fig. 2.10 below.

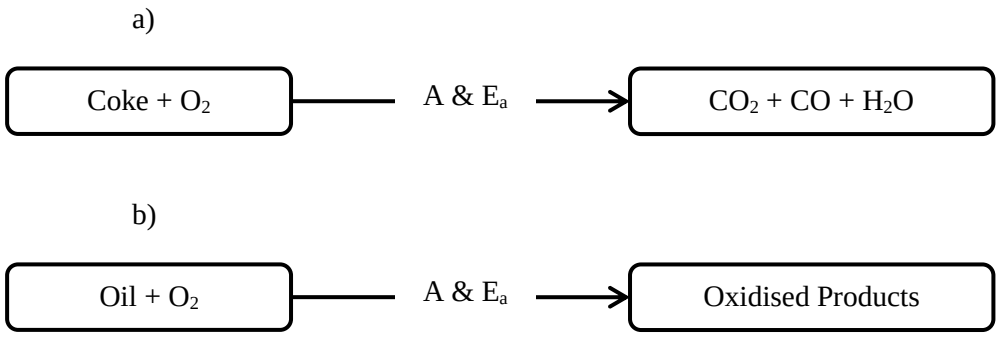

Fig. 2.10: Typical representation of: a) HTO and, b) LTO reactions

Another set of reactions often used in numerical simulations of in-situ combustion process are the individual pseudo-components combustion reactions. Typically, oil pseudo-component is oxidised to carbon oxides and water. Greaves et al. (2012a) and, Marjerrison and Fassihi, (1992) have found the effect of these reactions to the overall performance of in-situ combustion negligible. This is because oxygen has to by-pass the combustion front before it comes into contact with oil and be burned. While authors such as Lin et al.

(1984) and Anaya et al. (2010) have included them in their models but did not report their influence.

2.3.3 Analysis

From these different studies, it can be deduced that formation of coke, either due to thermal cracking or as a result of LTO, is not an instantaneous process but requires an induction period. The effect of LTO as mechanism of fuel deposition as applied to THAI has not been investigated. The effect of the choice of kinetics scheme on THAI has not been investigated. There exists only one model of THAI in the literature. The model used split conversion kinetics scheme which depends heavily on the selected stoichiometric coefficient of the products (Greaves et al., 2012a). Also, the Greaves et al. (2012a) model over predicted the fuel availability and did not accurately predict the time at which oxygen production began, and the concentration of the produced oxygen.

2.4 Determination of Kinetics Parameters

To incorporate any of the kinetics schemes described in the previous sections into a numerical model, two main kinetics parameters must be fully defined. These are: (i) the coefficient of the reaction rate, which is usually denoted by *k*, and (ii) the order of the reaction, which can be overall or with the respect to individual reactants or products. The parameters must be determined from experimental data except in the case of the later, where it becomes equal to the stoichiometric coefficient of the reactant(s), when the reaction involved is elementary in nature.

Thermal cracking is the main reaction that take place when heavy oil is subjected to heating at high temperatures of at least 400 ^{o}C and at a pressure of

620 kPa (Phillips et al., 1985). As outlined in section 2.2.2, during the THAI process, several zones with different set of conditions are created downstream of the combustion zone. Because of the large temperature gradient, the thermal cracking zone is located ahead of the combustion front. This means that any thermal cracking reaction scheme to be used to simulate THAI process must be capable of accurately predicting the dynamics of the zone. And, therefore, the choice of the most representative kinetics scheme must be accompanied by a selection of an appropriate reaction parameters. The parameters must be determined by fitting the model to the experimental data. This can usually be accomplished using differential or integral method depending on the complexity of the set of equations to be solved (Froment et al., 2010). In this section, attention is focused on the thermal cracking only since the combustion kinetics parameters are obtained in a similar fashion. This can be found in Thomas et al. (1985).

To determine the thermal cracking parameters, the composition of a sample of heavy oil is first analysed and grouped into different pseudo-components. This is either based on the range of boiling points, or based on solubility in n-pentane or toluene, or both. A specified amount of the heavy oil, or as a mixture with the core matrix is charged into a batch, semi-batch, or a flow reaction vessel (Phillips et al., 1985; Millour et al., 1987; Adegbesan et al., 1987; Belgrave et al., 1993). The temperature and pressure, for the batch reaction system, are noted periodically for the duration of the reaction. For isothermal batch runs, the change in the mass of the individual pseudo-components due to the thermal cracking is recorded as function of time. From these, the possible thermal cracking reaction mechanism of any given heavy oil or bitumen are formulated.

As an example, consider the four pseudo-components model proposed by Phillips et al. (1985) and identified with paths 1,2,3,4, & 8 in Fig. 2.8, which is reproduced below (Fig. 2.11).

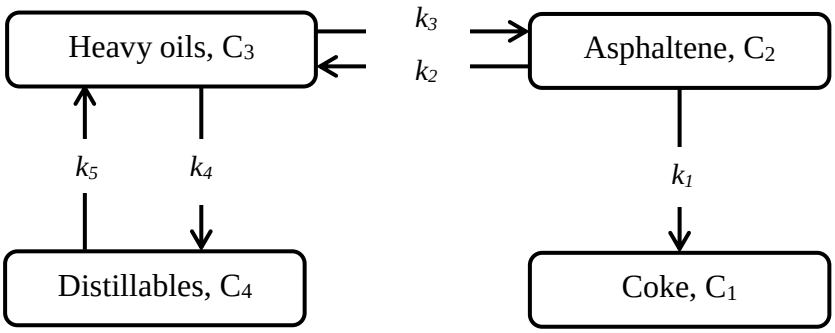

Fig. 2.11: ''Model A'' as proposed by Phillips et al. (1985)

This reaction scheme is considered because it is obtained by thermally cracking the Athabasca bitumen in the presence of core sand. The inclusion of the sand matrix was shown by Phillips et al. (1985) to have catalytic effect by increasing the yield of light fractions. They also showed that the activation energies of the cracking reactions are lower in the presence of the core sand compared to thermally cracking bitumen only. For temperatures of less than 540 ^{o}C, the cracking reaction for petroleum components follows first order. As a result, the only unknown parameter is the rate constant. For the constant volume and density batch reaction, the above reaction scheme can be described by the following set of differential equations.

$$\frac{dC_1}{dt} = k_1 C_2 \tag{2-1}$$

$$\frac{dC_2}{dt} = -(k_1 + k_2)C_2 + k_3 C_3 \tag{2-2}$$

$$\frac{dC_3}{dt} = k_2C_2 - (k_3 + k_4)C_3 + k_5C_4 \tag{2-3}$$

$$\frac{dC_4}{dt} = k_4C_3 - k_5C_4 \tag{2-4}$$

where C_1 to C_4 represent the mass concentration of each pseudo-component, and k_1 to k_5 represent each of the rate constants for each reaction since k_i may vary, depending on the direction of the reaction. As there is no simple analytical solution to the above set of equations, a numerical solution must be obtained. This can be accomplished using Gauss-Newton procedure outlined in Kalogerakis and Luus, (1983). It involves minimising the performance index, *S*, based on comparison between the experimental and numerically calculated mass concentrations using the current estimated kinetics parameters:

$$S = \sum_{i=1}^{n} [\hat{\boldsymbol{y}}(t_i) - \boldsymbol{y}(t_i)]^T \boldsymbol{Q}(t_i)[\hat{\boldsymbol{y}}(t_i) - \boldsymbol{y}(t_i)] \tag{2-5}$$

where $\hat{\boldsymbol{y}}(t_i)$ and $\boldsymbol{y}(t_i)$ are the experimental and calculated mass concentration vectors each with *m*-dimensions respectively, $\boldsymbol{Q}$ is a positive definite, symmetric weighting matrix with an $m \times m$ dimension.

The best fit between the model and experimental data is obtained at the minimum performance index. However, the model, often, has to be applied outside the constraints used to validate it. Stitt et al. (2015) have shown that reliance on the quality of fit is not enough a measure of a model's predictive capability. To ensure the model predicts physically meaningful results, statistical analysis is usually conducted to investigate the extent of uncertainty in the estimated parameters using confidence interval of 95%. In addition to

that, Stitt et al. (2015) have argued that it is very important to validate a model against more than one parameters. This is essential in ensuring all the processes describing the given phenomena are considered in explaining the model predictions. Once the validity of the model is fully established, it can then be implemented to investigate different scenarios. An example is the implementation of the Phillips et al. (1985) cracking kinetics to model THAI process as can be found in Chapter 4 of this thesis.

2.5 Summary

Conventional in-situ combustion is the most efficient and environmentally friendly technique for heavy oil recovery as it is not compromised by excessive heat losses to overburden and underburden or from the wellbore to the overburden and does not generate greenhouse gases. Compared to the steam recovery processes, conventional ISC is not water intensive process and therefore has potentially low surface footprint. However, it is difficult to control due to gravity segregation and the mobilised oil has to travel over hundreds of metres before it is produced to the surface. The banking of the mobilised oil ahead of the combustion front is another major problem associated with conventional ISC as it can restrict the gas flow path resulting in pre-mature termination of the combustion. The development of THAI, which has more advantages than conventional ISC, has helped in overcoming most of the problems associated with conventional ISC. The mobilised oil does not bank as it is instantaneously gravity-drained into the exposed section of the horizontal well. It also does not suffer from gravity segregation as oil drainage becomes the dominant driving force. An added advantage of THAI is the possibility of

embedding catalyst around the horizontal producer (THAI-CAPRI) to achieve further upgrading in-situ.

From the literature reviewed, it is determined that the mechanism through which fuel for the sustenance of HTO is deposited remains a contentious issue. It is also determined that only one model for predicting the performance of THAI exists. The model does not accurately predict the most critical parameters (i.e. fuel availability and produced oxygen concentration) affecting the performance of THAI. Therefore, it is the aim of this work to validate 3D THAI experiment using three distinctly different kinetics schemes. The first scheme uses Phillips et al. (1985) direct conversion cracking kinetics, the second uses modified Greaves et al. (2012a) split conversion kinetics while the third scheme uses Belgrave et al. (1993) direct conversion kinetics with LTO reactions for fuel deposition and upgrading. The two former schemes included combustion of oil pseudo-components together with HTO combustion reactions while the latter considers HTO combustion reaction only. This allows the dominant mechanism through which fuel is deposited in THAI to be established. Two of the three kinetics schemes that best matched the experimental results will then be scaled up to field scale. The model that provides the best representation at the field scale is then used to study the effect of reservoir heterogeneity, bottom water and gas cap on THAI.

3. Chapter Three: Conservation Equations and Solution Techniques

3.1 Introduction

Hydrocarbon reservoirs usually contain not only liquid petroleum but also water or gaseous hydrocarbons or both. Therefore, it follows that modelling of petroleum reservoir must take into account the multiple phases present – namely oil, water, and gas (Aziz et al., 1979). In addition to that, most thermal heavy oil recovery processes involve chemical reactions which often result in phase change. Also, the reservoir water is vaporised with increase in reservoir temperature as a result of heat addition at constant pressure. For the specific case of THAI, at temperatures of 300 to 400 ^{o}C, thermal cracking of heavier fraction of petroleum leads to the formation of solid residue, liquid, and gaseous hydrocarbons. Furthermore, the solid residue deposited on the rock matrix is oxidised to provide the needed energy to mobilise the cold viscous oil downstream of the combustion zone. Thus, in order to capture all the physicochemical processes in a simple way, the oil must be divided into different pseudo-components. Therefore, it follows that modelling air injection enhanced oil recovery is a multiphase reactive transport system which is described by specific mathematical formulations. This Chapter contains those formulae and the summary of the methodology employed to solve them.

3.2 Material Balance

The general material conservation equation can be stated as:

$$\text{Flow In} - \text{Flow Out} = \text{Accumulated} + \text{Sources}$$

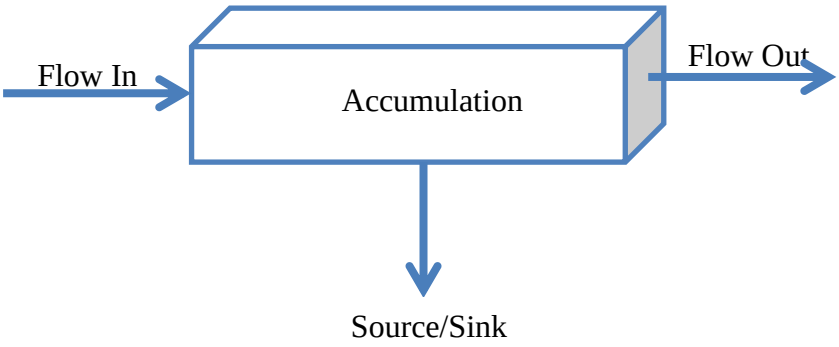

Fig. 3.1: Control volume element

The above equation conserves the mass of a given component flowing into a porous control volume ΔV, reacting with another species, being produced via a given sink, and the remaining flowing out at the other end. Mathematically, it can be expressed as follows:

$$\left[(\dot{m}_x - \dot{m}_{x+\Delta x})A_{yz} + (\dot{m}_y - \dot{m}_{y+\Delta y})A_{xz} + (\dot{m}_z - \dot{m}_{z+\Delta z})A_{xy}\right]\Delta t$$

$$= \left[\frac{\partial}{\partial t}(\rho\varphi\Delta V)\right]\Delta t - \check{q}\Delta V\Delta t + r\Delta V\Delta t \qquad (3\text{-}1)$$

where A is the cross-sectional area perpendicular to the direction of flow, Δt is the time interval over which the fluid is displaced from inlet point $x, y,$ or z to outlet point $(x + \Delta x),$ or $(y + \Delta y),$ or $(z + \Delta z)$, φ is the porosity of the void space, ΔV is the control volume, ρ is the density of the fluid, $\check{q}$ is the mass production rate per unit volume and r is the rate of consumption of the given component.

Dividing through by the control volume ΔV and time interval Δt and taking the limit as $\Delta V \rightarrow 0$, equation 3-1 can be written as:

$$-\left(\frac{\partial \dot{m}_x}{\partial x}+\frac{\partial \dot{m}_y}{\partial y}+\frac{\partial \dot{m}_z}{\partial z}\right)=\frac{\partial}{\partial t}(\rho\varphi)\ -\ \check{q}+r$$

Using the divergence operator ∇, the above equation can be written as:

$$-\nabla\cdot\dot{\mathbf{m}}=\frac{\partial}{\partial t}(\rho\varphi)\ -\ \check{q}+r \tag{3-2}$$

where $\dot{\mathbf{m}}$ is the mass flux vector which can be expressed in terms of superficial velocity as $\rho\mathbf{u}$.

As water and oil pseudo-components can respectively exist in both liquid and vapour phases, the material conservation equation 3-2 for component i in phase j can be written as j

$$-\nabla\cdot\dot{\mathbf{m}}_{ij}=\frac{\partial}{\partial t}\left(m_{ij}\right)\ -\ \check{q}_{ij}+r_{ik} \tag{3-3}$$

where $\dot{\mathbf{m}}_{ij}=\rho_j\mathbf{u}_j x_{ij}$ is the mass flux of component i in phase j and $m_{ij}=\rho_j\varphi_f S_j x_{ij}$ is the accumulated mass of component i in phase j per unit reservoir volume. r_{ik} is the rate of consumption/generation of component i in reaction k.

Therefore, the **general** mass conservation equation for i-th component in the reservoir is the summation over the number of phases π and the number of reactions n_r given by:

$$-\nabla\cdot\sum_{j=1}^{\pi}\rho_j\mathbf{u}_j x_{ij}=\frac{\partial}{\partial t}\sum_{j=1}^{\pi}\rho_j\varphi_f S_j x_{ij}\ -\ \sum_{j=1}^{\pi}\check{q}_{ij}+\sum_{k=1}^{n_r}r_{ik} \tag{3-4}$$

S_j is the saturation of phase j which is the volume of phase j per unit volume of void space and x_{ij} is the mole fraction of component i in phase j. q is negative for a sink.

3.3 Auxiliary Relationships

The bulk volume of the control volume is given by:

$$V = V_r + \sum_{j=1}^{\pi} V_j \tag{3-5}$$

where V_r is the volume of the reservoir rock and V_j is the volume of phase j occupying the pore space. Therefore, it follows that the void porosity can be defined as:

$$\varphi_v = \frac{\sum_{j=1}^{\pi} V_j}{V} \tag{3-6}$$

The fluid porosity is the fraction of pore occupied by fluids and can be obtained from:

$$\varphi_f = \frac{\sum_{j=1}^{\pi} V_j - \sum_{i=1}^{n_s} V_{si}}{V} = \varphi_v \cdot \left(1 - \sum_{i=1}^{n_s} \frac{C_{si}}{\rho_{si}}\right) \tag{3-7}$$

where V_{si} is the volume of solid component i, C_{si} the concentration and ρ_{si} the density of component i in solid phase.

Fluid saturation is defined as the volume of fluid occupying a unit volume of pore space. Hence, for phase j, it is the fraction of the pore space occupied by phase j and is given by:

$$S_j = \frac{V_j}{\sum_{j=1}^{\pi} V_j - \sum_{i=1}^{n_s} V_{si}} \tag{3-8}$$

It then follows that

$$\sum_{j=1}^{\pi} S_j = 1$$

Also, in any given phase, the sum of the fractions of each component i must add to unity. Thus:

$$\sum_{j=1}^{\pi} x_{ij} = 1$$

3.4 Energy Balance

The accumulation term is described by:

$$\frac{\partial}{\partial t}\left[\sum_{j=1}^{\pi} \varphi_f \rho_j S_j U_j + (1-\varphi_v)U_r + \varphi_v C_s U_s\right]$$

where U_j is the internal energy of phase j per unit volume and U_r and U_s are the internal energies of rock matrix and solid components respectively, C_s is the total solid concentration.

The advection or convection term is given by:

$$-\nabla \cdot \sum_{j=1}^{\pi} \rho_j h_j \mathbf{u}_j$$

where h_j is the enthalpy of phase j.

The conduction term is described by:

$$\nabla \cdot (\lambda \nabla T)$$

where λ is the thermal conductivity of the formation.

The heat source/sink due to production and injection can be described using:

$$\sum_{j=1}^{\pi} \check{q}_j h_j^*$$

where h_j^* is the enthalpy of phase j at injection or production.

The heat source or sink due to reaction can be represented by:

$$\sum_{k=1}^{n_r} H_{rk} r_k$$

Such that H_{rk} is the enthalpy of reaction k and r_k is the rate of k^{th} reaction.

The heat loss source/sink term is denoted by:

$$\check{q}_{hc}$$

Therefore, the overall energy balance is given by:

$$\frac{\partial}{\partial t}\left[\sum_{j=1}^{\pi} \varphi_f \rho_j S_j U_j + (1-\varphi_v) U_r + \varphi_v C_s U_s\right] = \nabla \cdot (\lambda \nabla T) - \nabla \cdot \sum_{j=1}^{\pi} \rho_j h_j \mathbf{u}_j + \sum_{j=1}^{\pi} \check{q}_j h_j^* + \sum_{k=1}^{n_r} H_{rk} r_{ik} + \check{q}_{hc} \quad (3\text{-}9)$$

3.5 Darcy's Law and Injection/Production Equation

To obtain the relationship between the flow rates and pressure gradient, Darcy's law for multiphase flow is used (Aziz et al., 1979). The velocity of phase j is written as:

$$\mathbf{u_j} = -\frac{\mathbf{k}k_{rj}}{\mu_j}\left(\nabla P_j + \rho_j \mathbf{g}\right) \tag{3-10}$$

where k is the absolute permeability tensor, k_{rj} is the relative permeability of phase j, μ_j and ρ_j are the viscosity and density of phase j respectively, **g** is the gravitational acceleration vector given as g∇z.

During air injection enhanced heavy oil recovery, air to oil ratio (AOR) is one of the key parameters used to determine the economy of the process. As a result, the air injection and the oil production rates must respectively be monitored. However, prior knowledge of what this value would be at a given period of the process will results in substantial cost saving. This is achieved by numerical simulation and the injection or production terms for component i in j-th phase are represented by Darcy's law (Crookston et al., 1979) as:

$$\check{q}_{ij} = \frac{x_{ij} \cdot wi \cdot z}{V} \cdot \frac{\rho_j \mathbf{k}k_{rj}}{\mu_j}\left(P_j - P_w\right) \tag{3-11}$$

where w_i is the well productivity index, which gives the measure of the fluid production potential of a given well. The z is the gridblock thickness, V is the volume of the gridblock, P_j is the pressure of phase j, P_w is the pressure of the wellbore, and all other symbols have their usual meaning.

3.6 Chemical Reactions Terms

As reviewed in Chapter 2, THAI involves hydrocarbon upgrading and recovery due to heat from oxidation of heaviest oil fraction, namely coke. Therefore, to numerically model THAI, all the chemical reactions that are critical to its performance must be taken into account. Thus, the description of Phillips et al. (1985) cracking kinetics scheme and that of the accompanying combustion reactions are presented here. Therefore, the reactions are both homogeneous and heterogeneous in nature.

Tab. 3.1: Cracking and combustion reaction schemes

Number	Cracking Reactions (Phillips et al., 1985)
1	IC ➔ s_1 MC
2	MC ➔ s_2 IC
3	MC ➔ s_3 LC
4	LC ➔ s_4 MC
5	IC ➔ s_5 COKE
Combustion Reactions	
6	IC + s_6 O_2 ➔ s_7 CO_x + s_8 H_2O
7	MC + s_9 O_2 ➔ s_{10} CO_x + s_{11} H_2O
8	LC + s_{12} O_2 ➔ s_{13} CO_x + s_{14} H_2O
9	COKE + s_{15} O_2 ➔ s_{16} CO_x + s_{17} H_2O

where IC, MC, and LC designate the immobile, mobile, and light oil pseudo-components respectively. CO_x represents the combination of carbon (ii) and carbon (iv) oxides respectively while s_1 to s_{17} denote the stoichiometric coefficients in both cracking and the combustion reactions.

Mass conservation of reaction stoichiometry can be described as:

$$\sum_{i=1}^{n_c} s_{ik} M_i = 0 \tag{3-12}$$

where s_{ik} is the stoichiometric coefficients of i-th component in k-th reaction, M_i is the molecular weight of component i, and n_c is the number of components participating in the k-th reaction. Here, the M_i values for the reacting components are assigned negative signs while those of the produced components are assigned positive signs.

An Arrhenius rate expression for temperature dependence is used to model each reaction. As a result, the cracking reaction is modelled as first order overall (Phillips et al., 1985) while the combustion reactions are modelled as first order with respect to oxygen partial pressure and as second order overall. This is in accordance with experimental observations (Belgrave et al., 1993).

The k-th reaction rate expression for i-th component is accordingly modelled using (CMG, 2012):

$$r_{ik} = F_k \cdot e^{\left(-\frac{E_{ak}}{RT}\right)} \cdot \prod_{i=1}^{nc} {C_i}^{O_{ik}} \tag{3-13}$$

where r_{ik} is the rate of consumption/generation of component i in the k-th reaction, F_k is a constant number called the frequency factor for the reaction k,

E_{ak} is the activation energy which determines the temperature dependence of the k-th reaction. R is the universal gas constant and T is the absolute temperature in the k-th reaction zone. Other terms include C_i which is the concentration of ith component, and O_{ik} is the order of i-th component in the k-th reaction.

The concentration C_i is determined by the phase of the component i. For solid coke, it is given by:

$$C_i = \varphi_v C_s \quad (3\text{-}14a)$$

For fluid phase (oil, water, or gas) is given by:

$$C_i = \rho_j \varphi_f S_j x_{ij} \quad (3\text{-}14b)$$

where x_{ij} is the component mole fraction in the j-th phase it is reacting in. And for oxygen, it is partial pressure is substituted in place of concentration. Thus:

$$C_i = P_{O_2} = y_i P_g \quad (3\text{-}14c)$$

where y_i is the oxygen mole fraction and P_g is the gas phase pressure.

3.7 Vapour-Liquid Equilibrium Expression

Three fluids phases must be considered in the simulation of THAI in order to account for vaporisation and condensation of components. However, only two fluid phases are condensable under the typical reservoir operating conditions. These are grouped into oleic (oil-like) and aqueous (water-like) components respectively (CMG, 2012). These two phases exist both in the liquid and vapour phases respectively. Their movement from one phase to another is governed by vapour-liquid pressure and temperature-dependent equilibrium coefficients.

Thus, the interphase transfer is assumed to be in an instantaneous equilibrium. This means the fugacity of i-th component in the vapour phase, $f_i^{\,v}$ is equal to that in the liquid phase, $f_i^{\,L}$ (Chueh and Prausnitz, 1968; Lee and Edmister, 1971). As a result, the vapour and liquid phase fugacities, respectively, are written as:

$$f_i^{\,v} = \varphi_i y_i P_g \tag{3-15a}$$

$$f_i^{\,L} = \gamma_i x_i f_i^{\,0} \tag{3-15b}$$

where φ_i is the vapour phase fugacity coefficient and γ_i is the liquid phase activity coefficient of component i which are usually calculated either entirely or partly based on a cubic equation of state (Chueh and Prausnitz, 1968; Lee and Edmister, 1971), y_i and x_i are the i-th component mole fractions in the vapour and liquid phases respectively, $f_i^{\,0}$ is the fugacity coefficient of component i at the standard state and P_g is the gas phase pressure. Therefore, in simulating THAI, the VLE is established when the following conditions are met:

For the water-like components:

$$f_i^{\,wv} = f_i^{\,Lw} \tag{3-16a}$$

where $f_i^{\,wv}$ and $f_i^{\,Lw}$ are the fugacities of water-like component i in vapour phase and liquid phase respectively. And for the oil-like components:

$$f_i^{ov} = f_i^{Lo} \quad (3\text{-}16b)$$

where f_i^{ov} and f_i^{Lo} are the fugacities of oil-like component i in vapour phase and liquid phase, respectively.

However, since hydrocarbon mixtures are quite ideal and the equal fugacity criterion is a complex function of compositions, pressure, and temperature, a simplified analytical prediction method can be used to obtain the VLE data. This method involves the use of phase distribution ratio, the K-value, which can be defined as the ratio of mole fraction of i-th component in vapour phase to the mole fraction of the same component in liquid phase. Thus, in phase j, j being water or oil,

$$K_{ij} = y_{ij}/x_{ij} \quad (3\text{-}17)$$

To use equation 3-17, K_{ij} and one of the two mole fractions must be known. STARS has a built in correlation in which the K-values are calculated as function of pressure and temperature (CMG, 2012). The basic assumptions in the correlation are: the correction to fugacity coefficient is insignificant at relatively low vapour and reservoir pressures; the reservoir fluid mixture in either liquid or vapour phase is ideal; liquid volume is small compared to vapour volume; and the heat of vaporisation is constant. Therefore, by combining Raoult's law with integrated Clausius-Clapeyron equation, a simplified exponential K-value prediction equation is obtained. Thus:

$$K_{ij} = \left(\frac{K_{V1}}{P}\right) e^{\left(\frac{K_{V4}}{T - K_{V5}}\right)} \quad (3\text{-}18)$$

where the $K_{V1}, K_{V4}, and\ K_{V5}$ are constants and component dependents. For water, the constants are taken from STARS manual (CMG, 2012).

STARS also allows for tables of K-values as function of temperature and pressure to be inputted (CMG, 2012). The Wilson K-value correlation is used (Almehaideb et al., 2003), which is given by equation (3-19), to generate the table for each oil pseudo-component.

$$K_{ij} = \frac{P_{ic}}{P} e^{\left[5.37(1+\omega_i)\left(1-\frac{T_{ic}}{T}\right)\right]} \tag{3-19}$$

where P_{ic} and T_{ic} are the critical pressure and temperature for i-th component respectively, and ω_i is the acentric factor of component i. The Wilson equation performs well for both ideal and non-ideal systems except for liquid-liquid equilibrium system (HYSYS, 2016). There is the need, however, to calculate the critical properties of the given pseudo-component. This can be achieved using, depending on the normal boiling point (NBP) of the component, Lee-Kesler, Twu, Riazi-Dauber, Bergman, Cavett, etc. methods. Since in the Aspen Hysys, the default method used is automatically chosen based on the NBP of the component so that error is maintained within the negligible limit, the software is chosen to estimate the critical temperature, critical pressure, and eccentricity. Since there is still uncertainty associated with these estimated values, different number of pseudo-components are used in the numerical reservoir simulation study. On the overall, however, the choice of kinetics scheme was found to be the source of uncertainty in the simulation results.

3.8 Fluid Physical Properties

For heavy oil and tar sands to be thermally recovered, their physicochemical properties must be altered. Therefore, the functional dependencies of these properties must be included in the model for realistic predictions to be obtained.

3.8.1 Density

Due to the ideal nature of reservoir fluids, the density of any phase is calculated by assuming the applicability of the linear mixing rule (CMG, 2012). Thus:

$$\frac{1}{\rho_j} = \sum_{i=1}^{n_c} \frac{x_{ij}}{\rho_{ij}} \tag{3-20}$$

where ρ_j is the molar density of phase j, x_{ij} and ρ_{ij} are the mole fraction and molar density of component i in phase j respectively.

As function of temperature and pressure, the density of liquid phase (i.e. j being water or oil) is calculated using:

$$\rho_{ij} = {\rho^0}_{ij} e^{\left[\alpha_{ij}(P-P^0)-\beta_{ij}(T-T^0)-\frac{1}{2}\gamma_{ij}\left(T^2-(T^0)^2\right)\right]} \tag{3-21}$$

where ${\rho^0}_{ij}$ is the molar density of i-th component in phase j at reference pressure, P^0 and temperature, T^0 and α_{ij} is the liquid compressibility coefficient of i-th component in phase j. β_{ij} and γ_{ij} are the first and second thermal expansion coefficients of i-th component in phase j respectively.

For the gas phase, the molar density of gas is calculated using:

$$\rho_{ij} = P/RTZ_{ij} \tag{3-22}$$

Here j denoted the gas phase only. The compressibility factor Z_{ij} is calculated using Redlich-Kwong cubic equation of state (EOS). Thus:

$$Z_{ij}{}^3 - Z_{ij}{}^2 + (A - B^2 - B)Z_{ij} - AB = 0$$

Such that the constants A and B are respectively expressed as:

$$A = 0.427480 \cdot \left(\frac{P}{P_c}\right) \cdot \left(\frac{T_c}{T}\right)^{2.5}$$

$$B = 0.086640 \cdot \left(\frac{P}{P_c}\right) \cdot \left(\frac{T_c}{T}\right)$$

3.8.2 Viscosity

Similarly, the viscosity of any phase is calculated using the logarithmic mixing rule (CMG, 2012). Therefore, for any liquid phase (i.e. water or oil), it is given as:

$$\mu_j = \exp\left[\sum_{i=1}^{n_c} x_{ij} \cdot ln(\mu_{ij})\right] \tag{3-23}$$

where μ_{ij} is the viscosity of component i in phase j.

As function of temperature, the viscosity for the i-th component in liquid phase can be expressed in exponential form (Crookston et al., 1979; Zhu et al., 2011; CMG, 2012) as:

$$\mu_{ij} = a_{ij} \cdot exp\left(\frac{b_{ij}}{T}\right) \quad (3\text{-}24a)$$

Such that a_{ij} and b_{ij} are constants and T is absolute temperature.

For the gas phase, the viscosity is calculated as function of temperature using:

$$\mu_j = 0.0136 + 3.8 \times 10^{-5} T \quad (3\text{-}24b)$$

3.8.3 Enthalpy, Internal Energy, and Latent Heat

In the same way as density, due to the ideal nature of reservoir fluid, the enthalpy of any fluid phase j is calculated using linear mixing rule (Crookston et al., 1979; Zhu et al., 2011; CMG, 2012). Thus

$$H_j = \sum_{i=1}^{n_c} x_{ij} \cdot H_{ij} \quad (3\text{-}25)$$

where H_{ij} is the enthalpy of i-th component in phase j which is defined as

$$H_{ij} = \int_{T^0}^{T} C_{pij}(T)\, dT \quad (3\text{-}26)$$

Such that C_{pij} is the specific heat capacity of component i in phase j. The internal energy of any fluid phase U_j is given by:

$$U_j = H_j - P_j/\rho_j \tag{3-27}$$

where P_j and ρ_j are the pressure and density of phase j respectively. In addition, for solid phase, the internal energy is

$$U_s = \int_{T^0}^{T} C_{ps}(T)\, dT \tag{3-28}$$

The latent heat of vaporisation for component i in any condensable phase j (j being water or oil) is calculated in similar fashion as in STARS (CMG, 2012). This is given as

$$L_{ij} = L_{cij}(T_c - T)^{\Psi} \tag{3-29}$$

where L_{cij} is component dependent constant, T_c is the critical temperature, and Ψ is a constant usually with value ranging from 0.375 to 0.380.

The enthalpy of component i in phase j in vapour phase is calculated accordingly using

$$H_{ijv} = H_{ij} + L_{ij} \tag{3-30}$$

3.9 Relative Permeability

Permeability generally is the measure of the fluid conducting capacity of a porous medium. For reservoir rock which contains multiple phases, the measure

of the ability of any given phase, say oil, to flow in the presence of other phases (say water and gas) is termed as it is effective permeability. The absolute permeability of a porous reservoir rock gives the measure of the total flow capability of fluid at 100% saturation.

The ratio of the effective to the absolute permeability gives the relative permeability. For each fluid phase j, the relative permeability has values range from 0 to 1 and is denoted by

$$k_{rj} = \frac{k_j}{\boldsymbol{k}} \tag{3-31}$$

For the three phases, the modified Stones second model, which is built in as default in STARS, is used (CMG, 2012). In the model, the water relative permeability in the three phase system is considered the same as that in the two phase water-oil system and is function of water saturation (S_w) only. Similarly, the gas relative permeability in the three phase system is taken to be the same as that in the two phase gas-oil system and is function of gas saturation (S_g) only. This resulted in three phase relation given by:

$$k_{ro} = k_{rocw}\left[\left(\frac{k_{row}}{k_{rocw}} + k_{rw}\right)\left(\frac{k_{rog}}{k_{rocw}} + k_{rg}\right) - \left(k_{rw} + k_{rg}\right)\right] \tag{3-32}$$

where k_{rocw} is the relative permeability to oil at connate water and zero gas saturation.

3.10 Solution Technique

As outlined in the equations above, the phenomena of air injection enhanced oil recovery is fully described by a set of strongly non-linear partial differential equations (PDEs). These equations are too complex, if not impossible, to be solved analytically. Therefore, they must be solved numerically. This is accomplished by discretising the equations with intent of finding an approximate solution on the finite set of different points, called mesh or grid points, in space and time. This entails replacing the PDEs by a system of algebraic equations which are easier to solve. The three techniques available for discretisation of any PDE are: (i) Finite Difference or the Taylor series method, (ii) Finite Volume or the Integral method, and (iii) Spectral or Variational method (Aziz et al., 1979; Ferziger and Peric, 2001). While any of these methods can be employed to discretise the reservoir, traditionally, only the finite difference method is usually used in reservoir simulations (Crookston et al., 1979; Youngren, 1980; Hwang et al., 1982).

The details (both derivation and solution) involve in discretising the nonlinear equations using the finite difference method are not discussed here as these are not the subject of this thesis. This is justified given that the thermal reservoir simulator, STARS (CMG, 2012), implemented and used throughout this work, solves the above equations. However, briefly, here is the general basic procedure (Crookston et al., 1979; Youngren, 1980; Hwang et al., 1982; Zhu et al., 2011; CMG, 2012): The nonlinear PDEs are, most often, discretised using central finite difference method with the time discretised using backward finite difference method so that a fully implicit solution is seek. The n-ith basic conservation equations are solved together with the energy balance and phase

constraint, or mole fraction, equations. For the former cases, the choice depends on whether natural or overall variables are solved as the primary variables with the latter involving no switching between different phases. The resulting fully implicit discretised equations are solved using the Newton's method.

3.11 Summary

The complexity of the hydrocarbon mixture, and the presence of multiple phases namely: water, oil, gas, and solid, implies requirement to specify very large number of variables prior to numerically simulating the THAI process. These range from the physico-chemical properties to chemical reactions to petro-physical data. The use of heat to upgrade and recover the heavy oil results in phase change, which means the K-values of the individual condensable pseudo-components must be specified. The dependent parameters are then obtained by solving the resulting discretised reservoir equations.

4. Chapter Four: Experimental Scale Simulation of the THAI Process

4.1 Introduction

From the literature surveyed, only one numerical model validation of THAI, at experimental scale level, was performed since the invention of the oil recovery process. The model used split conversion kinetics which depends heavily on the selected stoichiometric coefficients of the cracking products and does not take into account the induction period before coke formation. Also, the model over predicted the average fuel availability and is not capable of accurately predicting the concentration of the produced oxygen. These will give rise to unsafe designs. Given the wide range of kinetics schemes available as identified in Chapter 2, however, the best possible history match can only be achieved by validating the experiment with different schemes. As a result, in this chapter, three distinctly different kinetics schemes were used to validate THAI models against 3D combustion cell experiment using CMG's STARS, which is a commercial thermal reservoir simulator. The first scheme uses Phillips et al. (1985) direct conversion cracking kinetics, the second uses modified Greaves et al. (2012a) split conversion kinetics while the third scheme uses Belgrave et al. (1993) direct conversion kinetics. The two former schemes included combustion of oil pseudo-components together with HTO reactions while the latter considers both HTO and LTO reactions. From the comparative study of the predictions of the three kinetics schemes, Belgrave et al. (1993) scheme deviated the most from the experimental result while the modified Greaves et al. (2012a) scheme provided fairly close history match. It is observed that

Phillips et al. (1985) scheme accurately predicts the dynamic conditions in the reservoir and also has the benefit of being easily scalable which allows a variety of field scenarios to be investigated. As a consequence, the THAI model which uses the Phillips et al. (1985) scheme has the added advantage of being independent of the stoichiometry of the reacting products. This means that the extent of the uncertainty in the simulation results is lowered as the number of unknowns is reduced. Accordingly, only the results of history matching of the Phillips et al. (1985) model is presented in this chapter while those of the Greaves et al. (2012a), model G, and Belgrave et al. (1993), model B, can be found in Appendix A.

The oil production rate and cumulative oil produced were well predicted using Phillips et al. (1985) kinetics scheme, with the latter deviating from the experimental value by only 4%. The improved ability of the model to emulate real process dynamics meant it also accurately predicted when the oxygen was first produced, thereby enabling a more accurate assessment to be made of when it would be safe to shut-in the process, prior to oxygen breakthrough occurring. The increasing trend in produced oxygen concentration following a step change in the injected oxygen rate by 33 % was closely replicated by the model. The new simulations have now elucidated the mechanism of oxygen production during the later stages of the experiment. Unlike previous models, the new simulations have provided better quantitative prediction of fuel laydown, which is a key phenomenon that determines whether, or not, successful operation of the THAI process can be achieved. The new model has also shown that, for completely stable operation, the combustion zone must be restricted to the upper

portion of the sand pack, which can be achieved by using higher producer back pressure.

The effect of air injection flux, as well as that of oil viscosity, and as predicted by the Phillips et al. (1985) model are presented in this chapter. It is found that the increase in oil recovery with the air injection flux is not directly proportional thereby causing corresponding increase in cumulative air-to-oil ratio (CAOR). The study also showed that THAI operates in a much more stable manner in a highly, compared to low, viscous reservoir. In addition, the study reveals that the CAOR increases with the increase in oil viscosity.

The chapter concludes by detailing the comparison of the pre-ignition heating cycle (PIHC) method and it is effect on the THAI process. It is shown that steaming, instead of electrical heating, results in slight increase (i.e. around 2 to 5%) in oil recovery albeit with the decrease in oxygen utilisation.

4.2 Models Development

To validate the experimental scale THAI model, results from physical laboratory tests must be used. As highlighted in section 2.2.2 of chapter 2, more than fifty physical THAI experimental tests were conducted at the IOR Laboratory in the University of Bath. The tests, conducted in three-dimensional and low pressure combustion cell, provided the measure of the THAI performance parameters such as oil production rate, cumulative oil production, peak temperature, degree of upgrading, produced oxygen concentration, volumetric and areal sweep, temperature distribution, air requirement, etc. and allowed to elicit and further the understanding of the underpinning mechanisms controlling the stability of THAI. Most of the tests used Canadian oil sand or

heavy oil from the Alberta region which contains the largest known tar sand or heavy oil deposit in the world. The largest of the three Canadian oil sand reserves is in the northeastern part of Alberta and is referred to as Athabasca oil or tar sands. However, only 10% of the entire reserve, which is composed of approximately 10% bitumen, 4% water, and 86% solid sediments, is deposited at shallow depth of around 40 to 60 m (Mossop, 1980; Hyne, 2012). It therefore follows that at least 90% of the whole deposit must be recovered using in-situ oil recovery techniques. That is why one of the physical tests that had used Athabasca bitumen is chosen to validate the numerical model.

4.2.1 Physical Laboratory Experiment

The three-dimensional physical experiment, run 2000-1, was performed in a rectangular stainless steel combustion cell which has dimensions of 0.6 m × 0.4 m × 0.1 m (Xia and Greaves, 2002). The cell was designed with thickness of 4 mm and to operate at pressures of 200 to 300 kPa. It was equipped with a pressure relief valve so as to avoid excessive pressure build-up during the experiment. In order to keep track of the combustion front propagation and thus measure the temperature distribution, the cell was fitted with 85 thermocouples. These were located at the top, middle, and bottom of the cell and their ends bolted above and below the cell from where they were connected to the computer for data acquisition. In order to maintain as close to adiabatic operation as possible, nine automatically computer-controlled electrical heating tapes were wounded around the combustion cell (Xia et al., 2002a). The heating tapes kept the cell wall temperature around 20 ^{o}C below the average temperature inside the combustion cell. This allows heat losses to the surrounding to be compensated. The combustion cell was then put into an aluminium box with

dimensions of 0.9 m × 0.9 m × 0.4 m and the empty space filled with insulating material – the vermiculite powder.

The combustion cell was fitted with a horizontal injector well (HI) and a horizontal producer well (HP) arranged in a staggered line drive pattern (Fig. 4.1). The HI was connected to the air injection system while the HP was connected to gas-liquid separation unit with the gas being sent for compositional analysis and to the fluid analysis units. The cell was then fully packed with virgin Athabasca tar sand.

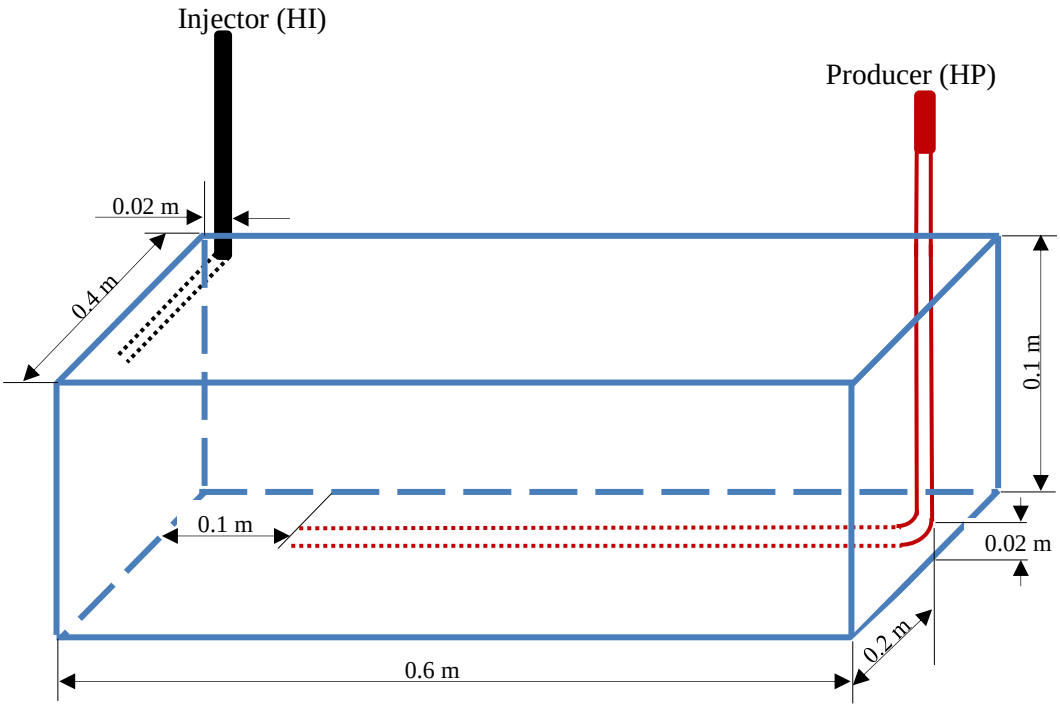

Fig. 4.1: Combustion cell dimensions and injector and producer wells arrangement

An electrical heater/ignitor, imbedded around the inlet face of the sandpack, was switched on until the temperature of the air entrance zone (i.e. around the HI perforations) was 450 to 500 ^{o}C (Xia and Greaves, 2002). Air was then injected immediately at a rate of 8000 Sm^3 min^{-1}, which is equivalent to an air flux of 12 m^3 $m^{-2}h^{-1}$. After 190 minutes, the air injection rate was then increased by one-

third thereby increasing the air injection flux to 16 $m^3 m^{-2}h^{-1}$. This flux was maintained up to the end of the dry combustion period of 320 minutes. During the process, the performance parameters controlling the THAI process, such as the oil rate, cumulative oil production, API gravity, produced oxygen concentration, and the combustion peak temperature, etc. were recorded to allow for history matching with the numerical model.

4.2.2 Numerical Model

The 3D THAI experiment, carried out by Xia and Greaves, (2002), is numerically modelled using the CMG's STARS, which is a commercial thermal reservoir simulator. The combustion cell is discretised into small-sized gridblocks, with the number of the grids ranging from 12,000 to 50,000, to allow for the choice of the optimum mesh size. The simulator solves the discretised governing equations, described in chapter 3, using fully implicit finite difference method. STARS also incorporates a discretised wellbore (DW) option, which allows the transient multiphase flow and heat transport in the HP well to be rigorously modelled. The resulting DW equations are then coupled with the discretised reservoir reaction and transport equations for simultaneous solution. However, to solve the set of the Algebraic equations, some reservoir input parameters, such as porosity, permeability, initial pressure, temperature, and fluid saturations, etc. are required. Also, the kinetics parameters of the multiple reactions taking placing during air injection enhanced oil recovery must be specified. For the cracking reactions, the Phillips et al. (1985) kinetics parameters, obtained from their experiments on the thermal cracking of Athabasca bitumen have been slightly adjusted for use in the model, as explained later. However, the PVT data for the individual oil pseudo-

components has to be, and is, generated separately, since this was not reported by Phillips et al. (1985).

4.2.2.1 Petro-physical Parameters

The porosity and absolute permeability used were taken from Greaves et al. (2012a) and presented in Tab. 4.1.

Tab. 4.1: Fluid saturation, porosity, and absolute permeability (Greaves et al., 2012a)

S_o	S_w	Porosity	Vertical permeability (md)	Horizontal permeability (md)
0.85	0.15	0.34	3450	11500

The adjusted oil/water relative permeability, shown in Fig. 4.2a, is based on the data in Prowse et al. (1983). The gas/oil relative permeability curve (Fig. 4.2b) has been adjusted to increase numerical stability consistent with the experimental result. The adjustment has been found to have negligible influence on the simulation results. This could be because it is only the curves that are smoothen and the end points are not changed.

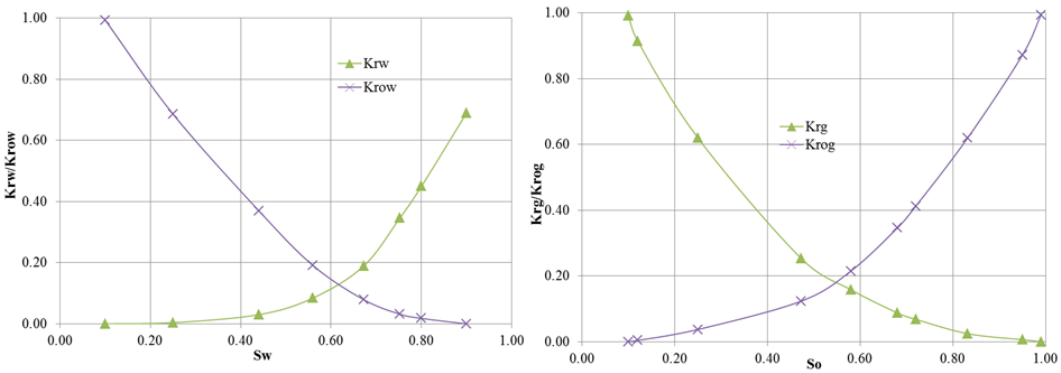

(a) (b)

Fig. 4.2: (a) oil/water, and (b) gas/oil relative permeability curves for the Athabasca bitumen (Prowse et al., 1983). K_{rw} and K_{row} are the water and oil relative permeabilities at water saturation S_w respectively while K_{rg} and K_{rog} are the gas and oil relative permeabilities at oil saturation S_g respectively.

4.2.2.2 PVT Data

The Peng-Robinson Equation of State (PR-EOS), available in Aspen HYSYS software as a fluid package, was used to form an oil blend from which the three Athabasca bitumen pseudo-components were generated (Tab. 4.2). Phillips et al. (1985) defined the initial boiling point (IBP) of the pseudo-components without specifying their respective molecular weights. Also, in some cases, the final boiling point (FBP) of the pseudo-components was not specified. These make it difficult to define, exactly, the pseudo-components as represented by the authors. However, a close enough combination was formed such that the combination of ‘‘Heavy oils’’ and ‘‘Asphaltene’’ is taken to account for 84 wt% of the Athabasca bitumen compared to 89.7 wt% considered by Phillips et al. (1985). The pseudo-components and PVT data are given in Tab. 4.2, where LC, MC, and IC are defined as the light-, mobile-, and immobile components respectively.

Tab. 4.2: PVT Data used in this study

Pseudo-components	LC	MC	IC
Fraction (mol%)	42.5	23.91	33.59
Molecular weight (g/mol)	210.82	496.81	1017.01
P_c (kPa)	1682.88	1038.46	729.22
T_c (^oC)	464.68	698.53	940.36
ρ (kg m^{-3})	828.24	961.66	1088.04
Eccentricity	0.62	1.18	1.44
T_B (^oC)	281.47	549.67	785.78

The variation of Athabasca bitumen viscosity with temperature was taken from Mojarab et al. (2011) and is shown in Fig. 4.3a. The viscosities of the LC and MC components are respectively the same as those of ‘‘Light oils’’ and ‘‘Heavy oils’’ available in STARS. A logarithmic mixing rule, shown by equation 3-23, was then used to estimate the viscosity of the IC pseudo-component (Fig. 4.3c). The phase equilibrium K-values, which are required to account for phase change and were observed to significantly affects the simulation results (Lin et al., 1984), were estimated based on Wilson equation, given as equation 3-19 (Fig. 4.3d).

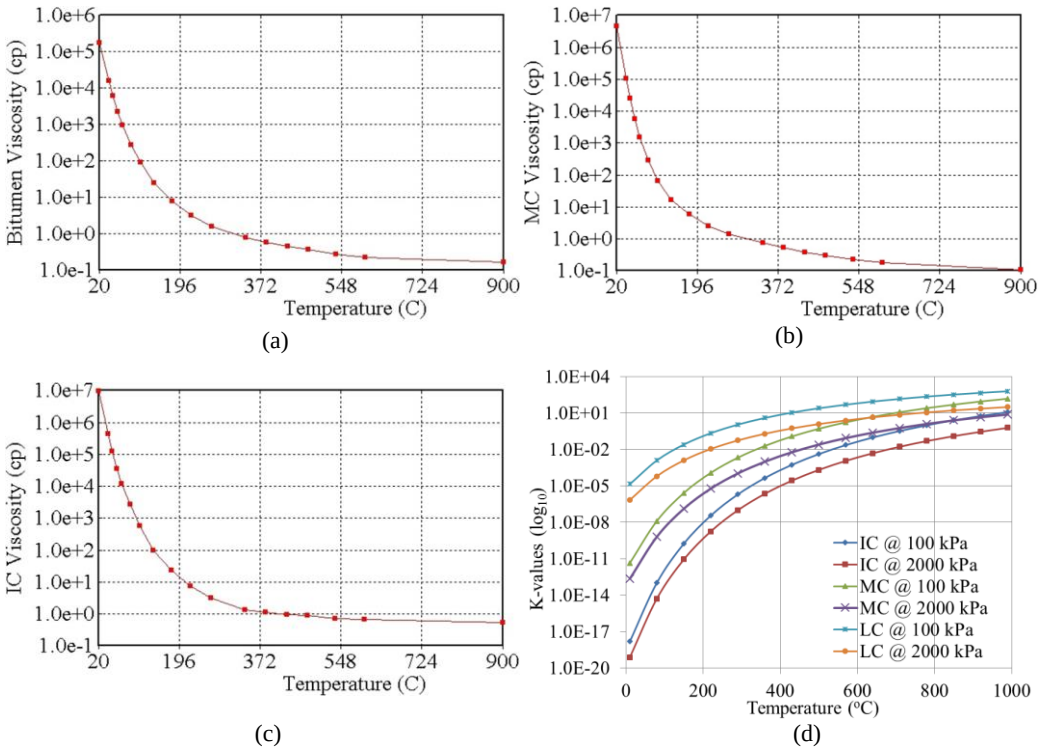

Fig. 4.3: (a) Bitumen, (b) MC, and (c) IC viscosities at 101.3 kPa, and (d) K-values, for the individual components, as function of temperature

4.2.2.3 THAI Kinetics Scheme

Tab. 4.3 shows the original Phillips et al. (1985) kinetics parameters and those used in the current study. After running the model with the original Phillips et al. (1985) parameters, it is observed that the rate of coke deposition was not

high enough to meet the THAI requirement and to history match the experimental results. Therefore, the kinetics parameters for the coke deposition reaction have to be adjusted. Also, the frequency factors and activation energies for Reactions 3 and 4 were 'tuned' using a trial and error search, in order to match the experimental parameters reported by Xia and Greaves, (2002). This is necessary given that the LC as defined in this study is initially present as a higher fraction (16 wt%) compared to the 10.3 wt% given by Phillips et al. (1985). However, the adjustment results in only minor change in the rate constant of the affected reactions. They are, in-fact, still quite similar to the original Phillips et al. (1985) values as the rate constant of the coke forming reaction at 400 ^{o}C is 97.5 % of the original value.

Tab. 4.3: Phillips et al. (1985) and the adjust cracking kinetics parameters for bitumen-sand mixture

No.	Thermal Cracking Reactions	Phillips et al. (1985)		Current study	
		Frequency Factor (min^{-1})	Activation Energy (kJ/mol)	Frequency Factor (min^{-1})	Act. Energy (kJ/mol)
1	IC ➔ 2.0471 MC	3.822×10^{20}	239.01	3.822×10^{20}	239.01
2	MC ➔ 0.4885 IC	3.366×10^{18}	215.82	3.366×10^{18}	215.82
3	MC ➔ 2.3567 LC	3.132×10^{15}	180.88	1.132×10^{15}	184.88
4	LC ➔ 0.4243 MC	1.224×10^{15}	180.95	1.524×10^{15}	180.45
5	IC ➔ 77.4563 COKE	6.960×10^{14}	174.28	2.320×10^{15}	180.88

The frequency factor for the coke combustion reaction and the heat of reaction were adjusted to match the peak combustion temperature in the experiment. A constant $CO_2/(CO_2 + CO)$ ratio of 95 to 97 % was used to calculate the stoichiometry of the combustion reactions in order to match the experimental mole fractions.

Each combustion reaction satisfies the respective mass balances, and the rounded stoichiometric coefficients are shown in

Tab. *4.4*. Although the combustion reaction for each pseudo-component is included in the model, their effect on the simulation results have been found to be insignificant. This is to be expected since, following ignition, the pre-heated inlet zone of the sandpack contains only residual coke – the other lighter fractions having been evaporated off. The establishment of an expanding vigorous combustion zone then also ensures that this process continues, leaving only coke as fuel for combustion. As a result, the peak temperature is controlled by the heat released from the high temperature oxidation (HTO) of coke.

The heat of reaction was tuned in order for the experimental peak temperature to be matched. The value of 390 kJ/mol chosen has been found to lie within the 247.94 and 427.8 kJ/mol reported by Lin et al. (1984) and Belgrave et al. (1993) respectively.

Tab. 4.4: Combustion reactions and respective kinetic parameters

Combustion Reactions	Frequency Factor $(kPa\ min)^{-1}$	Activation Energy (kJ/mol)	Heat of Reaction (kJ/mol)
IC + 106.7 O_2 ➔ 78.9 CO_2 + 4.2 CO + 46.9 H_2O	1.812×10^8	138.00	4.00×10^4
MC + 37.1 O_2 ➔ 28.1 CO_2 + 1.5 CO + 22.4 H_2O	1.812×10^9	138.00	1.60×10^4
LC + 32.025 O_2 ➔ 11.2 CO_2 + 0.6 CO + 14.5 H_2O	1.812×10^{10}	138.00	4.91×10^2
COKE + 1.22 O_2 ➔ 0.93 CO_2 + 0.03 CO+ 0.57 H_2O	1.000×10^{10}	123.00	3.90×10^2

4.2.2.4 Boundary Conditions

To simulate the combustion cell, no flow boundary condition is assumed all over the cell boundary except via the HI and HP. The HI well is flow-controlled with the air injection rate at the early stage set to 8000 cm^3 before it was increased by one-third to 12000 cm^3 at 190 minutes and maintained until 320 minutes. Bottom hole pressure (BHP) of 170 kPa and total liquid production

rate of 25 cm^3 min^{-1} are respectively specified as the primary and secondary boundary conditions for the HP well. This allows the simulator to enforce either the pressure or the flow, depending on which one is violated, as the primary constrain. Also, it is assumed that, during the experiment, heat loss only occurred from both overburden and underburden. Therefore, the heat loss parameters were selected via trial and error until all the experimentally measured performance parameters of the THAI process are matched. It should be noted that since there is no material flow in or out of the overburden and underburden, the heat loss only occurred via conduction.

On running the model, it is found that the high viscosity of Athabasca bitumen (Fig. 4.3a) causes substantial pressure build up during the PIHC. This is due to thermal cracking (i.e. formation of lighter/gaseous components) and blockage of the HP well by the cold viscous oil downstream of the mobilised oil, around the toe of the HP well. However, at typical Athabasca reservoir temperatures of 5 to 15 ^oC (Gates and Larter, 2014), no oil is expected to be present inside the horizontal producer except if it has some initial mobility or the viscosity is lowered by pre-heating. Therefore, unlike in the case of Greaves et al. (2012a) model, it is the distinct feature of this model that no oil is considered to be present inside the HP prior to mobilisation.

4.2.2.5 Grid Sensitivity Study

In order to choose the optimum mesh size, simulations were run for six different grid types (Tab. 4.5) in order to determine which one gave sufficient resolution to model the dynamics of the combustion zone, commensurate with computational efficiency. From Tab. 4.5, it can be seen that the ‘fine mesh’ and

the ‘fine dynamic mesh’ have the same number of gridblocks. The same goes to ‘finer mesh’ and ‘finer dynamic mesh’. The difference between each set lies in the use of the conditional dynamic grids, the DG option in STARS. This allows the removal of child gridblocks from a parent gridblock, to restore the latter to it is original size prior to refinement. The criterion used to, dynamically, ‘‘REFINE’’ and ‘‘DE-REFINE’’ the mesh is such that when the global mole fraction of any component is $\leq 3\%$, oil mole fraction is $\leq 2\%$, pressure variation is within 20 kPa, cell temperature variation is within 30 ^{o}C, etc. then the cell sizes should be restored to their original dimension before refinement. The software checks when to dynamically refine or de-refine after a certain number of time steps, specified by the user, is passed. However, this requires careful calibration so that the simulation time is shortened while obtaining accurate results. In this work, 121 time steps is found to result in substantial decrease in overall simulation run time (Tab. 4.5).

The resulting Algebraic equations, due to discretisation, were solved using PARASOL, which is a parallel processing solver available in STARS. The computer used to run the models has two parallel processors each with 8 cores (i.e. 16 cores and, thus, 32 threads in total). However, only 25% of the CPU is used as the maximum number of threads that can be specified to PARASOL is 8.

The effect of grid size on combustion peak temperature is not very significant, overall. As can be seen from Fig. 4.4a, during the lower air flux period (up to 190 minutes), regardless of the number of GBs, there is a divergence from the experimental trend after the initial start-up, but the difference subsequently

diminishes considerably, after about 120 minutes, and even more so into the higher air flux period. Also, sensitive to the number of GBs is the time when a spike appears on the peak temperature. The spike could be caused by the combustion front reaching high coke concentration spot which will cause a sharp rise in the reaction rate and hence the rate of heat generation. It is observed that the time at which the spike appears experimentally is closely predicted by 'fine mesh' (Fig. 4.4a).

Tab. 4.5: Number of gridblocks (GBs) and the time elapsed for numerical convergence

Grid	Number of GBs	Run Time (h)
Coarse Mesh	12,000	0.43
Medium Mesh	19,000	1.13
Fine Mesh	38,000	3.80
Fine Dynamic Mesh	38,000	2.40
Finer Mesh	50,000	5.48
Finer Dynamic Mesh	50,000	2.88

However, prediction of time at which oxygen production begins and the concentration of the produced oxygen is more critical to ensuring the success of the THAI process. Also, as already mentioned, the earlier Greaves et al. (2012a) model was seriously deficient in that it failed to accurately predict the time when oxygen was first detected at the production well. The 'fine dynamic mesh' was selected for the simulation study because it accurately predicts this event (Fig. 4.4b), as well as the subsequent increasing trend, albeit in an oscillatory manner.

The other parameters in Fig. 4.4 are quite well-matched, especially the cumulative oil production (Fig. 4.4c). The prediction of oil upgrading is more variable, but generally lies within ±2 API points, and all of the different mesh predictions more or less converge on the same solution (Fig. 4.4d).

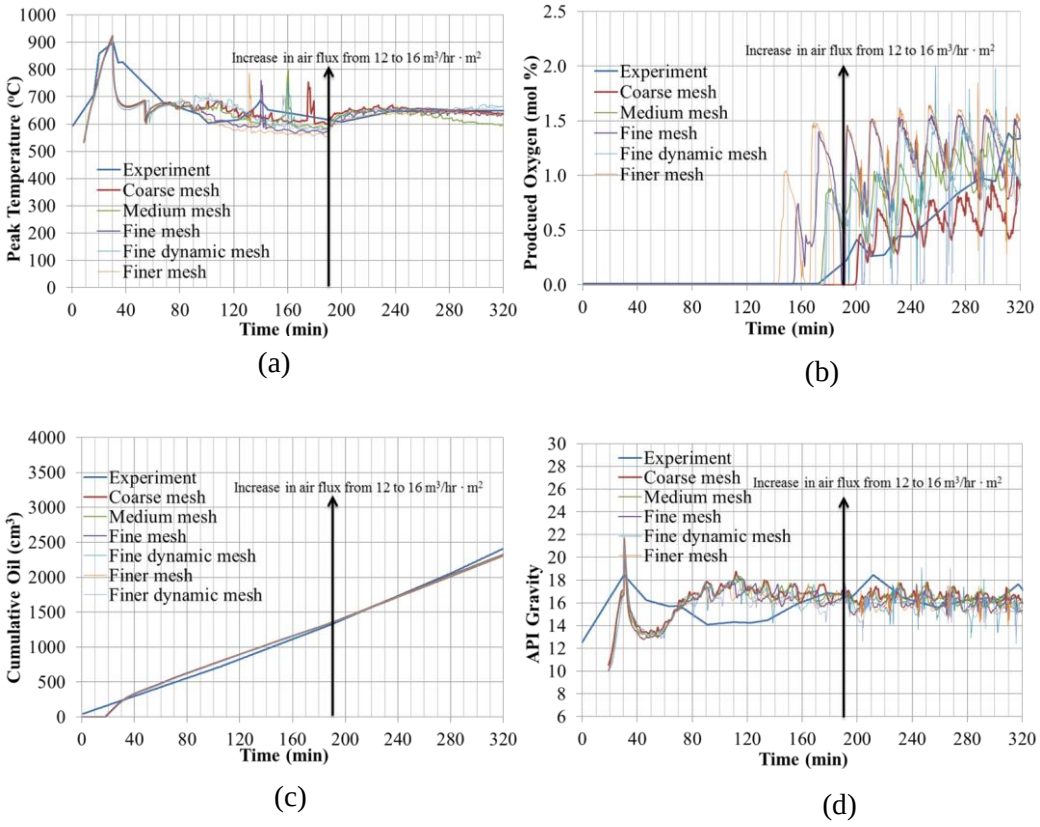

Fig. 4.4: Effect of different grid sizes on the prediction of (a) Peak temperature, (b) Produced oxygen, (c) Cumulative oil production, and (d) Degree of upgrading

4.3 Results and Discussion

4.3.1 History Matching Phillips et al. (1985)

In the following subsections, the results obtained from the THAI model, which uses the Phillips et al. (1985) thermal cracking scheme and is validated against the experimental result, are discussed.

4.3.1.1 Start-up and Oil Production

Liang et al. (2012) reported that one of the most critical factors affecting the overall stability of the THAI process was the start-up procedure. A distinct feature of the present model is that it takes into account the fact that no oil is present inside the horizontal producer (HP) prior to the pre-ignition heating cycle (PIHC). During the first 18 minutes of the PIHC, no oil was produced, because the oil has to first become mobile before it can flow to the HP (Fig. 4.5a). The use of electrical heaters to pre-heat the inlet zone of the sandpack, including near the toe of the horizontal injector (HI), results in the formation of thermally cracked products (gaseous/light hydrocarbons) causing a build-up in pressure around the toe of the HP during the start-up period. As a result, during the next 12 minutes (i.e. from 18 to 30 minutes), the predicted oil production rate greatly overshoots the experimental rate (Fig. 4.5a). The experimental oil rate did not show a spike because of the averaging out due to low sampling rate during the experimental measurement of the oil flow rate.

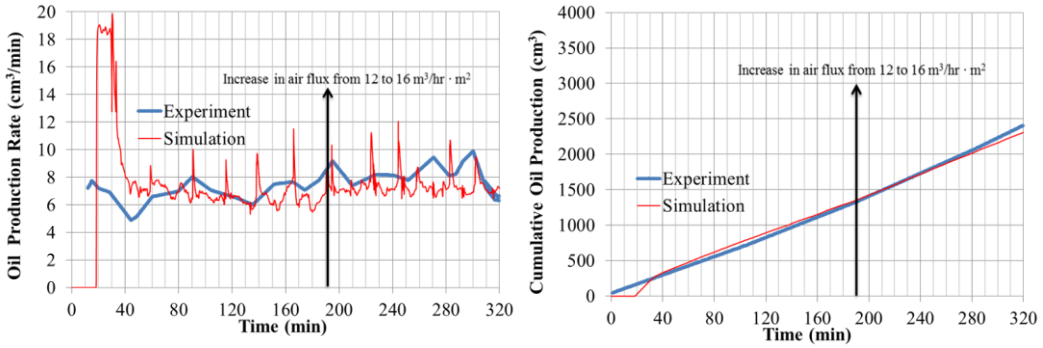

(a) (b)

Fig. 4.5: (a) Oil production rate, and (b) Cumulative oil production

As the pressure in the combustion cell settles to a steady value, the predicted oil rate quickly converges on the experimental trend. Overall, the simulation

showed good agreement with the experimental trend, particularly during the lower air flux period, where the deviation is less than 0.5 cm^3 min^{-1}. There is also generally excellent agreement between the predicted and experimental trends in cumulative oil production (Fig. 4.5b). At the end of the combustion period (Fig. 4.5b), the overall relative error is only 4%, compared to 7.2% in the results of Greaves et al. (2012a).

4.3.1.2 Peak Temperature

In Fig. 4.6, the experimental and the predicted peak combustion temperature plots show good overall agreement. There is a very good match of the maximum temperature following ignition (≈ 900 ^oC) and also in the higher air flux period, after 190 minutes. However, there are some significant deviations during the first, lower air flux period. Here, the predicted peak combustion temperature twice undershoots by 100 ^oC, and also overshoots by a similar margin. It is possible that the tape heater control strategy employed in the experiment over-compensated for the heat loss, allowing the sandpack temperature to increase, and then under-compensated causing the temperature to undershoot. However the simulation prediction during the higher air flux period is excellent.

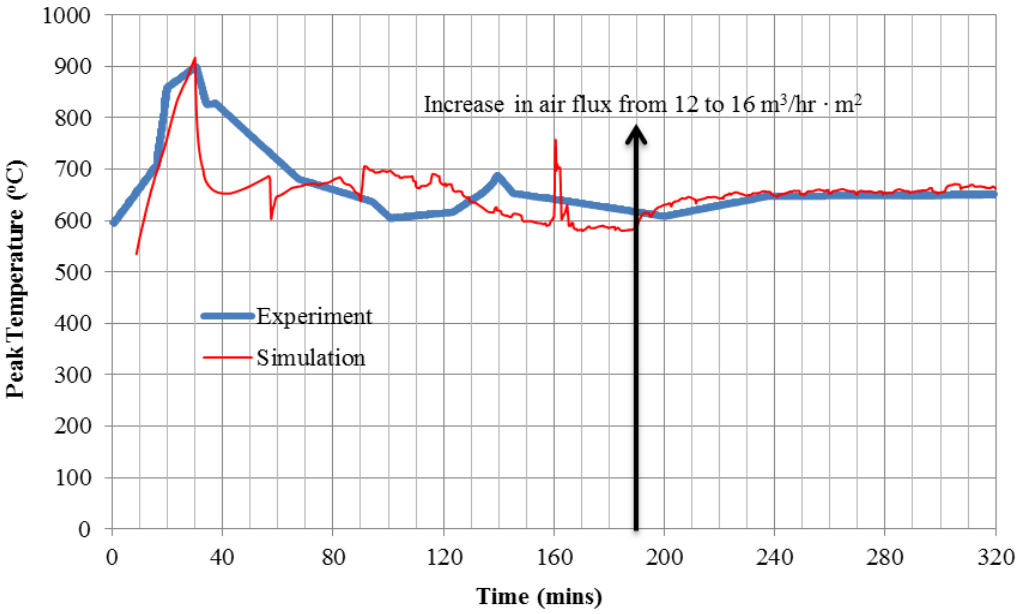

Fig. 4.6: Experimental and simulated peak temperatures

The experimental peak temperature has a small spike at 140 minutes. This is caused by the combustion front reaching a high coke concentration zone, possibly just before the toe of the HP well. The simulation predicted the spike to take place at 160 minutes indicating a 20 minutes lag compared to the experiment. However, despite this, a significant improvement is obtained when compared with the prediction by Greaves et al. (2012a), which lagged by 135 minutes.

4.3.1.3 Oil Upgrading

There were some differences between the API gravity predicted by the model and that observed experimentally (Fig. 4.7), of up to ±4 ^{o}API between times of 20 and 120 minutes. These differences occur mainly during the first period, when the air injection flux was lower, being only 12 $m^3m^{-2}h^{-1}$. The trends tend to reflect the variations in the combustion peak temperature described previously. This is to be expected, since in-situ upgrading of the oil is mainly

due to thermal cracking, the extent of which depends upon the temperatures generated in the combustion zone.

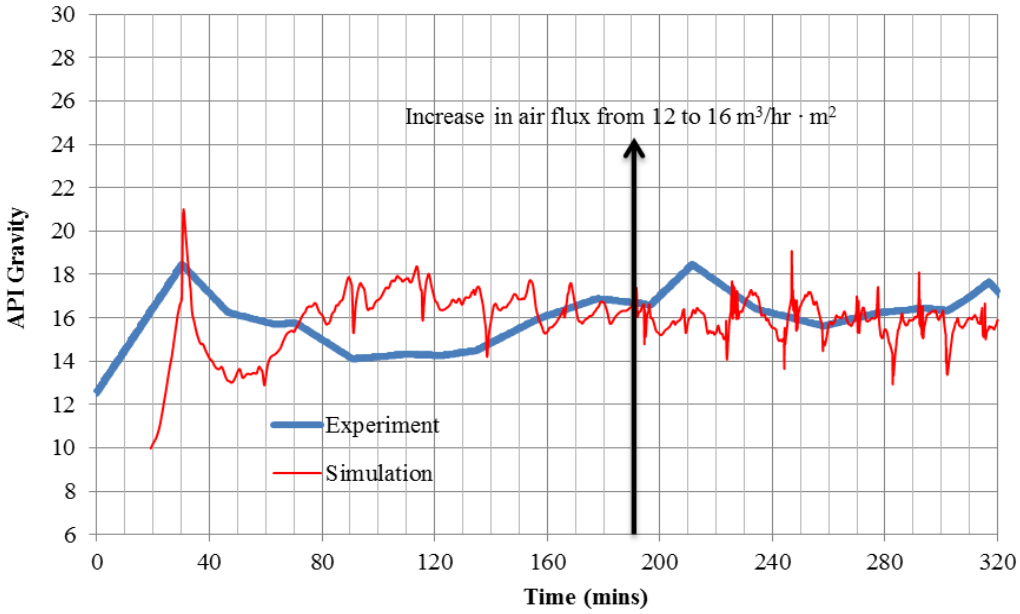

Fig. 4.7: Experimental and simulated API gravity

There is, generally, a fairly good agreement between the experimental and simulated API gravity values, especially during the higher air flux period where the maximum deviation is ±2 ^{o}API between 200 and 230 minutes. One slightly curious result is that, although the combustion peak temperature is slightly higher when the air flux is higher, the degree of oil upgrading is slightly lower on average, by about 1^{o}API.

4.3.1.4 Oxygen Production

In the 3D combustion cell experiment (Xia and Greaves, 2002), the gas composition showed that oxygen was first produced before the increase in air injection flux. This finding contradicted the assertion by Greaves et al. (2012a) that the first appearance of oxygen was due to the sudden increase in air

injection rate. This therefore, warranted further investigation and was key to understanding the dynamic behaviour of the THAI process.

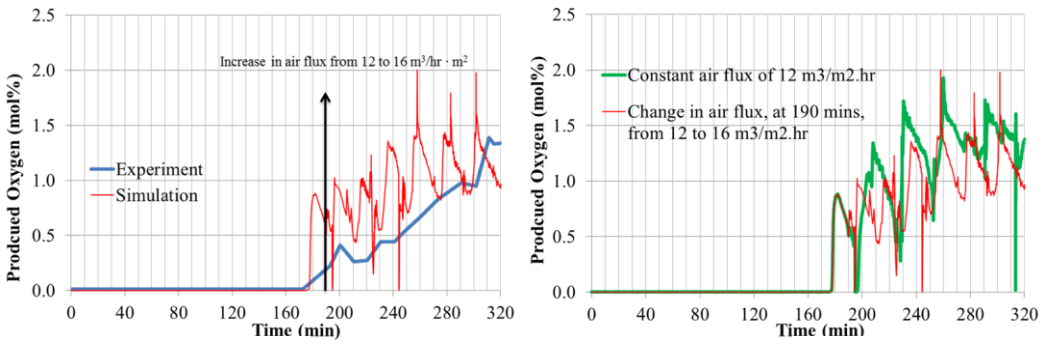

(a) (b)

Fig. 4.8: (a) Experimental and simulated produced oxygen mole fraction, (b) Effect of increase in air flux on the produced oxygen concentration

There are actually two possibilities as to why the produced oxygen began to increase before there was any increase in air injection rate. It could be due to a partial instability, in which case the oxygen response should either reach a new steady state or become zero. It could also have been due to channelling of air between the combustion cell wall and the sand pack, but this is not very likely because the experimental oxygen response appears to tend to a steady state after 310 minute (Fig. 4.8a). Further, Xia and Greaves, (2002) did not report any problem of this sort during the experiment. However, because the dry combustion experiment lasted for only another 10 minutes (to 320 minutes), it is impossible to conclude this with any certainty. It can be seen in Fig. 4.8a that the start of the oxygen increase in the producer well is accurately predicted, and the subsequent increasing trend is also well predicted, up to the end of the dry combustion period.

In order to investigate if there was any other potential reason for oxygen increasing in the producer well, the simulation was run again, but this time with

the air flux maintained at 12 $m^3m^{-2}h^{-1}$ for the whole dry combustion period. The increase in oxygen (Fig. 4.8b) occurred at exactly the same time, regardless of whether the injected air flux was increased or not. The overall trend was similar in both cases. The lower flux curve overlies the higher flux curve by a fraction of a percent. At the end of the dry combustion period, the fuel availability increased by up to 4 kgm^{-3} (that is 33 %) due to the increase in air injection flux by one-third. This is similar to the observation made by Alexander et al. (1962) that an increase in oxygen utilisation causes an increase in fuel availability.

Also, of note is the oscillatory nature of the predicted produced oxygen concentration (Fig. 4.8a). This has nothing to do with numerical stability issues, because it has been shown earlier that regardless of the mesh system/type used (Fig. 4.4), the trend of the produced oxygen concentration is oscillatory. To support this assertion, exactly similar trend was observed and reported by Kovscek et al. (2013). In a similar fashion, the experimental trend, though not to the same extent as the predicted, exhibits an oscillatory nature. It is found that the oscillation is directly related to the coke concentration along, and the amount of oxygen that reached the HP well. This is reflected by the coke profile along the vertical mid-plane. It shows an alternating high and low coke concentration along the HP well. When the concentration is high, major part of the oxygen that reached the toe of the HP well is consumed. On the other hand, when the deposited coke concentration is low, less amount of oxygen is consumed.

4.3.1.5 Shape of Combustion Front and O_2 Utilisation

During the dry in situ combustion period, the region swept by the combustion front had 100% gas saturation (Burger et al., 1985). The same should apply in

THAI, so that the region behind the combustion front will be occupied by the injected air. The shape, or leading edge of the combustion front should, therefore, coincide with the boundary where the oxygen concentration falls to zero (Greaves et al., 2012a). Fig. 4.9 provides an indication of the approximate shape of the combustion front, since the oxygen concentration at the leading edge of the combustion front is not everywhere zero.

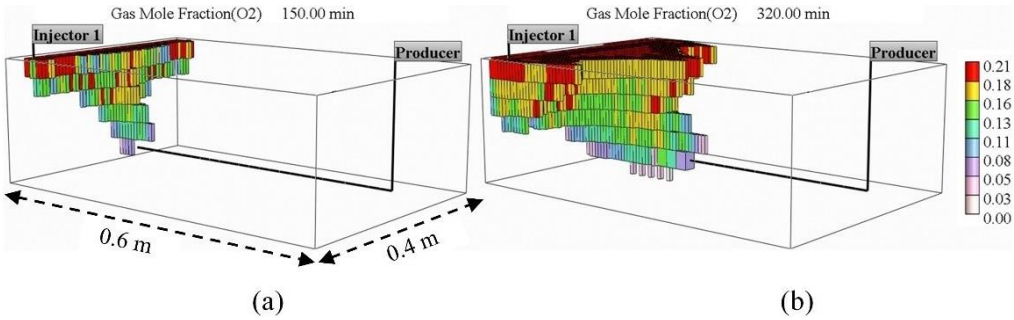

Fig. 4.9: Approximate shape of the combustion front at (a) 150, and (b) 320 minutes

The combustion zone in the upper part of the sandpack (Fig. 4.9a) has expanded across the entire width of the cell by 150 minutes after the start of air injection. There is a gradual tapering of the combusted zone, downwards towards the horizontal well, as the combustion front advances through the sandpack (Fig. 4.9b). After 320 minutes (Fig. 4.9b), the burned zone covers about 30 % of the axial length of the sandpack.

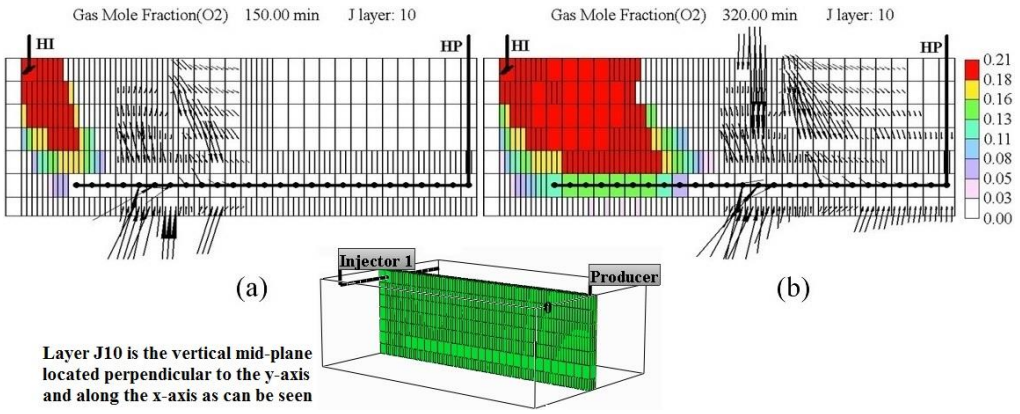

Fig. 4.10: Oxygen concentration profiles along the vertical mid-plane at (a) 150, and (b) 320 minutes

Fig. 4.10a also shows that, in the vertical mid-plane, the combustion front is about 2 cm away from the toe of the HP. Since the combustion front velocity is steady at 6 cm h^{-1} over the next 20 minutes, the inlet region of the sandpack, up to the toe of the HP, will therefore have been swept by the combustion front. Most strikingly, in Fig. 4.10b, although there is oxygen in the HP along about 30 % of its length from the injection end of the sandpack, downstream of this there is no oxygen present. Nevertheless, increasing the air injection flux by 33 % would be expected to push the process much closer to instability, and in practice, therefore, it would be safer to design for a lower air injection rate. Even though the oxygen concentration in the HP reaches up to 16 % for about one-third the distance from the toe, it then decreases to almost zero. This is due to the sealing effect provided by the deposited coke downstream of the combustion zone, inside the HP well.

The penetration of oxygen into the toe of the HP well begins around 170 minutes, which is 20 minutes after the combustion front reached a distance of 2 cm away from the toe of the HP. It can be observed that oxygen production began at around the same time (Fig. 4.8a). This shows that once the combustion front starts to propagate along the HP well, the process is only partially stable.

Under this condition, the combustion front along the vertical mid-plane is characterised by backward leaning shape, with the lower end leading into the HP well (Fig. 4.10a). These observations are similar to those made by Liang et al. (2012) after performing 3D combustion cell experiment. They suggested that to ensure the combustion is mostly restricted to the upper portion of the reservoir, proper start-up design and implementation must be carried out. During their study, when they detected that the process was tending to partial instability, they tried to reverse the trend by lowering the air injection rate while increasing the injection pressure. However, the strategy failed to prevent oxygen production but only delayed it is occurrence. The measure, on the other hand, as claimed by the authors, helped in increasing oxygen utilisation. What is not clear was whether it was lowering the air injection rate on one hand and or increasing the air injection rate on the other that resulted in the increased oxygen utilisation. In order to investigate the effect of changing the air injection flux after the start of oxygen production, the duration of the dry combustion was extended. At 320 minutes, three different scenarios were considered; namely decreasing, keeping constant, and increasing the air injection rate.

Decreasing the air injection rate resulted in an increase in the concentration of the produced oxygen. This is due to decrease in the intensity of the combustion. A corresponding decrease in peak temperature as well as fuel availability was observed. Increasing the air injection rate caused an increase in oxygen utilisation (i.e. a decrease in the concentration of the produced oxygen). Fuel deposition as well as the peak temperature have been observed to increase. As a result of that, a vigorous combustion front was propagated. By keeping the air

injection rate constant, the produced oxygen concentration varied between the two extremes (i.e. between when the air rate was decreased, and increased).

4.3.1.6 Fuel Availability

Because of the critical importance of fuel availability during ISC, it is accurate prediction could be considered as one of the most robust qualities of a numerical model. The amount of fuel consumed per unit volume of a reservoir is a parameter that would allow the evaluation of both the stability and the economy of ISC. Greaves et al. (2008) reported that getting a 'right' fuel laydown during the start-up phase of THAI is one of the main requirements for a successful combustion front propagation to be established. The amount of fuel deposited should not be so high that it stalls the combustion front or require excessive air injection rate.

In this study, a substantial improvement in predicting the fuel laydown has been achieved, compared to the result of Greaves et al. (2012a). At the end of the dry combustion period at 320 minutes, the predicted average fuel availability is 52.3 kg m^{-3} of reservoir volume. Greaves et al. (2012a) predicted an average fuel concentration of 85.4 kg m^{-3}, which is nearly 40% higher than obtained in this study. The predicted fuel laydown ahead of the combustion front has, therefore, been reduced by over 40% giving a value which lies within the expected range for Athabasca Oil Sands. Based on the work of Alexander et al. (1962), the estimate for fuel availability for Athabasca bitumen, which has a H/C of 1.53 and an API gravity of 9 points, at 25 ^{o}C, ranges from 50 to 57 kg m^{-3} of bulk reservoir volume.

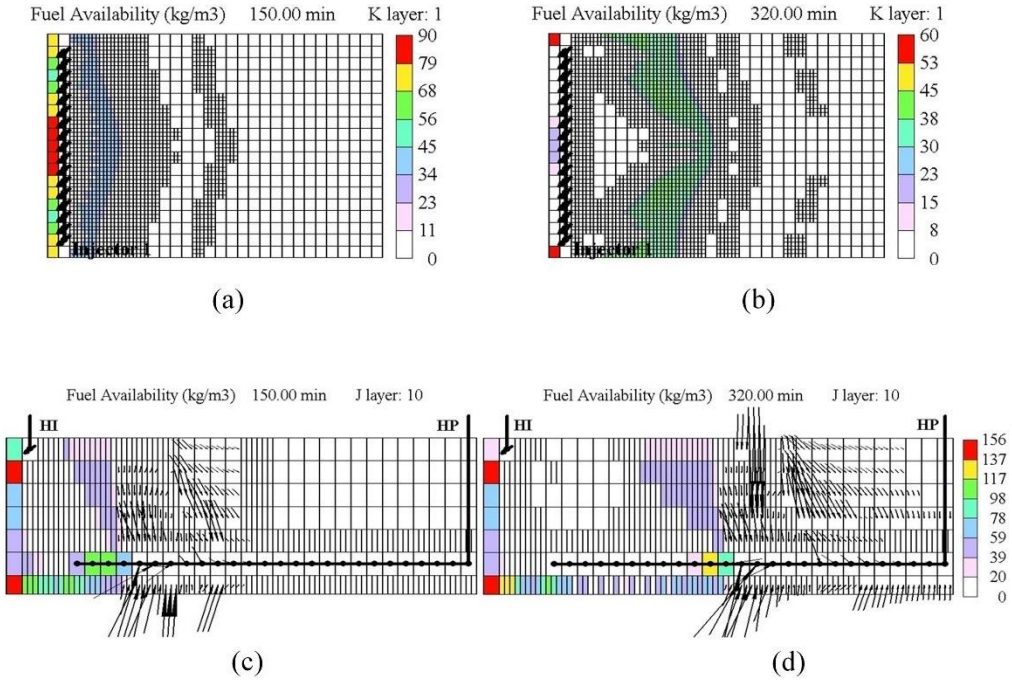

Fig. 4.11: Coke concentration profiles (kg m^{-3}); at top horizontal plane (K layer 1) at (a) 150, and (b) 320 minutes; along vertical mid- plane (J layer 10) at (c) 150, and (d) 320 minutes

It is clear from Fig. 4.11 that the predicted fuel concentration varies considerably, depending on position in the sandpack. The fuel concentration immediately ahead of the combustion front remains constant, in the range of 35 to 40 kg m^{-3}. Traversing downwards through the sandpack there is an increase in the fuel concentration from 40 to 156 kg m^{-3}. The highest coke concentration is found in the bottom layer of the sandpack, directly below the HP. Because the mobilized oil flows by gravity towards the HP, generally less coke is deposited along the vertical mid-plane. This is because this is the region which experiences the most intense drawdown. The form of the coke profiles in Fig. 4.11 are very similar to those obtained from the post-mortem examination of the 3D THAI combustion cell experiment (Greaves et al., 2012a). The region swept by the expanding combustion front has zero coke concentration, which is a finding that has also been reported by Chen et al. (2012) after conducting their post-mortem analysis.

4.3.1.7 Temperature Distribution

The simulated temperature distributions provide a more detailed indication of the extent of the combustion reaction and heat transfer in the sandpack, not easily obtained from experimental measurements. The different regions over which the low temperature oxidation (LTO) and the high temperature oxidation (HTO) take place are usually identified by specific ranges of temperature. The top horizontal plane and vertical mid-plane temperature profiles are presented in Fig. 4.12. The temperature around the combustion zone is generally greater than 400 ^{o}C, implying that only coke combustion takes place there, and hence the incidence of LTO is negligible.

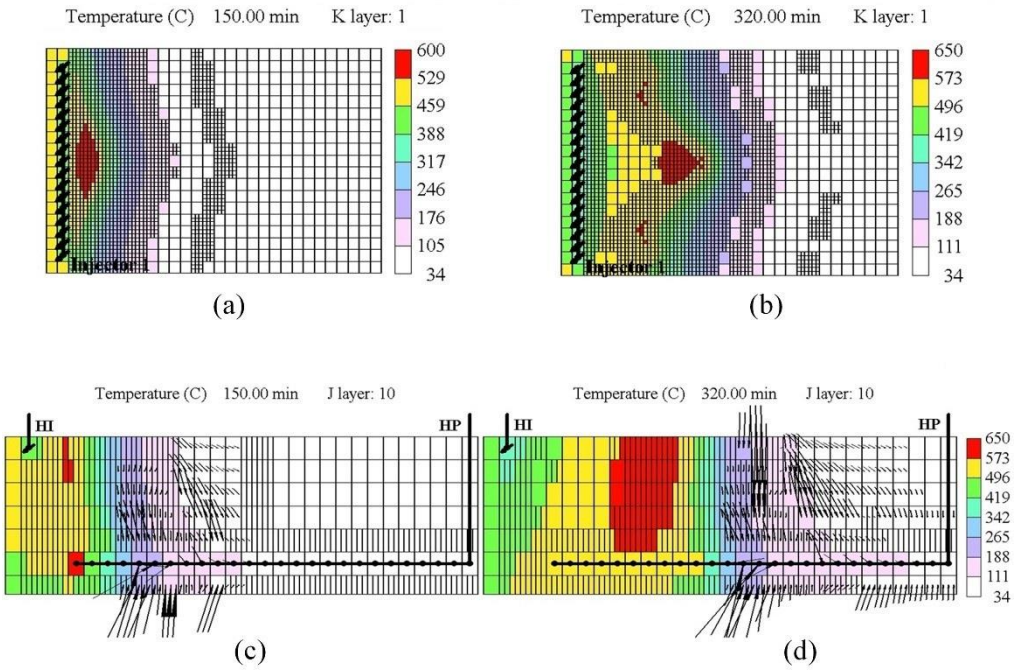

Fig. 4.12: Temperature distribution: top horizontal plane (K layer 1) at (a) 150, and (b) 320 minutes; vertical mid-plane (J layer 10) at (c) 150, and (d) 320 minutes

4.3.1.8 Oil Saturation

In Fig. 4.13, the Mobile Oil Zone (MOZ) is identified by the oil flux vectors superimposed on the oil saturation profile. They indicate the relative magnitudes of oil flow rate. The temperature in the MOZ (Fig. 4.12) along the

HP well axis ranges from around 111 ^{o}C near the cold oil layer, to around 265 ^{o}C upstream of this, at the trailing edge. Further out into the predominantly cold oil zone of the sandpack, the highest temperatures are about 50 ^{o}C lower than this. These show, just like shown by Greaves et al. (2012a), that the temperature of the MOZ is not enough for catalytic effect to be achieved.

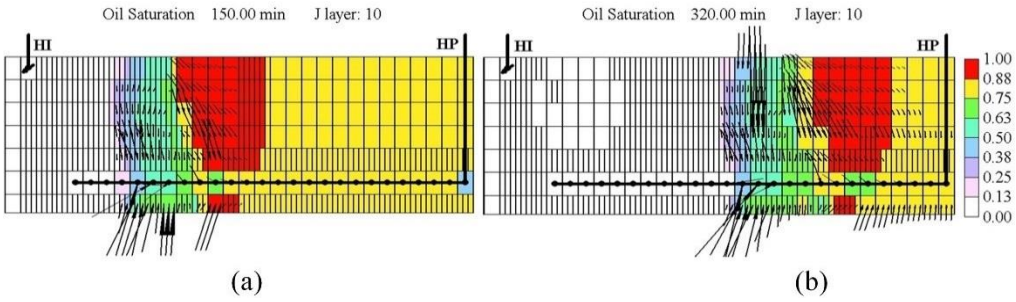

Fig. 4.13: Oil saturation along vertical mid-plane (J layer 10) after (a) 120, and (b) 290 minutes of the start of ignition

The distance between the trailing edge of the MOZ and the combustion front is the main determinant affecting the temperature of the MOZ, and hence, the rate at which oil drains into the HP well. Overall, the distance varies from about 5 to 8 cm in Fig. 4.13, over the 170 minutes of combustion time. This is equivalent to 7 to 15 % of the length of the sandpack (or HP well). In the field, this would be equivalent to approximately 35 to 70 metres for a 500 m long HP. Initially, it was assumed that the more oil is displaced in preparation for air injection, the further should the MOZ be away from the combustion front. By decreasing the initial electrical heating rate, it was observed that the distance separating the MOZ from the combustion front, is only marginally decreased. This is despite the smaller quantity of oil displaced during the PIHC. This finding is very important as it shows that manipulating the start-up has negligible effect on the location, and thus the temperature of the MOZ, where catalytic upgrading is envisaged.

For the most part, the oil rate vectors are either vertical or forward leaning, downwards, into the HP. There are also upwards-directed vectors, indicating that there is significant flow of oil from beneath and into the HP. The smaller oil rate vectors located in the cold oil zone, indicate that some oil drainage occur there. It is also very evident that oil banking occurs immediately ahead of the MOZ. Overall then, the picture is one of higher oil rate from the upstream section of the MOZ from a region of lower oil saturation (25 to 60 %), but lower rates (about half) from the banked oil region ahead of it, where the oil saturation is highest (80 to 100%), but also colder.

4.3.2 Effect of Air Flux on the THAI Process

To study the effect of air flux on the THAI process, seven different models were developed. The performance indicators discussed here are the percent oil recovery, oxygen utilisation, fuel availability, and cumulative air to oil ratio (CAOR) as function of the average air flux over the same operation time. At the lowest air flux studied (Fig. 4.14a), an oil recovery of only 17.0 % OOIP is achieved. The oil recovery increases with an increase in the air flux. This is due to the increase in the rate of heat generation and thus oil mobilisation and drainage rates. At the highest air flux of 18 $m^3 m^{-2}h^{-1}$, 41.6 % OOIP is recovered implying non-linear relationship, since quadrupling the air flux resulted in 145% increase in the oil recovery. This is partly due to the drop in oxygen utilisation as the air flux was increased (Fig. 4.14b).

The oxygen utilisation (Fig. 4.14b) initially dropped rapidly with the increase in air flux, reaching a minimum of 97.2 % at air flux of 12 $m^3 m^{-2}h^{-1}$ before increasing gently to 98.1 % at the highest air flux. The model shows that at the

lowest air flux, the front did not propagate along the HP well and, consequently, no oxygen was produced. As the air flux was increased, the combustion front quickly reached, and hence propagated along, the HP well. This is the reason for the fall in oxygen utilisation. However, further increase in air flux, beyond 12 $m^3 m^{-2}h^{-1}$, resulted in an increase in fuel availability, which in turn resulted in delaying the combustion front from quickly reaching the toe of the HP. Apart from the drop in oxygen usage, the increase in fuel availability with the increase in air flux (Fig. 4.14c), which is caused by increased intensity of the combustion front and the rate of heat generation, is also responsible for the non-linearity of the oil recovery. At higher air flux, larger combustion zone temperatures accelerate the rate of thermal cracking, thereby increasing the fuel availability. Correspondingly, the oil left inside the cell decreases with the increase in the air flux.

Ideally, the cumulative air to oil ratio (CAOR) should remain constant with increasing air flux, most especially since the variation in the oxygen utilisation (i.e. 97.5 to 100%) is negligible. However, all the models show that the CAOR rises with the increase in air flux (Fig. 4.14d), which is the further indicator that the cumulative oil recovery is not in direct proportion to the cumulative air injected. Therefore, it can be inferred that to obtain accurate air requirement, the factor by which the oil recovery increased should be taken into account by varying the air flux and running a series of simulation. Also, the simulation reveals that there is a maximum air flux beyond which the economy of the THAI process deteriorates. As a consequence, careful determination of the optimum operating conditions (i.e. recovery duration and cost of air injection) should be carried out prior to deployment.

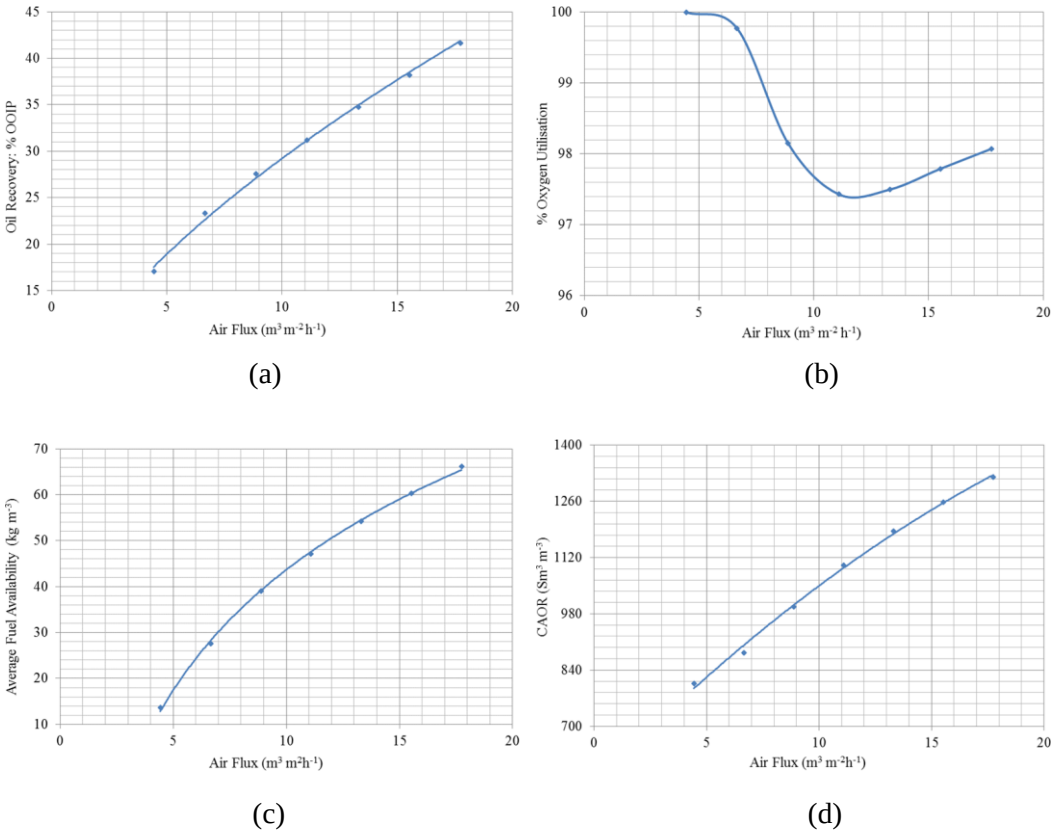

Fig. 4.14: (a) Oil recovery (% OOIP), (b) Percent oxygen utilisation, (c) Average fuel availability, and (d) Cumulative air-oil ratio (CAOR), as function of air flux at the end of 320 minutes

4.3.3 Effect of Viscosity on the THAI Process

The effect of reservoir viscosity on the THAI process is studied by running four more models in addition to the validated model described earlier. The viscosity-temperature curve of the base case model is multiplied by factors of 4, 2, 1/2, and 1/4 respectively. This allows the heavy oil to be represented by viscosity similar to that of Wolf Lake, Lloydminster, and Athabasca. Different performance indicators are plotted against the initial reservoir viscosity at 25 ^{o}C. For the same air injected and the same combustion time, as the heavy oil became more viscous, the volume of reservoir swept by, and hence affected by the heat from, the combustion front is reduced. The decreased oil mobility, therefore, causes a sharp decline in the oil recovery (Fig. 4.15a).

As the mobility of the oil is reduced with the increase in viscosity, the quantity of oil that is thermally cracked, due to heat from the high temperature combustion, is increased. Therefore, the fuel availability increased with increase in oil viscosity (Fig. 4.15b). These show that the recoverable oil left inside the cell at the end of 320 minutes increases as the oil viscosity is increased. Therefore, it can be drawn that it will require longer time to completely produce a given reservoir containing a highly viscous heavy oil than that containing moderately viscous heavy oil. The oxygen utilisation is expected to increase with the increase in fuel availability. This can be seen in Fig. 4.15c, where the model predicted a 100% oxygen utilisation at the highest viscosity considered in this study. This shows that the THAI process is very stable in highly viscous heavy oil reservoir, mainly because the combustion is restricted to the upper portion of the reservoir above the HP well.

The reduction in oil mobility, and therefore recovery, due to the increase in viscosity is reflected in the increase in the CAOR (Fig. 4.15d). At the lowest viscosity, 22800 cP at 25 ^{o}C, the CAOR is lowest (i.e. 821 Sm^3 m^{-3}) despite having lowest oxygen utilisation when compared to at the highest viscosity, where the CAOR is 1600 Sm^3 m^{-3}. This shows that highly viscous reservoirs are costlier to produce using the THAI process despite it is high recovery potential.

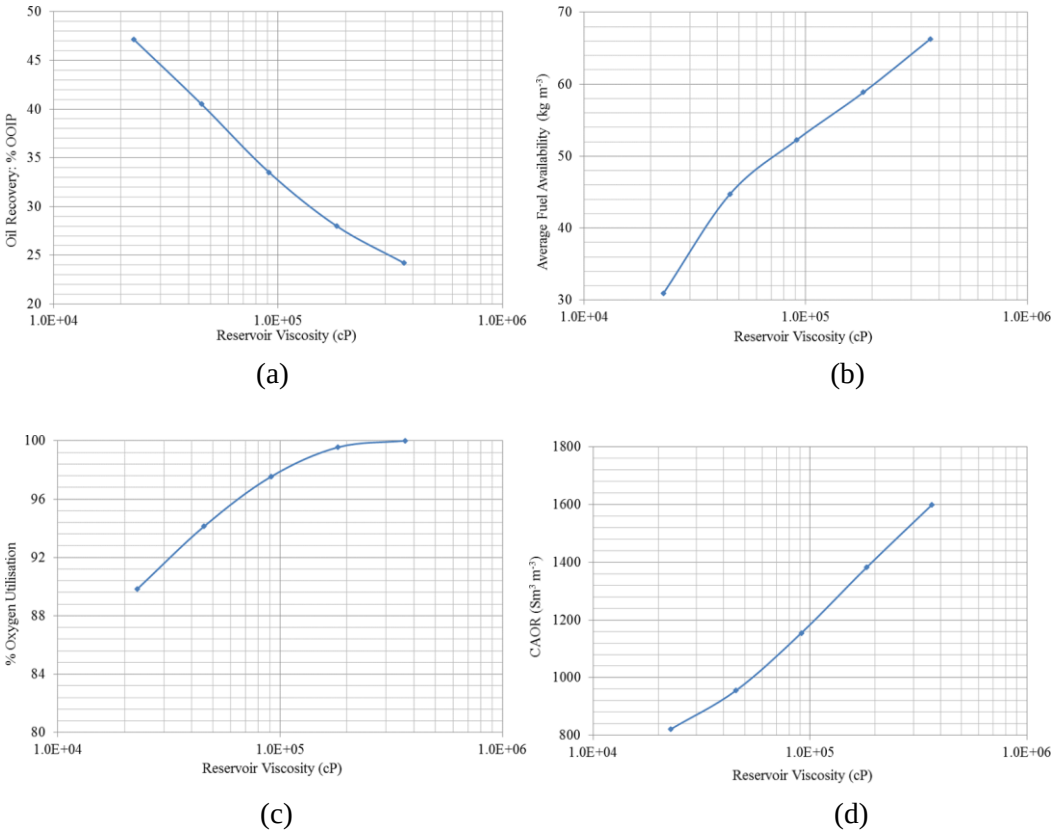

Fig. 4.15: (a) Oil recovery (% OOIP), (b) Average fuel availability, (c) Percent oxygen utilisation, and (d) Cumulative air-oil ratio (CAOR), as function of initial reservoir viscosity at 25 ºC and at the end of 320 minutes

4.3.4 Effect of PIHC method

In the laboratory scale model, heat energy was supplied, around the 17 gridblocks into which the HI well is located, at a rate of 35.25 W. This is based on an electrical mode of pre-ignition heating cycle (PIHC). Therefore, to use steam to pre-heat the inlet zone of the HI well, the same quantity of energy must be supplied. Saturated steam of 100 % quality at 2600 kPa and 226 ºC has heat of condensation of 1831 kJ kg^{-1}. This means that at the experimental model, the rate of steam injection is 21.17 cm^3 min^{-1} cold water equivalent (CWE).

Two models, in which steam is used for the PIHC, were simulated and the results compared against the base case model which used electrical mode of pre-heating. The base case model 1P has a horizontal-injector and horizontal-

producer (HIHP) well arrangement and it is result has already been presented in section 4.3.1. Model 2P has the same well arrangement as model 1P except that steam was injected, at the rate of 21.17 cm^3 min^{-1}, into the HI well for the 30 minutes of PIHC. In the case of model 3P, the wells were arranged in a staggered line drive (SLD) as two vertical injectors and a horizontal producer (2VIHP). Steam was then injected via each VI at the rate of 10.585 cm^3 min^{-1} over the 30 minutes of PIHC. All the models were run under the same conditions, with the electrical ignitor used around the injectors to initiate the combustion at the beginning of air injection.

Fig. 4.16a shows that ignition is achieved immediately air injection commenced and regardless of the PIHC method. The peak temperature in model 2P rises rapidly to 800 ^oC within 10 minutes after the start of air injection. Similar sharp increase in peak temperature occurred in model 3P except that the maximum it reached, at 40 minutes, is 670 ^oC. Comparing models 2P and 3P with the model 1P, the peak temperature reached maximum in the latter 10 minutes earlier. This is caused by the difference in the fuel availability at the end of the PIHC in which high fuel is available in model 1P, due to the severity of the thermal cracking caused by the electrical conductive heating. It is observed that model 1P peak temperature lies above those of models 2P and 3P for nearly all the combustion period. This happens as a result of decreased fuel concentration at any given location, noting that the one-dimensional peak temperature does not give the extent of the spread and vigour of the combustion front.

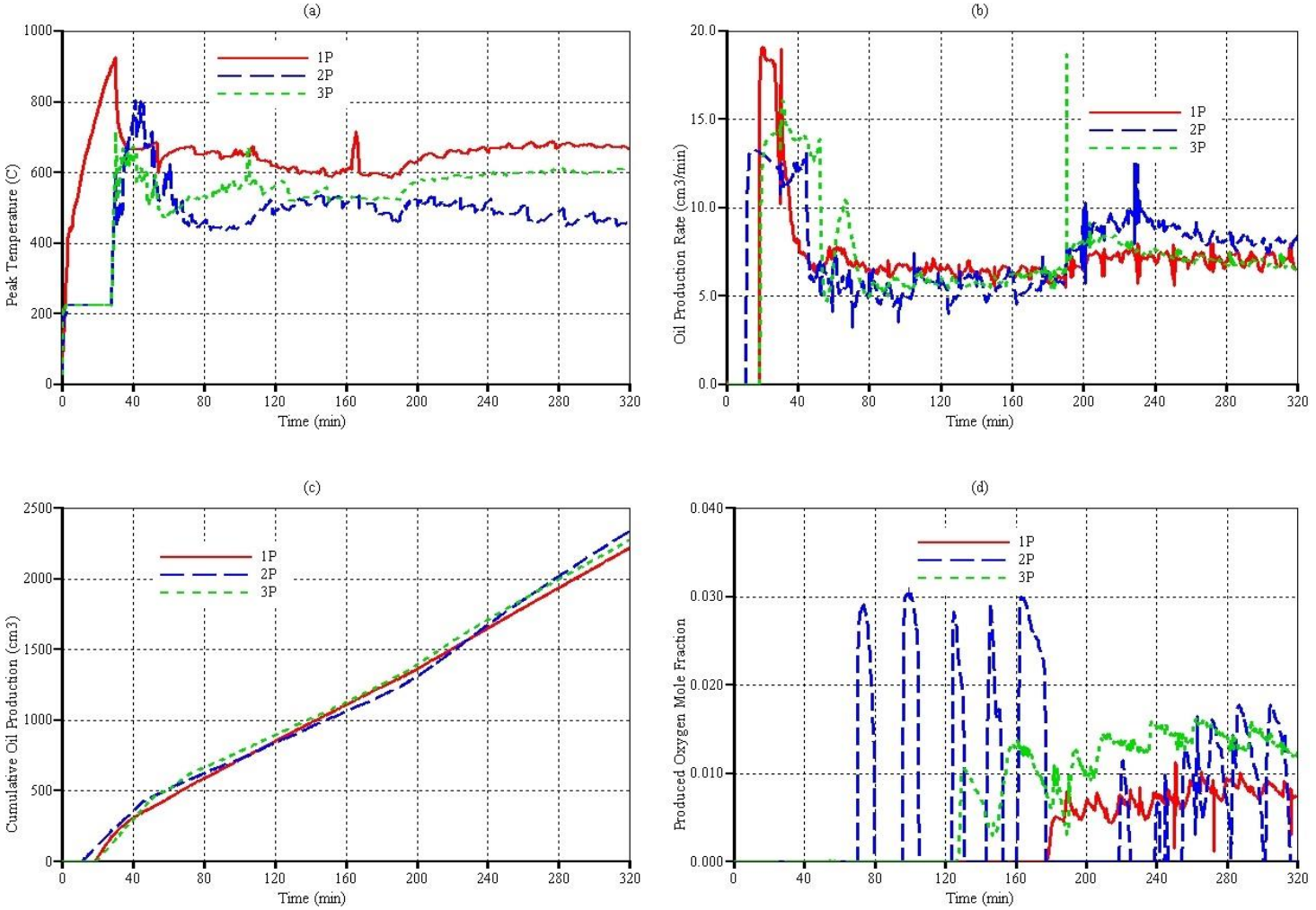

Fig. 4.16: (a) Peak temperature, (b)Oil production rate, (c) Cumulative oil production, and (d) Produced oxygen mole percent

All the three models have similar trend in terms of the oil production rate (Fig. 4.16b). However, the production began 8 minutes earlier in model 2P compared to the other models. This is because the use of HI and steam to convectively pre-heat the inlet zone of the sandpack resulted in a uniform oil displacement, and formation of condensing water, across the whole lateral length of the cell. Therefore, communication between the two wells is quickly established. In the case of the SLD arrangement (i.e. model 3P), the liquids have to flow laterally to the HP well. This requires time. However, despite this, the oil production began at the same time as in model 1P. From around 50 to 190 minutes, Fig. 4.16b shows that curve 1P overlies 2P and 3P with the latter two varying between 4.5 and 6.5 cm^3 min^{-1}. The increase in air flux by 33%, from 190 to 320 minutes, causes curve 2P to overlie the other curves by up to 2 cm^3 min^{-1}. Nevertheless the variability in the oil production rate, the cumulative oil production curves overlap during most part of the operation time (Fig. 4.16c). Cumulatively, at the end of the dry combustion period, 2217 cm^3 of oil is recovered in model 1P which is 58 and 127 cm^3 lower than that recovered in models 3P and 2P respectively.

Model 1P shows that oxygen production starts prior to the increase in air flux (Fig. 4.16d), that is when the combustion front reached the toe of the HP well, as explained in section 4.3.1. That is there is no oxygen presence ahead of, or bypassing, the combustion front as shown by the oxygen profile at the top horizontal plane (Fig. 4.17a, & b). In model 2P, periodic oxygen production began around 40 minutes into the start of combustion and lasted until 178 minutes (Fig. 4.16d). Thereafter, it dropped to zero before being produced again, at 218 minutes, until the end of the dry combustion period. The maximum mole

percent of the produced oxygen prior to the increase in air flux is 3% which is higher than that after the increase in air flux by up to 1.9 %. The early oxygen production is caused by the presence of low fuel concentration at both the toe and the heel of the HI well compared to in model 1P. This is reflected by the shape of the combustion front after one hour from the start of air injection (Fig. 4.17c), where oxygen can be observed to bypass the combustion front from either ends of the HI well. As a consequence, the bypassed oxygen is produced at the heel, in addition to that being produced at the toe, of the HP well. Fig. 4.17d shows that at the end of the dry combustion, there is still some oxygen around the heel of the HP well.

In model 3P, the use of vertical injectors arranged in an SLD manner aided in the creation of a localised and enriched heavier oil fraction around the toe of the VI wells. The use of the ignitors until the temperature at the inlet zone reached at least 450 ^{o}C has been observed to cause formation of a coke ring around each VI well. A vigorous combustion front, propagating outwards, in a circular manner, from each VI well is immediately established once air injection commenced (Fig. 4.17e). This is because the volume of air, at constant pressure, exiting each of the vertical injectors (i.e. VI in model 3P) is 8.5 times that exiting each perforation on the horizontal injector (HI) well of model 2P. Also, due to the lateral distance separating the VI wells from the HP well, the combustion front took an additional 50 minutes, compared to with model 2P, before it reached the toe of the HP well. And even at 320 minutes (Fig. 4.17f), the central axis, in a toe-to-heel manner, is not yet fully swept by the combustion front. That is why, the oxygen production in model 3P started at 120 minutes (Fig. 4.16d). It follows that the production of oxygen in model 3P, which has a

maximum concentration of 1.5 mol%, only occurs due to the combustion front propagating along the HP well. This is unlike in model

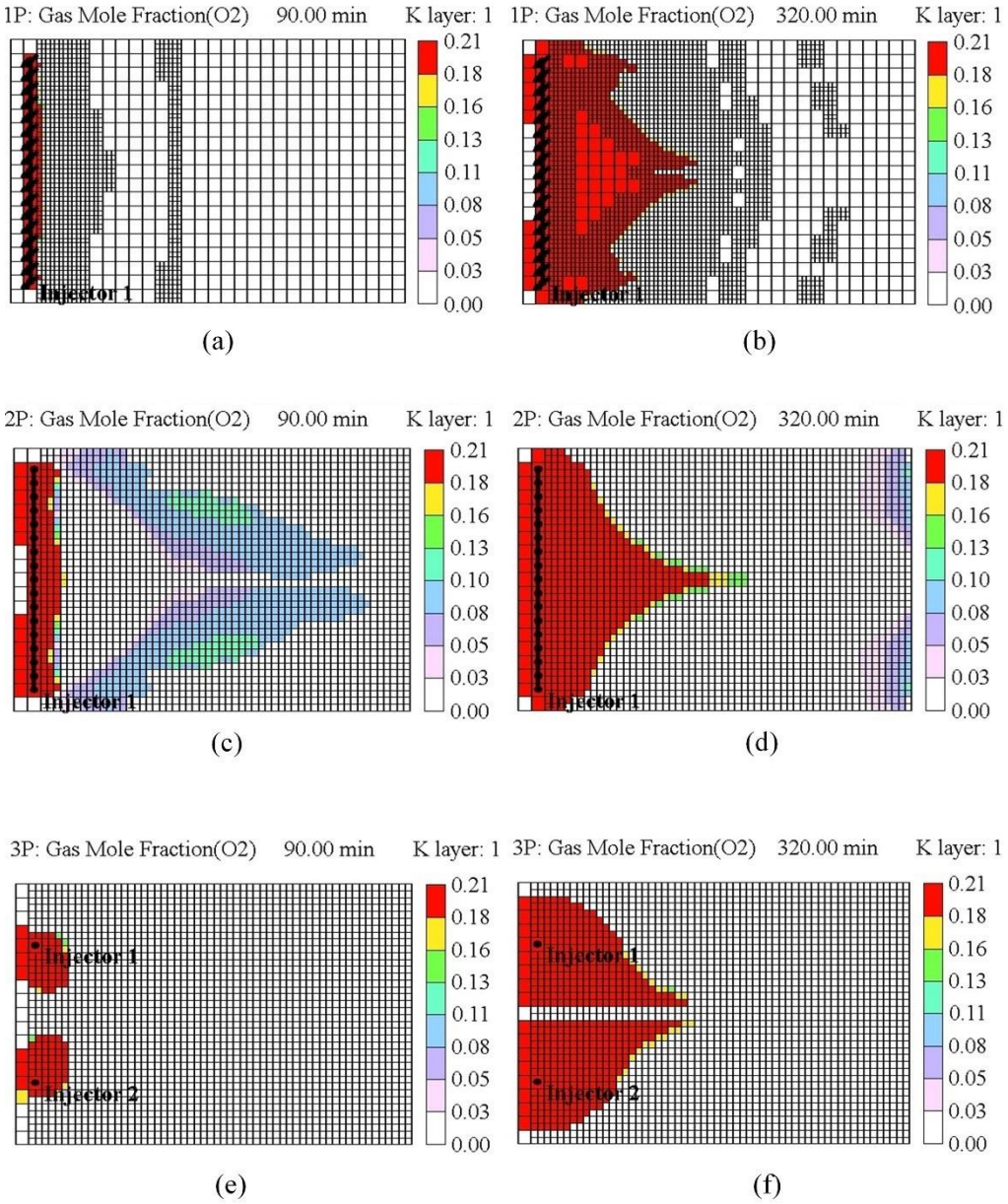

Fig. 4.17: Oxygen mole fraction profiles at the top horizontal plane (K layer 1) for model 1P at (a) 90, and (b) 320 minutes; for model 2P at (c) 90, and (d) 320 minutes,; and for model 3P at (e) 90, and (f) 320 minutes

2P, where oxygen bypassed the combustion front at the early stage of the process. However, because the oxygen production was continuous from 120 minutes up to 320 minutes, the oxygen utilisation in model 3P is 0.89% lower

than the 96.93 % achieved in model 2P. The use of electrical heating method for the PIHC is found to have 98.18% oxygen utilisation.

Overall, it is found that the use of steam for the PIHC results in an increase in oil recovery regardless of the well arrangement. However, it also cause a reduction in the oxygen utilisation. The use of HI well, in combination with the steaming during the PIHC causes some of the oxygen to bypass the combustion front during the early stage of air injection. However, when the combustion is increasingly developed (i.e. expanded), less oxygen bypasses the combustion front. Oxygen production delay is observed when the wells are arranged in an SLD manner.

4.4 Summary

The Phillips et al. (1985) thermal cracking kinetics, together with PVT data estimated using the PR-EOS, have been used to develop a more accurate numerical simulation model of the Xia and Greaves, (2002) 3D THAI combustion cell experiment. This was for the dry combustion part of the experiment. The new model also used three oil pseudo-components, as opposed to the two used by Greaves et al. (2012a). The new THAI model is also more accurately scaled for field studies as the stoichiometry of the fuel formation reaction is directly fixed by the relative molecular mass of the pseudo-component.

The validated model provided an excellent match for the oil rate, cumulative oil production, peak combustion temperature, and produced oxygen concentration over the dry combustion period of the experiment. However, the API gravity of

the upgraded produced oil is over-predicted by up to 2 API points, although during certain periods of the experiment, there is much closer agreement.

The simulation model provided new insight into the mechanism of oxygen production during the later stages of the experiment. Oxygen is first produced towards the end of the low air injection rate period showing that it is not caused by the increase in air flux at 190 minutes into the operation. The increasing trend of produced oxygen was predicted following a step change in the injected air rate of 33 %. The temperature profiles in the sandpack indicate that safe operation of the THAI process can be maintained using an air injection rate slightly lower than the lowest air rate used in the experiment.

The shape of the combustion front before any oxygen is produced is forward leaning, indicating that the process is entirely stable. Once the combustion front reaches the toe of the HP well, it tends to become more vertical and this is an indication that the process is marginally stable. The moment it becomes backward-leaning, the process is operating in an instable state. This means that any further increase in the air injection rate will exacerbate the instability. The simulation also shows that for completely stable combustion front propagation, the combustion zone should be restricted to the upper part of the sandpack. Otherwise, coke must be present inside the horizontal production well in order to prevent oxygen being produced.

The simulation model provides a more accurate prediction of the fuel availability, averaged over the sandpack volume. The predicted range is in agreement with typical values reported for Athabasca Oil Sands bitumen.

This study reveals that, to operate the THAI process in an economic and safe manner, an optimum air injection flux must be determined since the oil recovery increases non-linearly with the increase in air flux.

It is found that THAI operates more stably in a highly viscous reservoir albeit at higher operating cost, due to increased CAOR, compared to in a low viscosity reservoir. It is also shown that longer time is needed to recover the same sized reservoir, at the same air injection rate, when the oil in place is more viscous.

Overall, it is found that the use of steam for the PIHC results in an increase in oil recovery regardless of the well arrangement. However, it also causes a reduction in the oxygen utilisation. The use of HI well, in combination with the steaming during the PIHC causes some of the oxygen to bypass the combustion front during the early stage of air injection. However, when the combustion is increasingly developed (i.e. expanded), less oxygen bypasses the combustion front. Oxygen production delay is observed when the wells are arranged in an SLD manner.

5. Chapter Five: Field Scale Simulation of the THAI Process

5.1 Introduction

The kinetics parameters determined from the numerical modelling of the 3D combustion cell experiments cannot be used directly to upscale to field scale. This is due to the scale difference in which grid blocks are in centimetres in the case of lab scale model while they are in metres (i.e. several orders higher) in the case of field scale modelling. That means the gridblock resolution is not small enough to capture the physics of the approximately 2 cm thick combustion front. While the dependence of the reaction on temperature makes the reactions sensitive to gridblock size, the longer time (years) required to recover a given reservoir allows the cracking reaction to proceed at normal reservoir temperature. This results in excessive fuel deposition as thermal conduction becomes the dominant mechanism of heat transfer leading to overcoking. This implies that the rate of reaction is many times higher than it should be in the field scale. Due to these issues, this chapter will present a brief review of the available upscaling techniques. A new approach to upscaling is proposed and a comparative study of the field scale predictions by each of the two validated kinetics schemes that best matched the experimental results is discussed. Attention is then shifted to the kinetics scheme that provides the best representation with less uncertainty. The Chapter closes by discussing the nature of fluid production at field scale.

5.2 Literature Review

Various techniques to circumvent the problems of grid-size dependency and overcoking were developed. One of these ways is the tuning of kinetics parameters so that a converged solution is obtained. This involves altering either the activation energy or the frequency factor, or both, in the Arrhenius expression. This method was used by Greaves et al. (2012c) to carry out a full field scale simulation of THAI. The issue of overcoking and gridblock size effects can be overcome by fine tuning the chemical reactions in which, for example, the cracking and the coke oxidation reactions are combined to form a pseudo-reaction. By forming oxygen dependent pseudo-reaction, Marjerrison and Fassihi, (1992) were able to upscaled combustion tube results and conducted a field scale simulation of in-situ combustion.

The activation temperature, T_{act}, in combination with an Arrhenius expression was used to overcome the gridblock dependency of the combustion reactions. T_{act} is the upper limiting temperature that is used to determine the Arrhenius reaction rate in a gridblock with temperature lower than or equal to T_{act}. For gridblocks with temperature greater than T_{act}, the gridblock temperature is used to obtain the Arrhenius reaction rate in the block (Coats, 1983). The other method was the use of a moving fine mesh to simulate the combustion front. This was used by Hwang et al. (1982) with the assumption of the presence of just a single oil component, and instantaneous and complete combustion between oil and oxygen.

Another approach adopted by Kovscek et al. (2013) and Nissen et al. (2015) was extracting, from the lab scale model, the fuel availability which is then pre-

defined in the field scale model prior to the initiation of the combustion. Their model allowed the monitoring of the fuel consumption which burns instantaneously in the presence of sufficient oxygen. However, although their model reduced the dependencies on the grid size, it did not consider the variation in behaviour between the lab scale and the field scale most especially in terms of fuel laid down. Also, the overall air injection and the rate of oil production were not considered. Another limitation in which oxygen production rate was neglected in their scaling procedure was the assumption of 100% oxygen utilisation. This could have significant effect on the safety of the process as when to stop air injection to shut-in production will not be known with the high degree of certainty.

Hwang et al. (1982), and Ito and Chow, (1988), also specified the amount of fuel to be burned prior to the initiation of combustion. They included an algorithm to enhance the oil flow in which, when a certain amount of the pre-defined fuel in a given grid block was consumed, the excess oil in the grid block was forced to flow out so that the desired fuel consumption was realised. This, however, could mean the effect of fuel laid down on the actual processes (i.e. heat transfer, oil production, oxygen consumption, etc.) was not captured thereby resulting in an erroneous conclusion.

With regards to Toe-to-Heel Air Injection (THAI) only one field scale model, in which the kinetics parameters were tuned and the scaling was done based on the combustion front velocity, is available (Greaves et al., 2012c). By scaling the combustion front velocity from the experimental value of 3 – 6 cm/h to the field value of 12 – 24 cm/day (i.e. field air flux of 2 $m^3/h \cdot m^2$ from experimental air flux of 12 $m^3/h \cdot m^2$), Greaves et al. (2012c) assumed a linear relationship.

However, the lab scale numerical model has shown that the mobile oil zone (MOZ) was located at a significant distance downstream of the combustion front. This implies that either the combustion front does not have to sweep the whole producer length for the whole reservoir to be produced on the one hand, or, even if it covers the whole reservoir length, it does not mean producing the whole reservoir, on the other. Also, from their results, it was observed that the combustion front advance rate was about 6 to 12 times lower than they initially stated. Oil mobilisation was observed to be due to convection from the exhaust flue gas and conduction through the reservoir rock as opposed to advancement of the combustion front. It is also observed that the oil producer is over-coked to the extent that the porosity dropped to almost zero.

These deficiencies associated with available scaling methods, as well as the high potential of THAI compared to SAGD (as highlighted in the introductory section of chapter two, section 2.1) have motivated us to further investigate the factors affecting THAI operation at field scale.

5.3 Models Development

Through sequential volume upscaling, which involves progressive multiplication of the dimensions of the experimental scale model by increasing factors such as 1, 3, 9,…, the 3D laboratory scale model is upscaled.

5.3.1 Model P with the same Kinetics Parameters

To investigate the effect of the increasing reservoir size on the predicted parameters such as oil recovery, oil consumed as coke, recovery time, combustion front and mobile oil zone velocities, etc., the laboratory 3D combustion cell with dimensions of 60 cm × 40 cm × 10 cm was sequentially

upscaled by 5 different factors as shown in Tab. 5.1. For each scaling factor, each direction was upscaled by the same factor. It implies that the number of gridblocks was kept the same while the volume of the gridblock was increased. The models were run with the same kinetics data. The only parameters varied are the rate of heating during the pre-ignition heating cycle (PIHC) and the time period over which the PIHC was carried in order to reflect the increase in cell volume. Electrical heating was used throughout for the PIHC. The air injection rate was also increased until nearly the same peak temperature was recorded in each case. Every other thing was kept the same throughout. A reference percent oil recovery of 40 %OOIP is chosen. This is because at that percentage, the process is still at steady state and a more representative comparison is expected.

Tab. 5.1: Upscaling and predicted parameters for model P

Scaling Factor	Cell Volume (m^3)	PIHC Period (mins)	Air rate (cm^3/min)	Recovery Time (min)	%OOIP Recovered	%OOIP Consumed as Fuel
1	0.024	30	10667	360	40.0	21.7
3	0.648	270	35200	2648	40.0	19.7
5	3.000	750	70000	6800	39.8	26.9
7	8.232	1470	100000	14000	39.9	34.2
9	17.496	2430	161505	21395	40.0	37.4
11	31.944	3630	197395	34619	40.0	43.9

It is observed that the percentage of oil converted to coke increased with increase in combustion cell volume. This is due to the strong dependence of kinetics of fuel deposition on time and temperature. Marjerrison and Fassihi, (1992)

showed that the amount of fuel laid down depends heavily on heat conduction. Kovscek et al. (2013) and Nissen et al. (2015) observed overcoking due to increase in the volume of gridblock. As a result, they proposed that the amount of fuel to be burned be specified during the field scale simulations. The observation made in the current study is very similar to their's as can be seen in Tab. 5.1 and Fig. 5.1. With the time, as the mobilised oil travels at relatively low temperatures compared to that of combustion fronts, the cracking reaction dominates due to heat conduction. This resulted in the increase in percentage of oil converted to coke especially at the base of the reservoir. At the base case level, the oil at the bottom of the reservoir was easily swept and forced to flow to the producer by the advancing combustion front (Fig. 5.1i). As the volume of oil increased, the high coke concentration meant that the combustion advance rate is reduced and thus the combustion front is limited to the upper portion of the reservoir. This resulted in the conversion of the stagnant oil at the base of the reservoir to coke (Fig. 5.1ii).

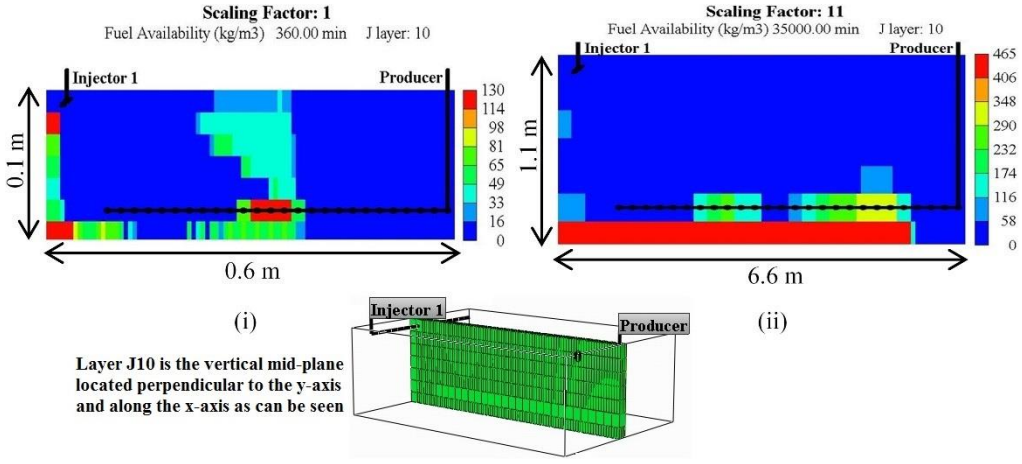

Fig. 5.1: (i) Base case and (ii) upscaled results showing the increase in the fuel available with the increase time and length scales. The profiles are along the vertical mid-plane (J layer 10).

With the scaling factor of 3, the percentage of oil converted to coke is slightly lower than that in the base case, which can be associated with lower combustion zone temperature compared to in the base case. As a result, instead of fuel availability, the log of mass of oil converted to fuel was plotted against the log of cell volume (Fig. 5.2). It can be observed that the increase in mass of fuel with the increase in cell volume were linearly related on the log-log graph, and hence described by power law (Fig. 5.2). This shows that the model predicted that the fuel availability (which is the slope of the curve) is not constant but varies with reservoir volume. The nonlinear equation of the line of best fit, together with associated standard error, is given by:

$$M_c = 10^{(1.8898 \pm 0.0344)} \times V^{(1.1026 \pm 0.0307)}$$

From the line of best fit, the mass of coke expected to be predicted by the model when upscaled to full field scale by a factor of 243 would be $9.882 \times 10^7 \pm 4.645 \times 10^7$ kg. However, the total mass of oil originally in place is 9.388×10^7 kg. In terms of average fuel availability, the predicted average coke concentration would be 287 ± 135 kg m^{-3}. This is unphysical as the maximum fuel available recorded from top-down combustion experiments for Athabasca tar sand was 128 kg m^{-3} (Coates et al., 1995). They observed the excessively high fuel availability to be due to inefficient drainage of the mobilised oil from ahead of the combustion zone. For the base case model, the predicted average fuel availability is 63 kg m^{-3} which is close to the reported range of 50 to 57 kg m^{-3} for Athabasca bitumen (Alexander et al., 1962). Furthermore, the 287 ± 135 kg m^{-3} predicted average fuel availability would be equivalent to 105 ± 49 %OOIP converted to coke. Overall, the prediction shows that at least 56 %OOIP would

be converted to coke when the base case is upscaled to full field scale which is not physically possible.

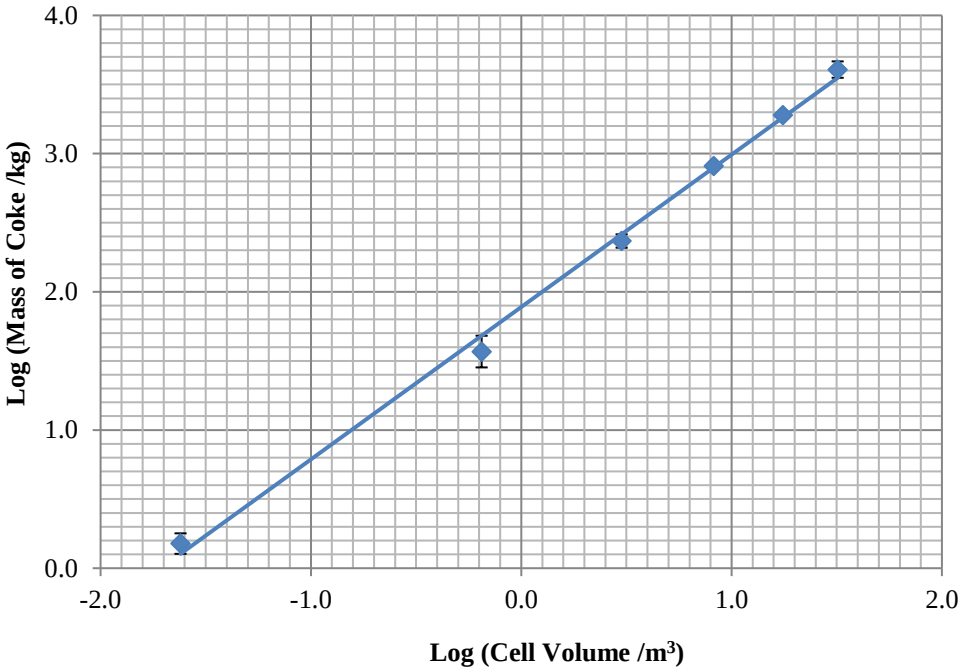

Fig. 5.2: Mass of coke versus combustion cell volume for model P

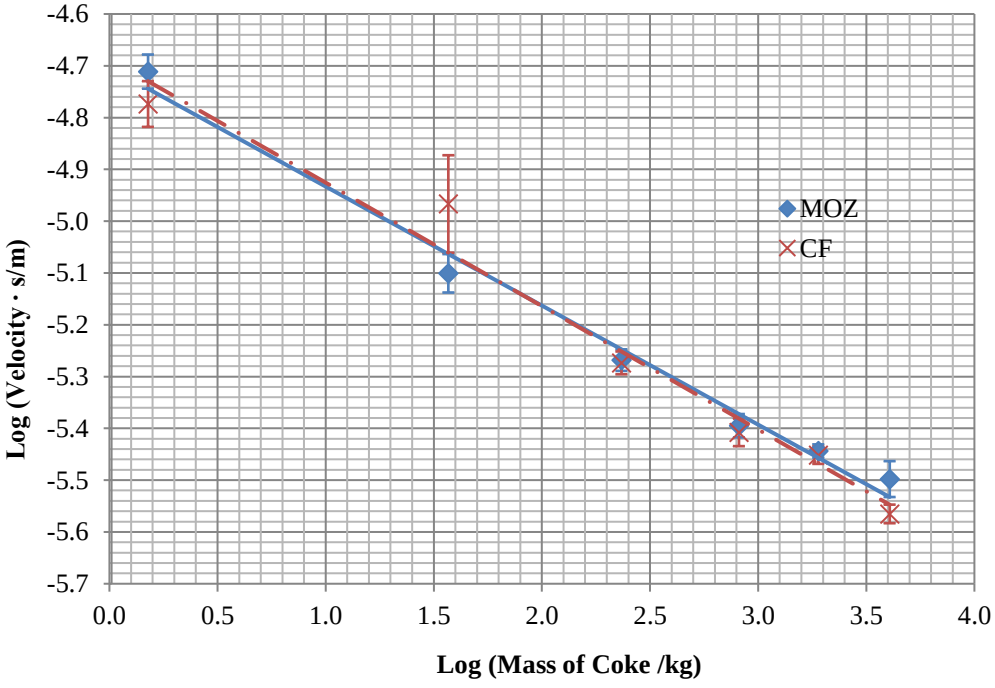

Fig. 5.3: MOZ and CF velocities versus mass of coke

Fig. 5.3 shows that as the combustion cell volume and hence the gridblock size is increased, both the velocities of the mobile oil zone (MOZ) and that of combustion front (CF) converge toward a common value. However, the MOZ is always ahead of the CF due to the displacement from PIHC. At 105 ± 49 %OOIP fuel consumption, the predicted velocity of the MOZ and CF are respectively 0.0010 ± 0.0003 and 0.0009 ± 0.0004 m hr^{-1} which cannot be used for upscaling because of the unrealistic nature of the fuel consumption.

From this analysis, it follows that the kinetics parameters should be altered, as done by many authors, in order to obtain a realistic representation of the physicochemical processes.

5.3.2 Model P with the Adjusted Kinetics Parameters

As shown in section 5.3.1 above, for the prediction of the fuel consumption at laboratory scale to be the same as at field scale (Kovscek et al., 2013), a new material balance approach which is detailed below has been adopted.

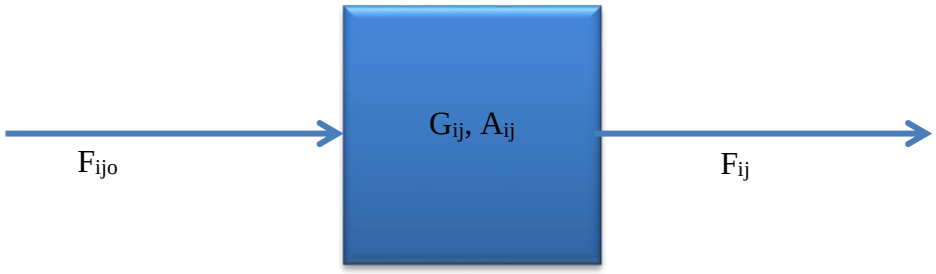

Fig. 5.4: Gridblock side view for material balance

A general material balance can be written for the grid block shown in Fig. 5.4 as follows:

Flow in (F_{ijo}) + Generation (G_{ij}) = Flow out (F_{ij}) + Accumulation (A_{ij})

$$F_{ijO} + \int_0^V R_{ij} dV = F_{ij} + \frac{dN_{ij}}{dt} \quad (5\text{-}1)$$

where F_{ijo} and F_{ij} are the inlet and outlet molar flow rates of component i in phase j respectively, R_{ij} is the rate of generation or consumption of i-th component in j-th phase, N_{ij} is the accumulated amount of component i in phase j inside the gridblock, and V is the volume of the gridblock.

By treating the gridblock as continuously stirred tank reactor (CSTR) and thus assuming the reservoir to be composed of a network of CSTRs (Hwang et al., 1982), the above equation can be simplified as follows:

- Steady state operation implying the accumulation term is zero
- Around the reaction zone, there is perfect mixing and the temperature at every point is the same
- It follows that the rate of reaction is uniform and independent of the reservoir volume

$$F_{ijo} - F_{ij} = -R_{ij} \int_0^V dV \quad (5\text{-}2)$$

Integrating equation (5-2) gives:

$$(-R_{ij})V = (F_{ijo} - F_{ij}) \quad (5\text{-}3)$$

Equation 5-3 above shows the moles of component i reacted. Because the fuel availability determined from the 3D combustion cell experiment is the same at field scale (Kovscek et al., 2013), it then follows that the fraction of i-th

component converted to fuel at the experimental scale is the same as at field scale. Therefore, from equation 5-3,

$$Fraction\ converted = \frac{(-R_{ij})V}{F_{ijo}} = \frac{F_{ijo} - F_{ij}}{F_{ijo}} \tag{5-4}$$

Thus

$$\left(\frac{-R_{ij}V}{F_{ijo}}\right)_{lab} = \left(\frac{-R_{ij}V}{F_{ijo}}\right)_{field} \tag{5-5}$$

5.3.2.1 Downscaling the Cracking Reactions

For the thermal cracking reaction, the rate of coke formation from component i in phase j (i.e. IC shown in section 4.2.3) is first order with respect to i-th component concentration. Thus, the rate of consumption of species IC is given by:

$$-R_{ij} = kC_{ij} \tag{5-6}$$

where k is the frequency factor (min^{-1}) and C_{ij} is the concentration of component i. Assuming the component around or in the reaction zone to have uniform temperature and therefore constant density, then:

$$C_{ij} = \frac{F_{ijo}(1 - X_{ij})}{q} \tag{5-7}$$

where X_{ij} is the conversion of component i and q is it is volumetric flow rate. Thus equation 5-6 becomes:

$$-R_{ij} = \frac{kF_{ijo}(1 - X_{ij})}{q} \tag{5-8}$$

And substituting equation 5-8 into 5-5 results in

$$\left(\frac{kF_{ijo}(1 - X_{ij})}{q}\frac{V}{F_{ijo}}\right)_{lab} = \left(\frac{kF_{ijo}(1 - X_{ij})}{q}\frac{V}{F_{ijo}}\right)_{field} \tag{5-9}$$

As the conversion is the same, it then follows that $(1\text{-}X_{ij})$ is independent on the scale and the above equation 5-9 reduces to:

$$\left(k\frac{V}{q}\right)_{lab} = \left(k\frac{V}{q}\right)_{field} \tag{5-10}$$

And the ratio V/q is the space time τ, the time taken to process a given volume of reactor (or gridblock) based on the feed entrance condition. Therefore equation 5-10 can be written as:

$$(k\tau)_{lab} = (k\tau)_{field} \tag{5-11}$$

$k\tau$ shown in equation 5-11 is effectively a dimensionless number referred to as the first Damkhöler number. The Damkhöler number, which is the ratio of the characteristic time scale for kinetics reactions to convective mass transport, gives an estimate of the extent of conversion achievable. However, Nissen et al. (2015) have assumed the Damkhöler number to depend on the model size despite assuming the fuel deposition at lab scale to be the same as at field scale. By considering the field scale Damkhöler to be 3 to 4 orders of magnitude higher than that at lab scale, they were saying higher fraction of oil is converted to coke in the field scale compared to in the lab scale. This is clearly contradictory.

From the laboratory scale numerical model, the left hand side of equation 5-11 is known. However, for the field scale side, neither k nor τ is known. Here, the frequency factor is taken as the adjustable variable as it has to be input as a fixed value in the simulation.

$$k_{field} = \frac{(k\tau)_{lab}}{(\tau)_{field}} = \frac{k_{lab}}{S_t} \tag{5-12}$$

where S_t is the time scaling factor. As the field scale time is many orders of magnitude greater than the lab scale time, it implies that to achieve the same representation at the field scale as observed in the lab scale, the frequency factor of the coke deposition reactions must be decreased by the same factor as the lab scale time was increased. However, how long it takes to produce the field scale reservoir is not known. Therefore, initial estimate must be made and iterative runs be used to get the feeling of the scaling factor.

To obtain an initial guess of the time scaling factor S_t, the THAI experimental model is up-scaled by the same factor of 243 in all the three directions to give 145.8 m × 97.2 m × 24.3 m reservoir dimension. Once the scaling factor is determined, the axial reservoir length can be increased by the appropriate factor to obtain a repeatable pattern, e.g. as in Petrobank's THAI field pilot at Conklin, Alberta with dimensions of 500 m × 100 × 25 m. Various approaches for initial guessing of S_t are possible viz:

1- **Trial and Error:** It has been shown mathematically that the frequency factor of the reactions in the field must be reduced by a certain factor so as to prevent excessive coking due to too high reaction rates, relative to the rate of fluid displacement. Using this approach, the frequency factor was

progressively decreased until the average fuel availability ahead of the combustion zone was around 22.5 kg m^{-3} i.e. around 8.2 % OOIP is consumed as fuel. This is in accordance with the experimentally determined value of 8.2 % OOIP for Athabasca Oil Sands bitumen (Xia and Greaves, 2002). Therefore, based on this overall fuel consumption, the frequency factor used in the experimental model was decreased by 59049 (243 × 243) for use in the field scale model.

2- **Air Injection Rate:** To a first approximation, dividing the reservoir volume scaling factor 14348907 (243 × 243 × 243) by the value by which the air injection rate was upscaled gives the time scaling factor S_t. The initial air injection rate in the experimental scale model was 8000 Scm^3 min^{-1}, corresponding to a flux of 12 m^3 $m^{-2}h^{-1}$ and that for the field scale was set to 20,000 Sm^3 day^{-1} which is equivalent to an air flux of 0.352 m^3 $m^{-2}h^{-1}$ (Burger et al., 1985). From this, it follows that the air rate was scaled up by a factor of 1740. If the air rate is maintained at 20,000 Sm^3 day^{-1} throughout the process period, then the time to produce the whole reservoir should be up-scaled by a factor of 8260. During the experiment and as predicted by the experimental scale model, 620 minutes is needed to produce the whole 3D combustion cell. It means that 9.8 years is required to produce the whole field scale reservoir.

3- **Oil Production Rate:** In the experimental model, the average oil rate during the steady state dry combustion period is 7.1 cm^3 min^{-1}. At an air injection flux of 0.352 m^3 $m^{-2}h^{-1}$, the up-scaled average oil rate is 18 m^3 day^{-1}. If the air flux is maintained constant throughout, to recover 85.5 %OOIP as was the case in the experiment (Xia and Greaves, 2002), 80,000 m^3 of cumulative

oil must be produced from the field scale reservoir. This would take 12.4 years at the constant air flux. Therefore, the time scaling factor is approximately 10500.

Tab. 5.2 summarises the different possible time scaling factors that can be used as an initial guess.

Tab. 5.2: Summary of initial guess of time scaling factor S_t

Methodology	Base Case	Field Values	S_t
Trial and error based on area	0.04 m^2	2361.96 m^2	59049
Air injection rate	11.52 Sm^3 day^{-1}	20000 Sm^3 day^{-1}	8260
Oil production rate	0.01 m^3 day^{-1}	18 m^3 day^{-1}	10500

5.3.2.2 Downscaling the Combustion Reactions

For the combustion reaction, the rate of consumption of oxygen is first order with respect to oxygen partial pressure and is second order overall. As a result, the Damkhöler number given in equation 5-11 becomes a function of oxygen partial pressure inside the reservoir (Fogler, 2006) and is given by:

$$(k\tau P)_{lab} = (k\tau P)_{field} \tag{5-13}$$

where P is the reservoir pressure and because air is used as the oxidising fluid, the mole fraction cancels out.

Rearranging equation (5-13) gives:

$$k_{field} = \frac{(k\tau P)_{lab}}{(\tau P)_{field}} = \frac{k_{lab}}{S_t \cdot S_p} \quad (5\text{-}13)$$

where S_p is the pressure scaling factor, equal to the ratio of the field reservoir pressure to experimental cell pressure. S_t is the same as determined from the cracking reactions. The experimental model was run at pressure of 200 kPa approximately, while in the actual reservoir, the pressure is 2800 kPa making S_p = 14.

5.3.3 Model G with the same Kinetics Parameters

The comparative study in Appendix B showed that the same cumulative oil production is obtained with model G regardless of the method of PIHC (i.e. whether steam or electrical pre-heating is used) and regardless of the type of well arrangement (i.e. 2VIHP or HIHP). However, since higher oxygen utilisation was obtained with steaming during PIHC and in 2VIHP arrangement, the 2VIHP lab scale model was progressively up-scaled in each direction by factors of 3, 9, 27, and 81. This means that the amount of energy needed to pre-heat the zone around the vertical injectors and establish communication between the wells must be a function of reservoir volume. The cumulative steam was up-scaled by the factor the model volume was up-scaled. All other parameters, such as the well internal diameter, the air injection rate, etc. were appropriately up-scaled.

For the case of model up-scaled by a factor of 3 in every direction, the model was run with steam injection rate up-scaled by 9 while the time over which the PIHC is carried out scaled by 3. However, it was realised that the time was too short for communication to be established between the wells. Later, the injection rate and the time were each upscaled by a factor of 5.2 such that the cumulative

amount of energy required was injected. However, the same issues were encountered. Then, the steam injection rate was scaled by 3 while the time over which the pre-heating was carried out scaled by 9. This allows enough time for communication to be established between the wells. As a result, the PIHC time of all the other models was up-scaled by the square of the steam injection rate scaling factor (Tab. 5.3).

Tab. 5.3: Upscaling and predicted parameters for model G

Scaling Factor	Cell volume (m^3)	PIHC Period (hr)	Recovery Time (hr)	Oil Recovery (%OOIP)	Residual Oil (%OOIP)	%OOIP Consumed as Coke
1	0.024	0.5	4.75	40.0	38.1	21.9
3	0.648	4.5	38.34	40.0	30.3	29.7
9	17.496	40.5	307.08	40.0	18.5	41.5
27	472.392	364.5	1979.48	40.0	16.9	43.1
81	12754.584	3280.5	16666.67	40.1	12.5	47.5

As in model P, the reference percent recovery chosen for comparing model G predictions is 40 %OOIP. This is because the process is still at steady state and thus gives a more representative comparison. It was found that as the volume of the model increased, the amount of coke deposited increased significantly to the extent that the maximum coke concentration is reached and that the fluid porosity (and thus the permeability) dropped to zero. This is because the rate of fluid movement becomes substantially smaller than the rate of reaction. It is also observed that a small increase in temperature downstream of the mobile oil zone causes overcoking (Fig. 5.5). This means that once the horizontal producer is

fully coked, the mobile oil upstream will have no path to flow to reach the uncoked perforations for production to the surface. Just like in the case of model P, model G predicted that the combustion cell volume and the mass of oil converted to coke are related by a power law as the plot on the log-log graph is perfectly linear (Fig. 5.6). The equation of the line of best fit is given by:

$$M_c = 10^{(1.9349 \pm 0.0272)} \times V^{(1.0582 \pm 0.0115)}$$

where M_c is the mass of Coke and V is the reservoir volume.

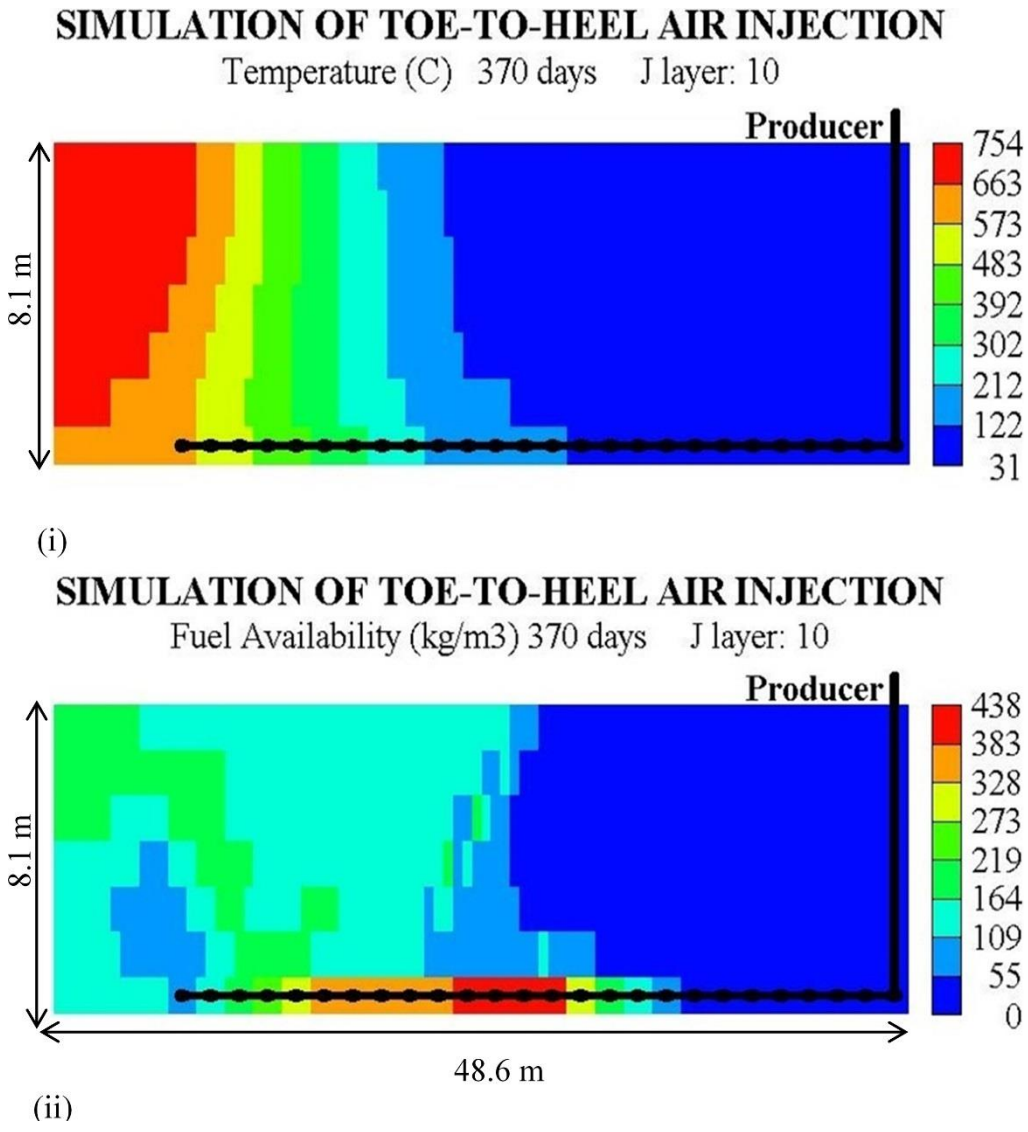

Fig. 5.5: (i) Temperature and (ii) fuel availability along the vertical mid-Plane for scaling factor 81

For the full field scale model which has scaling factor of 243, the predicted average fuel availability from the equation of the line of best fit is 181 ± 38 kg m^{-3}. This is clearly not physically meaningful as it is equivalent to 63 ± 13 %OOIP oil conversion to coke. Since the time over which a given reservoir is produced depends on the volume of the reservoir and the kinetics parameters are time and volume dependent, one of the only way to get around the over-coking problem is to adjust the kinetics parameters. This is similar to the conclusion drawn from the predictions of model P.

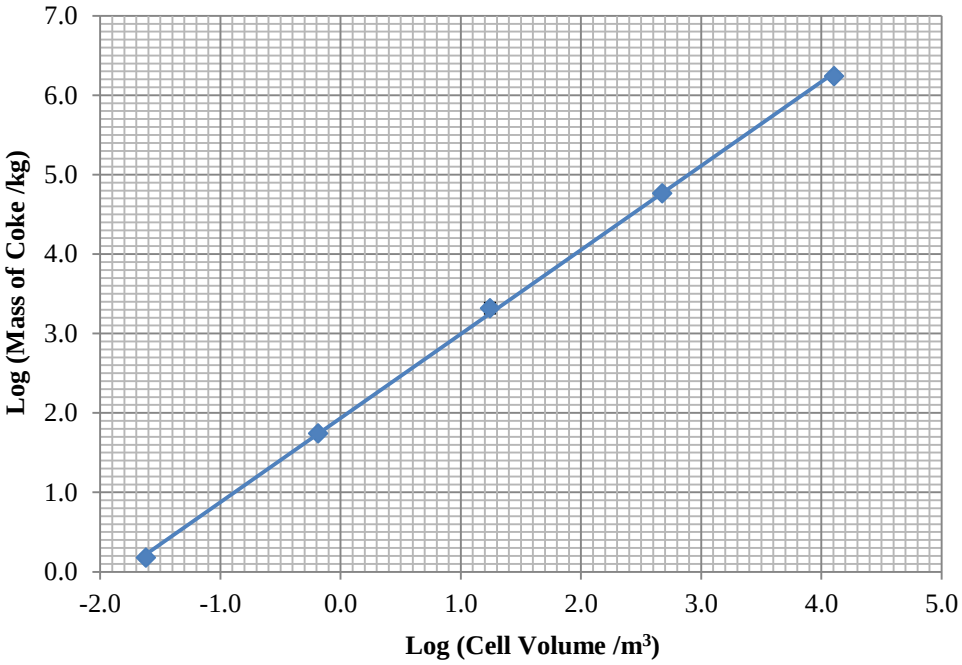

Fig. 5.6: Mass of coke against combustion cell volume for model G

5.3.4 Model G with the Adjusted Kinetics Parameters

After determining that the kinetics parameters in model G must be altered in order to successfully upscale the lab scale model, a similar procedure as in section 5.3.2 was followed to downscale the reactions frequency factors. This

means that the phenomena observed at the experimental model are the same as what should be observed at the upscaled 150 m × 100 m × 24 m model.

Initially, the cracking reaction frequency factor was downscaled by the time scaling factor (i.e. the factor by which the process time was up-scaled from that of the experimental model). However, no clear physical relationship could be obtained between the reservoir volume and the fuel availability. This was because the concentration of the fuel available varies randomly instead of being approximately the same. Apart from that, as the scale size increased significantly, the cracking reaction almost ceases resulting in no coke deposition. For the combustion reactions, the time and pressure scaling factors are used to downscale the frequency factor.

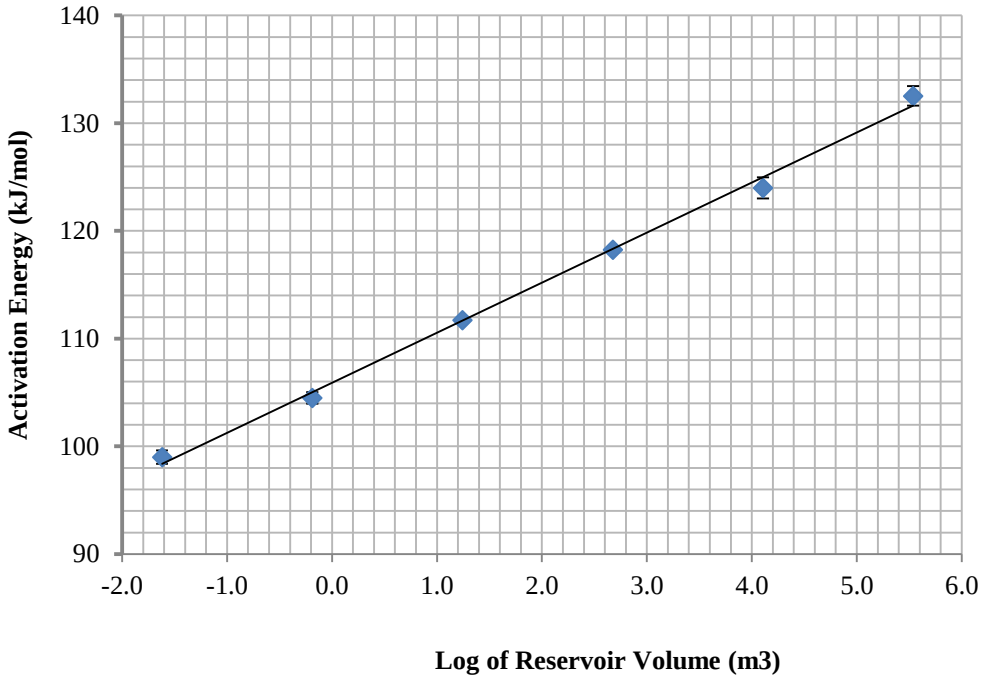

Fig. 5.7: Activation energy versus reservoir volume:

As no consistency is obtained with downscaling the frequency factor of the cracking reaction, it was kept constant throughout. The activation energy of the

reaction, which was set to 99.00 kJ/mol in the experimental model, was changed, through trial and error, with each increase in the reservoir volume until similar fuel availability is obtained. It can be observed that the variation of the activation energy with reservoir volume is described by power law (Fig. 5.7). It should be noted that cracking reaction activation energy of 132.53 kJ/mol, when the experimental model was upscaled by a factor of 243, is still within the range of the experimentally reported values for thermal cracking (Lin et al., 1984; Phillips et al., 1985; Kovscek et al., 2013). Once the activation energy for the cracking reaction at field scale is determined, the axial reservoir length can be increased by the appropriate factor to obtain a repeatable pattern. The upscaling results are presented in the following section.

5.4 Results and Discussion

The results of upscaling model P and model G are respectively discussed. This is followed by comparative study between the predictions by each model from which the best representative model is determined.

5.4.1 Model P Results

Based on the time scaling factor obtained through trial and error (Tab. 5.2), model P1 was developed with dimensions of 150 m × 100 m × 24 m. The model has two vertical injectors and one horizontal producer arranged in a staggered line drive pattern. Model P1 was run with a constant air injection rate of 20,000 $Sm^3\ day^{-1}$ and for combustion period of two years to give an indication of the fuel availability and oil production rate. Oil production begins after 2 months of the initiation of PIHC with oil rate peaking to 170 $m^3\ day^{-1}$ before declining to below 75 $m^3\ day^{-1}$ after further one week. The oil rate averaged around 36

m^3day^{-1} during the two years of combustion period (Fig. 5.8). The cumulative oil production curve over the two years of combustion has a constant slope implying that the oil rate is steady. The fuel availability ranged from 18 to 24 kg m^{-3} (Fig. 5.9i). As described by the experimental model, the cracking zone is ahead of the combustion front and behind the mobile oil zone (MOZ). The MOZ can be observed in Fig. 5.9ii.

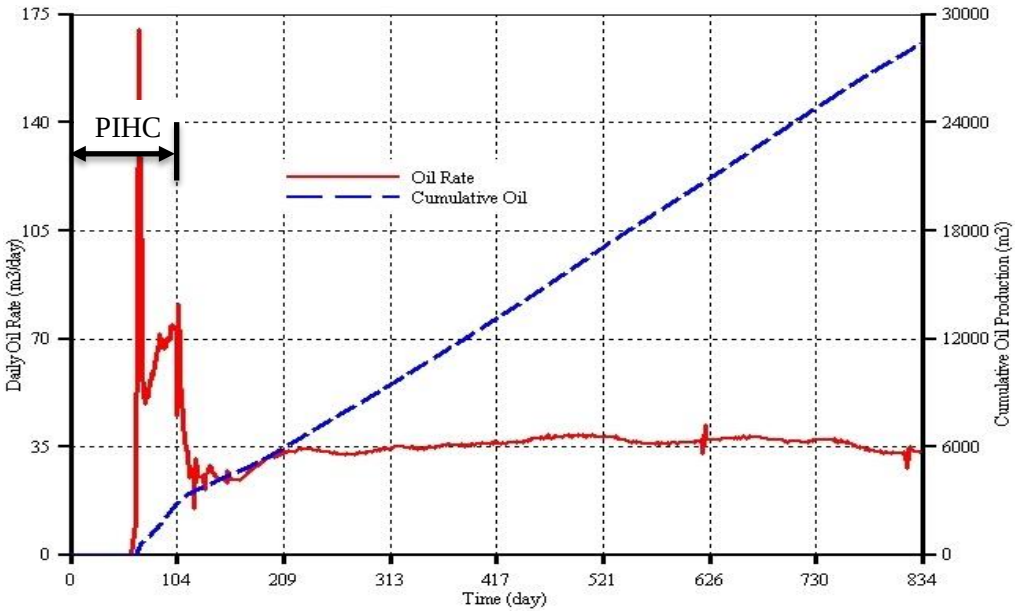

Fig. 5.8: Oil rate and cumulative oil for model P1

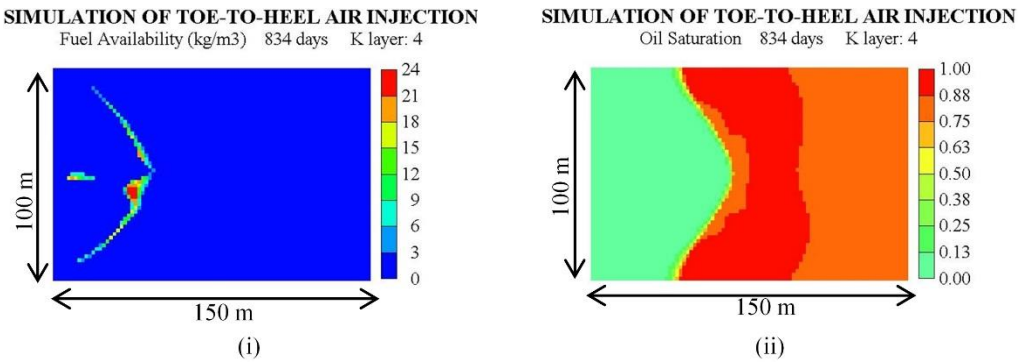

Fig. 5.9: Oil rate and cumulative oil for model P1

To judge how long it would take to produce the whole reservoir, a second run (model P2) was performed with the air injection rate ranging from 30,000 to

50,000 $Sm^3\ day^{-1}$. In this case, the average oil rate was 48 to 72 $m^3\ day^{-1}$, for air injection rates of 30,000 and 40,000 $Sm^3\ day^{-1}$, before entering the declining phase at the highest air rate of 50,000 $Sm^3\ day^{-1}$. At the termination of the simulation, the combustion was run for 3 years and 67.8 %OOIP recovery achieved. At that time, oil consumed as fuel was 5.7 %OOIP and 26.5 %OOIP recoverable oil remains inside the reservoir. As the production has already entered declining phase, the cumulative oil curve is used to extrapolate how long it will take to produce the remaining oil. From above figures, for every 1 %OOIP oil recovered, 0.084 %OOIP is consumed as fuel. It follows that to recover 92 %OOIP as oil, 8 %OOIP will be consumed as fuel. The former figure is not far off from what was reported experimentally while the latter value will be less than that as around 11 %OOIP was left as residual oil and coke (Xia and Greaves, 2002).

Therefore, the cumulative recovery of 81 %OOIP can be achieved by extending the combustion time by 2.25 additional years. This figure was obtained by plotting the cumulative oil production against time over the declining phase period (Fig. 5.10). It follows that the total combustion time required to produce the whole reservoir is 5.27 years which makes the time scaling factor S_t equal to 4670.

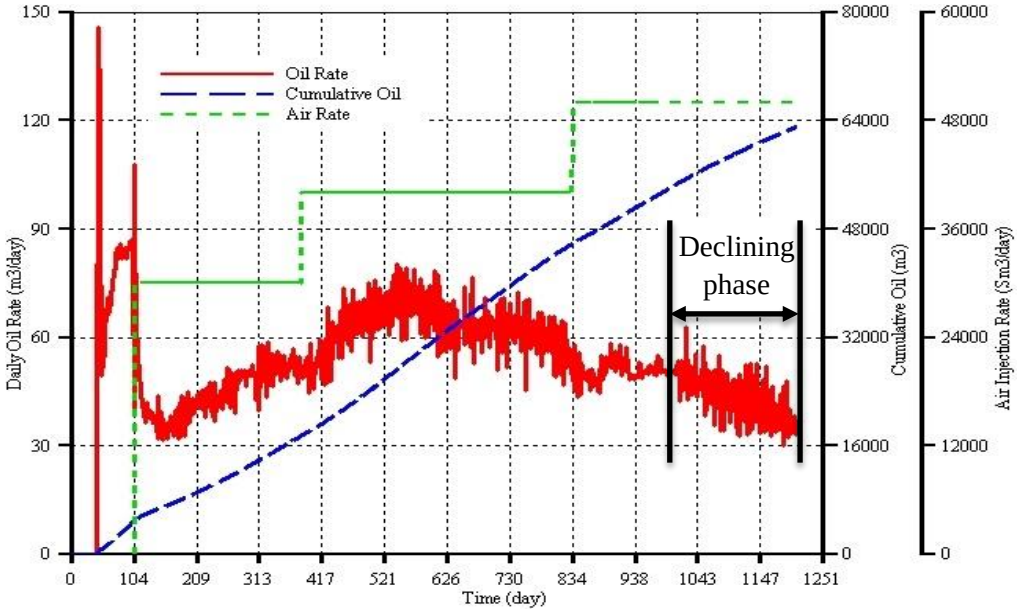

Fig. 5.10: Oil production rate, cumulative oil, and air injection rate for model P2

After the frequency factor of the cracking reactions was down-scaled by S_t = 4670 and that of the combustion reactions down-scaled by $S_t \times S_p$ = 65380, a new model P3 was run with air injection rate of 20,000 Sm^3 day^{-1}.The results from the model P3 and that obtained in model P1 will be compared below as they were run under similar conditions and the same well arrangement.

The predictions are quite close except that oil production begins earlier in the case of model P3 (Fig. 5.11). This is due to the increase in coke formation which resulted in a decrease in amount of heavy oil to be displaced by the injected steam. During most of the process, the oil rates match closely. At the end of the two years and three months production period, model P3 predicted cumulative oil recovery of 29450 m^3 (Fig. 5.12) which is equivalent to recovery of 31.6 %OOIP. Model P1 on the other hand predicted slightly lower cumulative oil recovery of 28420 m^3 which is lower than in model P3 by 1.1 %OOIP.

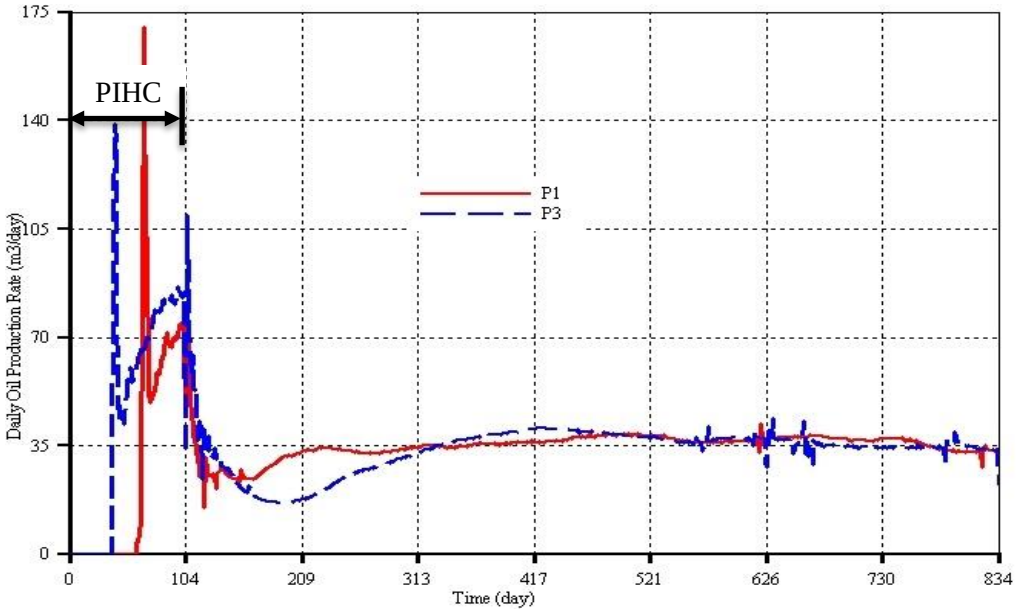

Fig. 5.11: Oil production rates for models P1 and P3

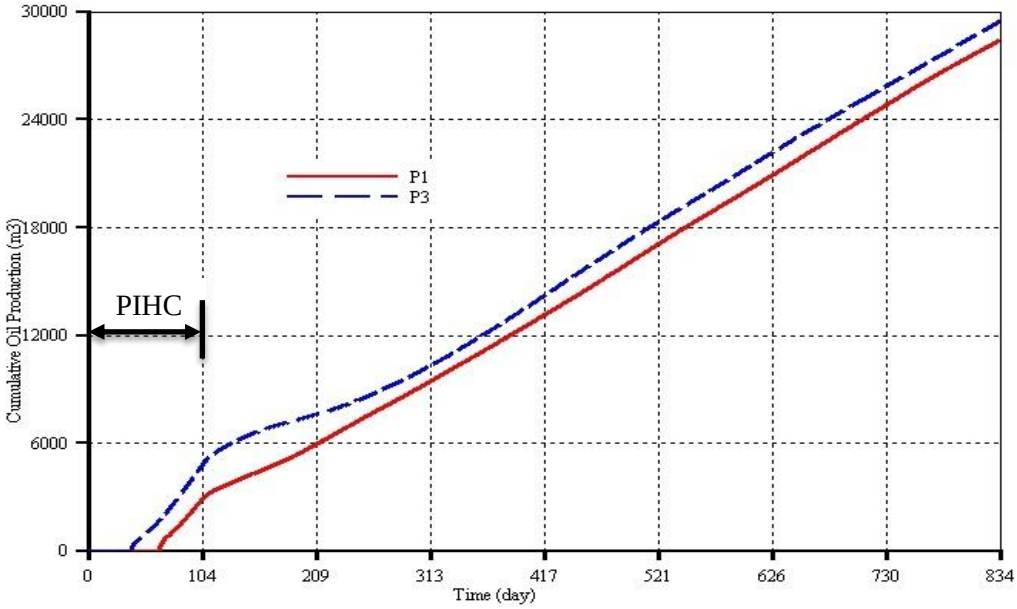

Fig. 5.12: Cumulative oil productions for models P1 and P3

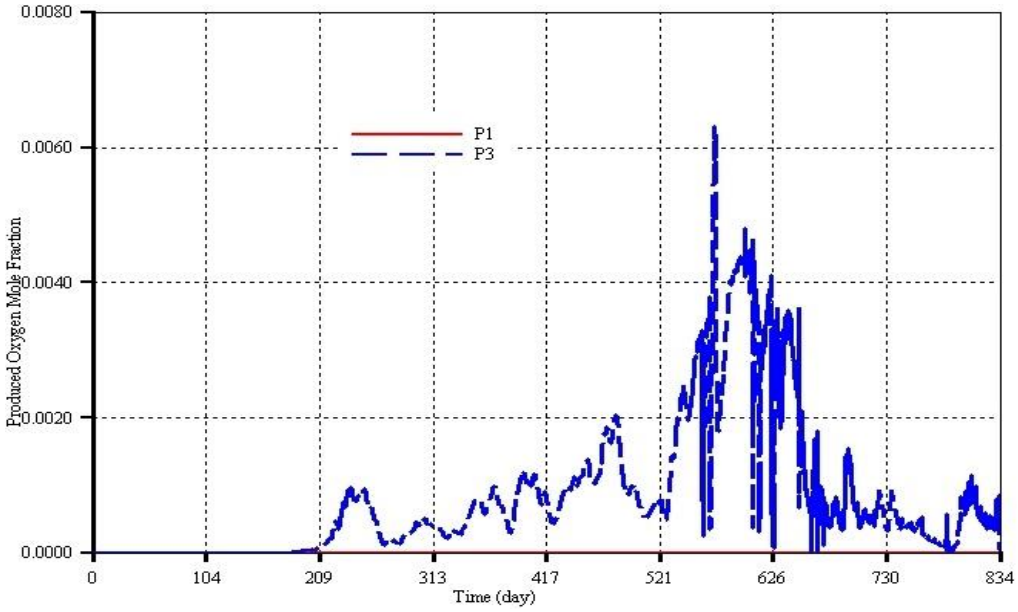

Fig. 5.13: Produced oxygen mole fraction for models P1 and P3

Despite the higher fuel concentration predicted by model P3, the predicted oxygen in the producer well has a maximum concentration 0.62 mol% (Fig. 5.13). However, this is not in accordance with experimental observation described in chapter 4. According to Alexander et al. (1962), oxygen utilisation increases with the increase in fuel availability. Also, the production of small amount of oxygen did not affect the predictions of oil production. In addition, model P3 predicted slightly higher peak temperature which is due to the presence of higher fuel concentration at a given location.

From the fuel availability profiles (Fig. 5.14), it can be seen that model P3 predicts a more broader and uniform fuel concentration which is because of the higher thermal cracking rate. The oil saturation profiles are observed to be quite similar. However, in model P3, the oil rate vectors are less forward leaning, and oil drainage is near to vertical, i.e. mainly gravity drainage compared to the model P1. This may be because the heat distribution in the MOZ is more uniform in model P3.

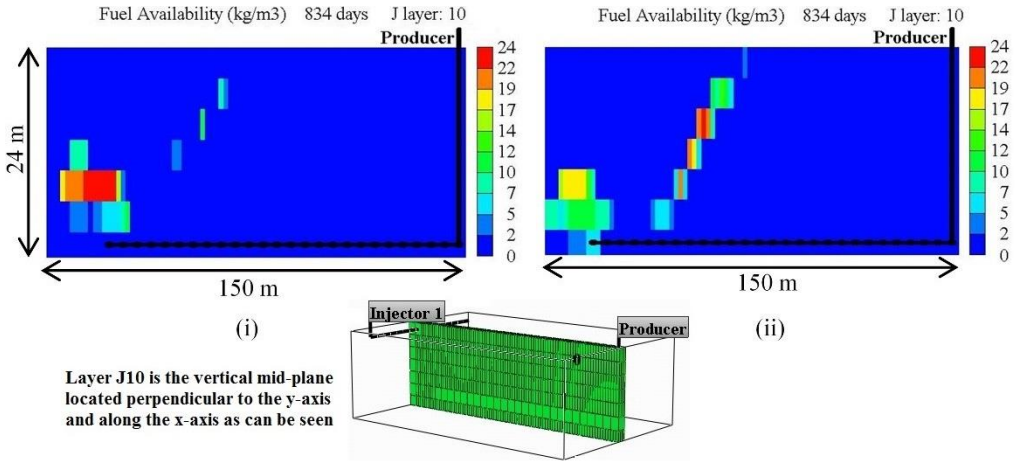

Fig. 5.14: Fuel availability along the vertical mid-plane (J layer 10) for models (i) P1 and (ii) P3

From these results, it implies that the estimated time scaling factor is satisfactory and not particularly sensitive between the range of 4670 to 59049 considered. Therefore, any of the three methods chosen to obtain the initial guess of the time scaling factor would result in realistic predictions. The comparison between the experimental and field scale frequency factors is shown in Tab. 5.4 below.

Tab. 5.4: Comparison of kinetics parameters for model P

Reactions	Frequency Factor (min^{-1})	
	Experiment	Field
IC ➔ 2.0471 MC	3.822×10^{20}	8.186×10^{16}
MC ➔ 0.4885 IC	3.366×10^{18}	7.209×10^{14}
MC ➔ 2.3567 LC	1.132×10^{15}	2.425×10^{11}
LC ➔ 0.4243 MC	1.524×10^{15}	3.264×10^{11}
IC ➔77.4563 COKE	2.320×10^{15}	4.969×10^{11}

IC + 98.869 O_2 ➔ 77.456 $CO_{1.947}$ + 46.904 H_2O	1.812×10^8	2.772×10^3
MC + 49.069 O_2 ➔ 37.075 $CO_{1.947}$ + 25.953 H_2O	1.812×10^9	2.772×10^4
LC + 32.025 O_2 ➔14.600 $CO_{1.947}$ + 35.623 H_2O	1.812×10^{10}	2.772×10^5
COKE + 1.22 O_2 ➔ $CO_{1.875}$ + 0.565 H_2O	1.000×10^{10}	1.530×10^5

5.4.2 Model G Results

In the case of model G, the frequency factors of the combustion reactions were downscaled by the time and pressure scaling factors. However, when the same was applied to the cracking reaction, it was found that at the end of the PIHC, not enough fuel is left behind to establish and sustain combustion. Therefore, through sequential volume up scaling, the activation energy of the cracking reaction was adjusted such that at the end of the PIHC, approximately the same concentration of fuel was deposited around the injectors. Steam was used to carry out the PIHC and the rate at which it was injected was appropriately upscaled such that the cumulative amount injected became the same as that injected in the base case times the volume upscaling factor. For the full field scale with dimensions of 150 m × 100 m × 24 m, approximately 50,000 bbl CWE (cold water equivalent) of steam is to be injected during the 104 days of PIHC. It should be noted that once the volume of steam needed to establish communication between the wells is determined, the reservoir length can be upscaled to obtain a repeatable pattern such as 500 m × 100 m × 24 m.

The upscaled models were then run until the oil inside the reservoir is fully recovered. Ideally, the fuel availability should be constant regardless of the volume of the reservoir. Fig. 5.15 shows the plot of log of mass of fuel available

as a function of log of reservoir volume. All the points fit perfectly linear relationship on the log-log scale, which shows that the fuel availability is constant regardless of reservoir volume. This is similar with what was observed in section 5.3.3 where the mass of coke and reservoir volume are related by power law. The slope of the mass of coke against reservoir volume gives the fuel availability which in this case can be obtained from the log-log scale plot as:

$$M_c = 10^{(2.0370 \pm 0.0117)} \times V^{(0.9931 \pm 0.0049)}$$

By taking the power on the V to be approximately unity, the slope is 109 ± 3 kg m^{-3}. It follows that in order for the slope to be within the reported range of 50 to 57 kg m^{-3} for Athabasca bitumen (Alexander et al., 1962), further tuning of the activation energy of the cracking reactions must be carried out.

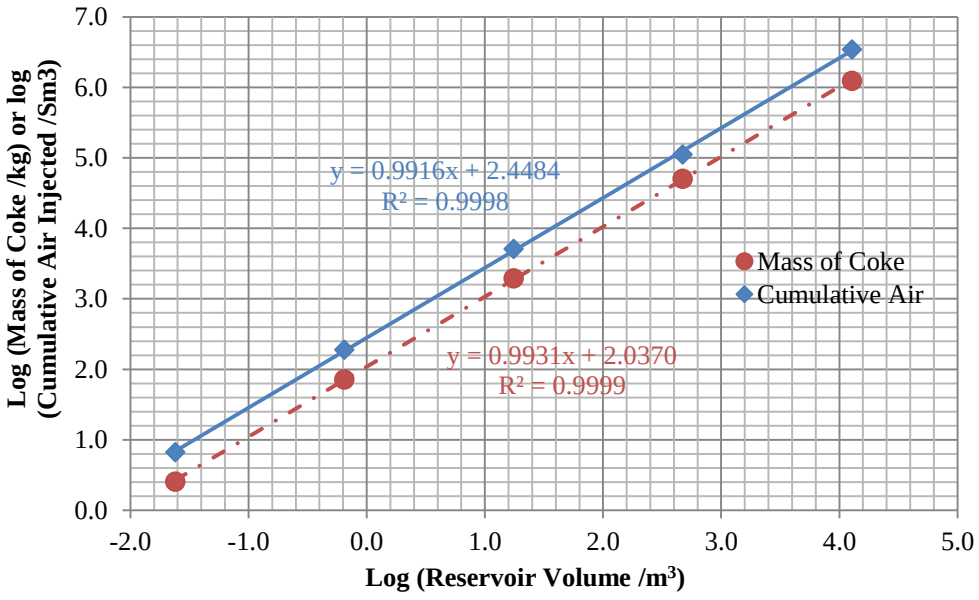

Fig. 5.15: Mass of coke or cumulative air injected versus reservoir bulk volume

When the upscaled cumulative air injected was plotted as a function of reservoir volume on a log-log graph, another power law relationship is obtained with the

slope of 281 ± 13 Sm^3 air per m^3 of reservoir. This shows that at any reservoir volume, the air requirement is the same and the value is within the typical range reported from field projects (Burger et al., 1985).

Tab. 5.5: Comparison of kinetics parameters for model G

Reactions	Activation Energy (kJ mol^{-1})		Frequency Factor (min^{-1})	
	Experiment	Field	Experiment	Field
HEAV oil ➔1.60 LITE oil + 46.62 Coke	99.00	132.53	1.500×10^9	0.500×10^9
HEAV oil + 80.03 O_2 ➔ 26.72 H_2O + 68.70 $CO_{1.94}$	138.00	138.00	1.812×10^{11}	3.069×10^6
LITE oil + 18.65 O_2 ➔ 14.50 H_2O + 11.75 $CO_{1.94}$	138.00	138.00	1.812×10^{12}	3.069×10^7
CH + 1.22 O_2 ➔ 0.50 H_2O + $CO_{1.94}$	123.00	123.00	8.600×10^7	1.456×10^3

Other linear relationships obtained, on log-log plot, were the plot of cumulative air injected against cumulative oil produced and the plot of cumulative oil produced as a function of oil originally in place. The slope of the former, on a linear plot, describes the air-to-oil ratio and has a value of 1541 ± 68 Sm^3 m^{-3} while that of the latter, again on a linear plot, gives the fraction of oil recovered and has a value of 62.4 ± 0.9 %OOIP. As all the points fit a perfect linear relationship, it implies that the upscaling is consistent and that the choice of the activation energies to limit the degree of coking is reasonable. However, one

factor that needs to be further investigated is the duration required to produce a given reservoir as it depends heavily on the air injection rate.

In summary, from this sequential volume upscaling, the estimate of the activation energy of the cracking reaction and the amount of steam needed for the PIHC are obtained. However, it should be noted that the figures obtained are when the process is operated at experimental producer back pressure of 200 kPa. Therefore, at the field scale, when the producer back pressure was increased to 2800 kPa, it was realised that further adjustment to the cracking reaction kinetics parameters need to be made in order to obtain reasonable fuel distribution (i.e. to limit the degree of overcoking and thus prevent the decrease in porosity to zero). This was achieved by tuning the frequency factor of the cracking reaction while keeping the activation energy the same as that obtained from the sequential volume upscaling. Tab. 5.5 below shows the comparison between the experimental and field scale reaction parameters.

5.4.3 Comparison between Model P and Model G

The comparison between models P and G based on the adjusted kinetics parameters at full field scale is presented under this section. The two models were run under the same conditions (Tab. 5.6) with all the wells located at the same positions.

5.4.3.1 Reservoir Model Parameters

The porosity is the same as that used in the experimental model while the absolute permeability has been changed to that reported by Petrobank, (2010). The initial reservoir pressure and temperature, as shown in Tab. 5.6, have also

been changed compared to those used in the experimental model. This is in order to properly represent the field conditions.

Tab. 5.6: Reservoir, injection, and production conditions

Reservoir Dimension	150 m × 100 m × 24 m
Number of GridBlock (nx × ny × nz)	90 × 57 × 7
Total Number of GridBlocks + Wellbore	38500
Well Arrangement	Staggered Line Drive (2VIHP)
Initial Reservoir Temperature and Pressure	20 ^{o}C and 2800 kPa
Initial Oil and Water Saturations	80 % and 20 %
Porosity	34%
Horizontal and Vertical absolute permeability	6400 mD and 3450 mD
Well Internal Diameter	178 mm
Producer back pressure	2800 kPa
Steam Injection pressure	5500 kPa
Steam Injection Rate (Cold Water Equivalent, CWE)	495 bbl day^{-1} (CWE)
Air Injection Rate	20000 Sm^3 day^{-1}

5.4.3.2 Start-up

During the pre-ignition heating cycle (PIHC), steam was injected at a rate of approximately 250 bblday^{-1} Cold Water Equivalent through each of the two vertical injectors (i.e. total of 500 bbl/day CWE at a steam condition of 271.3 ^{o}C and quality of 0.8) for 104 days. However, due to pressure build-up, the steam rates injected into models G and P averaged 433 bbl/day and 395 bbl/day respectively. This is reflected in the duration at which oil production began. The purpose of the steaming is twofold: first, to condition the zone around the vertical injectors so that enough fuel to initiate and sustain combustion is left behind, and, second, to mobilise the oil around the injectors to establish communication with the horizontal producer. Fig. 5.16ai & bi show the temperature distribution along the vertical mid-planes which is as a result of steam condensation. At the reservoir pressure of 2800 kPa, the affected zone has already reached the steam saturation temperature of 230 ^{o}C by the end of the PIHC. The oil around the affected zone was displaced due the expansion of the steam zone and sufficient heavier fraction left behind as fuel (Fig. 5.16aii & bii). The mobilised displaced oil from the top layers flows down to the horizontal producer which prior to steam injection contained no oil. By the end of the PIHC, the horizontal producer (HP) is filled with mobilised oil and full communication between the wells is established. The predicted profiles are very similar except that in model G the mobile oil only traversed around two-third of the HP length.

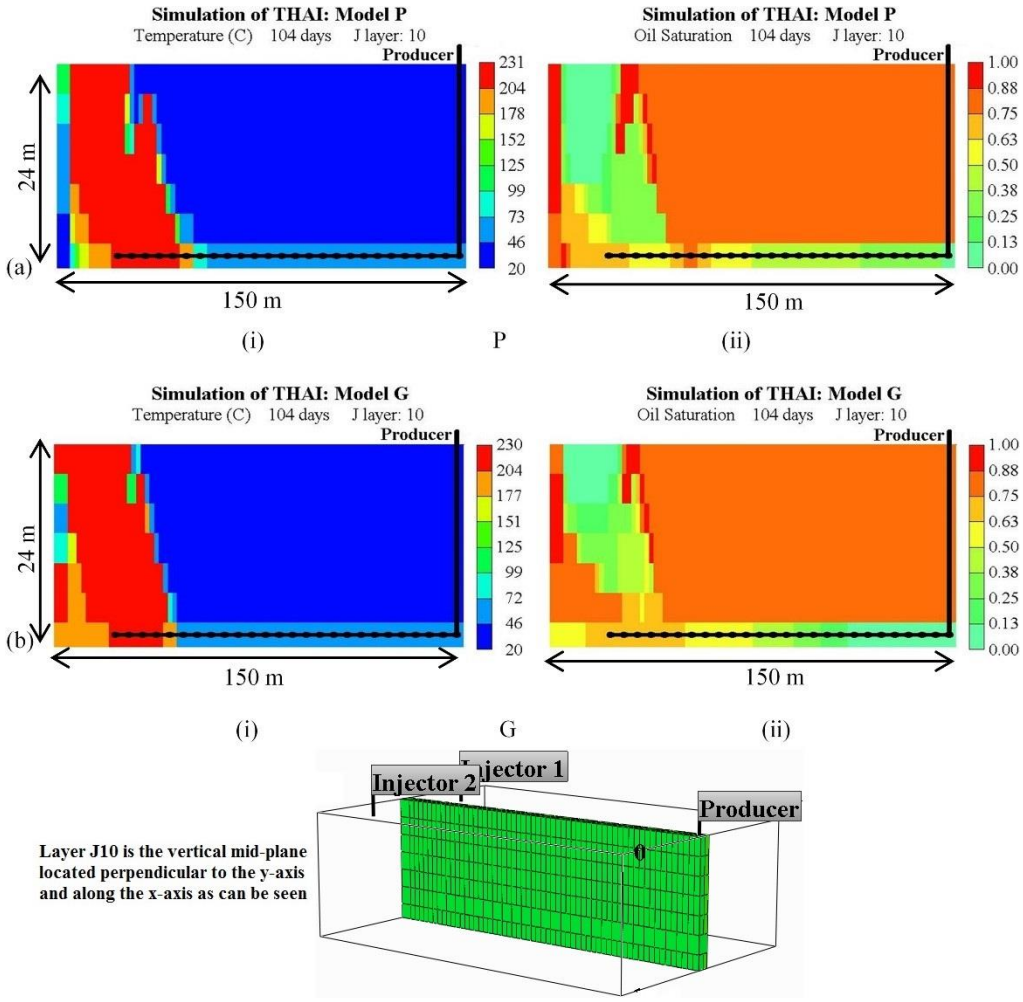

Fig. 5.16: (i) Temperature and (ii) oil saturation profiles for models (a) P and (b) G along the vertical mid-plane (J layer 10).

The oil production in model P started 58 days after the start of steam injection which is latter than in model G by 14 days (Fig. 5.17). However, the oil production started quite early compared to during the field pilot in which it started 90 days after the initiation of the steam injection (Petrobank, 2010). The difference could be due to the fact that these models did not take into account

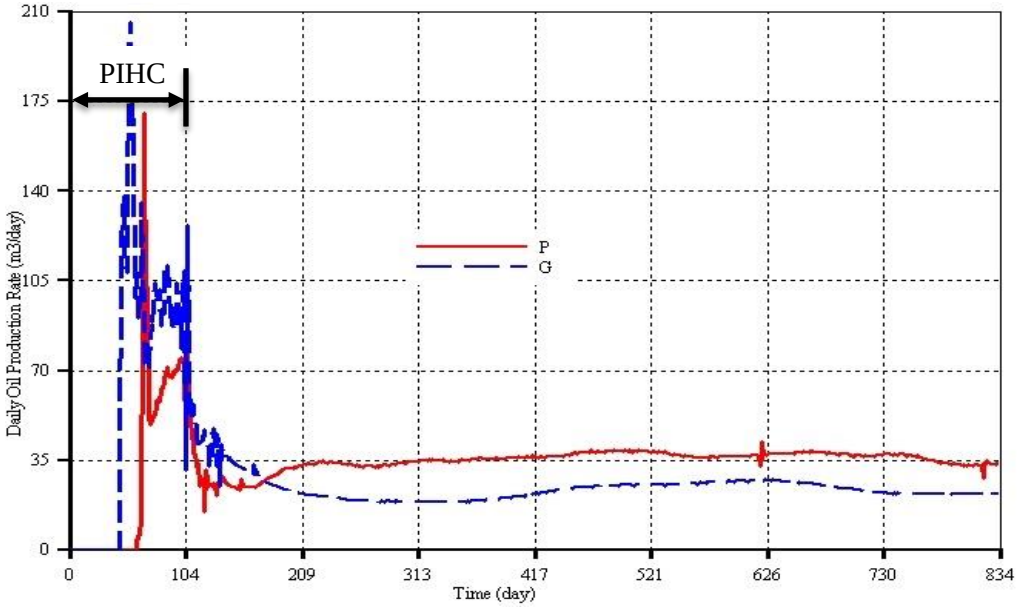

Fig. 5.17: Oil rates for models P and G

the reservoir heterogeneities. Initially, the oil rate predicted by model G peaked to 206 m^3day^{-1} before dropping and averaging around 100 m^3day^{-1} over the 104 PIHC days (Fig. 5.17). Similarly, for model P, it peaked to 170 m^3day^{-1} before declining and averaging around 70 m^3day^{-1}. The peaking in oil rate in both cases is as a result of significant pressure difference between the zone around the injectors and the outlet of the horizontal producer. This is similar to the observations made from the experimental models described in chapter 4. At the end of the 104 days PIHC, models G and P predicted 6.7 and 3.1 %OOIP recovery respectively. The expected recovery as observed experimentally is 4 %OOIP implying that model G deviated by 67.5% while model P deviated by 22.5%. It means that better prediction is obtained by model P. Overall, the recovery from model G due to PIHC only is 54% higher than that from model P. At the end of the PIHC, air was injected at a rate of 10000 m^3day^{-1} via each of the two injectors. Once the deposited fuel is ignited, the peak temperature increased sharply reaching the maximum of 946 ^oC within 10 and 2 days for

model G and P respectively. This is the main indicator that combustion has been initiated and that it is in HTO mode.

5.4.3.3 Oil Production

From Fig. 5.17, it can be seen in both curves that the oil production rate decreased in response to air injection. The decline is because most of the mobilised oil has already been produced and that the pressure built up during the PIHC has been relieved.

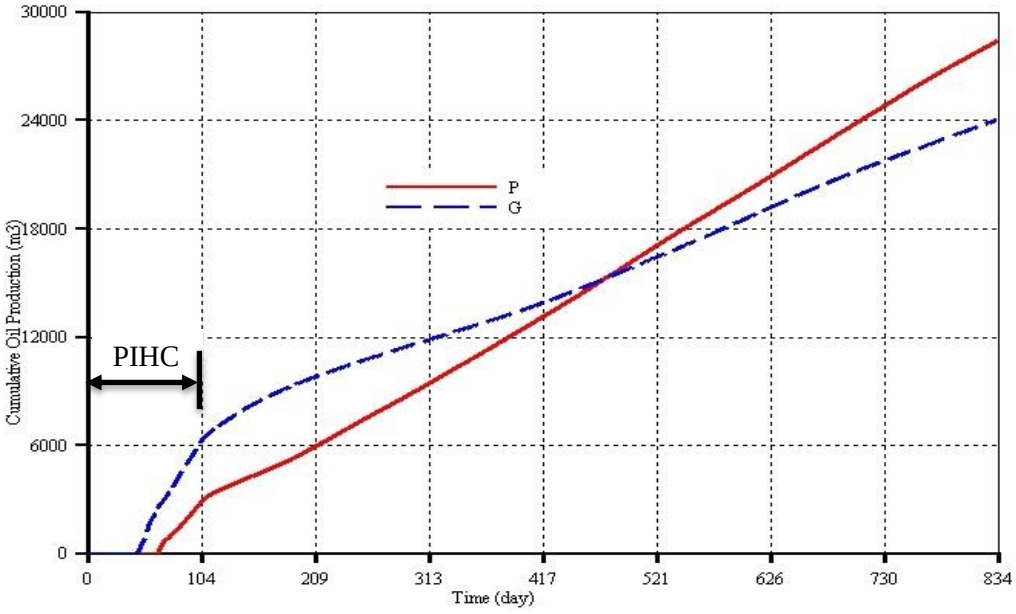

Fig. 5.18: Cumulative oil for models P and G

As the heat generated from the combustion is distributed inside the reservoir, more oil becomes increasingly mobilised and the oil rates pick-up until they stabilised at 204 days. Curve G was above curve P prior to air injection and 70 days into the air injection. After 174 days, the oil production rate, curve P, was above curve G by at least 12 $m^3\,day^{-1}$ for the remaining part of the combustion time. For the cumulative oil production, curve P is below curve G from the time when oil production begins to 470 days (Fig. 5.18). However, as the oil rate in

P is higher than in G, curve P was above curve G for the additional one year of combustion. It therefore follows that quite large portion of the oil recovered in model G is due to PIHC. The recovery due to the two years of combustion from models P and G are 27.4 and 19.1 %OOIP respectively. This means the recovery predicted by model P due to combustion only is 30% higher than that predicted by model G. Since the cumulative oil predicted by model P at the experimental level is closest to the experiment, it can be concluded that the oil production predicted by model P at the field scale is more representative.

5.4.3.4 Oil Upgrading

The API gravity gives the measure of the extent to which the Athabasca bitumen is upgraded. At the air injection rate of 20,000 Sm^3day^{-1}, the degree of upgrading predicted by model G is generally higher than that predicted by model P (Fig. 5.19). This is because the rate of cracking in model G is quite high leading to significant coke deposition. The values predicted by model G are quite similar to that observed during field trial by Petrobank, (2008). However, it should be noted that the rate of air injection during the field trial is higher than what is used here. It has been observed that the degree of upgrading in model P depends on the air injection rate and that as the air rate is increased to near that used in the field trial, the degree of upgrading approaches that observed from the field trial which ranges from 7 to 14 API points (Petrobank, 2008).

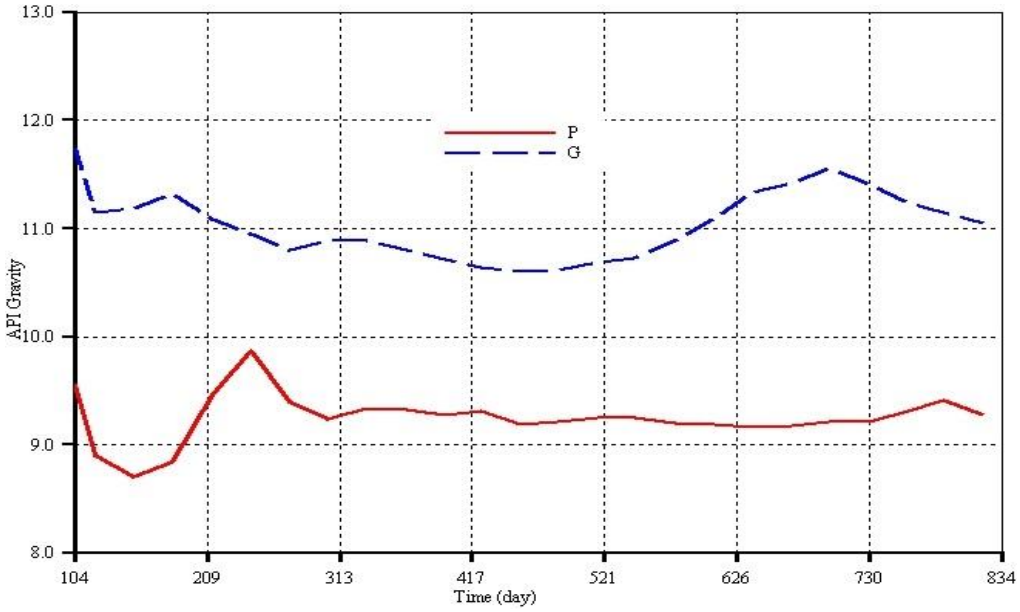

Fig. 5.19: API gravity for models P and G

5.4.3.5 Mobile Oil Zone (MOZ)

Higher areal sweep is achieved in model P compared to in model G (Fig. 5.20). This is due to higher advancement of the combustion front which implies that the oil displacement is not only due to heat transportation by conduction and convection but also as a result of the ‘‘bulldozing effect’’ of the combustion front. The MOZ is given by the oil flux vectors superimposed on the oil saturation and the temperature profiles (Fig. 5.20). In both models, two groups of oil flux vectors along the vertical mid-plane can be identified. Those that are fully vertical and downward-directed into the HP and the group that has their tail leaning forward and their head downward-directed towards the toe of the HP. The latter group indicates that the oil from the top of the reservoir drains in a direction opposite to that of the advancing combustion front while the former indicates that the oil directly above the well drains under the influence of gravity only. The slanting nature of the mobilised oil flow from the layers above the horizontal producer (HP) means that the already mobilised oil accumulated at

the base of the reservoir is only partially produced as can be seen by the horizontal oil flux vectors. This happens because the downward-directed and slanting nature of the mobilised oil flow in the offset vertical planes (planes away from and parallel to the vertical mid-plane) means that the mobile oil is directed towards the toe and parallel to the HP well. It could also be partly because the producer back pressure is quite high (i.e. 2800 kPa compared to 200 kPa in the experimental model) forcing the displacing fluid (flue gas) to be restricted to the upper portion of the reservoir. From this, we found that significant part of the oil produced comes from behind and either side of the toe of the HP (which can be identified by forward-directed horizontal oil flux vectors).

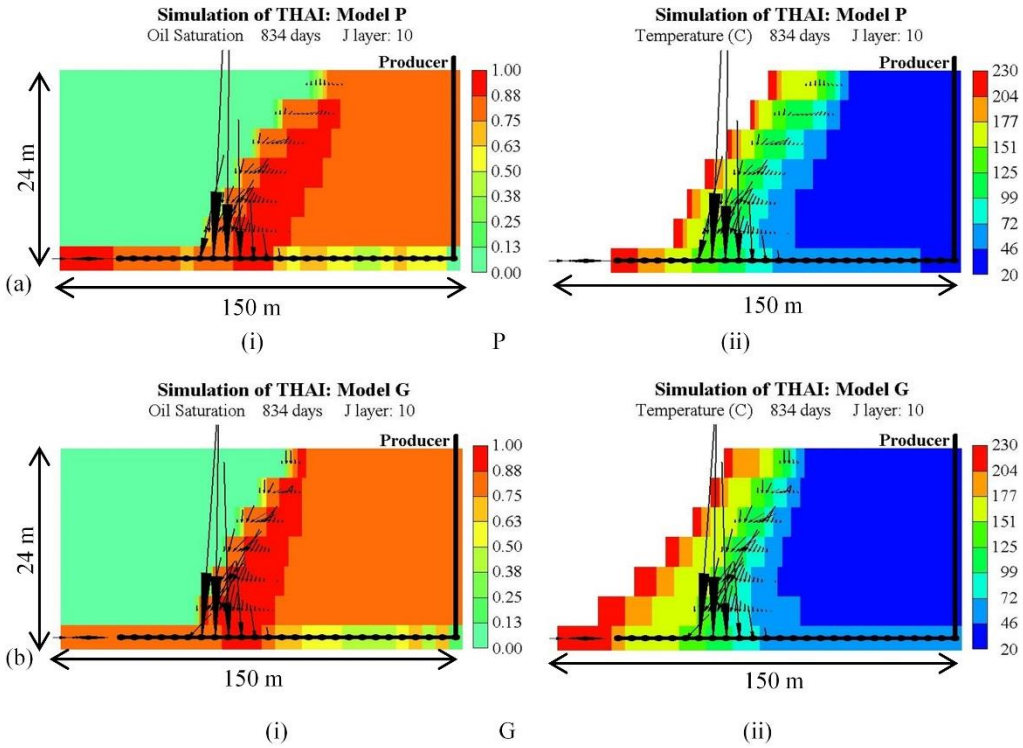

Fig. 5.20: (i) Oil saturations and (ii) temperature profiles for models (a) P and (b) G along the vertical mid-plane (J layer 10).

It thus follows that the rate of oil mobilisation and drainage is higher than the rate of production in the absence of an additional drive mechanism. Therefore,

to recover the mobilised oil from around the base of the reservoir, either horizontal pressure gradient must be created or displacing fluid such as water must be periodically injected to operate the process in alternating dry and wet modes.

The temperature in the MOZ along the vertical mid-plane, as predicted by both models, ranges from 72 ^{o}C near the cold oil layer to 150 ^{o}C close to the combustion front (Fig. 5.20aii & bii). Around the toe of the HP where there is accumulated mobilised oil and substantial oil production takes place, the temperature is up to 250 ^{o}C while farther downstream at approximately half the length of HP, the temperature is 70 ^{o}C. Between these extremes lies the thickness of the MOZ which can be identified by observing the spread of the longest oil flux vectors in the HP over a distance of roughly 60 m. This distance is equivalent to 45% of the length of the HP and means that the oil drainage into the HP and production occurs over a large distance regardless of how relatively far ahead the combustion front is. This is advantageous, since by regulating the producer back pressure, a high enough column of hot mobile oil can be created and maintained inside the reservoir. The hot mobile oil can then be forced to follow over a bed of catalyst as in THAI-CAPRI. However, it is observed in the experimental model as well as at field scale that both models P and G showed that if a bed of hydro-treating catalyst is to be wrapped around the HP, the temperature of the MOZ will not be high enough for further catalytic upgrading to be achieved when the THAI oil flowed over the catalyst. It follows that for catalytic upgrading to be achieved in THAI-CAPRI at field scale, an external source of heat must be used to bring the temperature to 420 ^{o}C. Given this, the source of hydrogen needed for the catalytic reaction could be from water-gas

shift (WGS) and steam gasification (SG) reactions. The former involves carbon monoxide and steam generated from the combustion reactions, while the latter involves the interaction between steam and gaseous hydrocarbons. Therefore, this reaction could take place ahead of the combustion front where the steam and the mobile oil zones overlap. This shows that apart from the decrease in oil viscosity resulting from steam condensation, a further chemical upgrading is achieved. Belgrave et al. (1997) have shown the formation of H_2, H_2S, & CO_2 by subjecting a mixture of Athabasca tar sand and water to pyrolysis at temperatures of 360 to 420 ^oC. In their proposed cracking reaction scheme, however, they did not explicitly show how the water interacted with the hydrocarbon.

5.4.3.6 Fuel Availability

Fig. 5.21 shows the temperature distribution and fuel availability profiles at the base of the reservoir after two years of combustion. The heat is transported to the base of the reservoir via conduction in the reservoir rock and convection from the mobilised oil. The maximum temperature achieved near the toe of the HP as predicted by both models is 252 ^oC (Fig. 5.21ai & bi). However, at the same location, model G predicted very high coke concentration with maximum of 330 kgm^{-3} while the maximum coke concentration predicted by model P is 0.55 kgm^{-3} (Fig. 5.21aii & bii). This shows that the prediction from model P is more reliable as at the indicated maximum temperature, only small conversion should take place. It follows that if the process time is extended beyond two years, model G will predict excessive coke concentration at the base of the reservoir. That means the HP will become easily coked as observed in Greaves et al. (2012c).

At the end of the two years of combustion and 104 days of PIHC (i.e. total of 834 days), material balance showed that model G predicted 3.5 %OOIP fuel consumption with 70.7 %OOIP recoverable oil left in the reservoir. This amount of oil can be recovered by continuing the air injection. In the case of model P, the predicted fuel consumption after 834 days is 1.5 %OOIP with 68.0 %OOIP recoverable oil left in the reservoir. It will appear that fuel consumption by model G is more accurate. However, this is not the case as, when model P was run until 67 %OOIP recovery was achieved, the overall fuel consumption was 5.7 %OOIP, which is within the range of 5 to 10 %OOIP stated in the literature (Gutierrez et al., 2009; Kovscek et al., 2013).

In summary, both models P and G provided a very similar qualitative predictions of the oil saturation and temperature profiles. However, the prediction of such very high fuel concentration at relatively low temperature at the base of the reservoir by model G was unphysical. As model P provided a more realistic prediction of the physicochemical processes taking place during the air injection enhanced oil recovery, it was chosen to carry out further studies and thus the focus of the reminder of this thesis is shifted accordingly.

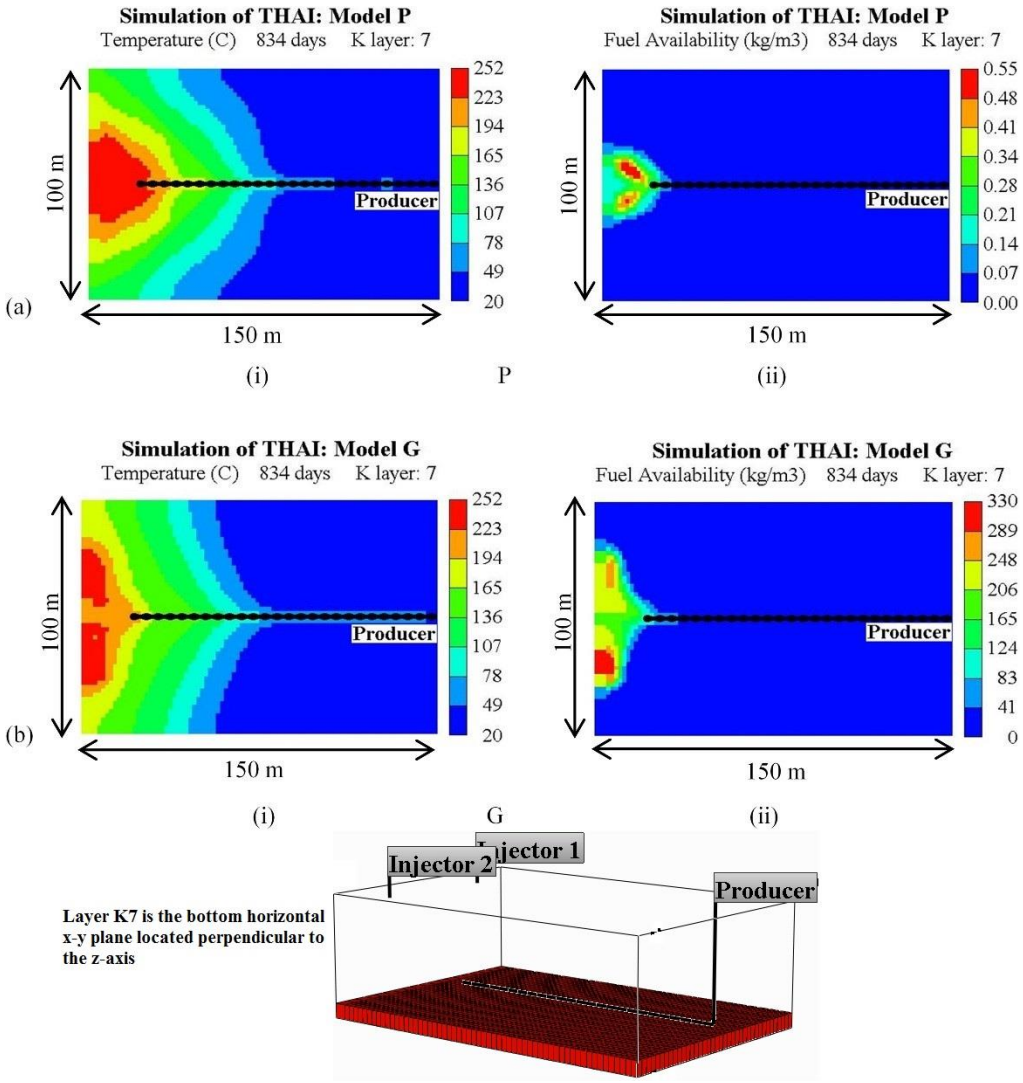

Fig. 5.21: (i) Temperature and (ii) fuel availability profiles for models (a) P and (b) G along the base of the Reservoir (K layer 7).

5.4.4 Comparison between DLD and SLD

Based on model P, a comparative study of THAI arranged in both the direct line drive (DLD) and the staggered line drive (SLD) is presented under this section. In the DLD (Fig. 5.22a), a single vertical injector, which is 9 m long and has it is toe located 14 m above the HP, was used while in the SLD (Fig. 5.22b), two vertical injectors, which are respectively 1.8 m long and located 21 m above the HP, are used. All the vertical injectors were located at offset distance of 12 m from the toe of the HP. Both models were steam pre-heated at rate of 495 bbl day^{-1} (CWE) for 104 days before the commencement of air injection. In the

DLD, 20,000 Sm^3 day^{-1} of air was injected via the single vertical injector while in SLD, 10,000 Sm^3 day^{-1} of air was injected through each vertical injector for a period of two years.

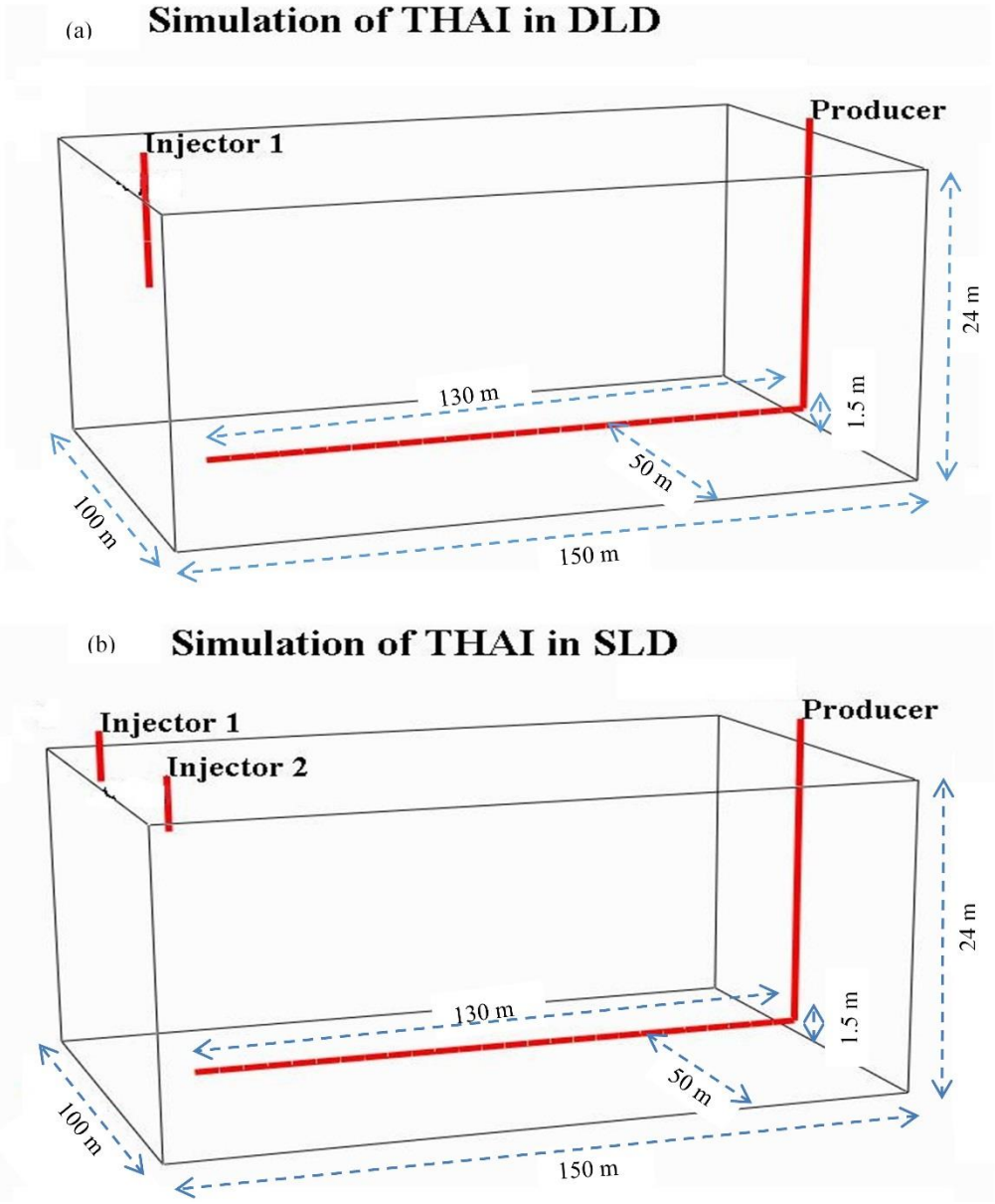

Fig. 5.22: (a) DLD and (b) SLD well arrangements

5.4.4.1 Oil Rate and Recovery

With DLD arrangement, oil production began 8 days after the start of steam injection and it steadily increases to 82 m^3 day^{-1} by the end of the PIHC. On the other hand, the oil production in the SLD arrangement started 36 days after the

initiation of steam injection. After initial spike at the time when oil production began, the oil production rate rises to a maximum value of 82 $m^3 day^{-1}$ at the end of the PIHC (Fig. 5.23). Prior to the start of air injection, 6.5 %OOIP is recovered in model DLD which is higher than in SLD by 1.4 %OOIP (Fig. 5.24). This difference is due to the delay in the oil production in SLD. It is also because the injector and the producer in the DLD are on the same plane and are separated by shorter offset distance compared to in SLD. On air injection at 104 days, the oil production rate peaked in both models before sharply declining to minimum at 209 days (Fig. 5.23).

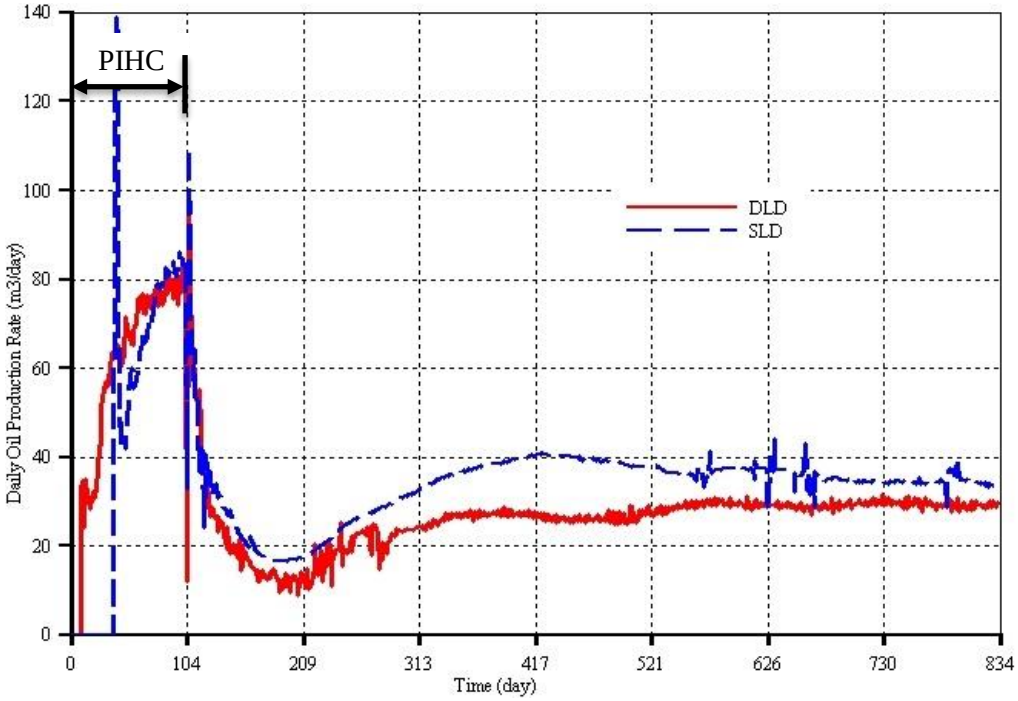

Fig. 5.23: DLD and SLD oil production rates

As heat from the combustion is distributed inside the reservoir, more oil became mobilised and both models predicted an increasing oil rate from 209 to 313 days. After this period, the oil production rates remained at steady state value up to the end of the two years of combustion. The SLD oil production rate curve overlies the DLD curve throughout the combustion period. Similarly, higher oil

recovery is predicted by SLD compared to DLD (Fig. 5.24). These mean the reservoir volume swept by the combustion front in SLD is higher than that in DLD.

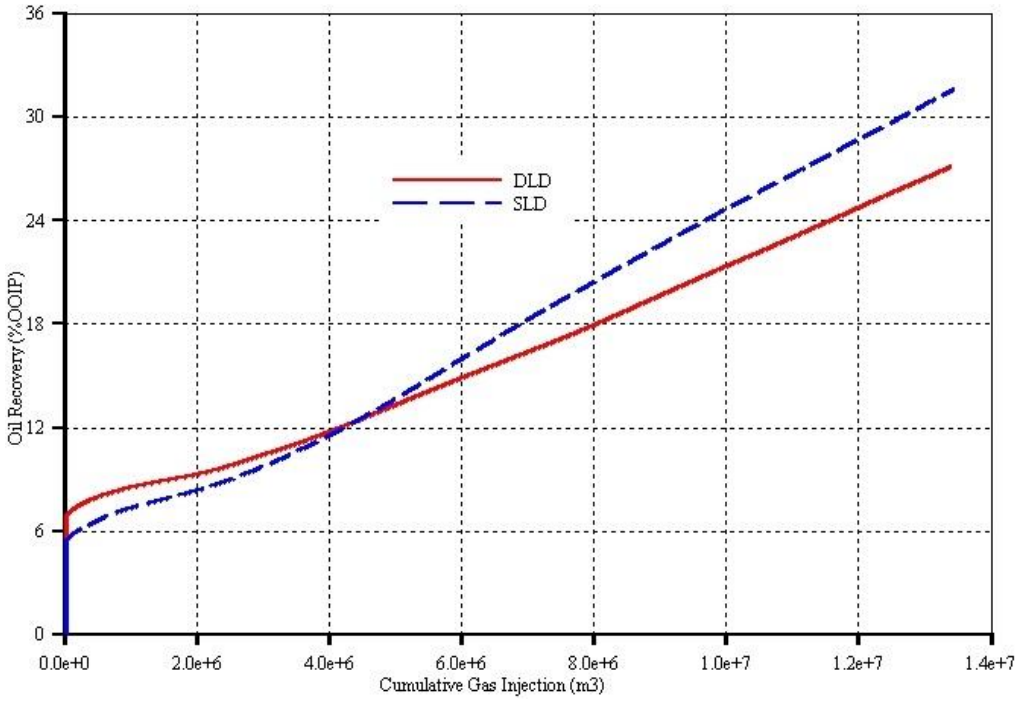

Fig. 5.24: DLD and SLD percent oil recovery

5.4.4.2 Oxygen Production

As the injector in the DLD arrangement is longer, lies on the same plane as the HP, and thus closer to the toe of the HP, DLD oxygen production began just 30 days after the start of air injection (Fig. 5.25). In the case of SLD, the oxygen production began much latter – after 104 days of the start of air injection (Fig. 5.25). At these times, it was observed that the oxygen production began as a result of small portion of oxygen bypassing the combustion zone. However, the rising trend in DLD is maintained for a period of 136 days before levelling out over time period of 215 days. This is as a result of formation of oil seal on the bottom layer of the reservoir where the HP is located. The DLD oxygen

production rose again over 485 to 507 days before further levelling out until 780 days even when the combustion front approached the toe of the HP well.

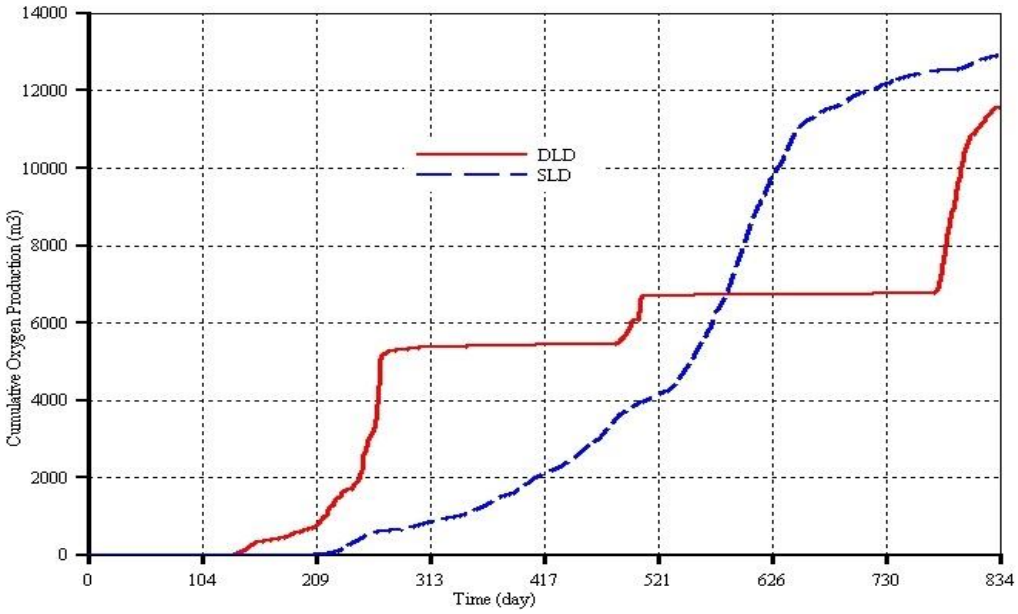

Fig. 5.25: DLD and SLD cumulative oxygen production

5.4.5 Field Scale Oil Production along the HP well

Under this section, the location of the HP well at which fluid is produced compared to the observation made in the laboratory scale model of chapter 4 and that in Greaves et al. (2012a) is discussed. For this, only the SLD results are discussed as the behaviour is found to be quite similar to that in DLD, so long as it is at field scale. Fig. 5.26 shows the rate of oil entering into the HP well at different times. Throughout the 833 days simulated, the highest oil rate occurred at the toe of the HP well (Fig. 5.26). This is contrary to what was observed in the experimental scale model, which has some partial instability due to oxygen production. The cause of the difference in the direction of oil drainage between the lab and field scale reservoirs is best captured in Fig. 5.27. In the field scale model, the cold oil zone temperature is not affected by the advancing combustion front. The oil there is immobile. The combustion front is forward

leaning implying that higher areal sweep is achieved at the top compared to near the base of the reservoir. This means the combustion front covers larger distance along the axis of HP well compared to perpendicular to it. It also implies that the shape of the high temperature (i.e. temperatures higher than that of the native bitumen) zone is forward leaning. Ultimately, the mobilised oil near the top of the reservoir must find a path to the producer. This path must not be restricted by the cold immobile oil. As a result, it takes the sloping path created by the combustion/steam front (i.e. the zone affected by the heat from the combustion).

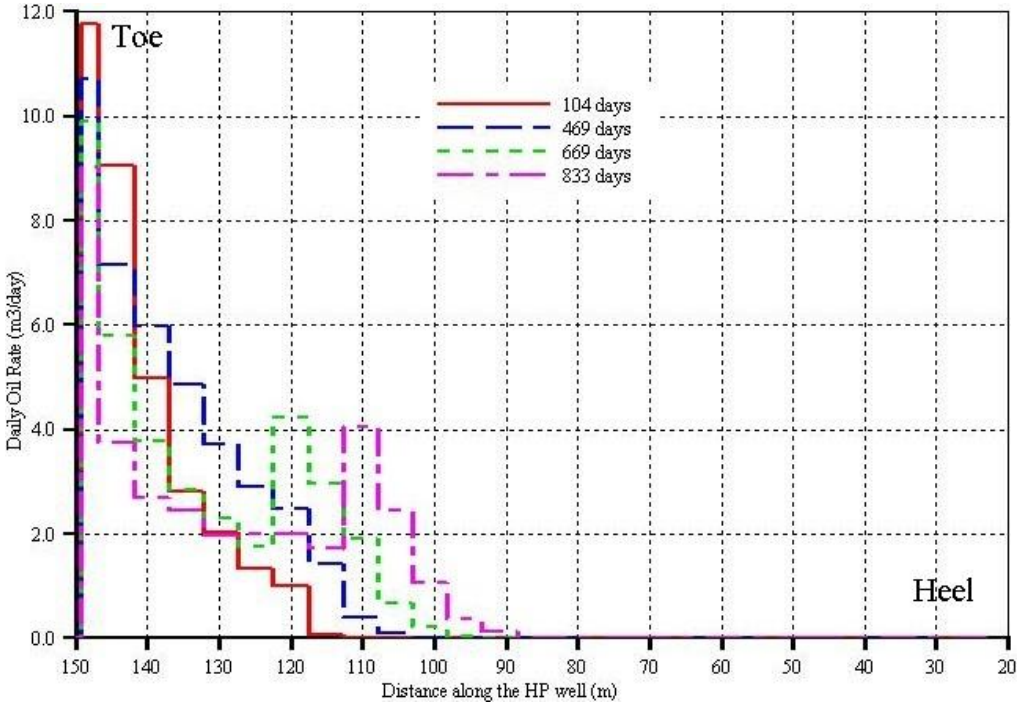

Fig. 5.26: Oil production rate along the HP well at different times

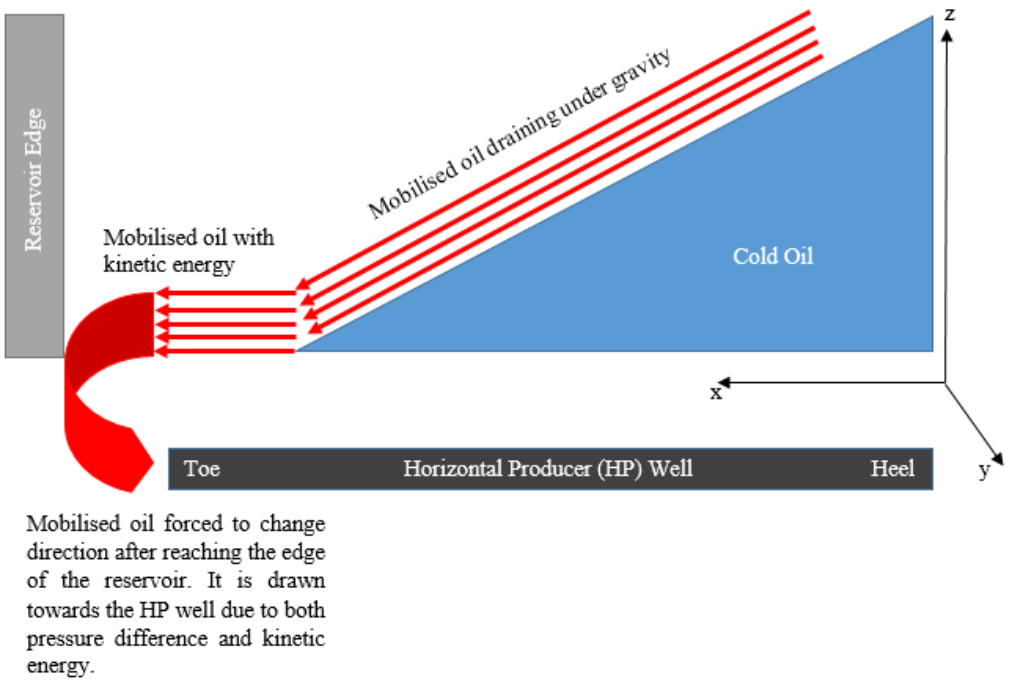

Fig. 5.27: Nature of oil flow into the HP well from adjacent vertical planes

Observing not only the vertical mid-plane but all the other vertical planes revealed that the mobilised oil in those plane finds it is way into the HP well after most of it drained to the base of the reservoir (Fig. 5.27). From the oil flux vectors, it is found that the oil is gravity drained at an angle (i.e. like flowing down an inclined plane) towards the toe and parallel to the HP well. When it reaches the edge of the reservoir, the streamline then slowly turned towards the toe and is produced from there (Fig. 5.27).

The oil is also produced from the mobile oil zone (MOZ), which advances, along the HP well, with the time (Fig. 5.26). The MOZ can be distinctly identified at 669 and 833 days respectively. Also, the fraction of the length of the HP well used to produce the mobilised oil is increases as the combustion time is increased. This is because of the bulldozing effect of the combustion front.

5.5 Summary

From the literature reviewed, it is concluded that the kinetics parameters obtained from an experimental scale model cannot be used directly to carry out field scale ISC simulation. However, in the case of the THAI process, the applicability of this conclusion was investigated through a sequential volume upscaling. It is found that implementing either of the two kinetics schemes, with their respective lab scale kinetics parameters resulted in an unphysical prediction of the fuel consumption at field scale. As a result, it is concluded that the kinetics parameters must be altered, as done by many authors, in order to obtain a realistic representation of the physicochemical processes.

A new upscaling procedure, which involved down scaling the reaction frequency factors, was proposed and a comparative study between the predictions by the two validated kinetics schemes is discussed. It is found that both models P and G provided very similar qualitative predictions of the oil saturation and temperature profiles. However, model G has been found to predict an unphysical high fuel concentration (206 to 330 kg m^{-3}) at relatively low temperature (i.e. 165 to 252 ^{o}C) at the base of the reservoir. As a consequence, model P provided a more realistic prediction of the physicochemical processes.

At field scale, when the wells are arranged in an SLD manner, more oil is cumulatively recovered by an additional 5 %OOIP compared to in a DLD manner. It is concluded that larger reservoir volume is swept by the combustion front in the SLD compared to in the DLD pattern. For the DLD pattern, oxygen

production began much earlier, compared to in an SLD pattern, due to the closeness of the vertical injector to the toe of the HP well.

The nature of oil drainage at field scale is found to be different from that at laboratory scale. In the field scale, the combustion front is completely stable and the tail of the oil flux vectors are forward leaning. This means the head of the oil flux vectors are downward directed and pointing towards the toe of the HP well. As a result, the mobilised oil is gravity drained at an angle (i.e. like flowing down an inclined plane) towards the toe of the HP well. It is found that throughout the two years of combustion period, the highest oil rate entering the HP well is at the toe.

6. Chapter Six: Applicability of THAI in a Geologically Realistic Reservoirs

6.1 Introduction

To successfully devise and implement any in situ oil recovery technique, the dominant geological features, which heavily influence the predictive capability of any numerical model, must be fully delineated and accordingly understood. As a result, this chapter is fully dedicated to studying the effect of these features.

6.2 Models Development

6.2.1 Heterogeneous Reservoirs

A laboratory scale model, which is similar in dimensions to that used in Chapter 4 (Fig. 4.1), is chosen to carry out the study of the effect of reservoir heterogeneity on the THAI process. This is because representing the heterogeneity on gridblocks of the same length as the thickness of the combustion front will not only capture the physico-chemical processes, but it will also reveal the potential for alteration to the continuity of the combustion front, which was observed in the homogeneous case. However, prior to this, the sensitivity of the three-dimensional combustion cell model to different absolute permeability values is investigated.

6.2.1.1 Homogeneous Model with Constant Kv/Kh

As given in section 4.2.2.1 of Chapter 4, an initial validation of the model (i.e. the base case) was made with horizontal, K_h, and vertical, K_v, absolute permeabilities of 11500 and 3450 md, respectively (i.e. $K_v/K_h = 0.3$). Here, three different runs were performed under the same conditions as the base case but

using K_h values of 8625, 5750, and 2875 md. This allows the variation of percent oil recovery, cumulative air to oil ratio (CAOR), etc. with absolute permeability to be determined as discussed in section 6.3.1.1.

6.2.1.2 Randomly Heterogeneous Model with Constant Kv/Kh

From the result of the preceding section, it was shown that, over the same combustion period, the oil recovery decreases while the fuel consumption increases with the decrease in absolute permeability. It follows that an introduction of heterogeneity into the homogeneous reservoir model should result in lower oil recovery and higher fuel consumption. This is because, in the heterogeneous case, the average absolute permeability is lowered. The laboratory scale model is discretised into 58 × 37 × 7 grid points. With the further refinement close to the wellbore region, the total number of gridblocks in the computational domain became 16300.

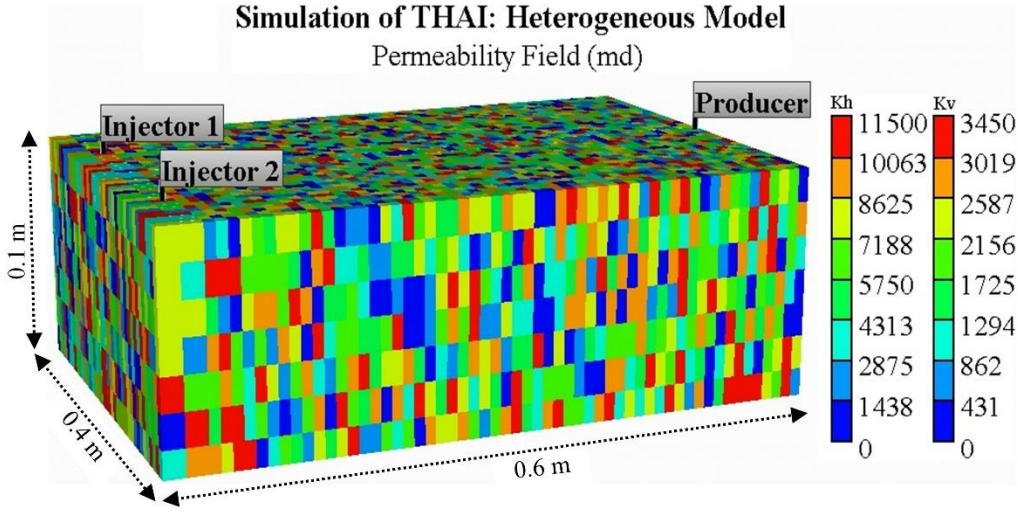

Fig. 6.1: Uncorrelated White Noise Permeability Field

Matlab functionality, *rand*, was used to generate a uniform distribution of random permeabilities over the interval of 0 to 11500 md. The resulting 259 × 58 matrix of the uncorrelated white noise permeability field represents K_h while

the K_v/K_h = 0.3 was maintained at every point in the model. The random uncorrelated heterogeneity is shown in Fig. 6.1. The model was run under the same conditions as in the homogeneous case.

6.2.1.3 Binary Phase Reservoir

Using the same permeability realisation as shown in Fig. 6.1, the effect of randomly distributed low permeability zones on THAI was investigated. However, in this case, the realisations are obtained by assuming that certain proportion of the reservoir volume is occupied by low permeability zones. Fig. 6.2a shows the permeability field in which the probability (P_{30}) of finding low permeability zones at any given point is taken to be at most 30%. Because uniform random distribution is used to generate the permeability field, it then follows that any location which has a permeability value of ≤ 30% of the maximum K_h is assumed to be low permeability zone. Any location which contains sand is assigned the maximum K_h of 11500 md while any low permeability zone is assigned K_h of 115 md. Throughout the model, every point has constant K_v/K_h of 0.3. As a result, this model has permeability contrast of 100%.

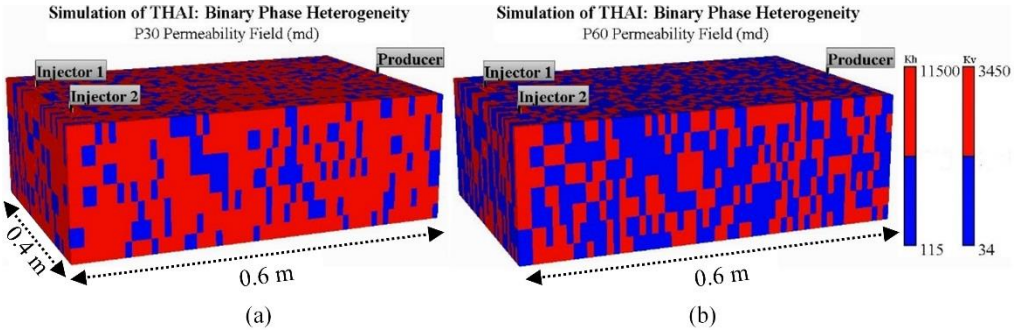

Fig. 6.2: Binary Phase Permeability Field with (a) 30%, and (b) 60% proportion of the low permeability zones

Another realisation is shown in Fig. 6.2b in which the reservoir is highly populated by low permeability zones. In this case, the probability (P_{60}) of finding low permeability zones at any given location is at most 60%. The discontinuous low and high permeability zones are assigned K_h values of 115 and 11500 md, respectively. Again, throughout the reservoir, the ratio K_v/K_h = 0.3 is kept constant. This model also has a permeability contrast of 100%.

6.2.1.4 Shaly Reservoir

To study the impact of shale inter-layers on the THAI process, a generic reservoir model is used. Here, the same realisation as in Fig. 6.2a is used except that the blue phase (i.e. the low permeability zones) is replaced by shales. The shales are assumed to have both zero horizontal and vertical permeabilities. Therefore, STARS assumed the shaly zones to have zero porosity and hence free of fluid (CMG, 2012). The absolute horizontal permeability of the red phase is kept the same (i.e. 11500 md) and the ratio Kv/Kh = 0.3 is kept constant throughout the reservoir.

6.2.1.5 Layered Reservoir

Based on the same dimensions as the base case homogeneous model, the effect of reservoir gradation on the THAI process is studied. This is because there was only one study in which the effect of layered reservoir on combustion front was investigated (Akkutlu and Yortsos, 2005). In order to properly represent the gradual decrease in both the permeability and porosity, the following permeability-porosity relationship is used.

$$K = K_o e^{\left[f\left(\frac{\varphi-\varphi_o}{1-\varphi_o}\right)\right]} \quad (6\text{-}1)$$

where K_o and φ_o are the initial permeability and porosity respectively. K and φ are the current permeability and porosity, respectively, and f is a multiplication factor.

The multiplication factor is calculated by using shale absolute horizontal permeability and porosity of 1 md and 1% respectively as reference values (Le Ravalec et al., 2009). In combination with the base case permeability and porosity, the f value used in the current study is 18.71. Depending on the depositional environment, in some oil reservoirs, the permeability and porosity could progressively decrease from the top to the base of the reservoir. In others, the reservoir could become more permeable and thus porous as the depth of burial is decreased. Another possibility is the cross-sectional progressive decrease or increase in permeability and thus porosity. As a consequence, four different realisations are proposed and modelled under the same conditions as the base case model. These are: (i) High Permeability Centre (HPC) in which the permeability and porosity progressively decrease radially away from the vertical middle plane (Fig. 6.3a), (ii) Low Permeability Centre (LPC) in which there is a progressive increase in both permeability and porosity in a radial manner away from the vertical middle plane (Fig. 6.3b), (iii) Top-down Permeability Increase (TPI) modelled the effect of gradual increase in permeability and porosity from the top to the bottom of the reservoir (Fig. 6.3c), and (iv) Top-down Permeability Decrease (TPD) involved the gradual decrease in permeability from the top to the base of the reservoir (Fig. 6.3d).

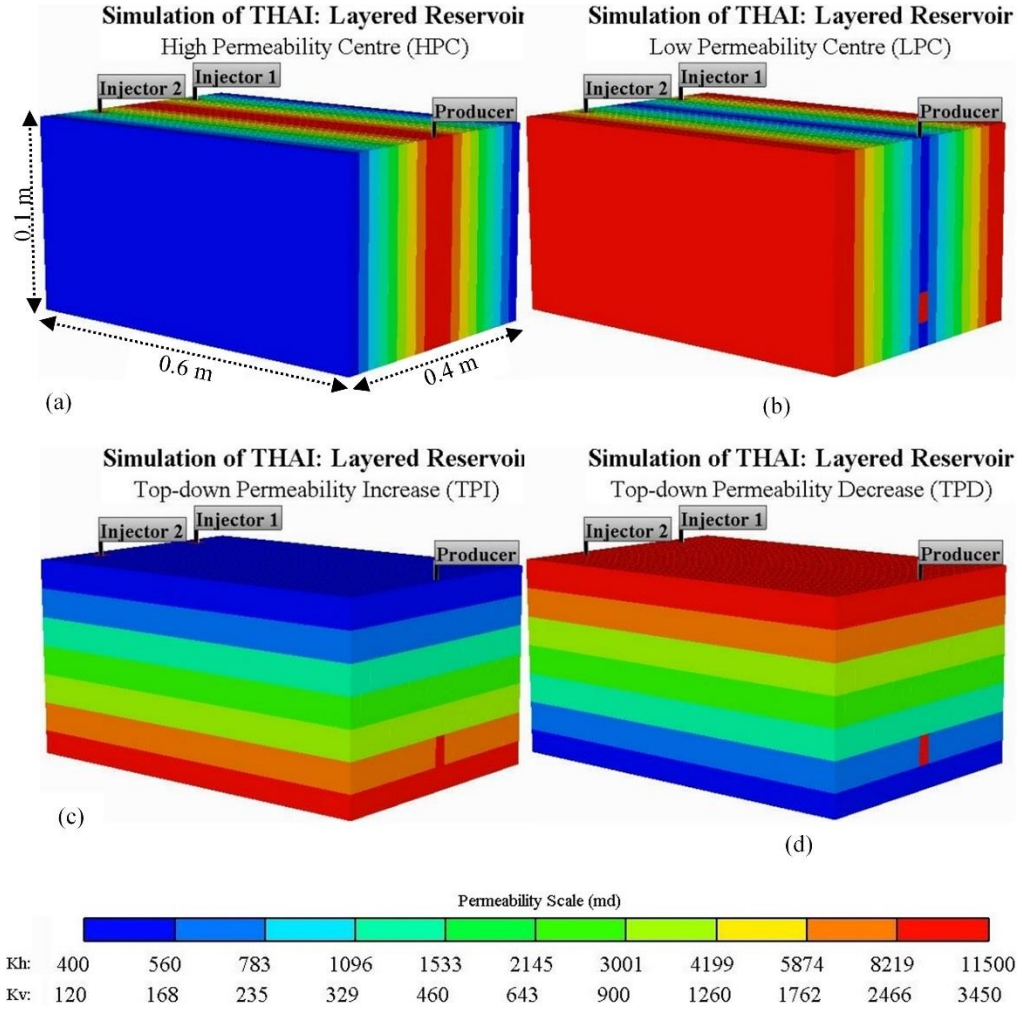

Fig. 6.3: Permeability Field in Layered Reservoir for (a) HPC, (b) LPC, (c) TPI, and (d) TPD Models

In all the four cases, the lowest absolute horizontal permeability is 402.5 md and corresponds to a porosity of 22.17%. In the HPC and LPC models, the change of permeability between every two adjacent vertical planes is by a factor of 150% while in the TPI and TPD models, the change in the permeability between every two adjacent horizontal planes is by a factor of 175%. Also, throughout each of the models, the ratio $K_v/K_h = 0.3$ is maintained. Each model was steam-preheated for 30 minutes prior to six hours of combustion period. This is to allow for the same quantity of heat to be supplied to the reservoir as in the experimental model.

6.2.2 Bottom Water Reservoirs

As reviewed in section 2.2.1 of chapter 2, no investigation of the effect of bottom water (BW) on the THAI process was available in the literature as at the time of writing this thesis. However, with regards to SAGD process, Sugianto and Butler, (1990) have shown that the higher the thickness of the BW compared to that of the oil layer (OL), the lower the cumulative oil recovery. Turta et al. (2009) have suggested that the THAI process may work when the BW thickness is less than 10% of that of the OL. They also offered a preliminary screening criterion, which suggested applying conventional in-situ combustion in BW reservoirs when the BW thickness is 25% that of the oil layer.

6.2.2.1 Effect of BW Thickness

Therefore, as a first stage, the effect of the thickness of the BW zone, compared to oil layer zone, is investigated at field scale. For this, two models, namely BW1, and BW2, are developed. In BW1, the BW to OL thickness ratio is 1:4 while it is 1:2 in the BW2. For both models, the BW zone is attached to the reservoir section which is modelled in section 5.4.4 of chapter 5. The adjusted Phillips et al. (1985) kinetics scheme, as in model P of chapter 5, is used in both models. This is because it has a better predictive capability. Fig. 6.4 shows the reservoir section, it is dimensions, and the included BW zone for BW2. In both models, the wells, two vertical injectors (VI) and a horizontal producer (HP), are arranged in a staggered line drive (SLD) configurations. The HP is located on the bottom horizontal layer of the OL, which is ≈ 1.5 m above the oil-water interface. This is very important as Lau, (2001) observed an increase in oil production rate when he modelled basal combustion with the HP located at the

oil-water contact. It should be noted that no water source or sink wells are included in the BW zone implying that the BW is static.

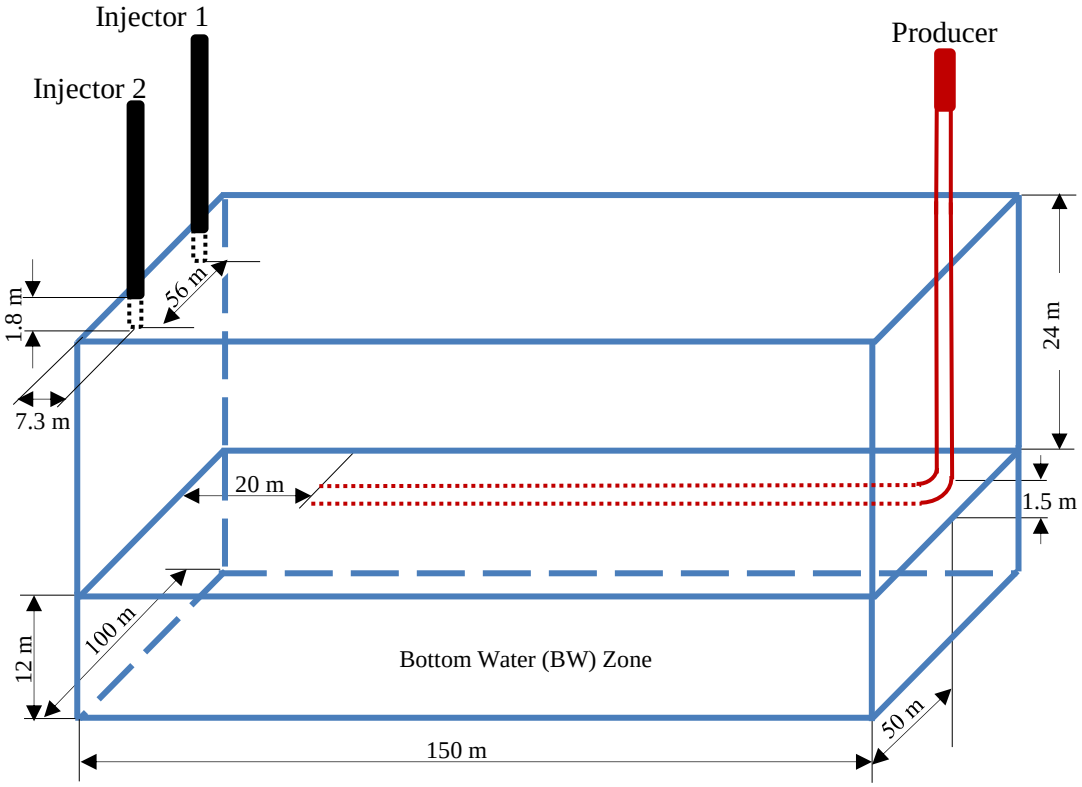

Fig. 6.4: Reservoir Section Showing the Thickness of the BW

6.2.2.2 Effect of the Location of HP

In a similar fashion as the basal combustion (Lau, 2001), the THAI process is a gravity stabilised process. As a consequence, the success, or otherwise, of recovering heavy oil from BW reservoir using the THAI process could well be determined by the location of the HP as in the case of SAGD. Sugianto and Butler, (1990) have shown that the performance of the SAGD depends heavily on the location of the production well. They reported an additional increase in ultimate oil recovery by 20%, when the production well was located at the bottom of the BW zone, compared to that realised with the production well located just below the oil-water contact. Further, they concluded that positioning

the production well as far above the oil-water interface as possible is unproductive since the oil production is substantially reduced. However, they did not consider the situations where the thickness of BW is ≥ 50% of that of the OL. In view of the foregoing, three different models were developed with the location of the HP varied to investigate the influence this has on the THAI process. In each of the three models, the BW to OL thickness ratio is 1:2 and the reservoir section and the dimensions are the same as that shown in Fig. 6.4. In the first model, L1, the HP was located 8 m above the oil-water interface (i.e. into the OL zone). For the second model, L2, the HP was positioned at the oil-water contact while the third model, L3, has the HP drilled 6 m below the oil-water interface (i.e. in the BW zone). Fig. 6.4 shows the reservoir section for model L2 and Fig. 6.5 shows that for model L3. The models were simulated under the same conditions as those in the preceding section 6.2.2.1.

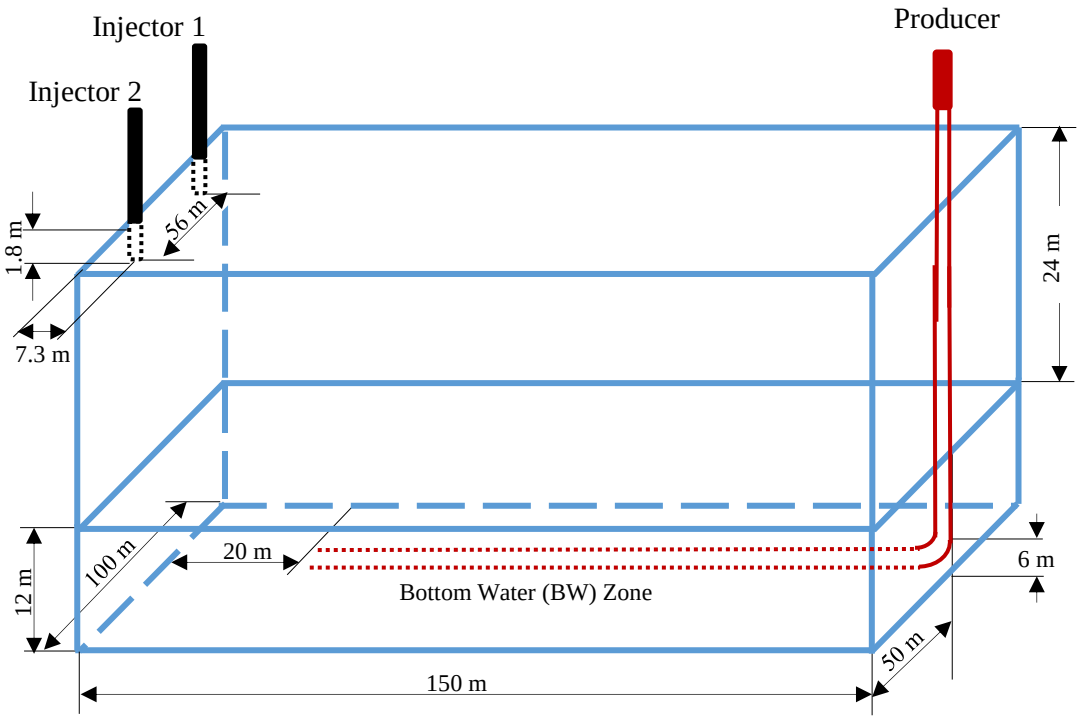

Fig. 6.5: Reservoir Section with the HP located in the BW zone

6.2.2.3 Limit to Production due to BW Thickness

Given the influence the thickness of BW has on the oil production rate, knowing the maximum BW thickness above which no oil production takes place will be crucial in deciding whether THAI process is deployed or not. In view of this, four different models were developed. In all the models, the wells are arranged in an SLD fashion. As it has already been determined from the previous studies, of sections 6.2.2.1 and 6.2.2.2, that more oil is produced when the HP well was located within the BW zone, all these models have their HP located within the BW zone. Thus, the location of the HP was varied within the BW zone to investigate how quick the oil production begins. Tab. 6.1 shows the BW/OL thickness ratio and the location of the HP below the oil-water interface for the four different models. Models 1A and 1B have the same BW/OL thickness ratio. However, in the case of the former, the HP is located at a distance of 50% that of thickness of the BW while in the case of the later, the HP is located 4 m above the base of the BW. Likewise, the same applies to models 2A and 2B except that the later has the HP located 6 m above the base of the BW.

Tab. 6.1: Shows the BW/OL thickness ratio and the location of the HP

Model	Thickness of BW (m)	BW/OL Thickness ratio	Location of HP below oil-water contact (m)
1A	24	1:1	12
1B	24	1:1	20
2A	36	3:2	18
2B	36	3:2	30

The four models were run under the same conditions as those in the preceding sections.

6.2.2.4 Effect of Active Aquifer

In all the previous BW reservoir models, no water source or sink was included to simulate the effect of active aquifer on the THAI process. By simulating static aquifer, which means the base of the BW zone has no flow boundary conditions, the mobilised oil that drained into the BW zone could be captured and produced. However, if water source and sink wells are present, the oil that drained into the thief zone could be swept away laterally and thus be prevented from entering the HP perforations. This will not only increase the water cut in the produced fluid but could also result in no oil production. To carry out this study, two models were developed each with BW/OL thickness ratio of 3:4. The first model, BWN has static aquifer while the second model, BWA has an active aquifer, which is represented by water source and sink wells (Fig. 6.6). For the later, the source and sink wells were alternately placed at the base of the BW zone as can be seem in Fig. 6.6b. All the models were run with the air injection wells and HP arranged in an SLD manner. In each case, the HP was located 4.5 m above the base of the BW zone.

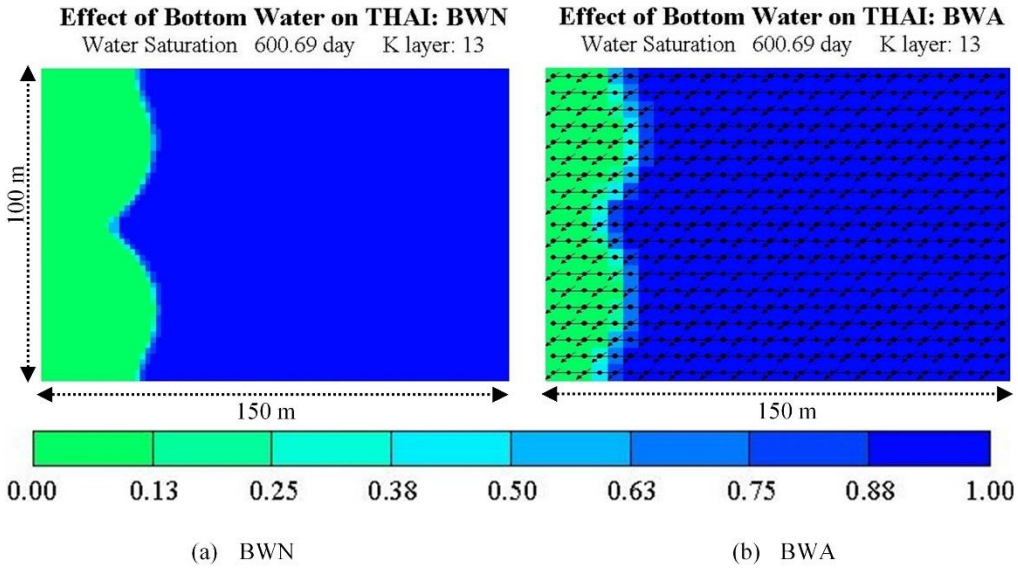

Fig. 6.6: Bottom Horizontal Layers Showing the Presence or Absence of Water Source and Sink Wells

6.2.2.5 Combustion at the Oil-Water Interface

From the findings from field operations and numerical studies, Lau, (2001) highlighted that most of the gas injected into a BW reservoir flows along the oil-water interface just below the OL zone. As a result, it forms a ‘‘basal gas layer’’ at the top of the BW zone. A similar observation is made in this thesis from the results of section 6.2.2.2. However, it is found that the ‘‘basal gas layer’’ is only formed when the HP is drilled in the BW zone, and that its thickness depends on the location of the HP. Just like in the basal combustion, if air is injected into the reservoir, combustion can be initiated and sustained at the oil-water transition zone. This will heat the overlaying oil from below and, hence, mobilise it for production. The combustion will then be propagated in a toe-to-heel manner (THAI) rather than in the kind of ‘‘long-distance displacement’’ manner proposed by Lau, (2001). The potential benefit of this could be an early oil production compared to if the combustion is initiated at the top of the reservoir. It could also reduce the percent of water cut in the produced fluid as mobilised oil forms a blanket around the HP. However, these have to be numerically investigated to elicit the necessary information for potential field applicability. Therefore, two numerical models were developed each with BW/OL thickness ratio of 3:4. The wells were arranged in a direct line drive (DLD) in model D (Fig. 6.7a) while they were in an SLD configuration in model S (Fig. 6.7b).

In both cases, the HP is 130 m long and is located 1.5 m above the base of the BW. The models were run under the same conditions as in the previous sections.

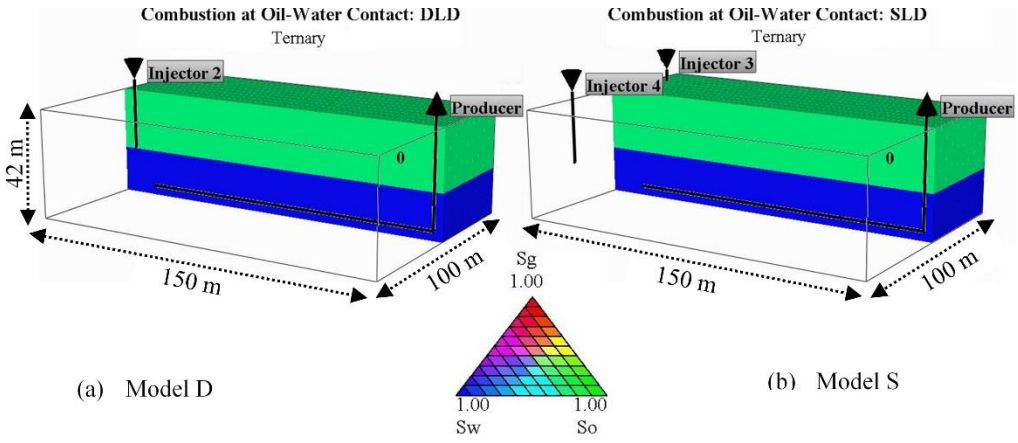

Fig. 6.7: THAI with the Combustion Initiated at the Oil-Water Contact

6.2.3 Gas Overlying Reservoirs

The Athabasca oil sand, which is the largest of the three Canadian oil sand reserves and is considered in the current study, is contained within the Lower Cretaceous McMurray formation –the oldest formation in the so-called Mannville group (Mossop, 1980; Petrobank, 2010; Deschamps et al., 2012). The McMurray formation divides into three units, with the highest concentration of the tar sand being located in the middle unit. This is separated from the upper unit by a thin shale layer which is followed by very fine- to medium-grained estuarine bayfill cross-bedded sand deposit with gradual upward-coarsening. Directly overlaying the upper McMurray zone is the Wabiskaw sand which is the bottom part of the Clearwater formation and is made up of silty marine sand. Laying above this is the shale layer that provides the cap rock which trapped the bitumen in place. This shale layer, also known as the lower Clearwater shale, together with the Wabiskaw sand, constitute the first sand-shale sequence of the Clearwater formation. The second sand-shale sequence is the Clearwater sandstone and the upper Clearwater Shale. The former is made up of a marine shore-face complex and contains a very large quantity of gas while the latter is

composed of sandy siltstone and provides the seal for the underlying gas reservoir. The two sand-shale sequences of the Clearwater formation are overlain by the Grand Rapids formation which is the youngest member of the Mannville group (Mossop, 1980; Petrobank, 2010).

Petrobank, (2010) observed, from the result of well logs, a very small gas zone in the upper McMurray unit. They also reported that the bitumen cap rock (i.e. the lower Clearwater shale), grades rapidly, in an upward fashion, into the Clearwater sandstone. This shows that in their project area, going vertically downward, one will find two shale-gas sequences which are followed by shale-bitumen sequence. A quite similar observation, reported by Pooladi-Darvish and Mattar, (2002), was made in another project site in the Athabasca region. Therefore, before any fluid injection in situ heavy oil recovery technique is implemented, the effectiveness of the lower Clearwater shale in providing the necessary sealing, separating the richest two hydrocarbon pools, must be investigated. This will involve establishing whether there is a direct hydraulic communication between the tar sand reservoir and the overlaying Clearwater sandstone gas deposit. This is very important most especially as far as the deployment of the THAI process, where the sustenance, and thus the stability, of the combustion front is critical to the success of continuous oil production, is concerned. Therefore, the injected air must be confined within the tar sand reservoir for two essential reasons: (i) the continuity of the process so that enough air always reaches the combustion front to maintain economical air to oil ratio, and (ii) the prevention of auto-ignition of the overlying gas in the event that enough heat, from the bitumen combustion zone, is conducted, or convected, or both, to the gas reservoir.

The fluid migration into an overlying gas reservoir could take place due to the presence of one, or a combination, of the following: (i) discontinuity in the cap rock, (ii) some permeability in the cap rock, and (iii) presence of fractures due to pressure build up and thermal stress. Where the cap rock is continuous, such as the case in the Athabasca region (Pooladi-Darvish and Mattar, 2002; Petrobank, 2010), proper control of the fluid injection pressure to less than the shale fracture pressure could prevent the mass and heat convection transfer to the gas reservoir. The study of the effect of pressure build up and thermal stress on the integrity of the cap rock requires geomechanical modelling and, consequently, is not considered here.

In the light of the above, only the effect of permeability of the cap rock on confining the injection fluid in the bituminous reservoir is investigated at field scale. This is because the STARS software does not allow discretised wellbore model option to be used in conjunction with the geo-mechanical simulation. To accomplish this, four different models were developed for a generic tar sand reservoir section. For each model, the cap rock is attached to the top of the oil reservoir, which has the same dimensions as that presented in section 5.4.4 of chapter 5. The thickness of the cap rock is assumed to be 50% of that of the oil reservoir (i.e. 12 m) making each model to have 36 m overall thickness (Fig. 6.8). This is high enough to allow the typical effect in a non-synthetic reservoir to be observed. The bitumen reservoir has the same oil properties and petrophysical data, in each model, as in the other chapters. The cap rock contains no oil and has very low absolute vertical permeability ranging from 10^{-6} to 10^{-3} md (Pooladi-Darvish and Mattar, 2002; Chen, 2009). However, a further literature search revealed that some authors used the maximum permeability

value of 0.001 md (Le Ravalec et al., 2009; Fatemi, 2012) and in one case, a value of 0.1 md was used (Pooladi-Darvish and Mattar, 2002). The porosity and permeability of the cap rock, used in each model, are shown in Tab. 6.2. In each case, it is assumed that only gas is present in the pore space of the cap rock.

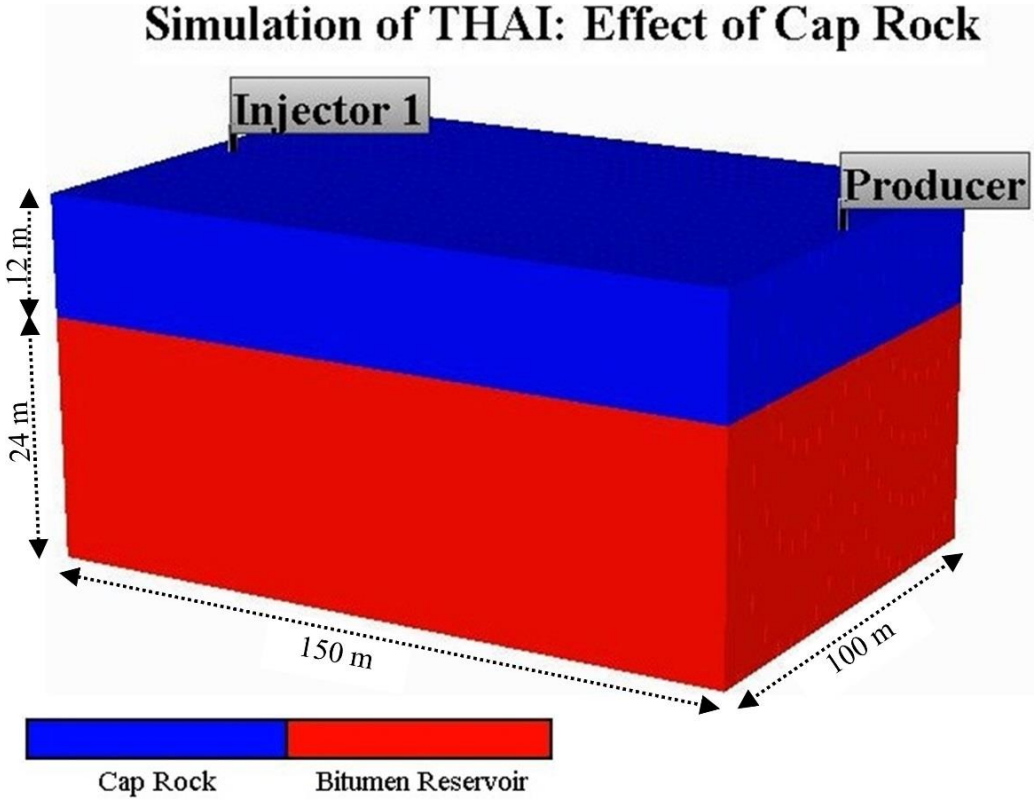

Fig. 6.8: Simulation Domain Containing Cap Rock and Bitumen Reservoir

Each model has the vertical injector and the horizontal producer wells arranged in a direct line drive (DLD) configuration. In each model, steam was injected at the rate of ≈ 500 bbl day^{-1} (CWE) during the PIHC for a period of 104 days. Air injection rate was 20000 Sm^3day^{-1} and was kept constant for 2 years. All the models were run under exactly the same conditions in order to allow for comparison.

Tab. 6.2: Cap Rock Porosity and Permeability

Model	Model Description	Porosity	K_H (md)	K_V (md)
C1	Contains no cap rock	-	-	-
C2	Contains cap rock	0.01	1	0.1
C3	Contains cap rock	0.01	1	0.3
C4	Contains cap rock	0.09	10	3.0

6.3 Results and Discussion

6.3.1 Effect of Reservoir Heterogeneity on THAI

6.3.1.1 Effect of Absolute Permeability

At the constant ratio of absolute vertical to absolute horizontal permeability of 0.3, the effect of change in absolute permeability values was investigated. As can be seen in Fig. 6.9a, the oil recovery (%OOIP), at the end of the 320 minutes of combustion, increases linearly with the increase in absolute permeability. This is because the oil mobilisation rate increases with the increase in absolute permeability, as is in accordance with the Darcy's law. Since the cumulative oil recovered is higher at higher absolute permeability, for the same cumulative air injected, the cumulative air to oil ratio (CAOR) decreases linearly with the increase in absolute permeability (Fig. 6.9b). Over the range of 2875 to 7200 md, the fuel availability increases slowly with the increase in permeability. It means that further decrease in permeability below 2875 md will have negligible effect on the fuel availability. However, from 7200 to 11500 md, the increase in fuel availability becomes linear with increase in permeability (Fig. 6.9c). At high permeability, the ease with which the mobilised hot fluid flows means heat

is easily distributed through the reservoir. This results in an increase in thermal cracking, causing more fuel to be deposited. Fig. 6.9d shows that the average peak temperature increases with the increase in absolute permeability over the range of 2875 to 7200 md. As the permeability is increased beyond 7200 md, the average peak temperature stabilizes, implying insensitivity to further increases in the permeability. The increase in peak temperature can be attributed to the higher fuel concentration at the high permeability. At higher permeabilities, it is observed that oxygen production begins earlier, despite the fact that more fuel is deposited, compared to when the permeability is low. This is because at high permeability, the combustion front reaches the toe of the horizontal producer (HP) earlier than at low permeability. On the overall picture, oxygen utilisation decreases with the increase in permeability.

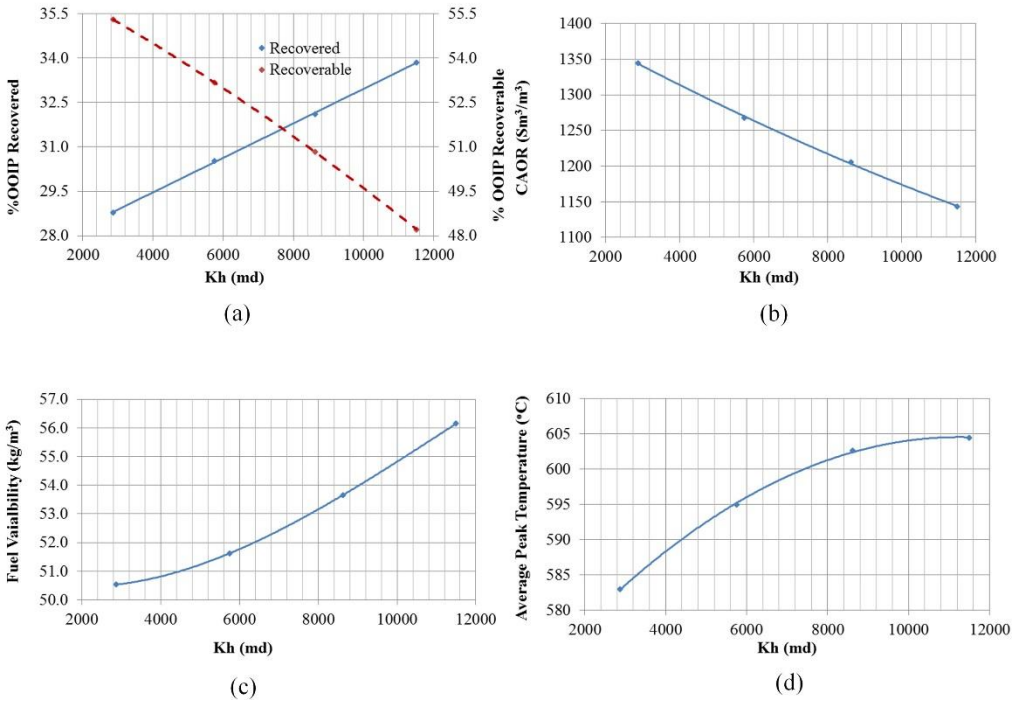

Fig. 6.9: (a) %OOIP recovery, (b) CAOR, (c) Fuel Availability, and (d) Average Peak Temperature as Function of Horizontal Absolute Permeability with the K_v/K_h = 0.3

From Fig. 6.10a, it can be seen that a higher percentage of the reservoir volume is swept by the combustion front, when the horizontal permeability is 11500 md, compared to when it is 2875 md (decrease of 75%). The same can be observed from the temperature distribution profile (Fig. 6.10b), where the high temperature zone (542 to 610 ^{o}C) is closer to the mobile oil zone (MOZ) as can be seen in Fig. 6.10c when the permeability is higher compared to when the permeability is reduced by 75%. The concentration of the oil flux vectors, superimposed on Fig. 6.10b & Fig. 6.10c, above the HP is lower at higher permeability compared to when the permeability is 75% smaller. Below the HP, however, the MOZ is densely populated, at higher permeabilities, by the oil flux vectors. This is because the mobilised oil easily reaches the bottom horizontal plane, from the adjacent vertical planes, before it flows upward into the HP. Another effect that the decrease in permeability has on the process is in terms of the areal or volumetric zone, ahead of the combustion front, occupied by higher oil saturation (88 – 100%). The expanded oil banking zone, at the higher permeabilities, is also due to the ease with which the fluids flow horizontally thereby mixing with the unaffected heavy oil in the cold oil zone. However, overall, it is noticeable that the nature of the oil drainage, as well as heat distribution, is quite similar. Interestingly, also, the position of the MOZ in the sandpack, as indicated by the largest oil flux vectors, indicates that the temperature is in the range of 150 ^{o}C to nearly 300 ^{o}C, regardless of the value of the permeability used.

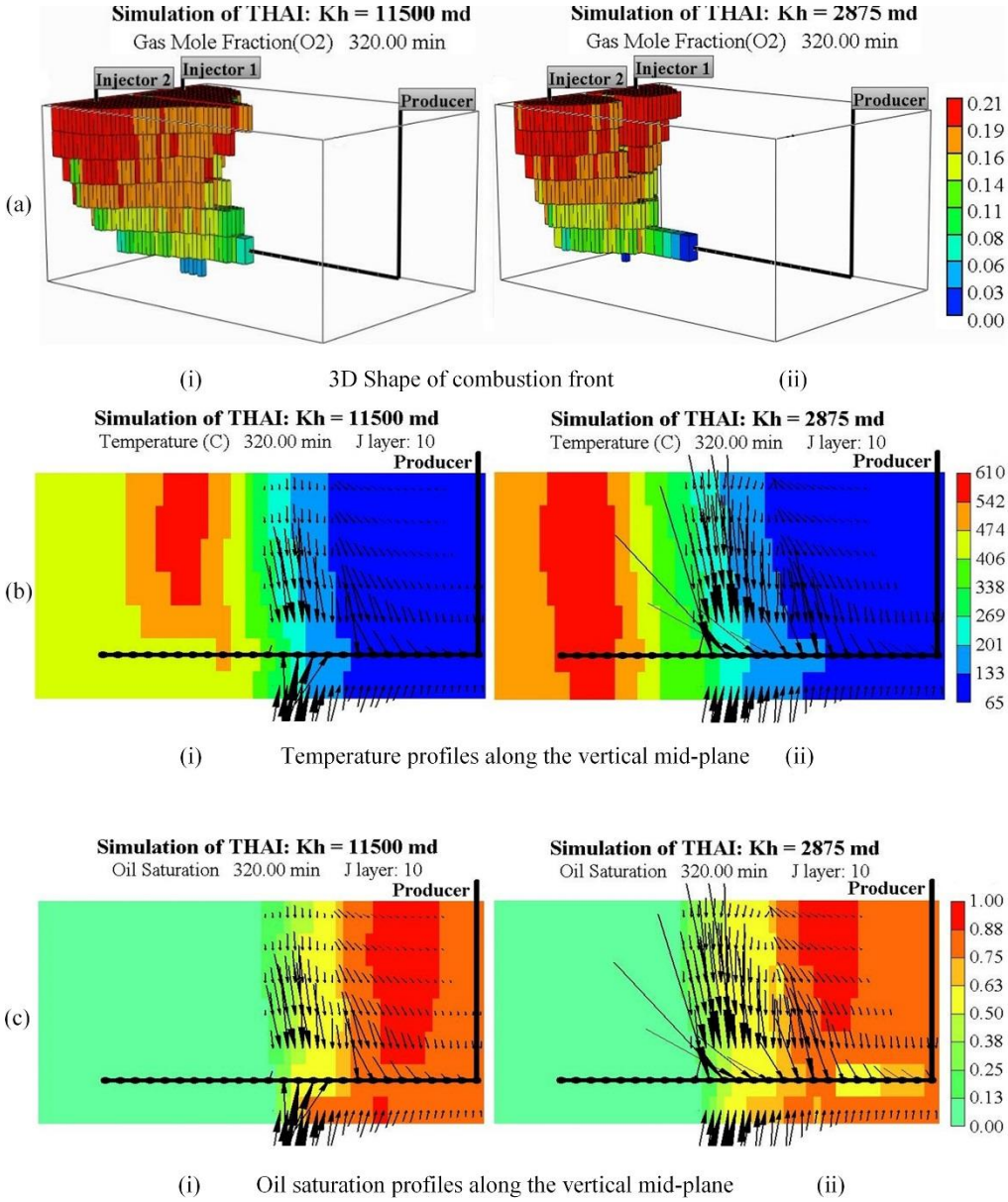

Fig. 6.10: Combustion front, temperature, and oxygen profiles in the homogeneous sandpack, for (i) Kh = 11500 md and (ii) Kh = 2875 md. J layer 10 means the vertical mid-plane x-z.

6.3.1.2 Random Reservoir Heterogeneity

As shown in the preceding section, over the same combustion period, the oil recovery decreases and the fuel availability increases with the decrease in absolute permeability while maintaining K_v/K_h constant. Therefore, the introduction of heterogeneity into the homogeneous reservoir model, is expected to result in lower oil recovery and higher fuel consumption. This is because the

mean of the permeability distribution is 5750 md and always less than the maximum value.

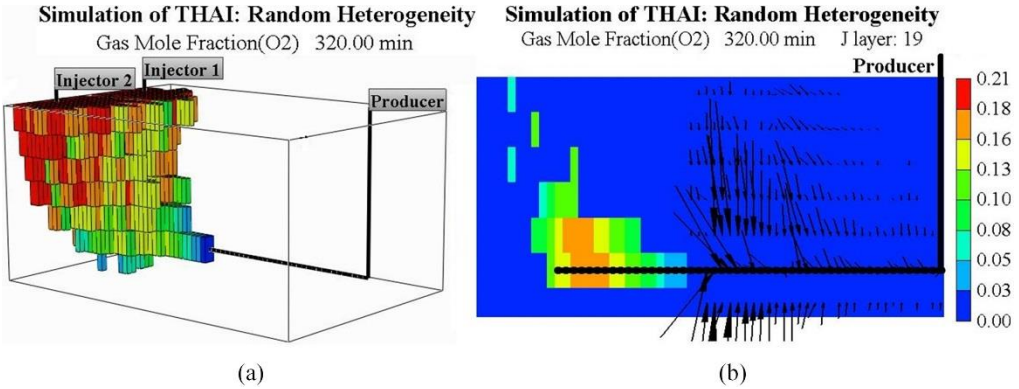

Fig. 6.11: Combustion front profiles (a) in three-dimension, and (b) along the vertical mid-plane x-z (J layer 19)

The shape of the combustion zone, at 320 minutes, is shown in Fig. 6.11a. It can be observed that the volume of the reservoir swept by the combustion front, as shown approximately by the oxygen profile, is smaller than when the absolute permeability is homogeneously 11500 md (Fig. 6.10ai) but is bigger than when the permeability is homogeneously reduced to 2875 md (Fig. 6.10aii). In both the homogeneous (Fig. 6.10a) and the heterogeneous (Fig. 6.11a) models, the 3D shape of the combustion front, in the radial direction away from the HP, is forward leaning, which is one of the indicators of stability. However, there is an increased penetration of oxygen along the HP, which shows that the process is tending to partial instability. Overall, the shape of the combustion front can be described as parabolic in the upper half of the sandpack, with a tendency to be a more wedge-like protrusion in the top- and bottom-most layers.

Along the vertical mid-plane, where the HP is located, a discontinuous oxygen distribution, from the top of the reservoir to the toe of the HP, can be observed (Fig. 6.11b). However, due to the uniform combustion front propagation from

the top to the base of the reservoir along the adjacent vertical planes, a large oxygen ‘cluster’ is formed around the toe of the HP. The same sized oxygen cluster is also observed in the homogeneous models, except that they do not have isolated oxygen zones, around the top of the reservoir, like in the heterogeneous models. The reason could be due to the use of the same absolute permeabilities along the HP in both the homogeneous and heterogeneous models. This, therefore, is expected to result in approximately the same extent of oxygen utilisation.

For the purpose of comparison, Fig. 6.12i shows the shape of the oxygen profile at the top horizontal plane for two homogeneous (11500 and 5750 md) and the heterogeneous models. Unlike the homogeneous case (Fig. 6.12ai & Fig. 6.12bi), the shape of the combustion front, for the heterogeneous case, is irregular and distorted (Fig. 6.12ci). This is due to the variability of the fuel concentration ahead of the combustion front. It means that the process will be difficult to control, where the combustion front progressively advance towards, and along, the low fuel concentration zone thereby forming oxygen fingers. Once the combustion front reaches highest permeability zones which directly connect to the HP, oxygen breakthrough could occur. This would lead to unsafe or uneconomical operation. However, these are not observed in this current study, since the oxygen utilisation efficiency is 95.4% for the homogeneous high permeability reservoir and 95.1% for the heterogeneous reservoir. The slight decrease in the oxygen utilisation can be explained by the difference in the average fuel availability. The average fuel availability, for the 11500 md homogeneously permeable reservoir, is 56.1 kg m^{-3}, which is 3.9 kg m^{-3} higher than that for the heterogeneous reservoir.

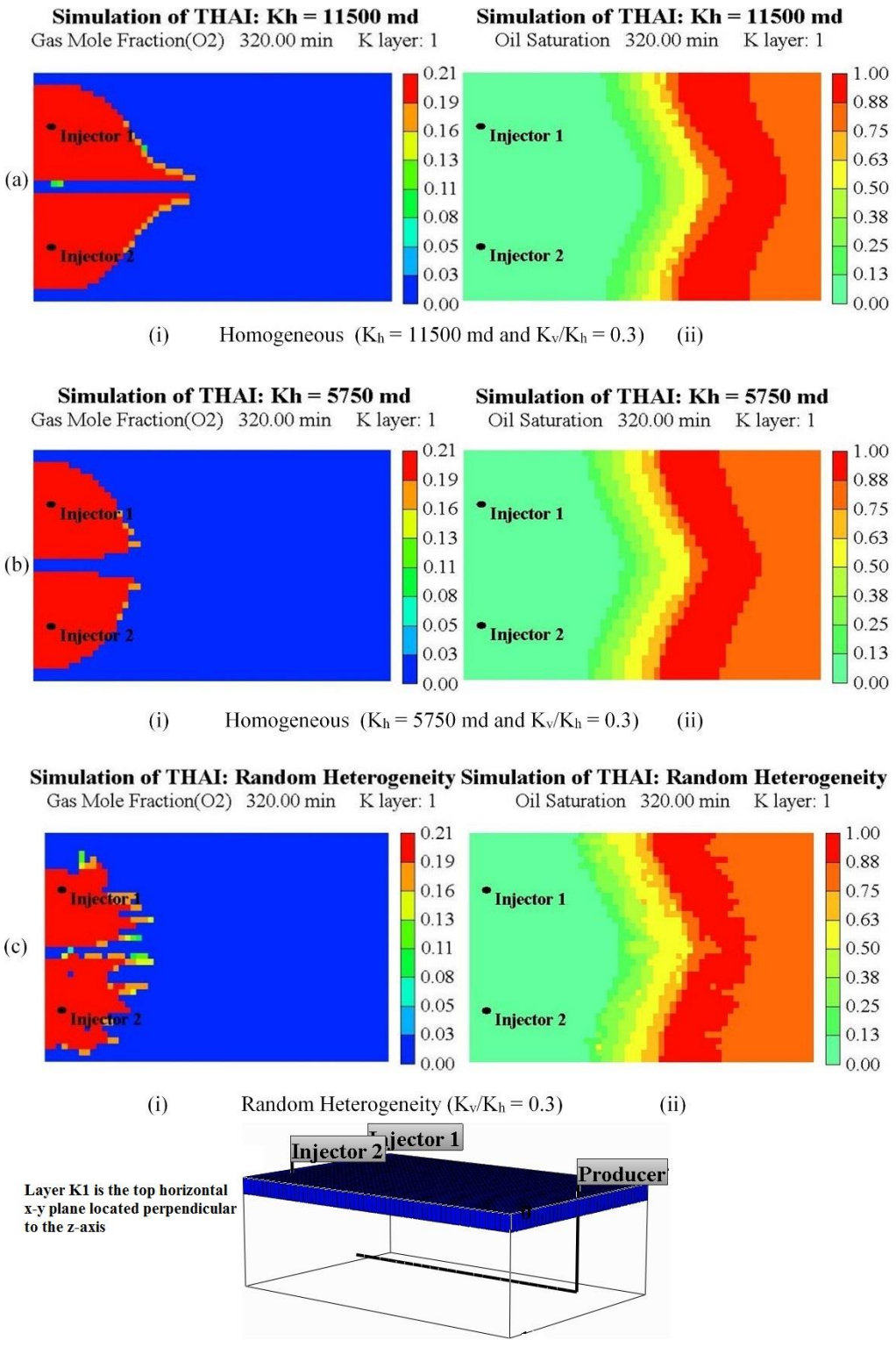

Fig. 6.12: (i) Oxygen concentration, and (ii) Oil saturation profiles along the top horizontal x-y plane (K layer 1)

The oil saturation profiles show that the areal displacement of oil is higher at the higher permeability, decreasing with decrease in permeability (Fig. 6.12aii &

Fig. 6.12bii). The oil flow pattern in the heterogeneous reservoir is quite tortuous (Fig. 6.12cii). The oil recovery, after 320 minutes of combustion, is 29.8 %OOIP for the heterogeneous model, which is 4.1 %OOIP and 0.8 %OOIP lower than in the case of homogeneous reservoirs with horizontal permeabilies of 11500 md and 5750 md respectively.

Since the oxygen utilisation is approximately the same regardless of whether heterogeneity is incorporated in the model or not, it follows that the presences of the level of heterogeneity studied here has negligible effect on the THAI process. Similar conclusion can be drawn by considering the fact that the oil recovery, for the 5750 md homogeneous reservoir and that for the heterogeneous reservoir are roughly the same.

6.3.1.3 Two Phase Permeability Reservoir

The 3D shape of the combustion front predicted by P_{30} (Fig. 6.13a) is essentially vertical, filamentary and swept larger portion of the reservoir compared to that predicted by P_{60} (Fig. 6.13b). This is because the ease with which the mobilised fluid flows is decreased with increase in the probability of finding the low permeability zones. The models show that the shape of the combustion front is determined by the dominant phase (i.e. low or high permeability). When the dominant phase is highly permeable (i.e. P_{30}), the combustion front preferentially propagates via the high permeability zones thereby bypassing the low permeability regions (Fig. 6.13c). On the contrary, when the reservoir is populated by low permeability zones (i.e. P_{60}), the combustion front becomes less channelized and propagates evenly via the low permeability zones (Fig. 6.13d). Fig. 6.13e shows the tortuous and quasi-vertical shape of the combustion front along the vertical mid-plane. Both at the top and along the HP near the

base of the reservoir, the combustion front has the same velocity. However, in model P_{60}, the advance rate of the combustion front along the HP is higher than at the top of the reservoir (Fig. 6.13f). It shows that the combustion front is backward leaning. The wedge-like protrusion of the combustion front into the HP, predicted by P_{60}, is caused by the continuity of the high permeability zones along the HP. Because the speed of the combustion front is controlled by the dominant phase, the presence of continuous high permeability zone in the midst of large proportion of low permeability zones would cause the combustion front to become channelized. It, therefore, follows that oxygen production would increase with the increase in the probability of finding low permeability zones.

To investigate further, a comparison of the plots of oxygen mole fraction as a function of combustion time for the two different models was made. The plot shows that oxygen breaks through earlier when the reservoir contains large proportion of low permeability zones. The oxygen utilisation efficiency at the end of the 320 minutes combustion period for P_{60} is 89.1%, which is lower than for P_{30} by 5.8%.

The oil flux vectors superimposed on Fig. 6.14a shows an ordered uniform oil drainage pattern compared to when the proportion of the low permeability zones is increased (Fig. 6.14b). In addition, the flow pattern for P_{60} is asymmetrical despite the use of two vertical injectors. It can be observed from Fig. 6.14b that there is still significant amount of oil to recover around the ‘‘Injector 2’’. The oil recovery at the end of the 320 minutes of combustion is 23 %OOIP for P_{60} which is 6.3 %OOIP lower than that for P_{30}. This is quite similar to the observation made earlier that oil recovery decreases with the decrease in mobilised oil flow rate, which decreases with the decrease in permeability. It

follows that assuming an element of symmetry during reservoir simulation could significantly results in over-estimation of the oil production. Therefore, in order to obtain reasonably accurate simulation results, the full pattern should be simulated.

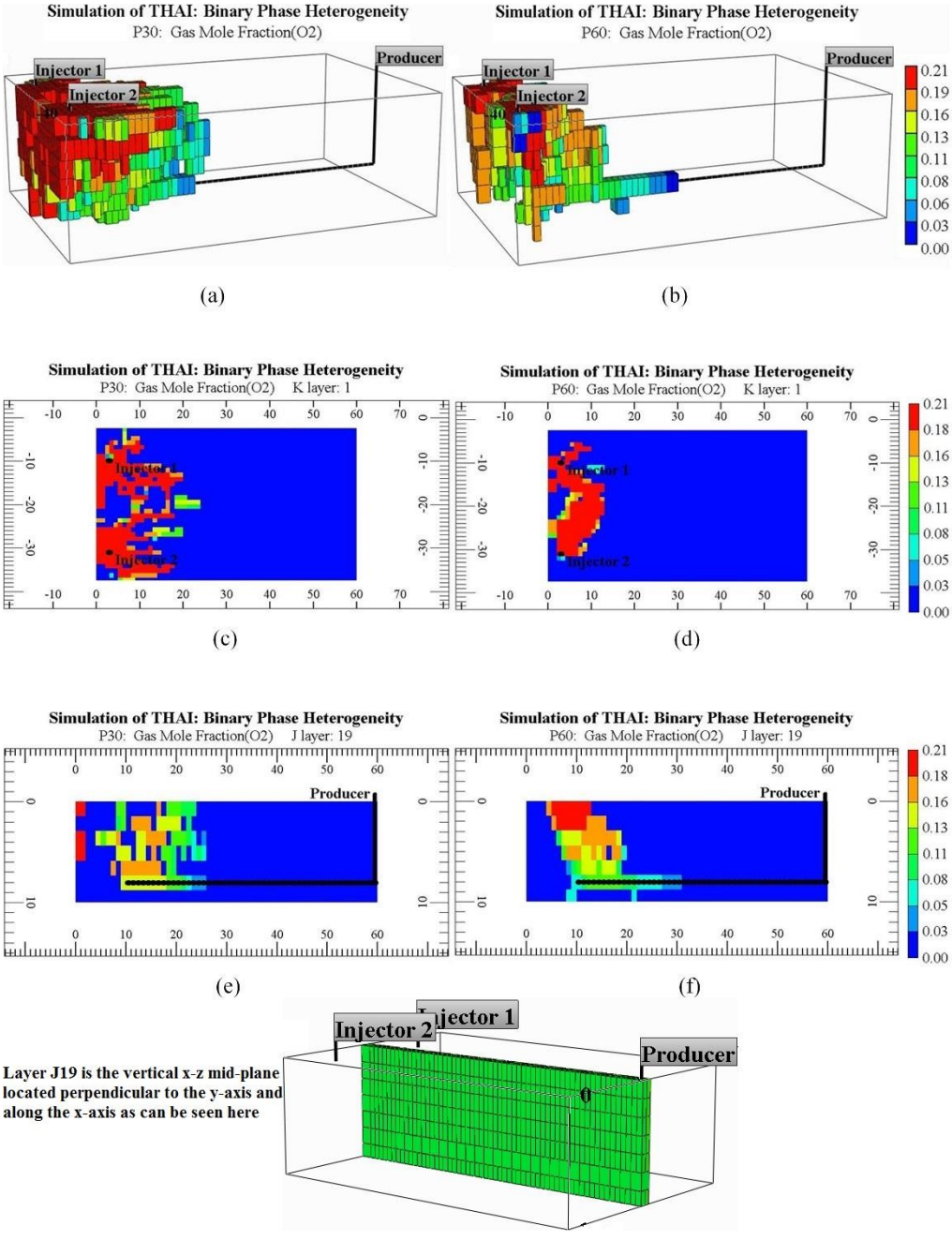

Fig. 6.13: 3D shape of combustion front for (a) P30, and (b) P60, oxygen concentration profile along the top horizontal layer for (c) P30 and (d) P60, oxygen concentration profile along the vertical mid-plane for (e) P30 and (f) P60 at the end of 320 minutes of combustion.

This also shows that the performance of the THAI process is affected by the proportion of low permeability zones presence in the production zone. This is because as the percentage of the low permeability zones is increased, say from P_{30} to P_{60}, the advancement and hence the bulldozing effect of the combustion front is restricted. This, in turn, limits the volume of oil mobilised and drained into the producer. Future work could investigate whether a change in the location of the producer well will result in an increased oil recovery.

The average peak temperature is observed to be higher for P_{30} (Fig. 6.14c) compared to in the case of P_{60} (Fig. 6.14d) model. This could be attributed to the high oxygen utilisation and the fact that more fuel is available in the case of P_{30} (i.e. 57.7 kg m^{-3} which is 15 kg m^{-3} greater than that generated in the case of P_{60}).

In summary, it can be deduced that the shape of the combustion front and, thus, the volume of reservoir swept, depends on the dominant phase (i.e. low or high fraction of low permeability zones). Oxygen utilisation efficiency is low in a channelized reservoir (i.e. high presence of low permeability zones). However, the presence of the discontinuous low permeability zones does not adversely affect the performance of the THAI process except where a long continuous low permeability zone is formed. This, then inhibits the flow of mobilised oil.

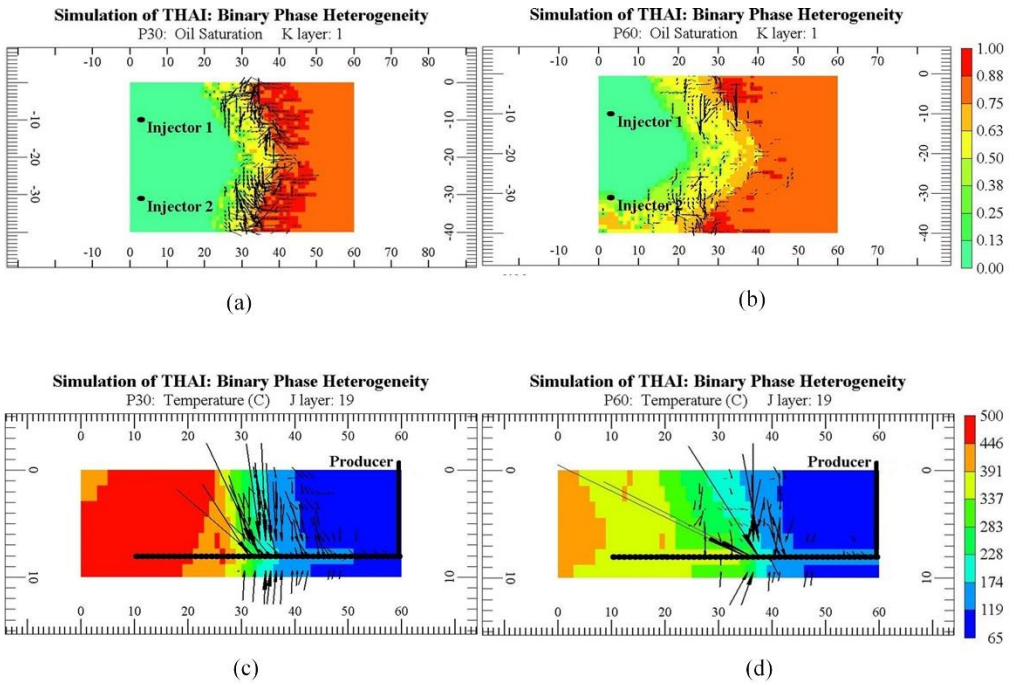

Fig. 6.14: Oil saturation profile along the top horizontal plane for (a) P30, and (b) P60, temperature distribution profile along the vertical mid-plane for (c) P30, and (d) P60 at the end of 32minutes of combustion.

6.3.1.4 Shaly Reservoir

In this section, the results of the simulation of shaly reservoir is presented. The permeability field of the realisation is such that the probability (PS_{30}) of finding shale at any given point is taken to be at most 30%. As a result, the reservoir has the same realisation as that shown in Fig. 6.2a with the exception that the low permeability zones are now shaly zones.

The oxygen concentration profile for the shaly reservoir (PS_{30}) is quite similar to that shown in Fig. 6.13c and fairly tortuous as the combustion propagates along the permeable zones (Fig. 6.15a). However, as the combustion is forced to propagate along the permeable zones only, it has to travel extra distance in all directions in order to sweep the same reservoir volume as in the case of P_{30}. That is why along the vertical middle plane, at the end of the 320 minutes of

combustion, the combustion front covered 30 cm (Fig. 6.15d) which is 5 cm high than the distance it covered in P_{30} (Fig. 6.13e).

The presence of impermeable zones results in the decrease in the overall oxygen utilisation from 94.9 % in the presence of low permeability zones to 94.0 % in the presence of shales. However, there is no evidence suggesting oxygen breakthrough due to preferential channelling into the production well. For the same realisation, fuel availability decreased from 57.7 kg m^{-3} in P_{30} to 52.0 kg m^{-3} when impermeable zones are present. This could explain why there is a slight difference in the oxygen utilisation.

Fig. 6.15b shows that presence of shales results in asymmetrical temperature distribution. The combustion preferentially propagates on the area less populated by the presence of shales. Comparing the temperature distributions along the vertical middle plane, it can be observed that the presence of shale results in a decrease in the peak temperature (Fig. 6.14c and Fig. 6.15e). This is due to the high specific heat capacity of sand compared to that of oil.

From Fig. 6.14a and Fig. 6.15c, the oil saturation profiles along the top horizontal plane can be compared. It can be observed that the profiles are quite similar except that when the shale is introduced, high volume of reservoir is swept for the same air injection. Also, in the case of the shaly reservoir, there are closed zones where the trapped oil is irrecoverable even though the oil is heated by conduction. As a result, the oil in these zones is coked. This will significantly reduce the quantity of oil that will be cumulatively recovered.

The oil recovery at the end of the 320 minutes of combustion for the shaly reservoir is 38.7 %OOIP which is 9.5 %OOIP higher than achieved in P_{30} model.

This shows that the presence of shale has resulted in an increased percent oil recovery compared to the 33.4 %OOIP realised in the base case experimental model, which is homogeneously permeable. However, for the same air injection, 1870 cm^3 of oil is cumulatively recovered in the presence of shale compared to the 2015 cm^3 recovered from the P_{30} model and 2310 cm^3 recovered in the base case. It shows that discontinuous shale distribution in the reservoir results in larger air to oil ratio. It should be noted that this study did not extend into looking into the effect of larger or lower proportion of shale on the THAI process.

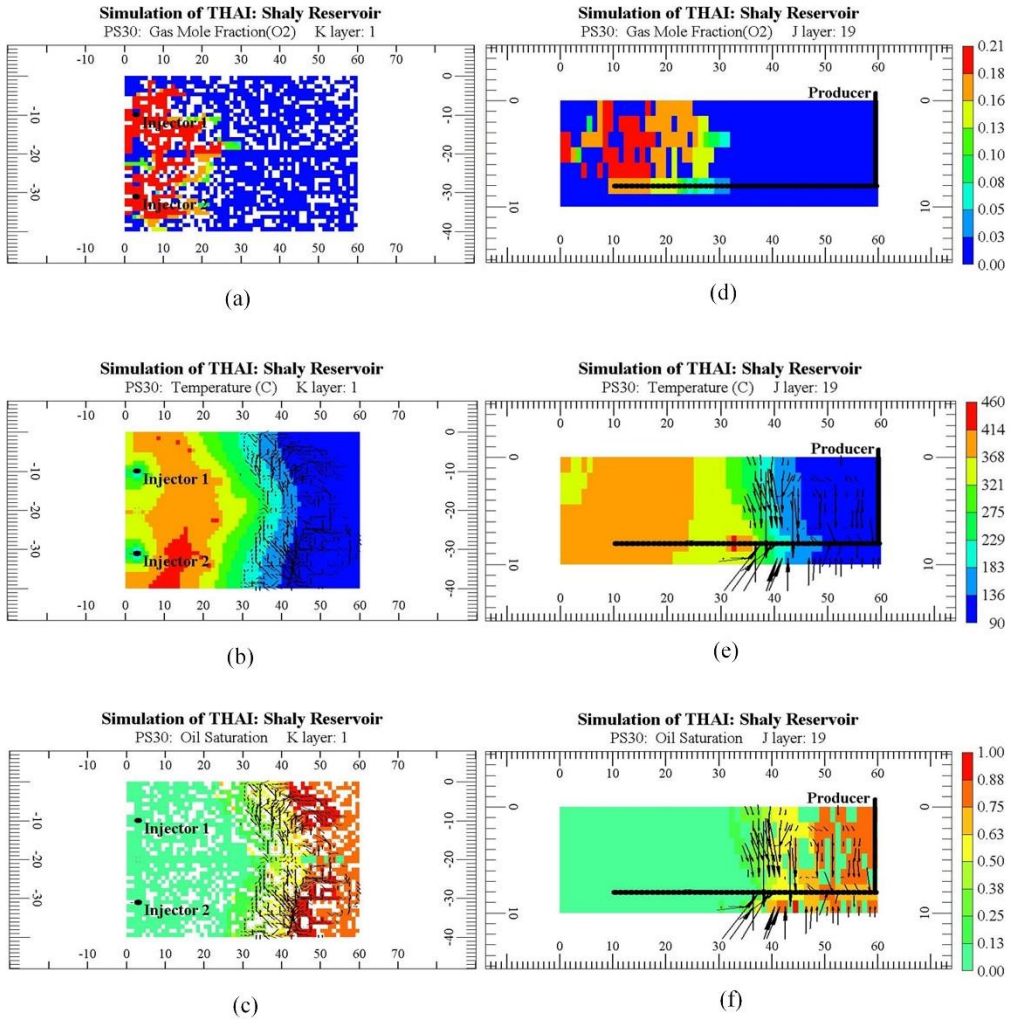

Fig. 6.15: Profiles along the top horizontal plane are (a) oxygen, (b) temperature, and (c) oil saturation, and profiles along the vertical mid-plane includes (d) oxygen, (e) temperature, and (f) oil saturation. The white phase on the oxygen and oil saturation profiles represent the shales.

6.3.1.5 Layered Reservoir

In this section, the result of the effect of gradual decrease or increase in permeability and hence porosity is discussed. Regardless of the absolute permeability assigned to the horizontal layer six, where the horizontal producer (HP) is located, the HP was assigned horizontal absolute permeability of 11500 md. As a result, all the models have the same permeability around the HP. In Fig. 6.16, the 3D shape of the combustion front shows a general trend: that the combustion is skewed and, thus concentrated in the highest permeability zones. This is because the resistance to fluid flow decreases with the increase in permeability. That is why the air preferentially flows to those zones.

For the HPC model (Fig. 6.16a), the combustion advance rate is highest along the central axis, in a toe-to-heel manner, thereby forming a funnel-like shape with the narrow end towards the heel. This shows that implementing THAI process with the wells arranged in an SLD manner, and the HP located in the highest permeability zone, would result in an unstable operation. This is because the combustion zone is increasingly tending towards the heel of the HP, which, if results in oxygen breakthrough, could be economically costly both in terms of production lost and safety. In terms of oil recovery, 41.9 %OOIP is recovered in the HPC model, which is due to the ease with which the mobilised oil flows to the producer well. Fig. 6.17a shows that most of the produced oil comes from around the central axis of the model, where the permeability is highest. Also, the HPC model shows no rich banked oil region (i.e. 80 – 100 % oil saturation) ahead of the high mobile oil zone (MOZ). Also, on either side of the central axis, where the permeability is lowest, there is still significant quantity of oil to be

recovered (i.e. oil saturation of 25 – 60 %). In addition to that, HPC model has the highest oxygen utilisation of 92.9 % (Tab. 6.1).

The combustion front in the LPC model splits along the central axis (i.e. toe-to-heel plane) and forms two nearly independent fronts, which can be broadly described as conical in shape (Fig. 6.16b). The narrow ends of each front is vertically downward towards the toe of the HP. Each of the fronts propagates stably in the high permeability zones on either side of the central axis. Around the toe, the combustion fronts recombine to form a wedge-like protrusion into the HP, where the front advances at faster rate compared to other parts of the fronts, tending to partial instability (Fig. 6.16b). However, the distance covered by the combustion front into the HP in the LPC model is 26 cm, which is considerably lower than that covered in the HPC model by 20 cm. This shows that implementing THAI process to recover oil from an LPC reservoir would provide safe operation as oxygen production is delayed. No coke is consumed along the central axis and directly above the HP due to the restriction to the fluid flow constituted by the presence of the smallest permeability in the reservoir.

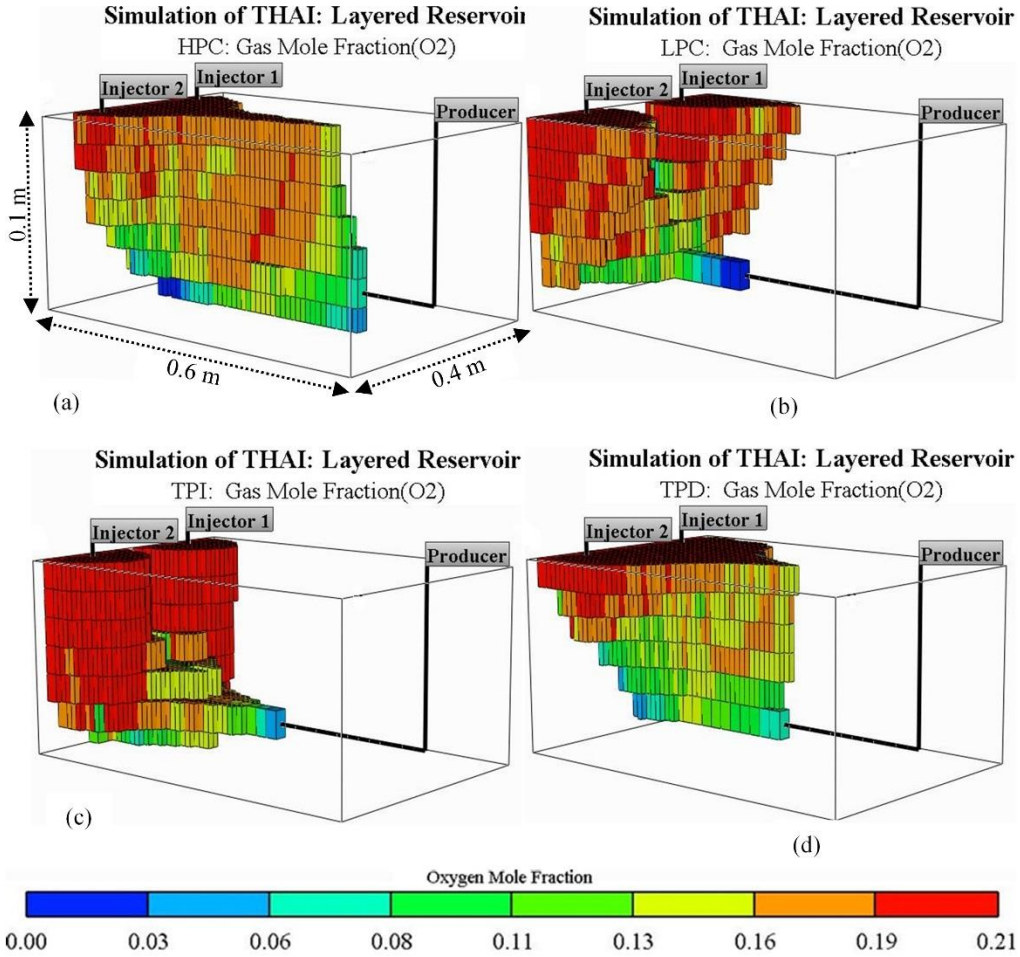

Fig. 6.16: 3D shape of combustion front for (a) HPC, (b) LPC, (c) TPI, and (d) TPD after six hours of combustion.

Tab. 6.1: Oil recovery, fuel availability, oxygen utilisation, and CAOR after 6 hours of combustion

Model	%OOIP Produced	%OOIP Recoverable	Fuel Availability (kgm^{-3})	$\%O_2$ Utilisation	CAOR (Sm^3m^{-3})
HPC	41.9	34.9	55.7	92.9	1427
LPC	36.6	41.5	53.8	92.2	1594
TPI	39.6	42.0	43.6	91.6	1524
TPD	38.9	35.2	62.4	92.4	1532

With the regards to oil recovery, 36.6 %OOIP is recovered in the LPC reservoir, which is lower than that recovered in HPC as can be seen in Tab. 6.1. This is due to the resistance, to the mobilised oil flow, provided by the low permeability central axis, which in chapter 4 was shown to be the main pathway through which the mobilised oil, at experimental scale, reaches the HP. Therefore, it is interesting to compare the oil saturation profiles of the two models (Fig. 6.17a & Fig. 6.17b). Unlike in the case of HPC, LPC contains a large zone of rich oil bank located ahead of the MOZ. More so, for the HPC, the shape of the MOZ is parabolic while in the case of LPC, it is aligned both horizontally and vertically. It follows that more of the mobilised oil could have been recovered if the permeability of the central axis is increased while keeping the cumulative air injected the same. Similarly, the oxygen utilisation in the LPC reservoir model is lower than that in the HPC reservoir by 0.7 %. This could be explain by the difference in fuel availability in which 1.9 kg m^{-3} less fuel is produced in the LPC compared to that in HPC (Tab. 6.1). It should be noted that there is more oil to be recovered in the LPC reservoir by 6.6 %OOIP than in the HPC reservoir (Tab. 6.1). This again confirms that the main negative effect that low permeability along the central axis has on the THAI process is lowering the quantity of mobilised oil reaching the producer well.

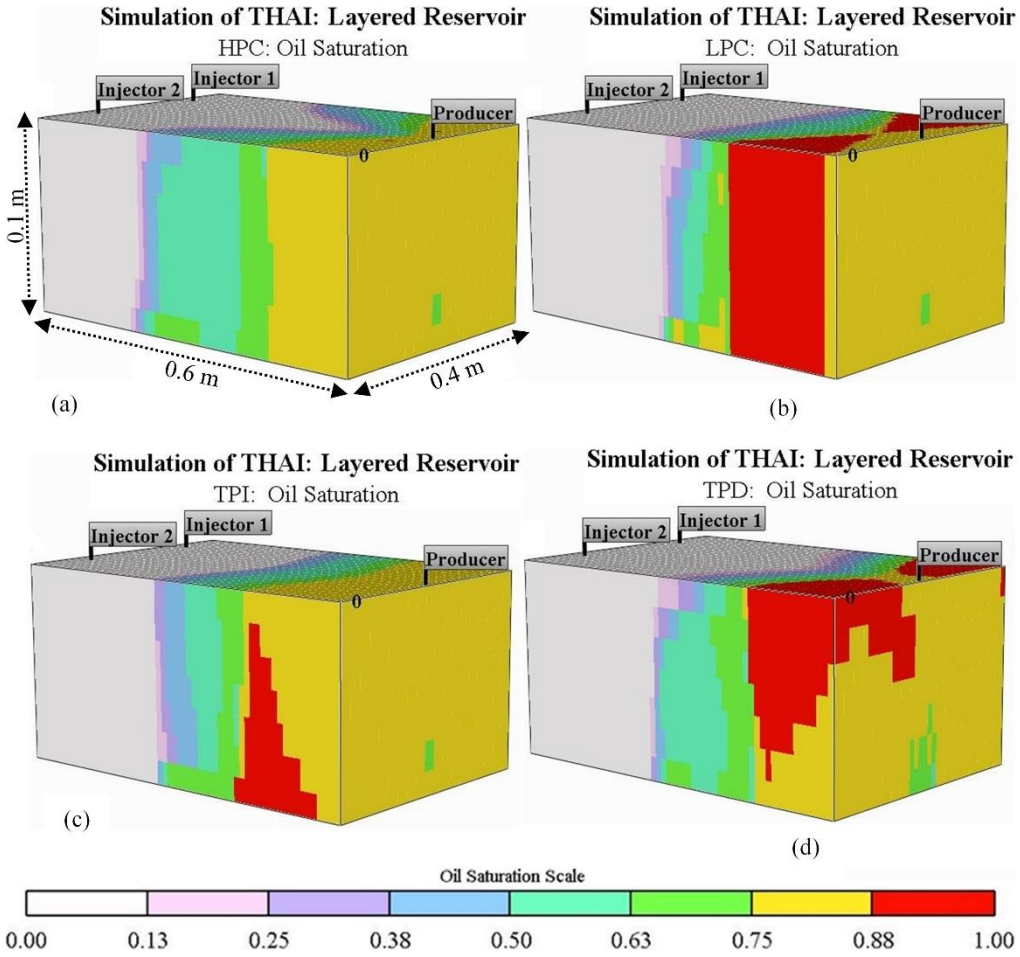

Fig. 6.17: 3D oil saturation profiles for (a) HPC, (b) LPC, (c) TPI, and (d) TPD after six hours of combustion.

In the TPI model, two independent combustion fronts, one around each vertical injector, were initially developed until around 60 minutes from the start of the combustion. The fronts propagates rapidly downwards while tilting towards the toe of the HP. This is because the permeability increases vertical downwards and therefore, it is more difficult for the fronts to propagate horizontally. Around the toe, the fronts combine and advances in the axial direction forming a wedge like protrusion into the HP. In the base of the reservoir, and two horizontal layers above that, the combustion front spreads laterally at higher rate to sweep a large area (Fig. 6.16c). This shows that deploying THAI process into this kind of reservoir would result in a partially stable operation due to the rapid

advancement of the combustion front inside the HP. At the end of six hours of combustion, the front inside the producer well has swept 46% of the well's total length. It, therefore, follows that the combination of this and the fact that the TPI model exhibits the lowest fuel availability among the four models should result in poor oxygen consumption. Overall, the TPI model predicted an oxygen utilisation of 91.6 %, which is the lowest among the four models. However, since the highest permeability is at the bottom of the reservoir, the mobilised oil in the TPI reservoir easily flows into the HP. It should be noted that THAI is a gravity stabilised process implying that the mobilised oil must be gravity drained to the base of the reservoir first before flowing into the HP. As a result, for the same cumulative air injected, more oil is recovered in the TPI than in the LPC reservoir (Tab. 6.1). Also, just like in the experimental model presented in chapter 4, the TPI model has rich oil bank ahead of the MOZ (Fig. 6.17c). In addition, the TPI predicted the highest percentage recoverable oil at the end of the six hours of combustion.

The shape of the combustion front in the TPD reservoir model (Fig. 6.16d) is quite similar to that in the HPC reservoir (Fig. 6.16a) except that the former is broader laterally and only covers 34 cm axially. The combustion zone is conical in shape with the narrow end pointing towards the heel of the HP. A large horizontal areal sweep is achieved around the vertical injectors implying that the highest permeability is located at the top horizontal plane. Comparing with the TPI (Fig. 6.16c), the combustion front in the TPD model did not reach the base of the reservoir showing that the bottom horizontal plane has the lowest permeability. At it is narrow end, the combustion front travels at, essentially, the same rate, which is an indicator of stability. Therefore, applying the THAI

process to this kind of reservoir should result in a stable operation. The predicted oxygen utilisation by the TPD model is 92.4% which is higher than that in the TPI model by 0.8% (Tab. 6.1). However, less oil is recovered in TPD by 0.7 %OOIP than in TPI. This could be explained by the restriction to mobilised oil flow into the HP caused by the presence of low permeability around the producer well. Among the four models, TPD has the highest fuel availability which is caused by increased residence time of the mobilised oil. Fig. 6.17d shows that ahead of the MOZ, a rich oil bank (saturation of 88 to 100 %) is formed in the TPD. Generally speaking, the displaced oil zones for the TPI (Fig. 6.17c) and TPD (Fig. 6.17d) models are quite similar. However, the rich oil bank is formed in the regions where the permeability is highest. Comparing the four models, it can be observed that the HPC model (Fig. 6.17a) has no rich oil bank as it is high permeability zone is directly above the HP.

6.3.2 Effect of Bottom Water on THAI

6.3.2.1 Thickness of Bottom Water

Under this section, the result of the effect of bottom water thickness on the THAI process is discussed. As mentioned in section 6.2.2.1, model BW1 has a bottom water (BW) thickness of 6 m which is 25% that of the oil layer (OL). In the case of model BW2, the thickness of BW is 12 m, making it 50% that of the OL. However, to assess the performance of these two models, their oil production rate and the cumulative oil recovery must be compared with the base case model (BW0). In all the three models (BW0, BW1, and BW2), steam was injected at the rate of ≈ 500 bbl day^{-1} for a period of 104 days. The combustion was run for two years by continuously injecting 20000 Sm^3 day^{-1} of air.

In BW0, which contains no bottom water, oil production began 60 days after the start of the PIHC. Fig. 6.18 shows that the presence of BW delays the oil production by 4 days in model BW1. In the case of BW2, the oil production only began after 190 days from the initiation of air injection. Throughout the PIHC, model BW0 lies above BW1 and BW2. However, on air injection, model BW1 exhibits a similar characteristic as BW0 in terms of a brief surge in the oil rate. This is cause by the displacement of already mobilised oil by the injected air. At around 210 days, the oil production rate in BW0 steadied out at ≈ 35 m^3 day^{-1} up to the end of the combustion period. For BW1, the oil rate, over 130 to 210 days, is maintained at 20 m^3 day^{-1}. The oil rate then increases steadily to reach a peak of 47 m^3 day^{-1} at 300 days before it declines and remains at a constant value of 32 m^3 day^{-1} between 470 and 530 days. At point A' (i.e. 530 days), indicated by the blue arrow, the oil rate dropped to almost zero for a period of 4 days before it picked up and increased to 30 m^3 day^{-1} at 834 days. Between 250 and 340 days, there is a steady increase in the oil rate in BW2 from 3 to 30 m^3 day^{-1}. From 340 to 470 days, the oil rate slightly increased to 32 m^3 day^{-1}. Similarly, just like in the case of BW1, BW2 also has a period of no oil production, which occurred at point B' (i.e. 470 days), indicated by the green arrow. Beyond point B', the oil rate increased slowly to 21 m^3 day^{-1} at 834 days. Overall, Fig. 6.18 shows that the oil production rate in the THAI process is adversely affected by the presence of BW. The severity of the negative effect the BW has on the THAI process depended on the thickness of the BW.

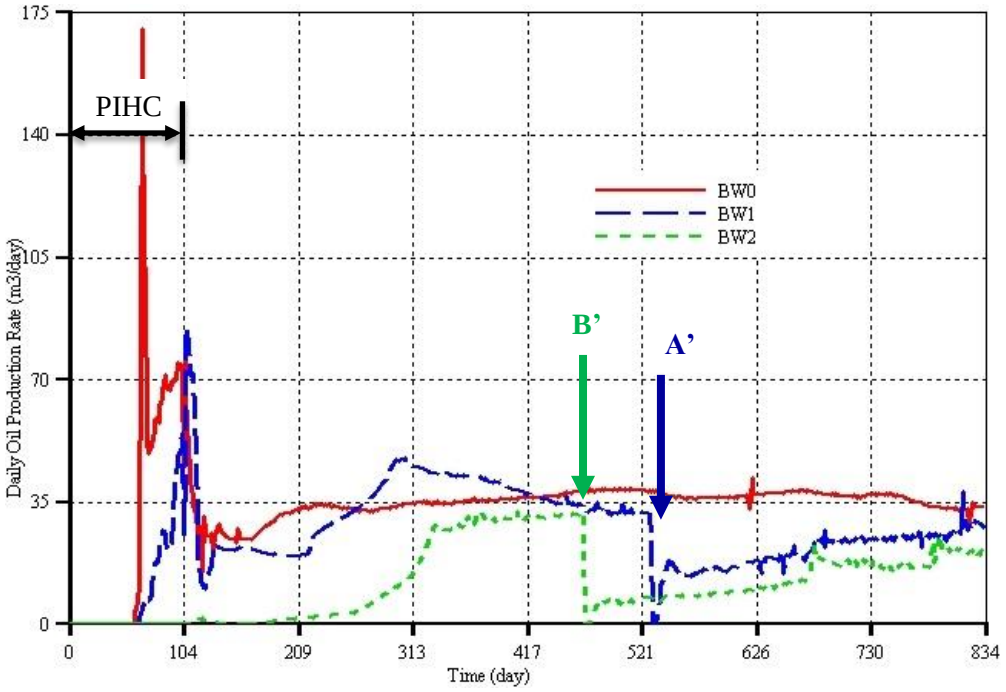

Fig. 6.18: Daily oil production rate at different BW thickness

Fig. 6.19 shows that the water production rate predicted by model BW0 lies below that of models BW1 and BW2 throughout the duration of the process. This is because only the native reservoir water and that condensed from the combustion flue gas is being produced. During the PIHC, models BW1 and BW2 has essentially the same water production rate, which indicates that nearly the same quantity of oil is mobilised by the steam. The large mobility contrast between oil and water means that the latter is forced to flow to the producer well. As BW2 overlies BW1 throughout the combustion period, it follows that the thicker the BW, the higher the water production rate. This is supported by the earlier observation showing that BW2 has lower oil production rate (Fig. 6.18). As will be shown later, the thick the BW zone, the larger the quantity of the mobilised oil that get trapped. An interesting trend in Fig. 6.19 is the presence of a period of surge in water production rate displayed by both BW1 and BW2 models. Curiously, the periods, marked point A and B for BW1 and

BW2 respectively, correspond to the periods of sharp drop in oil production rate discussed previously. The sudden rise and fall in water and oil rates respectively, and their respective gradual decrease and increase are caused by the drainage of the mobilised oil into the BW zone. This happens when the mobile oil zone (MOZ) approaches the 'end of the drained oil zone'. Further detail is provided latter.

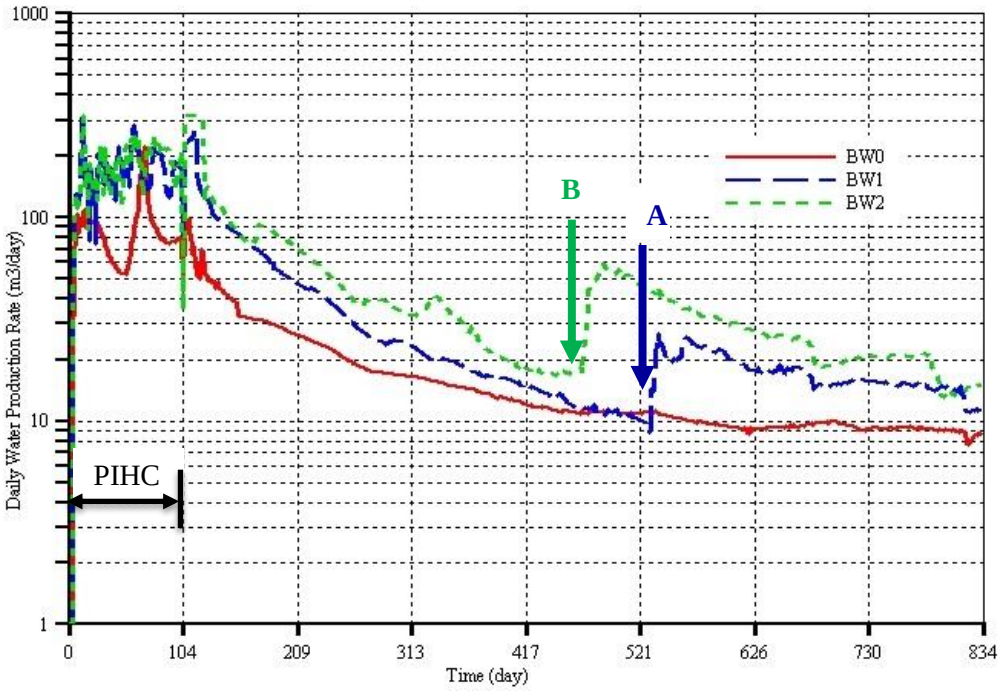

Fig. 6.19: Daily water production rate at different BW thickness

Fig. 6.20 shows the plot of cumulative oil production for the three different models. It is observed that for the same air injection rate (and hence the same cumulative air injection), the cumulative oil recovered depends strongly on the thickness of BW zone. When the BW thickness is a quarter of the OL thickness (i.e. BW1), the cumulative oil recovered decreased from 28420 m^3 in BW0 to 21660 m^3, which is a 24 % decrease. A further increase in the BW thickness to half that of the OL thickness (i.e. BW2) resulted in a decrease in the cumulative oil production by 65% of that recovered in BW0. This shows that an increase

in the BW thickness by a factor of two caused a reduction in the cumulative oil production by a factor of 3. Also, the periods of sharp decline in oil production could be observed on the cumulative oil curves BW1 and BW2, where they are marked by the sudden decrease in the slope of the curves (Fig. 6.20).

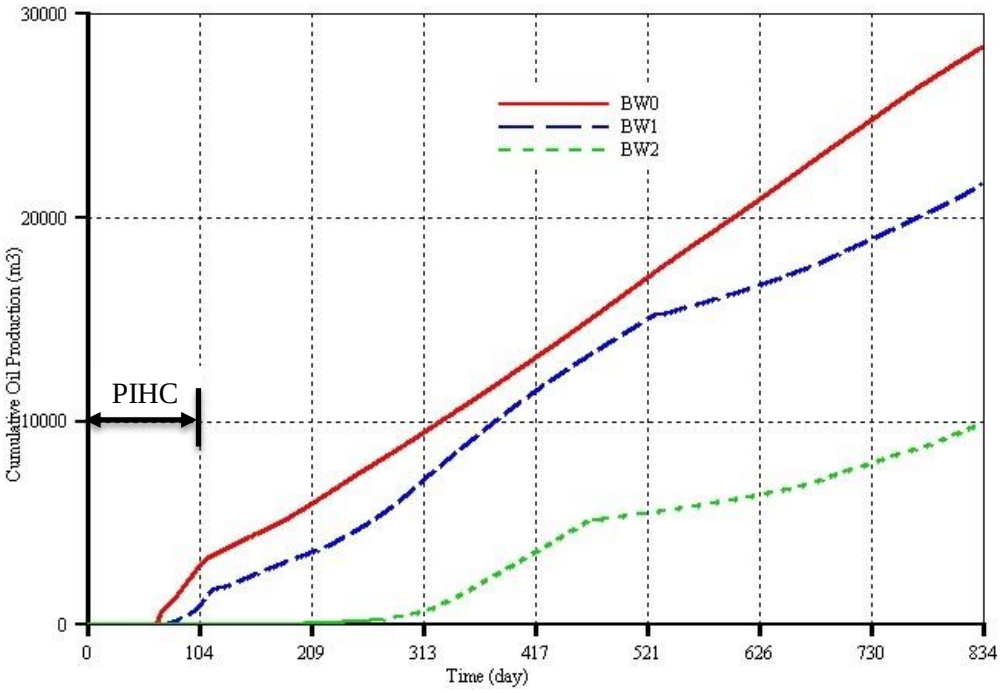

Fig. 6.20: Cumulative oil production at different BW thickness

The two models, BW1 and BW2, have similar shape of combustion fronts, which propagate stably and are restricted to the upper part of each reservoir, within the oil zone (Fig. 6.21a & Fig. 6.21b). Since the combustion fronts did not reach the toe of the HP in either case, and swept the same volume of reservoir, it implies that the thickness of the BW zone does not affect the combustion zone. This could be because of the presence of accumulated drained-oil around and just below the toe of the HP. Again, Fig. 6.21c and Fig. 6.21d show that, along the vertical mid-plane, the combustion fronts, regardless of the thickness of the BW, have approximately the same areal sweep. The fronts are forward leaning indicating that implementing the THAI process in BW

reservoir would result in a stable combustion initiation and propagation. However, despite this, the quantity of oil recovered depends on the BW thickness.

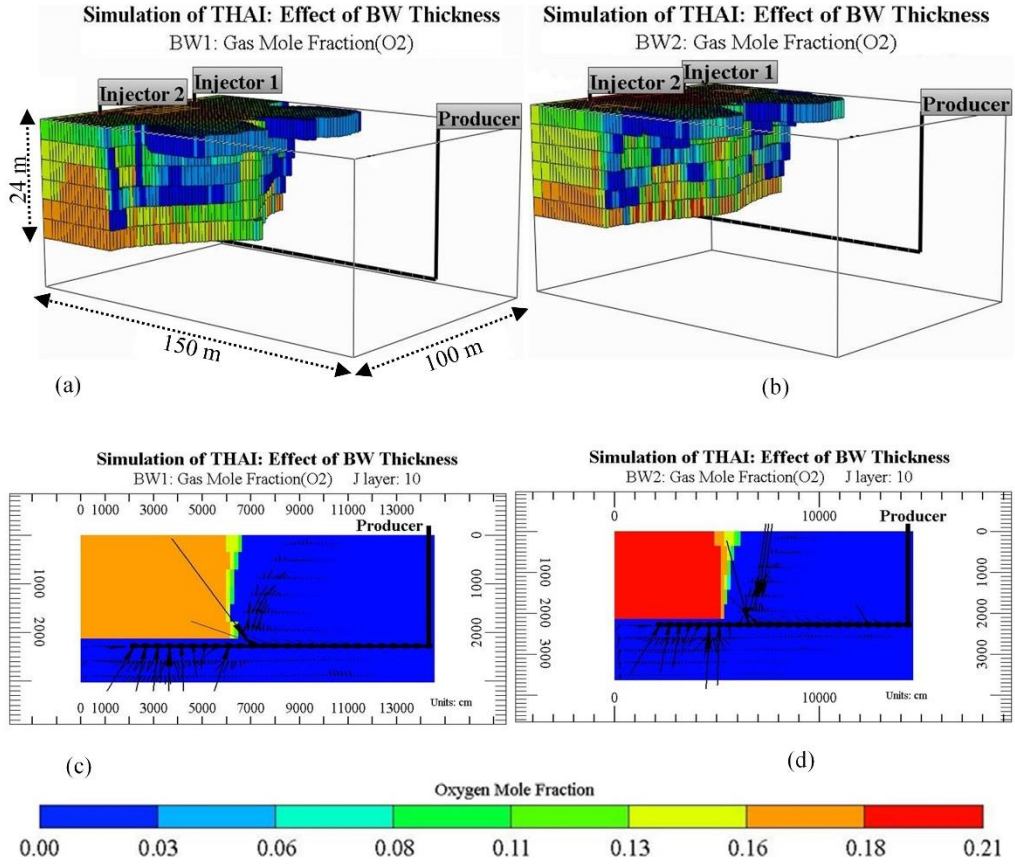

Fig. 6.21: 3D shape of combustion front for (a) BW1 and (b) BW2, and oxygen mole fraction profile along the vertical mid-plane x-z (J layer 10) for (c) BW1 and (d) BW2 all after two years of combustion

Since THAI is a gravity stabilised oil recovery process, it is natural to expect the oil flow to be downward directed such that the presence of HP near the base of the reservoir would enhance the oil recovery rate and hence increase the quantity of oil recovered. However, it has been observed to not always be the case where the reservoir contains bottom water. Despite placing the HP at the oil-water interface in both models BW1 and BW2, significant quantity of the mobilised oil in either case is not recovered. Rather, the oil drained into the BW zone regardless of the thickness of the latter (Fig. 6.22a and Fig. 6.22b). As a

consequence, water is displaced from the BW zone, and because of it is higher mobility ratio, compared to that of oil, the water is produced. That is why oil production only begins when the height of the accumulated mobilised oil in the BW zone equates to that of the displaced water from the BW zone. Therefore, as seen in Fig. 6.18, it can be drawn that the thicker the BW zone, the longer it takes before oil production begins in the BW THAI process.

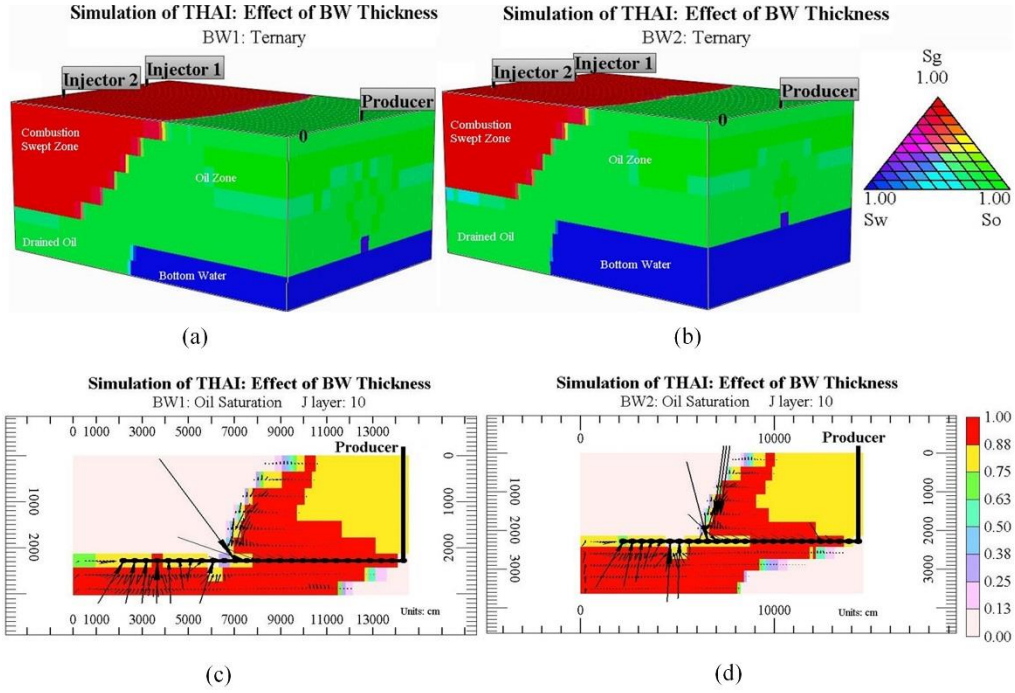

Fig. 6.22: Ternary diagram for (a) BW1 and (b) BW2, and oil saturation profile along the vertical mid-plane for (c) BW1 and (d) BW2 all after two years of combustion

From the ternary diagrams (Fig. 6.22a & Fig. 6.22b), it can be observed that the drained oil cannot be produced with THAI process implemented in it is conventional form. This is so most especially when the fact that the accumulation of the drained oil below the HP is considered. Also, the momentum from the injected and flue gases is not enough to force the oil to flow upward into the HP. The upward directed vectors, shown superimposed on the oil saturation profile along the vertical mid-plane, reveal that some of the

drained oil flows upward into the HP (Fig. 6.22c & Fig. 6.22d). However, closer observation reveals the cause to be the continuous gravity drainage of oil from the lateral vertical planes adjacent to the vertical mid-plane. The energy transfer from the inflowing mobile oil, from either side of the vertical mid-plane, forces the drained mobile oil to flow upward into the HP. Comparing the oil saturation profiles of BW1 (Fig. 6.22c) and that of BW2 (Fig. 6.22d) shows that larger quantity of oil is lost to the BW zone of the latter. This is reflected in the oil production rate (Fig. 6.18) and the cumulative oil recovered (Fig. 6.20).

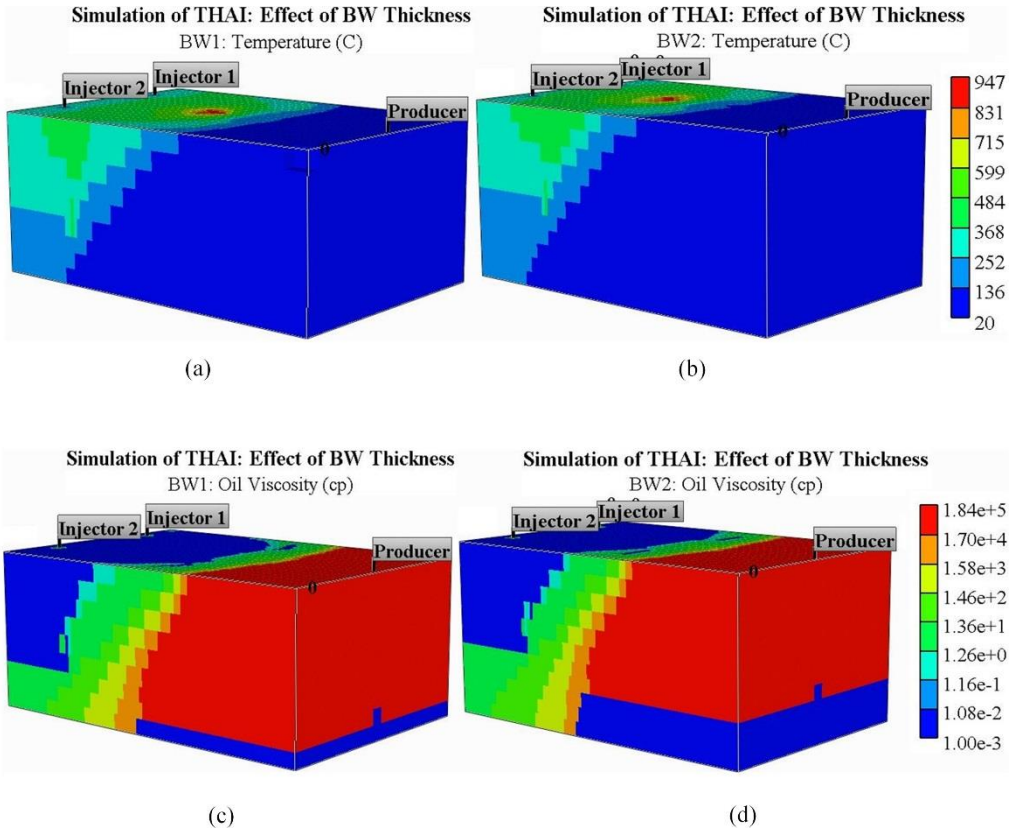

Fig. 6.23: 3D temperature profile for (a) BW1 and (b) BW2, and 3D viscosity distribution for (c) BW1 and (d) BW2 all after two years of combustion

The three dimensional temperature profiles for both models BW1 and BW2 exhibit similar characteristic (Fig. 6.23a & Fig. 6.23b), namely the combustion front in each case is restricted to the upper portion of the reservoir. Furthermore, they showed that there is heat transfer into the BW zone, mostly where the

drained oil accumulated. As a result, the heat is dominantly transferred via convection. Inside the BW zone, the temperature of the drained oil ranges from 136 to 252 ^{o}C implying that the oil should be mobile. From the oil viscosity profiles for models BW1 (Fig. 6.23c) and BW2 (Fig. 6.23d), the affected zone, from the heat due to combustion, where the oil has some mobility, can be observed. Broadly, the viscosity of the drained oil in both models ranges from 1.26 to 1580 cp. These values show that the oil is mobile since the typical viscosity of the THAI produced oil from the field is up to 10^4 cp (Petrobank, 2008).

Therefore, it is safe to infer that if the THAI process is to be run until all the oil inside the BW reservoir is fully mobilised (i.e. viscosity is reduced to mobility level), at least 25 %OOIP for the case of BW1 or 50 %OOIP in the case of BW2 will not be produced. It will remain sunk into, and trapped in the BW zone. Therefore, a new strategy, such as moving the horizontal well up into the oil layer zone, relocating the horizontal well, etc. needs to be explored to maximise the oil production rate and lower the water production rate.

6.3.2.2 Location of the Horizontal Producer

As surmised in section 6.2.2.2, and discussed in section 6.3.2.1 above, the success, or otherwise, of the THAI process, when implemented in a BW reservoir, could heavily be determined by the location of the HP. Therefore, three models were run to investigate the more appropriate location of the HP that would enhance the performance of the THAI process. The result of such an exercise is discussed herein.

In each of the three models, there is no oil production during the PIHC (Fig. 6.24) which is contrary to what was observed in the reservoir containing no bottom water. Oil production begins at 104 days when the HP well is located 8 m above the oil-water interface (i.e. in model L1). This is because the mobilised oil surrounding the toe of the HP well is forced to flow into the HP by the inflowing oil from the adjacent vertical planes. However, the production only lasted for 40 days before it dropped to nearly zero at point A' and lasting until 190 days (Fig. 6.24). This is caused by the continual oil drainage into the BW zone. Beyond this, the oil rate in L1 increases gradually to 20 m^3 day^{-1} at 834 days, which is due to continuous inflow of oil from adjacent vertical planes forcing upward flow of mobilised oil into the HP.

When the HP is located at the oil-water transition zone (i.e. model L2), oil production begins at 104 days at a rate of 1.5 m^3 day^{-1} which is maintained until 124 days. Thereafter, the oil rate dropped to 0.25 m^3 day^{-1} until 190 days when it rapidly ascends to 29 m^3 day^{-1} at 335 days (Fig. 6.24). This happens when enough oil has surround the toe of the HP well and inflow of oil from the adjacent vertical plane forces upward flow of mobilised oil into the HP. The oil rate then slowly increases to 32 m^3 day^{-1} from 335 to 470 days (i.e. to point B'). At this point, a sudden drop in oil production rate occurs over a period of 4 days, which is followed by gradual increase in oil rate up to 834 days. Just like in L1 model, this happens when there is continual mobilised oil displacement into the BW zone in order to surround the section of the HP well previously occupied by the BW.

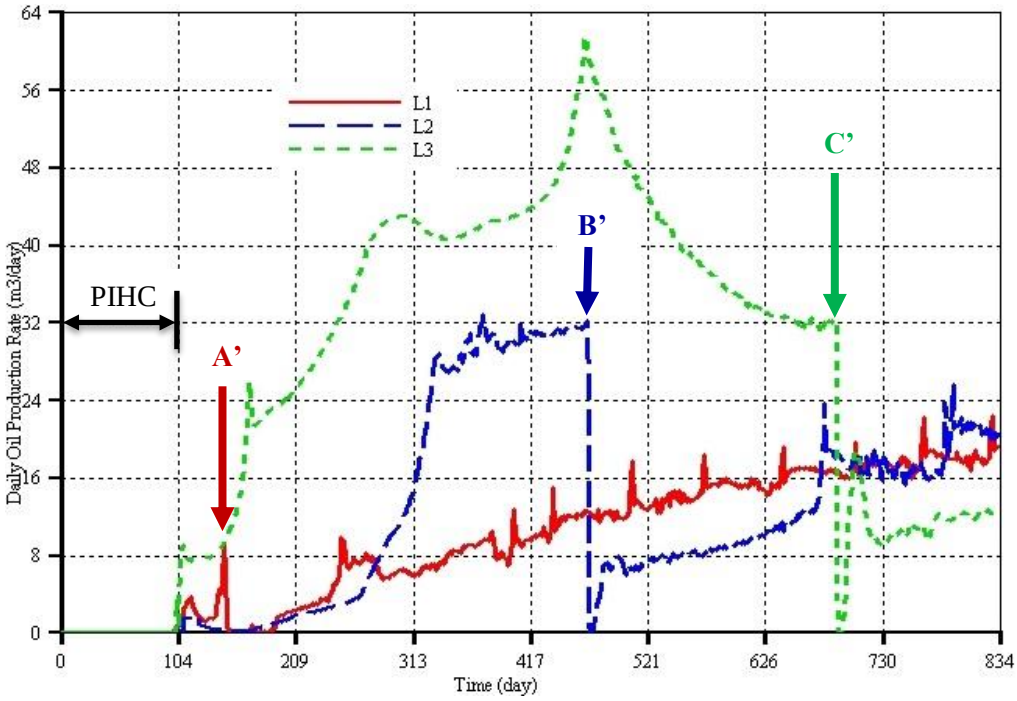

Fig. 6.24: Daily oil production rate for the different location of the HP well

With the HP well located 6 m below the oil-water contact (i.e. in model L3), oil production begins immediately at the end of the PIHC. This is because enough oil was already drained into the BW zone thereby surrounding the toe of the HP. The oil rate in L3 rises from 8 m^3 day^{-1} at 104 days to a peak value of 62 m^3 day^{-1} at 470 days before declining slowly to 32 m^3 day^{-1} between 655 and 690 days (Fig. 6.24). At point C' (690 days), the oil production rate drops suddenly to zero for a period of 4 days before it picks up to 16 m^3 day^{-1} at 706 days. It declines again and steadied out at 11 m^3 day^{-1} for the rest of the combustion period. From Fig. 6.24, four main observations can be made: (i) that the lower the HP well is located, the higher the oil production rate, (ii) that implementing THAI, in it is conventional form, in the BW reservoir results in a period of sudden drop in oil production regardless of where the HP well is located vertically, (iii) that points A', B', and C' are determined by how deep down the

BW reservoir the HP well is located, and (iv) that the deeper the HP well is located, the longer it takes before the sudden drop in oil production occurs.

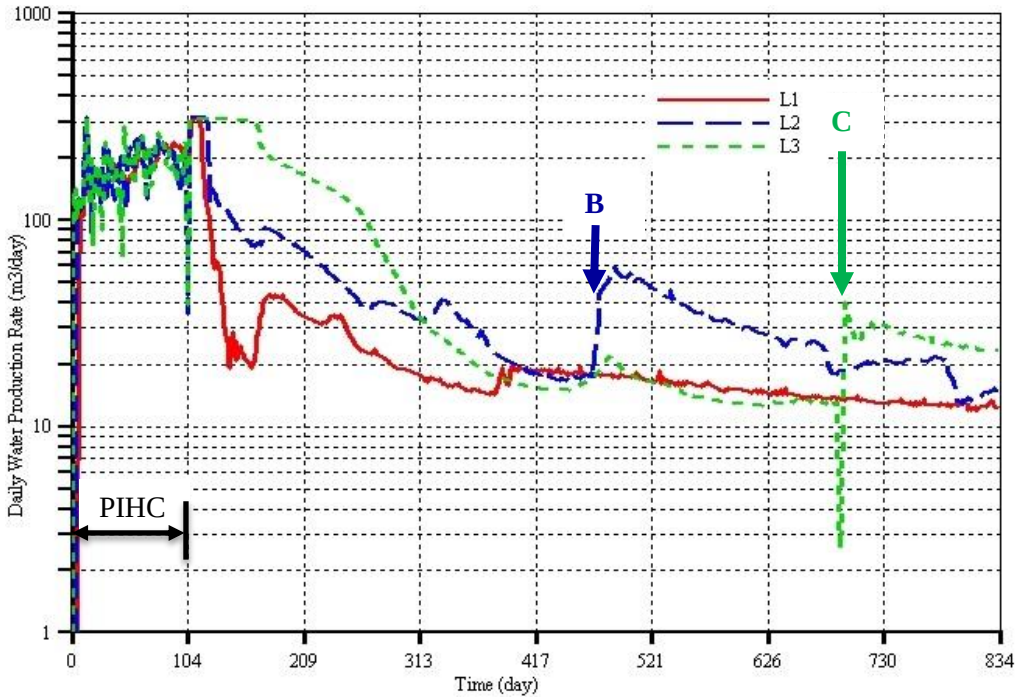

Fig. 6.25: Daily water production rate for the different location of the HP well

Regardless of the location of the HP well, the daily water production rate in each model averaged around 240 m^3 day^{-1} (Fig. 6.25) over the 104 days of the PIHC. This is due to the drainage of the mobilised oil into the BW zone, which displaces the water in the BW zone forcing it to flow into the HP well, and condensation of the pre-heating steam. Following air injection, the water rate peaked to around 305 m^3 day^{-1} for another two months when the HP well is located 6 m below the BW zone (i.e. for L3). From 104 to 315 days, the L3 water rate curve overlies both L2 and L1 curves indicating that more water has to be displaced before the mobilised oil reach the HP well. The periods of no oil production observed in Fig. 6.24 correspond to the periods of increased water production for L2 and L3 as can be seen marked by points B and C respectively (Fig. 6.25). Cumulatively, the volume of water produced increases with the

increase in depth at which the HP well is located. The cumulative water production, at the end of the two years of combustion are 36640, 50910, and 66520 m^3 for L1, L2, and L3 respectively.

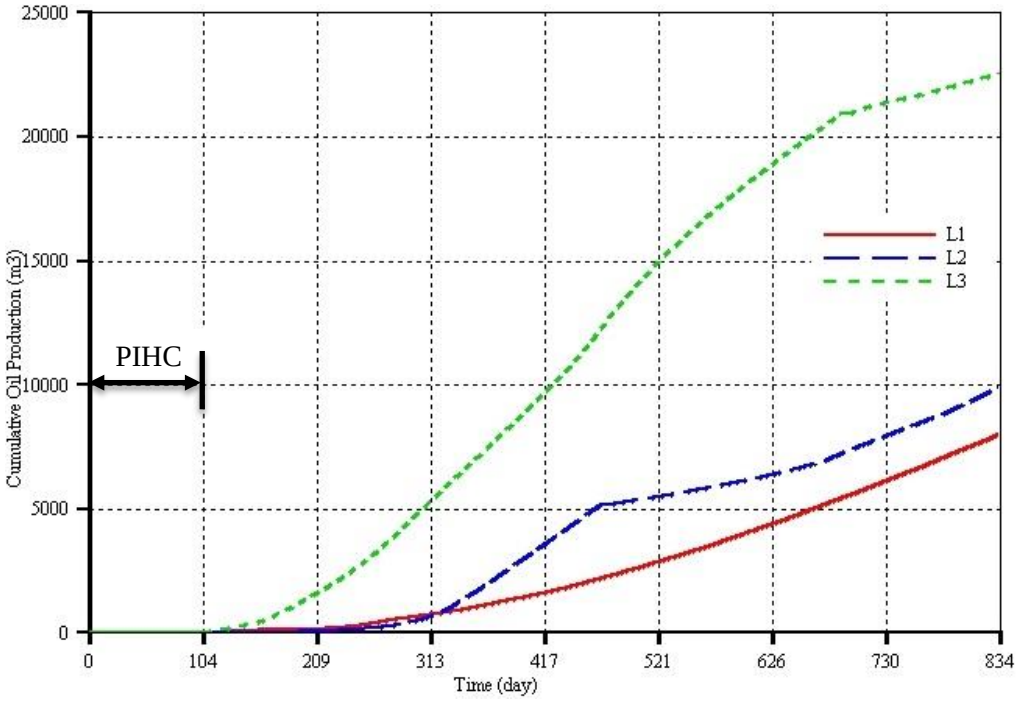

Fig. 6.26: Cumulative oil production for the different location of the HP well

In terms of the cumulative oil recovery, the simulation results show that, after two years of combustion, the highest recovery of 24.2 %OOIP is achieved when the HP is located inside the BW zone (i.e. model L3). The lowest recovery of 8.6 %OOIP is achieved when the HP is located inside the OL zone (i.e. model L1). Locating the HP well at the oil-water interface (i.e. model L2) resulted in a cumulative recovery of 10.6 %OOIP (Fig. 6.26). These observations are very similar to those made for SAGD by Sugianto and Butler, (1990) as summarised in section 6.2.2.2 earlier. Overall, it follows that by placing the HP well 6 m below the oil-water interface, an approximately three fold increase in oil recovery is realised compared to locating the HP well 8 m above, or at, the oil-water interface. However, the downside of operating THAI process with the HP

well drilled in the BW zone is the excessive water production, leading to increased water cut and, hence, an increased overall liquid production rate. It could also result in a high increase in pumping cost or larger diameter well requirement compared to that needed for L1 or L2 respectively.

The three phase (ternary) diagrams (Fig. 6.27) show in general that regardless of the location of the HP well, gravity drainage is the driving mechanism via which the mobilised THAI oil reaches the base of the reservoir, where the HP well is often located. Prior to the start of oil production in all the three models, it is observed that enough mobile oil must be displaced into the BW zone in order for an oil blanket to form around the HP well. Then, once the level of the drained oil reaches that of the water it replaces, an overall oil layer, which is directly communicated with the HP well, is formed. Consequently, Fig. 6.27a, b, and c show that below the toe region of the HP well, where the drained oil in each model accumulates, the superimposed oil flux vectors are upward directed into the HP. That is because of the transfer of potential/kinetic energy from the inflowing oil from the adjacent vertical planes. However, the higher the HP is located above the base of the BW reservoir, the larger the volume of the oil that becomes trapped below the HP well. This implies that more energy is needed to force the drained oil into the HP for production to the surface. Fig. 6.27c shows that the possible method to recover the gravity-drained trapped oil is by positioning the HP well as far below the oil-water interface as possible. However, this might not be a generalised inference most especially where the BW thickness is at least 100% of that of OL as will be shown later.

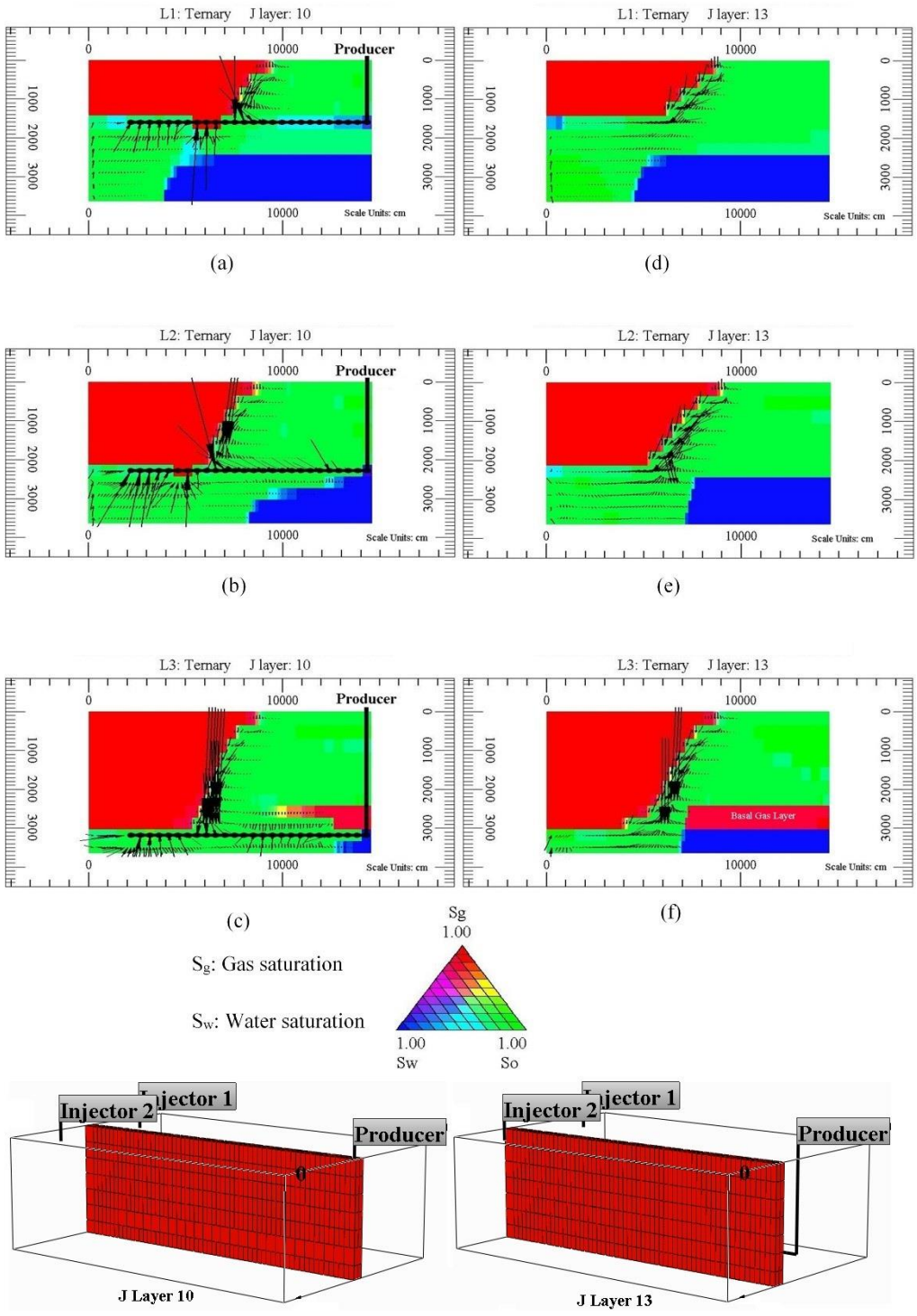

Fig. 6.27: Ternary diagram along the vertical mid-plane for (a) L1, (b) L2, and (c) L3, and along the vertical plane adjacent to vertical mid-plane for (d) L1, (e) L2, and (f) L3 and all after two years of combustion

The downward directed oil flux vectors above the HP well show that along the vertical mid-plane, the mobilised oil drained directly into the HP. However, depending on the number of grid blocks, at least 95 %OOIP comes from the

adjacent vertical planes in which the head of the oil flux vectors is downward-directed and backward-pointing (Fig. 6.27d, e, & f). This shows that the THAI process is operating in a stable mode. The revelation from the investigation of the effect of locating the HP well in the OL, the BW, and also at the oil-water interface is the formation of a ‘‘basal gas layer’’. This is exactly the same as the observation made by Lau, (2001) as described in section 6.2.2.5. The ‘‘basal gas layer’’, from here onwards called BGL, is the accumulation of flue gas formed just below the oil-water interface. Interestingly, the simulation results show that the BGL is only formed in L3, where the HP well is located below the oil-water contact (Fig. 6.27c & f). This is because the flue gas leaving the combustion zone must displace some of the native reservoir water ($S_w \approx 0.01$ to 0.08), and therefore create a gas flow path, before it reaches the HP well. Since the BW zone has 100% water saturation, the flue gas must displace some of it before it can reach the HP well in L3. However, for each case of L1 and L2, no BW water needs to be displaced before the flue gas is produced.

In the BW zone, where the ‘‘basal gas layer’’ is in direct contact with water, some of the combustion gases will dissolve as it displaces the water. This is evident given that at the reservoir pressure of 28 bar and the BW temperature of at most 170 ^{o}C, Nitrogen gas, which accounts ≈ 80 mol% of the total flue gas volume, has a solubility of 0.70 mL N_2/g H_2O (Pray et al., 1952). Since the basal gas is, however, only in contact with water during the ‘‘basal gas layer’’ formation, the extent of gas solubility in water will be controlled by diffusion. As a result, it is effect on the overall simulation result is negligible, and consequently, is not considered in this study. Future work should, however, look into this especially when the reservoir contains BW.

In each of the three models, the shape of the combustion zone is forward leaning (Fig. 6.28a, b, & c) indicating the stability of the THAI process even in the BW reservoir. It can be observed that the axial speed of the combustion front is not affected by the differences in the location of the HP well. The results also show that the vertical area swept by the combustion front increases as the HP well is lowered. As a result, how deep down the BW reservoir the combustion front reaches is determined by the location of HP. It follows that locating the HP well near the base of the BW reservoir could help prevent early oxygen production as the combustion front has to travel to a longer distance before reaching the toe of the HP well. The temperature distribution for each model also shows that there is a vigorous combustion front propagation (Fig. 6.28d, e, & f). They further reveal that the nearer to the base of reservoir the HP well is located, the larger the area affected by the combustion heat.

In summary, the oil recovery and the cumulative water production from BW reservoir, in which the conventional THAI process is implemented, are affected by the location of the HP well. Therefore, locating the HP well as far above the oil-water interface results in uneconomical oil recovery rate and potentially would result in early oxygen breakthrough.

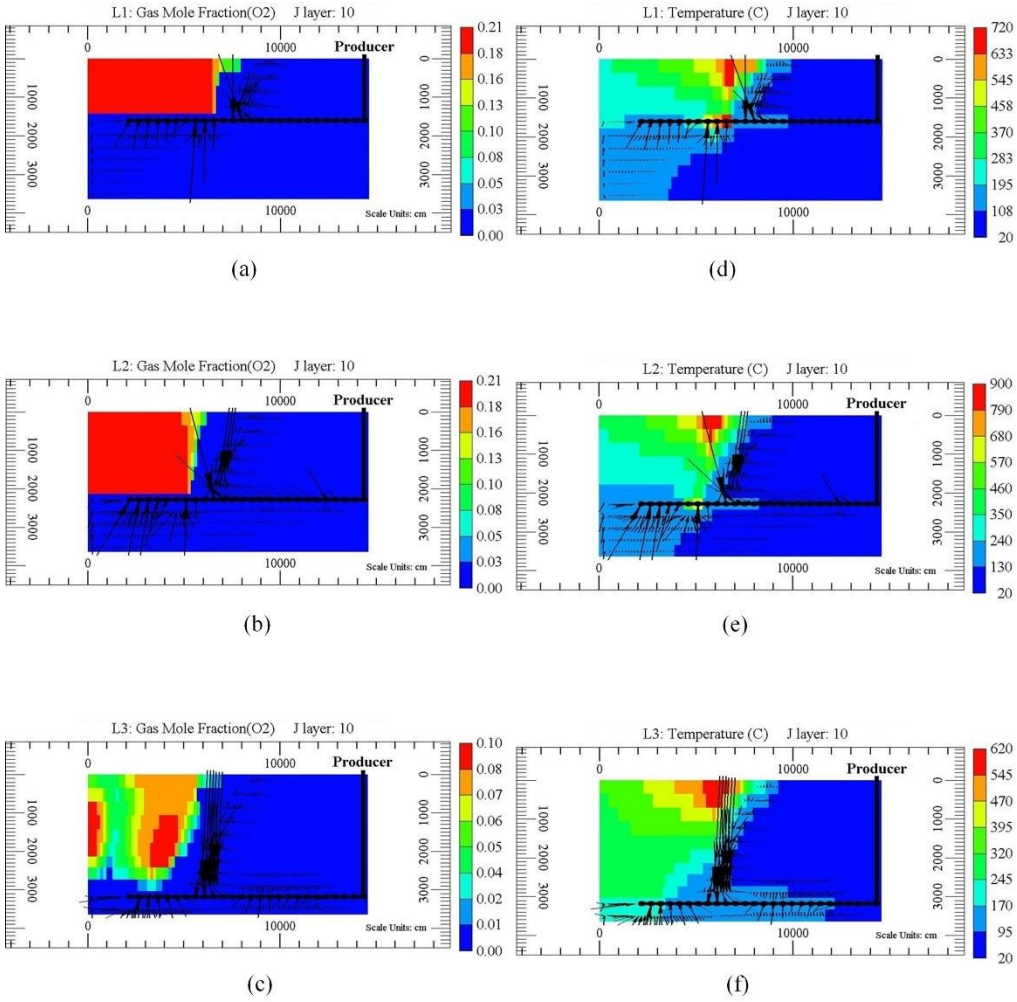

Fig. 6.28: Oxygen mole fraction profile along the vertical mid-plane for (a) L1, (b) L2, and (c) L3, and temperature distribution profile for (d) L1, (e) L2, and (f) L3 along the vertical mid-plane (J layer 10) and after two years of combustion

6.3.2.3 Limit to the Oil Production due to Bottom Water

The preceding section detailed the improved benefits of operating the conventional THAI process in BW reservoir with HP well located in the BW zone. However, that exercise was carried out with the BW thickness kept constant. Also, in section 6.3.2.1, it was shown that the performance of the THAI process is adversely affected by the presence of BW. In the view of the foregoing, the maximum BW thickness above which THAI, in it is conventional form, may potentially be inapplicable is determined under this section.

Fig. 6.29 shows the daily oil production rate for the four different models. It is observed that in all the models except 1A, no oil production takes place either during the 104 days of the PIHC or over the two years of combustion. Even in model 1A, the production begins at 570 days and the maximum production rate never went above 0.315 m^3 day^{-1}. As a result, the cumulative oil production, after additional 264 days of combustion, is 50 m^3 only, which is 0.05 %OOIP. This figure is negligible compared to that obtained in the base case (i.e. BW00, section 6.3.2.1). As explained earlier, this shows that it took more than a year of combustion time before enough mobilised oil reached, and hence formed a blanket around, the toe of the HP well in model 1A. For the same BW thickness, moving the HP well further down into the BW zone, as is the case in model 1B, leads to a larger volume of oil needing to be mobilised prior to the formation of drained oil blanket around the toe of the HP well. Since a further increase in the BW thickness implies an increase in the depth at which the HP is located, it naturally follows that not enough oil will reach the toe of the HP in models 2A and 2B. That is why no oil is produced in either model.

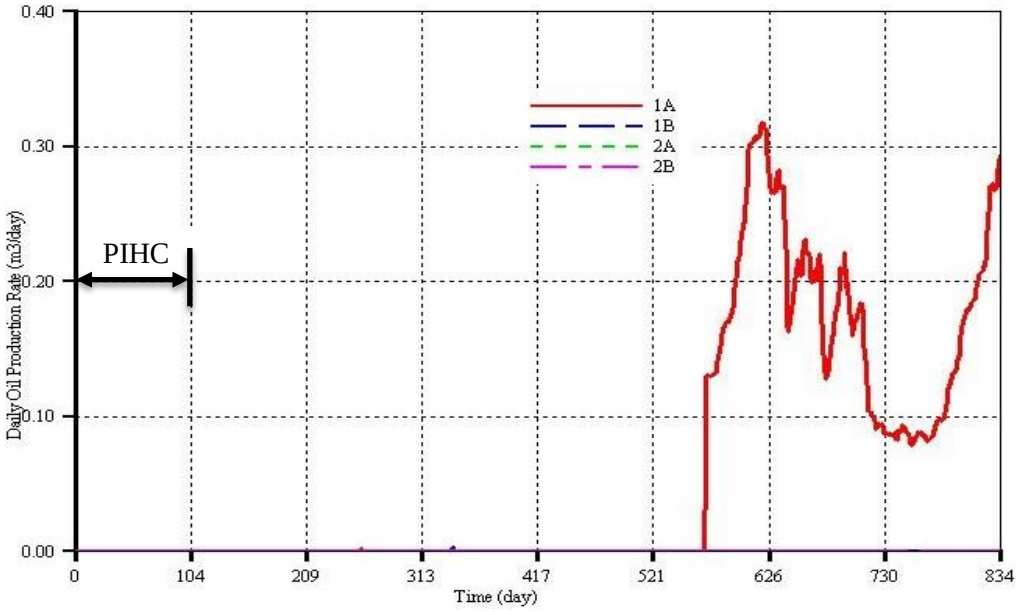

Fig. 6.29: Oil production rate for larger BW thickness

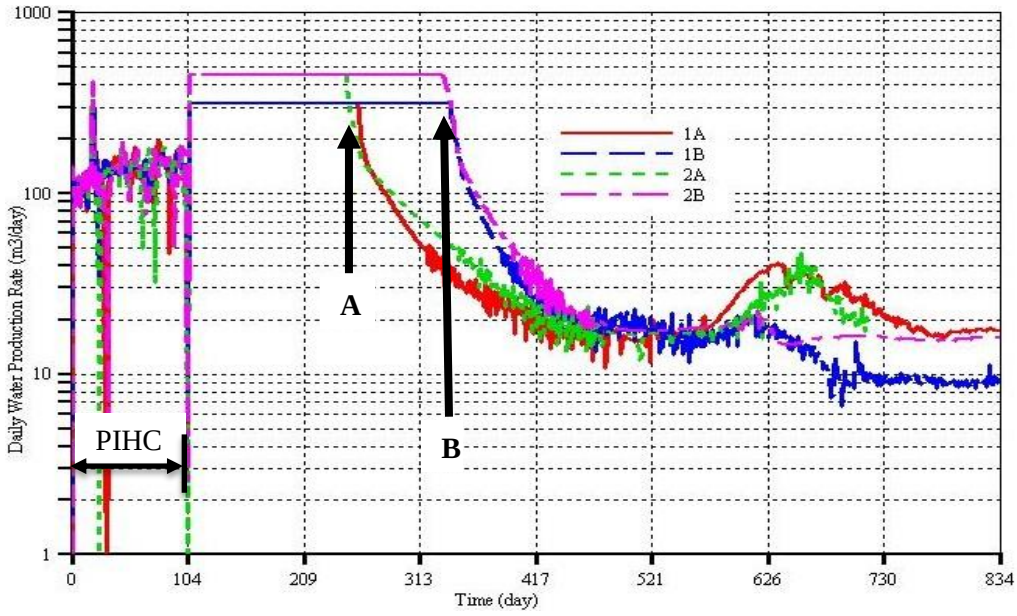

Fig. 6.30: Water production rate for larger BW thickness

The HP well in each case is 'watered-out' with the water production rate increasing as the depth, at which the HP is located below the oil-water contact, is increased (Fig. 6.30). This can be seen as the highest liquid production rate is maintained for much longer (i.e. 104 to 340 days for models 1B and 2B compared to 104 to 250 days for models 1A and 2A) when the HP well is located

near the base of the reservoir. The peaked water production rate period from 104 days to point A for models 1A and 2A has been found to correspond with the period of BGL formation. The drop in the water rate in each model is observed to be marked by the start of flue gas production. This further supports the earlier explanation that the formation of BGL is due to the lack of a direct gas flow path to the HP well. Similarly, for models 1B and 2B, the peaked water production period (i.e. from 104 days to point B) corresponds to that of BGL formation. These show that the lower the HP well is located into the BW zone, the longer it takes for flue gas communication with the HP well to be established. From point A to 470 days, models 1A and 2A have the same water rate signifying that the mobilised oil drainage rate into the BW zone is the same. Likewise, models 1B and 2B have the same water rate from point B to 470 days. Thereafter, the models converged to a common water rate of 18 m^3 day^{-1} until 580 days.

At the end of the two years of combustion, it is found that the lower the depth at which the HP well is located, and/or the thicker the BW zone, the more water is cumulatively produced (Fig. 6.31). Point C shows the difference the location of HP well, for the same BW thickness, has on the cumulative water production. This is mainly due to the formation of BGL.

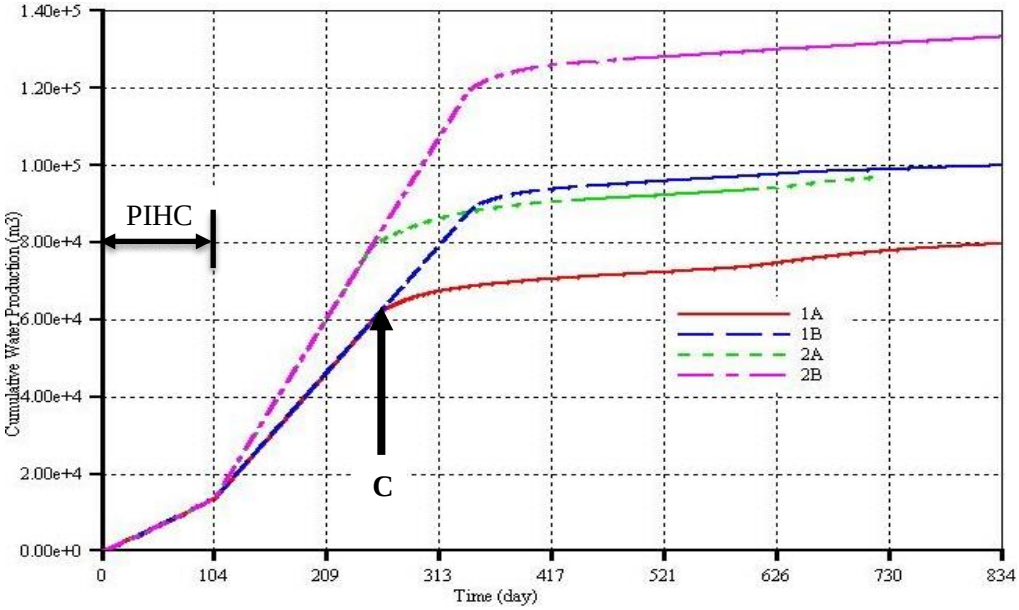

Fig. 6.31: Cumulative water production for larger BW thickness

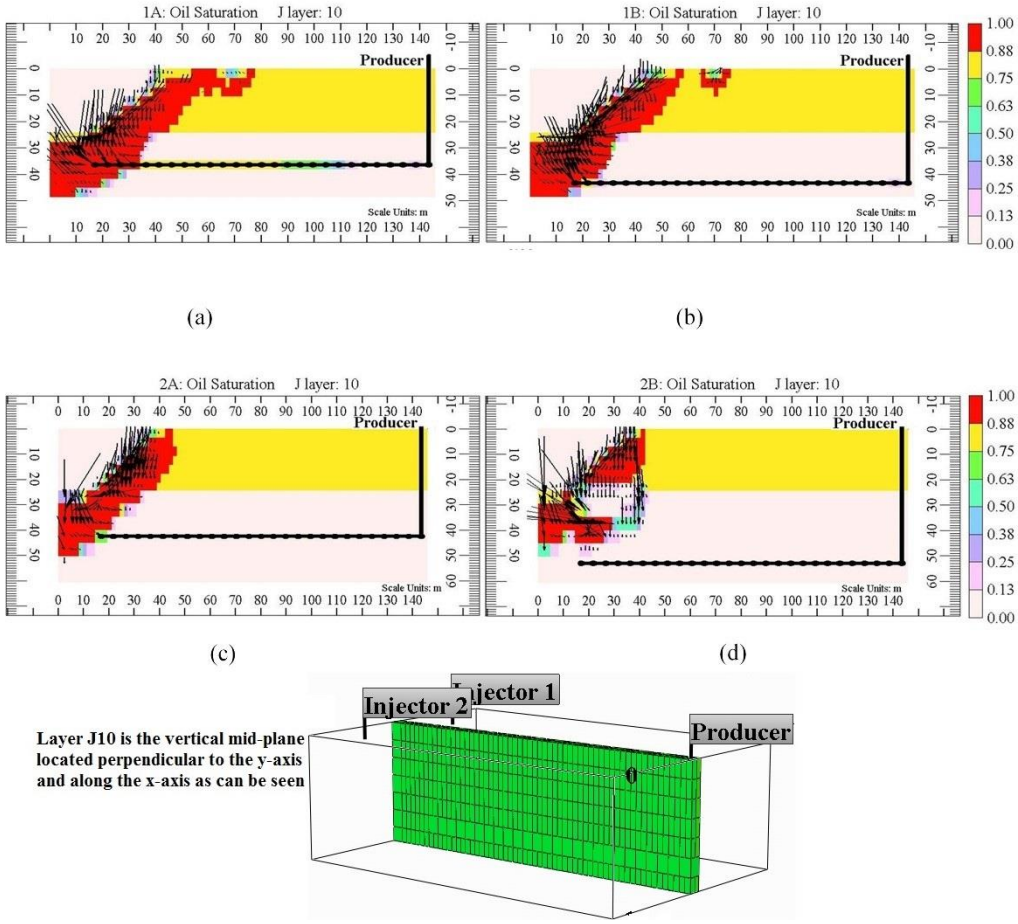

Fig. 6.32: Oil saturation profiles along the vertical mid-plane for (a) 1A at 834 days, (b) 1B at 834 days, (c) 2A at 715 days, and (d) 2B at 834 days

Fig. 6.32 shows that all the mobilised oil drained into the BW zone and for models 1A and 1B (Fig. 6.32a, & b), it will most likely take a very long time (more than two years) before any significant oil production begins. Also, when the HP well is located nearer to the base of the BW reservoir (Fig. 6.32b), more oil will be produced since the process is gravity-driven and the mobile oil has higher potential energy. However, in the case of model 1A (Fig. 6.32a), significant portion of the mobilised oil will be left sunk in the BW zone, underneath the HP well. The same explanation applies to models 2A and 2B (Fig. 6.32c, & d) except that the HP well must not be located so low that the mobilised draining oil cannot reach, and therefore forms an oil blanket around, the toe.

As seen in the preceded section, the BGL forms only when the HP well is located inside the BW zone. However, in that case, the location of the HP well within the BW zone was not varied. For the same BW thickness of 24 m (Fig. 6.33a, & b), it is found that the thickness of the BGL is determined by how far down, from the oil-water contact, the HP well is located. The thickness of BGL in model 1A is 10.4 m, which is 7 m shorter than that of model 1B. This is because the combustion flue gas has to establish a pathway, which involves forcing the native reservoir water into the HP well, prior to having direct communication with the HP well. This also explains the difference between the 7.98×10^4 m^3 of water produced in model 1A and the 9.99×10^4 m^3 produced in model 1B, at 834 days (Fig. 6.31). The same applies to models 2A and 2B which have the same BW thickness of 36 m but different BGL thickness for the same reason explained above (Fig. 6.33c, & d). In addition, the 9.91×10^4 m^3 of water

produced in model 2A and the 1.31×10^5 m^3 produced in model 2B, at 715 days, further explains why there is the difference in BGL thickness (Fig. 6.31).

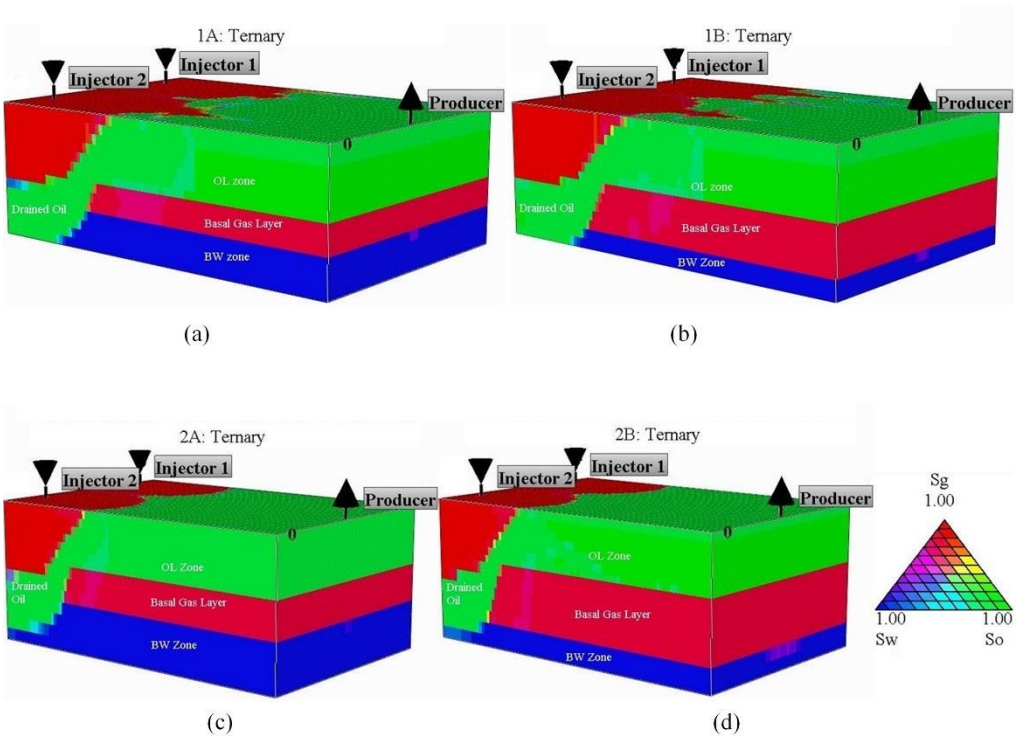

Fig. 6.33: Ternary diagram for models (a) 1A at 834 days, (b) 1B at 834 days, (c) 2A at 715 days, and (d) 2B at 834 days

In each of the four models, the combustion front propagates in the oil layer (OL) zone only and is restricted to the upper part of the reservoir (Fig. 6.34). As is the case in the previous sections, the combustion front is forward leaning, further indicating the stability of the THAI process, even when applied to BW reservoir. In addition, the results reveal that regardless of the thickness of the BW zone, no oxygen bypasses the combustion zone. Also, this shows that the BGL, shown in Fig. 6.33, contains no oxygen.

To summarise, there is a limit to BW thickness above which the performance of the THAI process is severely affected even though the combustion front can be stably propagated. The critical BW thickness, when the THAI process is

implemented in a BW reservoir with the wells arranged in an SLD pattern, should lie in the range of 50% OL < BW < 100% OL. However, future work is required to refine this.

The above findings beg the question: what should be done to either stop the mobilised oil draining into the BW zone or improve the recovery even if the oil continues to drain into the BW zone. For this, the temperature profile was checked to see if basal combustion could be used. The temperature profiles show that the drained oil, in each model, is at a high enough temperature (i.e. at least 115 ^{o}C) to be mobile. It follows that the static aquifer did not take out a significant quantity of heat from the combustion zone. This is because conduction is the dominant mechanism through which heat is transferred to the BW zone. The temperatures along the horizontal plane (oil-water interface) show that combustion can be propagated at the oil-water contact (OWC) in a similar fashion as in Lau, (2001). As a result, it would be used to investigate THAI with HP located near the base of the BW zone.

Furthermore, from these findings, it can be realised that even if the THAI process is successfully deployed in a BW reservoir, with the HP well located in the BW zone, addition of catalyst layer around the HP well, as in THAI-CAPRI, presents additional engineering problem. Apart from the need to force the oil to flow over the catalyst layer, external source of heat must be used around the catalyst bed, which would have been submerged in the bottom water. This could cause significant portion, if not all, of the heat to be used in heating up the surrounding water. As a result, there is need to study the feasibility of this in future.

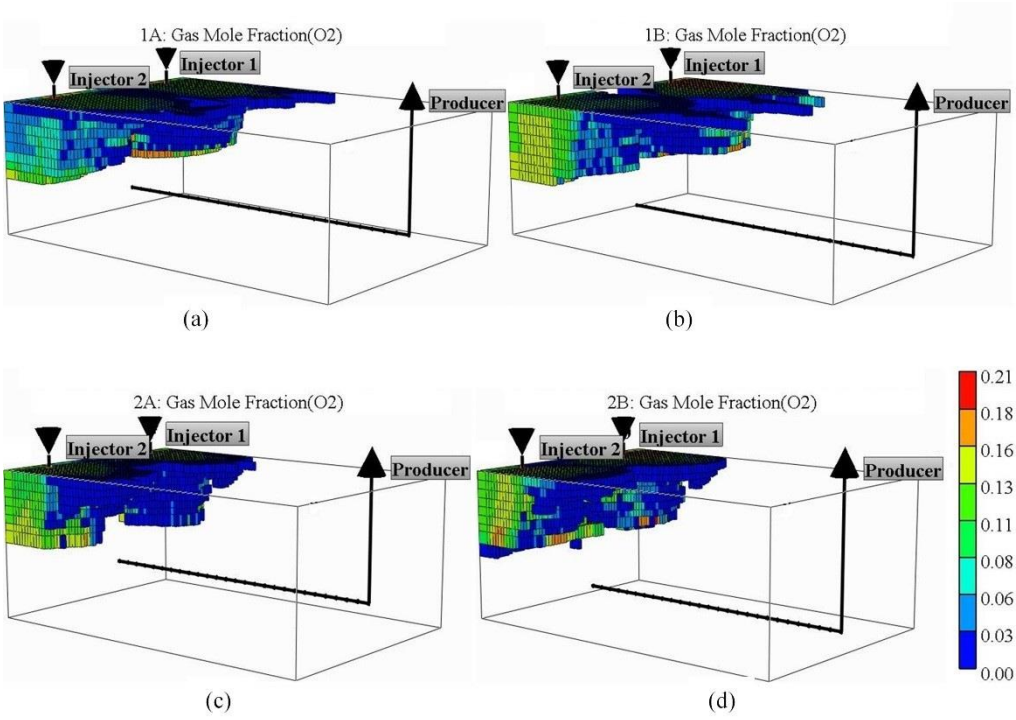

Fig. 6.34: 3D shape of combustion front for models (a) 1A at 834 days, (b) 1B at 834 days, (c) 2A at 715 days, and (d) 2B at 834 days

6.3.2.4 Effect of Active Aquifer

In this section, the impact of an active aquifer is analysed and discussed. As explained in section 6.2.2.4, the BW thickness in each model is 75% that of the OL. To recap, model BWN has a static aquifer, while model BWA has an active aquifer which is represented by water source/sink wells at the base of the BW reservoir (i.e. horizontal layer K13). The active aquifer allows the effect of in-flowing or out-flowing fluid into or from the BW zone to be simulated.

As with the previous models with BW thickness of ≥ 50% OL, no oil production is realised from either of the BWN or BWA models during the 104 days of PIHC. The combustion is run for 615 days and during this time, only a negligible amount of oil is recovered in BWN. No oil production is recorded in BWA (Fig. 6.35).

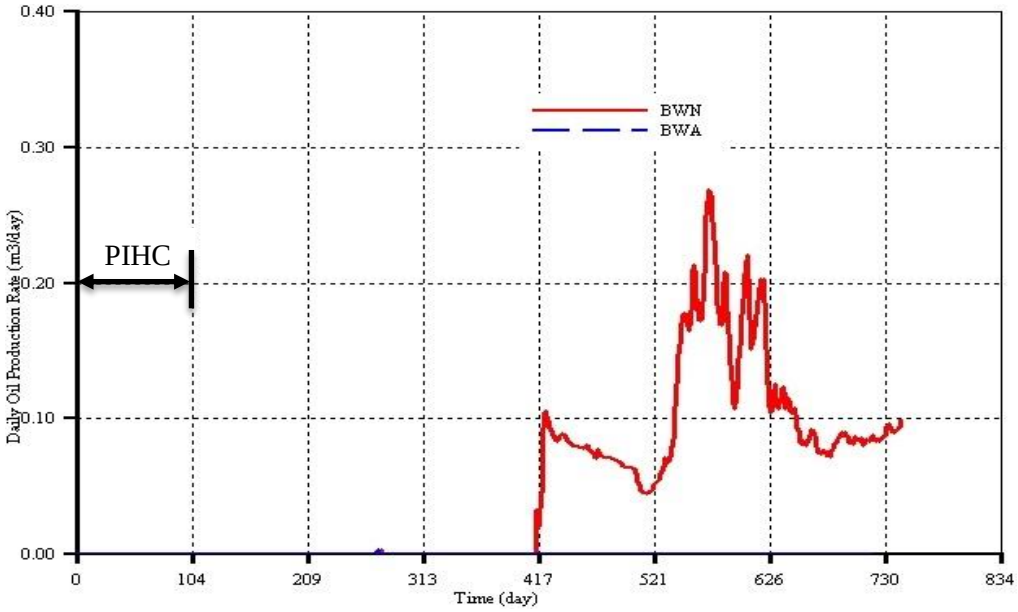

Fig. 6.35: Oil production rate for both active and non-active aquifer

The maximum oil production rate in BWN is below 0.3 m^3 day^{-1} and the cumulative oil produced is only 35 m^3 at 715 days. This minor difference between the two models is caused by the sealing effect provided by the no flow boundary condition assigned at the base of the static aquifer in BWN. As a result, the base of the static aquifer does not allow fluid transmission further down into the underburden (Fig. 6.36a). This is in accordance with the Petrobank's observation that below the middle McMurray, described in section 6.2.3 above, lies BW zone which is underlain by a shale layer (Petrobank, 2010).

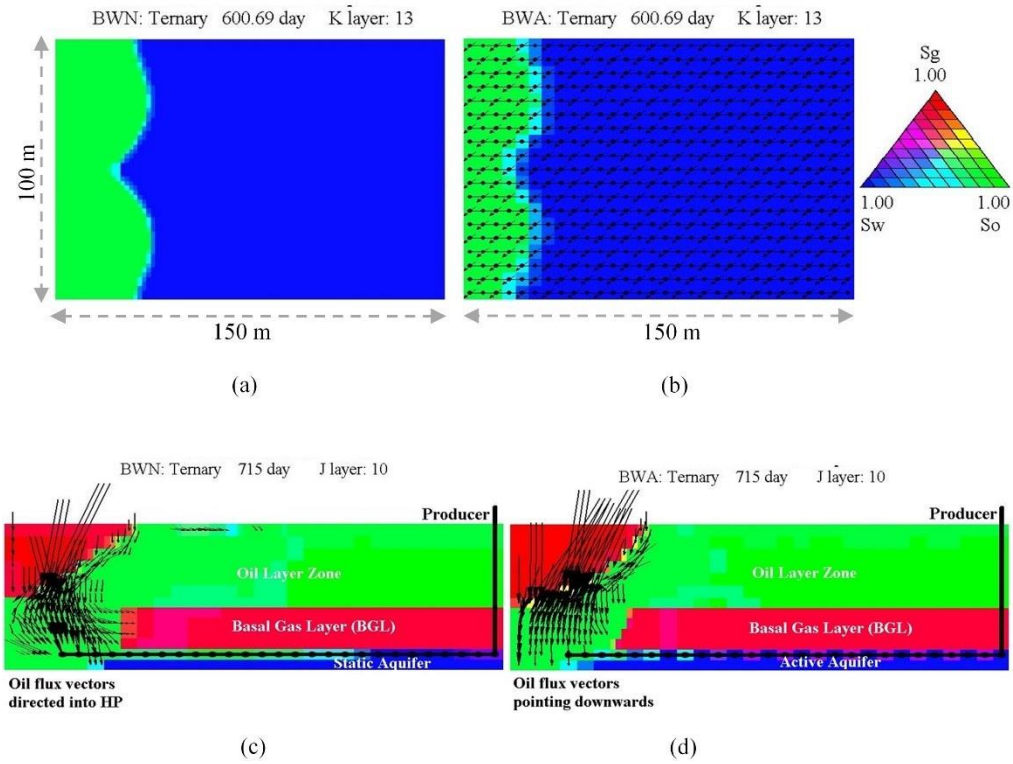

Fig. 6.36: Ternary diagram along the bottom horizontal plane for models (a) BWN, and (b) BWA and along the vertical mid-plane for models (c) BWN, and (d) BWA

The inclusion of active aquifer in the BW reservoir model showed that the mobilised oil, which is dragged into the BW zone, is not contained. Rather, it sank into the producers, which are used to simulate the active aquifer (Fig. 6.36b). Observing the oil flux vectors, superimposed on Fig. 6.36c and d, reveals that the small oil production achieved in BWN is due to containment. The continuous inflow of oil from the adjacent vertical planes and the no flow boundary at the base of the static aquifer force the mobilised oil towards the toe of the HP. This is signified by the toe-directed oil flux vectors of model BWN (Fig. 6.36c). In the case of model BWA, the absence of containment allows the continuously gravity draining oil to sink into the active aquifer. This is indicated by the vertically downward-pointing oil flux vectors, around the toe of the HP well (Fig. 6.36d). The drained oil front (Fig. 6.36a) is sharper in model BWN

than in BWA (Fig. 6.36b). This is caused by the use of larger gridblock size in BWA (i.e. nine times bigger than in BWN) to represent the source/sink well. However, despite this, the results are not affected quantitatively.

Despite the inclusion of active aquifer in BWA, the HP well in each model is watered-out. The water production rate is approximately the same regardless of whether active or static aquifer is used to simulate the THAI process in the BW reservoir (Fig. 6.37). The two models also have the same BGL formation period ranging from 104 to 275 days. Thereafter, model BWN overlies BWA, by up to 70 m^3 day^{-1}, until 345 days. This is due to the displacement of the stagnant BW into the HP well. From 345 to 560 days, the displacement of water from the second bottom-most horizontal layer by flue gas causes the water rate of model BWN to lie below that of model BWA by up to 15 m^3 day^{-1}. Beyond 560 days, the difference in the water rate is not pronounced. The cumulative water production at 715 days are 7.82×10^4 and 7.90×10^4 m^3 for BWN and BWA respectively. This is a difference of just around 1%.

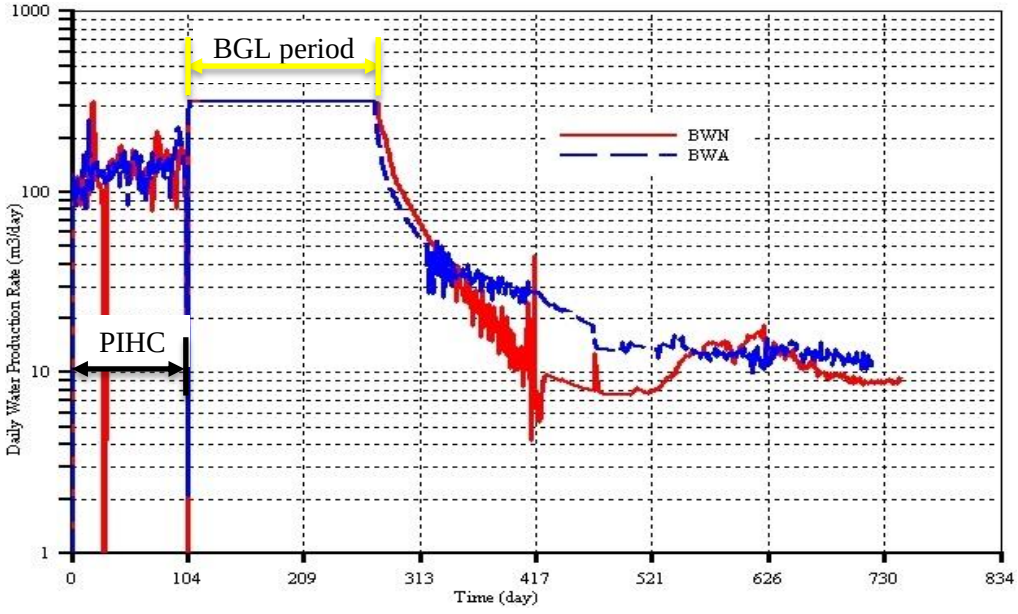

Fig. 6.37: Daily water production rate for both active and non-active aquifer

The two models predicted approximately the same peak temperature (Fig. 6.38). Therefore, comparatively, both the static and the active aquifers take the same amount of heat from the combustion front. Analysing the combustion front, it is found that in neither of the models does oxygen bypass the front. As in the previous sections, both fronts are restricted to the upper part of the reservoir, within the oil zone. This implies that even in the presence of active aquifer, the THAI process operates stably in terms of combustion propagation and sustenance.

So far, the studies of THAI process implementation in the BW reservoir have shown that for quite thick BW zone (i.e. thickness of > 50 % of OL thickness), almost all of the mobilised oil is not recoverable as it drained and get trapped into the BW zone for the case of static aquifer. For the case of active aquifer, the drained oil sank further down or is 'washed away' laterally. However, of note are the facts that all these models were run with the wells arranged in an SLD pattern and the combustion in each model was initiated at the top of the BW reservoir (i.e. in the oil zone around the vertical injectors). Therefore, new models with the combustion initiated at the oil-water contact and with the wells arranged in both the DLD and SLD patterns must be run to test if oil production could be increased.

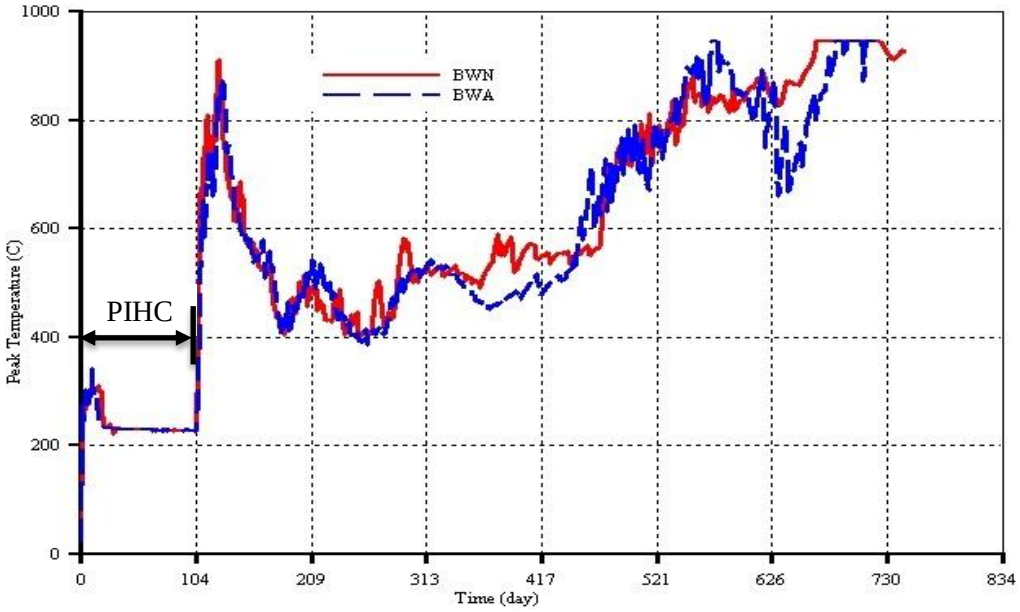

Fig. 6.38: Peak temperature for both active and non-active aquifer

6.3.2.5 Combustion at the Oil-Water Interface

The results of operating the THAI process with the combustion initiated at the oil-water contact of the BW reservoir are discussed under this section. To recall, even though it has already been stated in section 6.2.2.5, the thickness of the BW zone is 75% that of OL. For the DLD THAI arrangement (i.e. model D), an almost instantaneous oil production occurs at the end of the 104 days of PIHC (Fig. 6.39). The oil rate rises to a maximum value of 9.4 m^3 day^{-1} at 274 days before dropping slowly to 6.4 m^3 day^{-1} at 367 days. Thereafter, it increases steadily to 16.0 m^3 day^{-1} at 626 days and then the rate rises steeply to a peak value of 26.1 m^3 day^{-1} at 659 days. It then falls sharply and becomes oscillatory, due to the combustion front reaching the toe of the HP well, until 711 days. In the case of the SLD THAI arrangement (i.e. model S), no oil is produced until 510 days after the start of air injection (Fig. 6.39). This is despite initiating the combustion at the oil-water interface. The oil rate rise rapidly to 16.0 m^3 day^{-1} at 688 days before slowly increasing to 17.3 m^3 day^{-1} at 834 days.

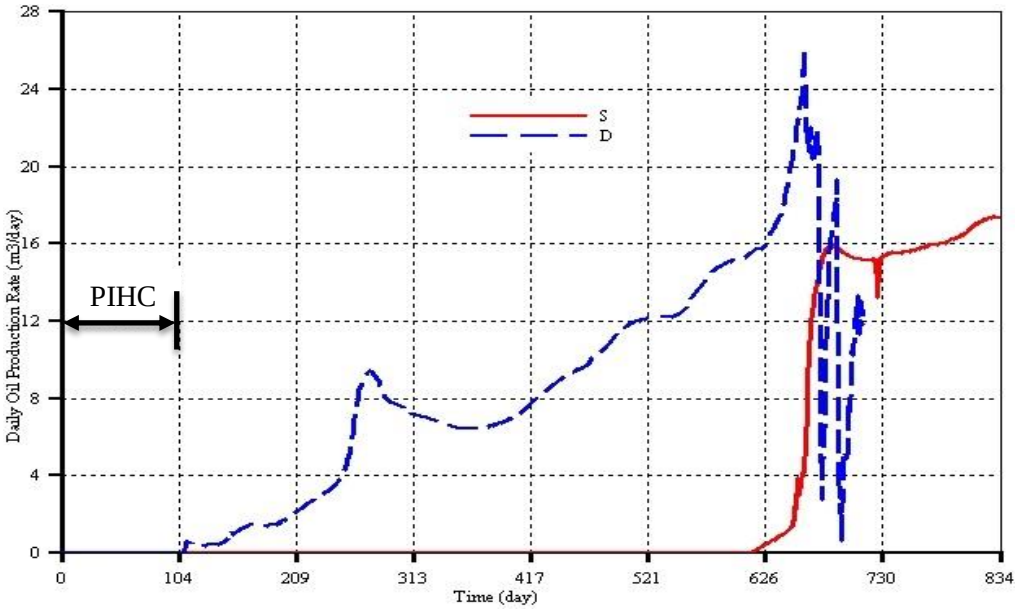

Fig. 6.39: Oil rate for combustion at the oil-water contact

The oil rate shows that operating the THAI process with the wells arranged in a DLD pattern, and combustion initiated at the oil-water interface results in a substantially improved oil recovery rate. The main reason for this is the use of the injector well in direct line with the HP well. However, it is also partly due to the placement of the heel of the injector well closer to the toe of the HP well. This is because, the initiation of the combustion at the oil-water interface in model S also did have too great an effect on the oil rate compared to that achieved when the combustion was initiated at the top of the reservoir (section 6.3.2.4, Fig. 6.35, model BWN). Peaked oil rate in model BWN is only 0.27 m^3 day^{-1} which is 64 times lower than that in model S. Despite that, the oil production response is faster in model BWN compared to model S. Overall, for model D, the closeness of the injectors to the HP well has resulted in a rapid creation of mobilised oil blanket around the toe of the HP well. At 714 days of the process, 5300 and 850 m^3 of oil are cumulatively recovered from models D and S respectively (Fig. 6.40).

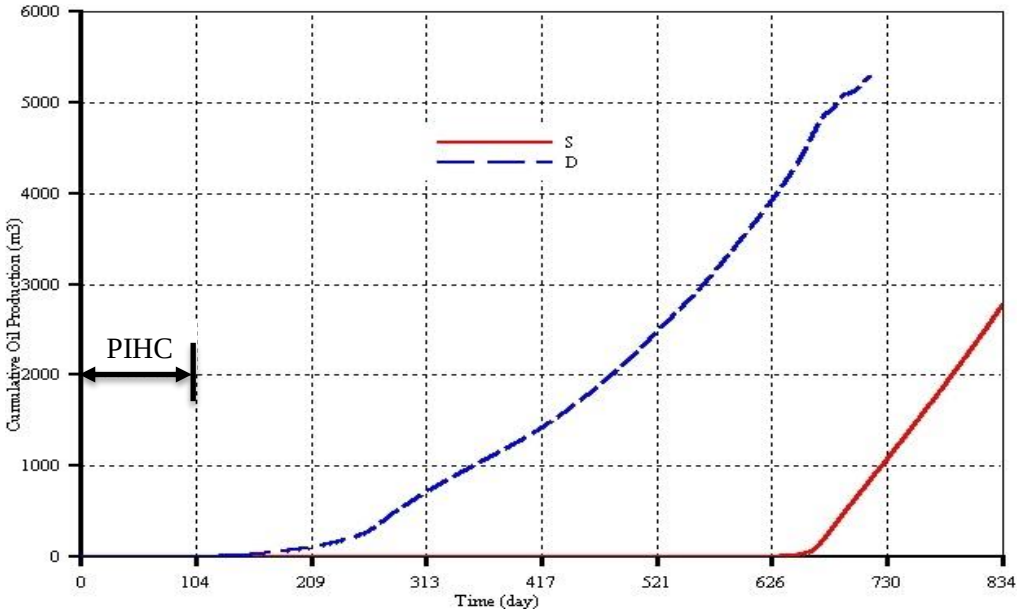

Fig. 6.40: Cumulative oil for combustion at the oil-water contact

In both models D and S, the daily water rate is quite the same during the PIHC. On injecting air, the water rate peaked to 450 m^3 day^{-1} in each model (Fig. 6.41). However, the peaked rate is sustained for a period of 46 days (i.e. from 104 days to point A) in the case of model D. This is because it becomes easier for the combustion flue gas to create a gas flow pathway to HP well. Where the injectors are laterally away from the HP well, it takes 96 days (i.e. from 104 days to point B) for communication to be established between the flue gas source (i.e. combustion front) and the HP well. From 236 to 711 days, the water rate in model D lies above that in model S because of the gradual displacement of water by the flue gas in the former. It is also because larger amount of water is already displaced during the BGL formation in model S. However, the same cumulative amount of water, 7.84×10^4 m^3, is produced in either model. Also, it is found that regardless of where the combustion is initiated (i.e. at the top of the BW reservoir or at the oil-water interface), the same cumulative amount of water is produced. This is observed by comparing models BWN and S.

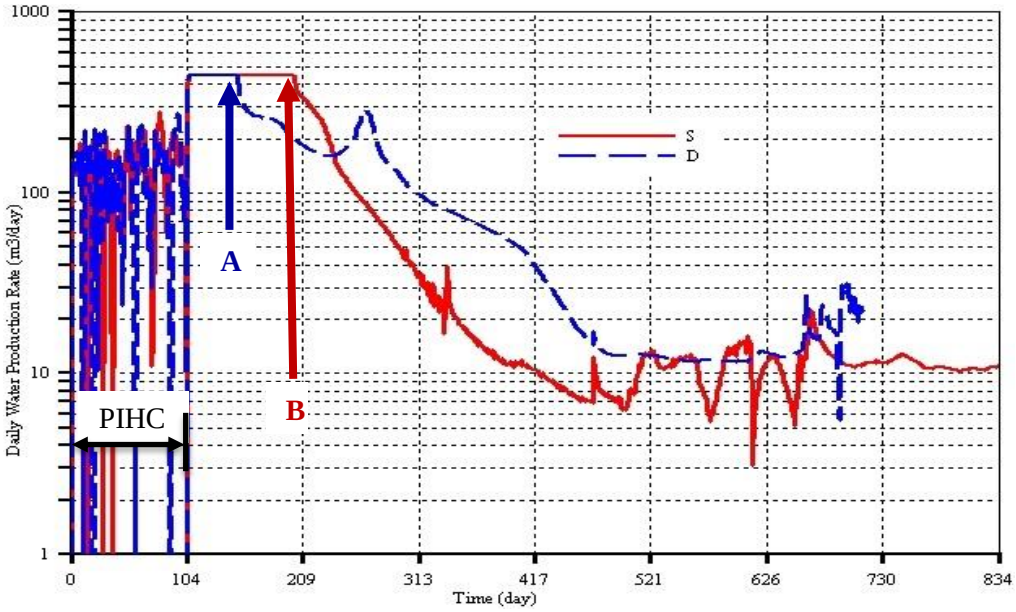

Fig. 6.41: Water rate for combustion at the oil-water contact

Fig. 6.42 shows the 3D shape of the combustion front at two different times: 30 and 608 days after the start of air injection. In both models, the combustion is successfully initiated at the oil-water interface (Fig. 6.42a, & b). It is found that instead of propagating along the oil-water interface in a toe-to-heel manner, and in the process forming the basal gas layer (BGL), the combustion rises rapidly into the oil zone, reaching the top of the reservoir. Then, controlled gravity override causes the combustion front to advance at faster rate at the top of the reservoir thereby forming a forward leaning front (Fig. 6.42c, & d). The larger pressure at the base of the reservoir, and the decrease in density of the injected air because of passing through the combustion swept zone, force the air to buoyantly rise to the top of the reservoir. Initially, the air was directed towards the heel of the injectors before flowing axially due to no flow overburden boundary condition (i.e. toe-to-heel). Once at the combustion zone, the air is completely consumed resulting in no oxygen production and hence stable THAI operation. This can be seen by observing the gas velocity vectors superimposed

on the ternary diagram shown in Fig. 6.43. Since the injector wells in model S are placed on the adjacent vertical planes, it is easier to visualise the gas flow pattern of model D, which is shown in the right column of Fig. 6.43 as (e) to (h). On leaving the combustion front, the flue gas flow is restricted to the top of the reservoir during the early stage of air injection. As the combustion zone expands, the gas flow area increases such that the whole reservoir thickness is occupied.

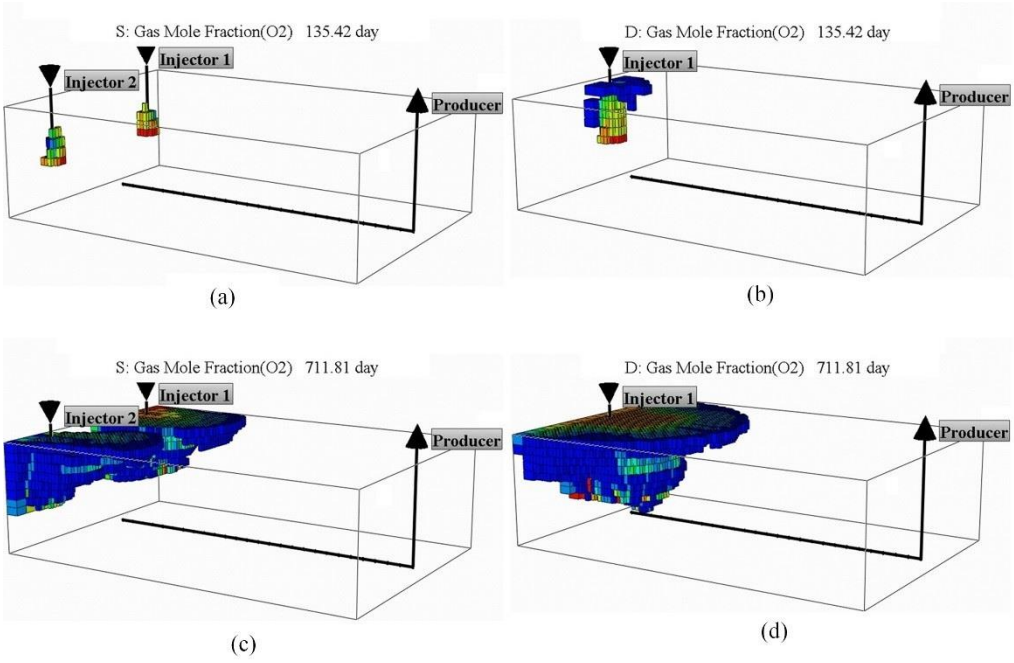

Fig. 6.42: Shape of combustion front after one month from the start of air injection for models (a) S, and (b) D, and at 711 days for models (c) S, and (d) D

Fig. 6.43 shows the gradual development of the BGL over time. One month after the start of combustion (Fig. 6.43a), the HP well is still fully submerged in the BW preventing the flue gas from being produced to the surface. This resulted in water displacement forming the first layer of BGL just beneath the oil-water interface. The same applies to model D (Fig. 6.43e). Around five months into the combustion period, the flue gas in model S (Fig. 6.43b) is in direct communication with the nearly the entire length of the HP well. In this situation,

the BGL thickness is the same as the distance separating the HP well from the oil-water interface. As a consequence, the BGL can be said to be fully developed as further inflow of gas does not increase it is thickness as shown by Fig. 6.43c and Fig. 6.43d. The same applies to model D (Fig. 6.43f) except that the BGL is in direct contact with the heel of the HP well only and thus thinner in size. This is because of the formation of a direct gas flow path from the toe of the injector to the BGL. Therefore, under this condition, the BGL is only partially developed and additional inflow of gas will displace more water to increase it's thickness as depicted by Fig. 6.43g. and Fig. 6.43h. This further supported the earlier explanation as to why curve D lies above S from 236 to 711 days (Fig. 6.41). It is also found that the BGL does not have to be fully developed before flue gas production begins.

Comparing models D and S in terms of oil displacement into the BW zone, it is found that oil blanket is quickly formed around the toe of the HP in the former (Fig. 6.43e) while it requires more than a year of air injection in the case of the latter (Fig. 6.43c). This is because the combustion has to expand laterally before the oil at the top middle part of the reservoir, directly above the toe of the HP well, is mobilised and drained. Once the oil blanket is formed, the continuous advancement of combustion front and drainage of oil lead to the formation of mobile oil zone (MOZ) separating the BGL from the combustion zone (Fig. 6.43d, & h). This, in addition to what is found earlier, partly explains why the

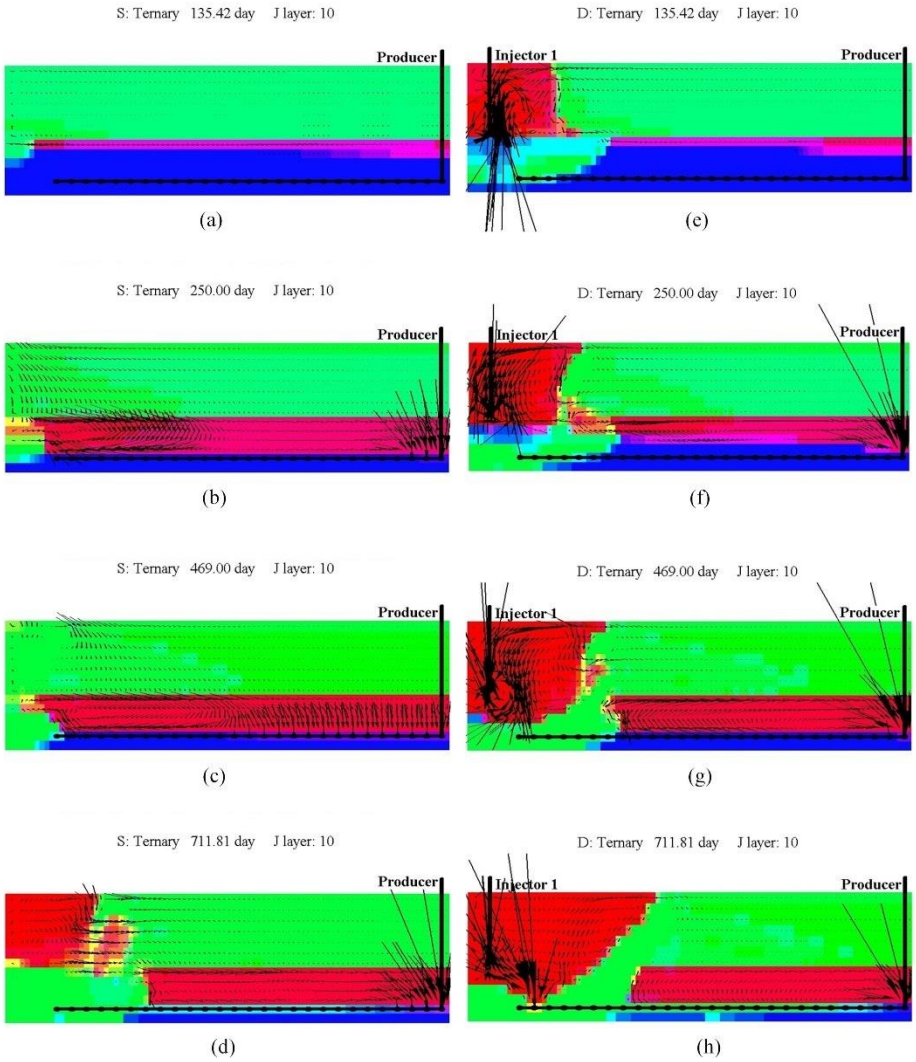

Fig. 6.43: Ternary diagrams along the vertical mid-plane (J layer 10) and at different times for models S (a to d) and D (e to h). Key: green = oil, red = gas, and blue = water.

combustion does not propagate along the BGL zone. Instead, the deduction that is made from these results is that the BGL is only formed as the combustion gases generated during the early period of air injection could not reach the HP well. It could be suggested that alternating injection and production could be employed so that the BGL is formed prior to initiating the combustion. This kind of operating strategy, even though not tried on the THAI process, did not work when attempted by Lau, (2001) on Basal Combustion process. However, it may work when implemented in the THAI process but only during the early stage of

combustion, before the MOZ provides sealing effect. Also, this strategy will result in excessive oxygen production.

In summary, initiating the combustion at the oil-water contact results in improved oil recovery rates, most especially when implemented in a DLD pattern. However, the combustion does not propagate along the BGL rather it rises and propagates as though it is initiated at the top of the reservoir.

6.3.3 Effect of Gas Cap on THAI

At the end of the PIHC, 6.7 %OOIP is recovered in the base case model, C1 (Fig. 6.44). This figure is higher than the recovery achieved, over the same period of time, in models C2 and C3 respectively by around 10%. For model C4, in which the cap rock permeability (Kh & Kv) and porosity are one order of magnitude larger than in C3 (Tab. 6.2), only 1.1 %OOIP is recovered prior to air injection (Fig. 6.44). With the vertical permeability (Kv) of 0.1 or 0.3 md and porosity of 1%, the cap rock is very tight that only negligible quantity of steam (less than 2 mol%) permeates through the rock. This can be seen in Fig. 6.45a and Fig. 6.45b which show, for models C2 and C3 respectively, that the injected steam is restricted to the oil zone only over the 104 days of PIHC. As a result, the heat transferred to the overlaying cap rock during the steaming is mainly due to conduction. That is why an increase in temperature by 29 to 115 ^{o}C, above the initial reservoir temperature of 20 ^{o}C, is observed in both models C2 (Fig. 6.45d) and C3 (Fig. 6.45e) respectively. These are the reasons why the oil recovery, in models C2 and C3, is slightly lower than in the model containing no cap rock (i.e. C1). However, when the Kv and the porosity are increased by a factor of 10 in model C4, significant quantity of steam escaped into the cap

rock, displacing all the pre-existing gas above the toe of the vertical injector (Fig. 6.45c). This explains the reason for the very low oil recovery in comparison with the base case model. Unlike in models C2 and C3, here, the heat is transferred to the cap rock via both conduction and convection with the later predominating. This is supported by the rise in the temperature of the steam swept zone at the end of the PIHC (Fig. 6.45f).

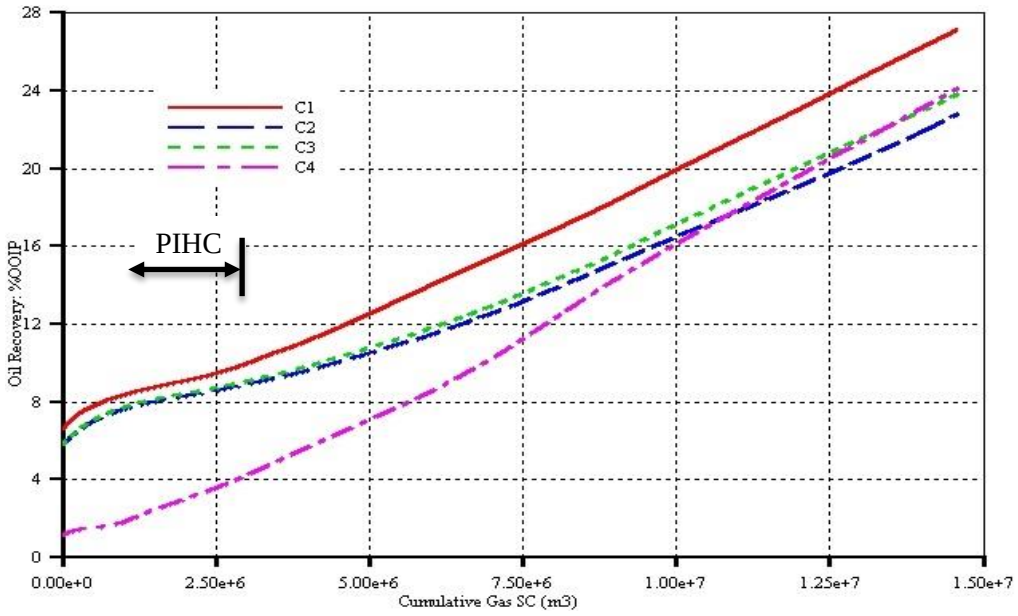

Fig. 6.44: Oil recovery showing the effect of cap rock

The inclusion of cap rock in the models also resulted in a lower oil recovery thoughout the additional two years of combustion (Fig. 6.44). At the end of the simulated period, 27.2 %OOIP is recovered in model C1, which is higher than that recovered in C2 by approximately 20%. Also, the recovery from C3 is 4.5% higher than that in C2. When the cap rock permeability and porosity are increased by a factor of 10, the recovery in C4 is 1.3% higher than in C3. Similar observations can be made from the oil rate curves (Fig. 6.46) in which model C1 overlain C2 and C3 throughout the combustion period. This could be attributed to the fact that part of the heat generated due to combustion is

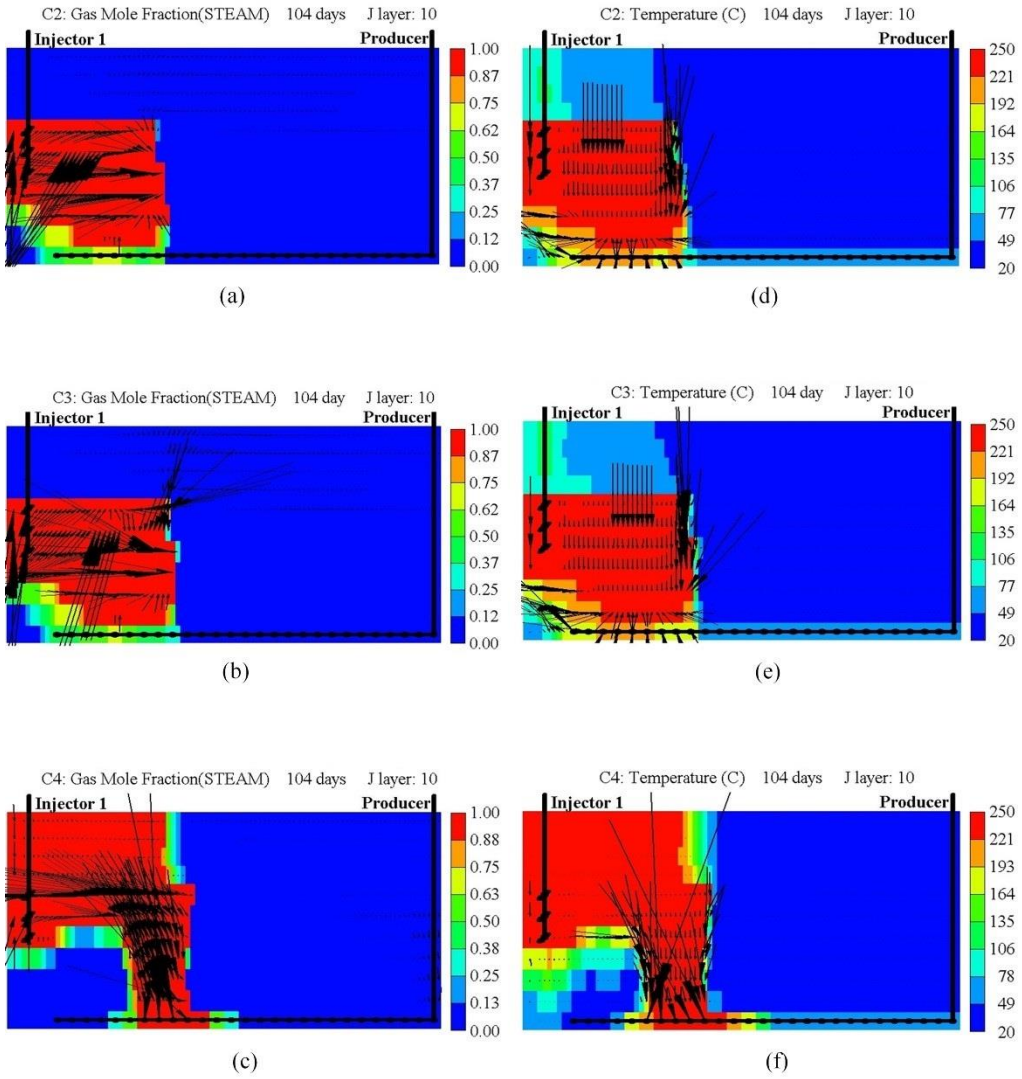

Fig. 6.45: Steam mole fraction profiles along the vertical mid-plane for models (a) C2, (b) C3, and (c) C4, and temperature profiles along the vertical mid-plane for models (d) C2, (e) C3, and (f) C4 all at the end of the PIHC

conducted (i.e. in the case of C2 and C3) to the cap rock. The oil rate curve for C4 on the other hand overlain all the three models from 153 days to the end of the combustion period. This was because less oil was mobilised during the PIHC as steam escaped into the cap rock. Also, it is due to decreased heat absorption by the cap rock as the porosity is increased. All the models have the same water production rate as the curves overlap one another throughout the process. This shows that inclusion of cap rock (with the range of Kv values considered) has no effect on the water production.

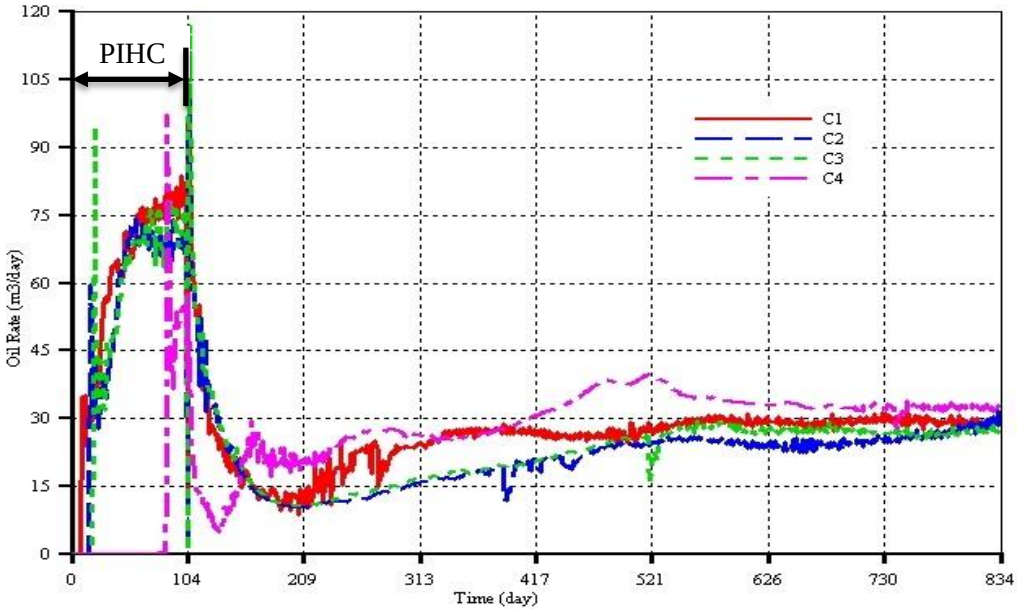

Fig. 6.46: Oil rate showing the effect of cap rock

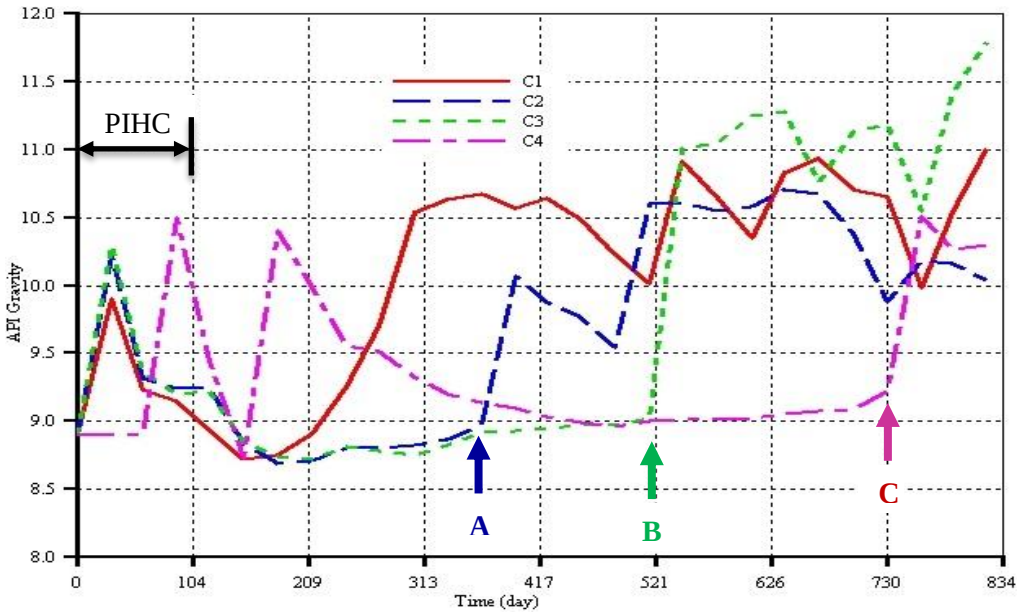

Fig. 6.47: API gravity showing the effect of cap rock

Fig. 6.47 shows the degree of upgrading in terms of API gravity. The API predicted by the models show increasing trends with the increase in process time. This is because as the combustion becomes more vigorous, the cracking rate increases and thus lighter pseudo-component is produced. The figure also shows that the higher the cap rock vertical permeability, the longer it takes

before the increase in API is observed as marked as points A, B, and C in Fig. 6.47.

Tab. 6.1 shows that oxygen production increases with the increase in the Kv of the cap rock. However, despite that, only 1.33 mol% of the injected oxygen is produced in model C4, which has the highest cap rock vertical permeability. As a result, less oxygen is utilised in model C4 compared to in C2 and C3. Also, from the observation of the cumulative oxygen production, it is found that it could be due to partial instability as the oxygen production takes place intermittently continual. These shows that the THAI process operates stably even where the cap rock is permeable since the produced oxygen did not reach the breakthrough level.

Tab. 6.3: Oxygen utilisation as mole percent of the cumulative oxygen injected

Model	Accumulated (mol%)	Produced (mol%)	Utilised (mol%)
C1	0.96	0.38	98.66
C2	0.95	0.42	98.63
C3	0.78	0.68	98.54
C4	0.98	1.33	97.70

The oxygen profiles along the vertical mid-plane (Fig. 6.48a, b, & c) and the adjacent vertical plane (Fig. 6.48d, e, & f) show the shape of the combustion front. Behind the front, small amount of oxygen accumulates before it is consumed on reaching the combustion zone. However, as shown in Tab. 6.1, a small amount of oxygen still bypassed the combustion front through the low-fuel-concentration zones to reach the HP well. In addition to that, some of this oxygen escaped into the cap rock, possibly via the low temperature region or via

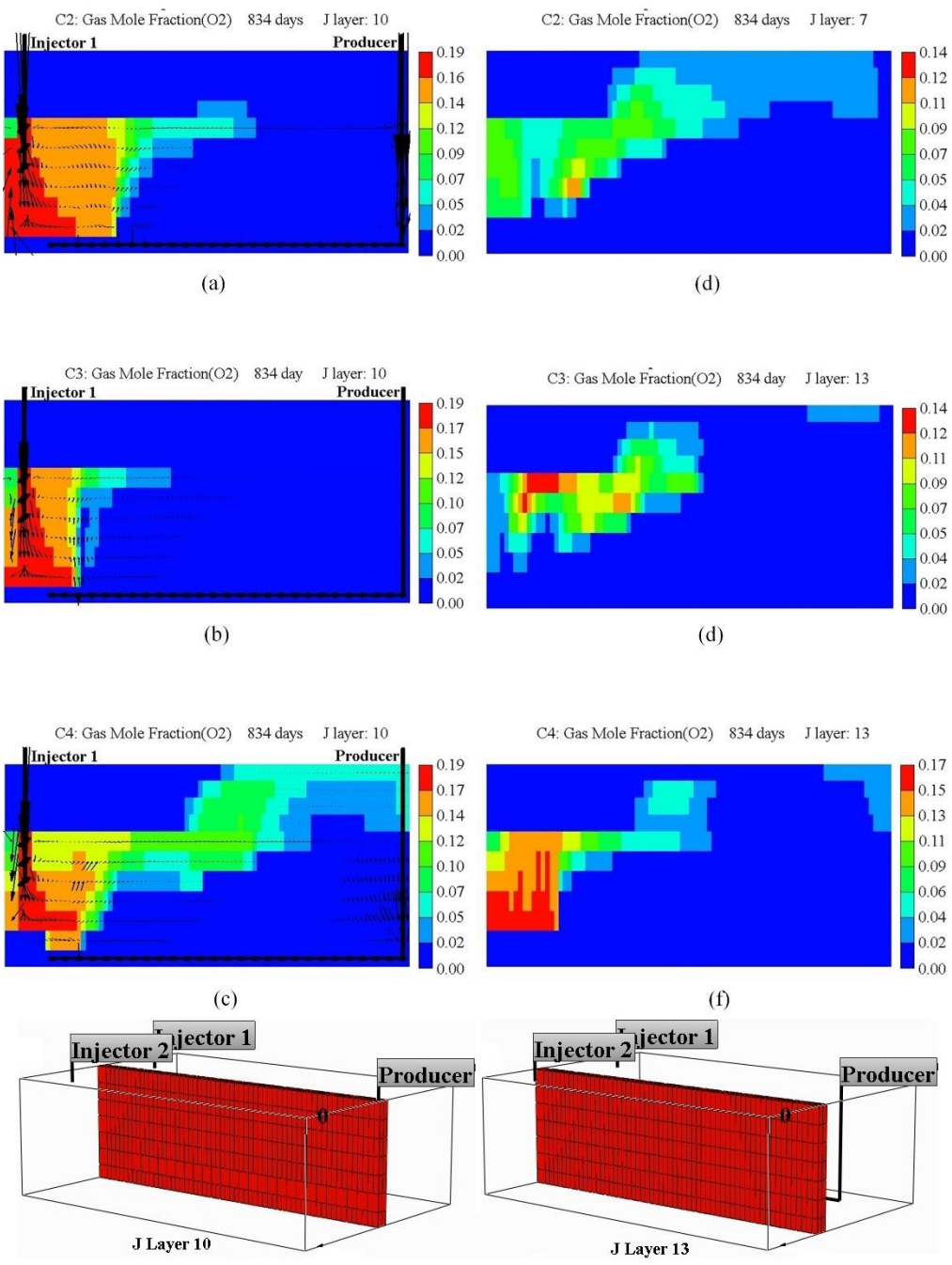

Fig. 6.48: Oxygen mole fraction profiles along the vertical mid-plane for models (a) C2, (b) C3, and (c) C4, and along the vertical adjacent planes for models (d) C2, (e) C3, and (f) C4

zones that contain no coke (Fig. 6.48). Because of the low vertical permeability in C2 (Fig. 6.48a, & b), most of the escaped oxygen (despite being very small in amount) is trapped in the cap rock. That is why there is an increase in oxygen production by 10% of that produced in C1. When the Kv value of the cap rock in C2 is tripled (i.e. to form C3), higher amount of oxygen escaped into the cap

rock. However, most of it is produced implying an increase in oxygen production by 80% of that produced in C1 (Tab. 6.1). Additional increase in both Kv and Kh resulted in an increase in the accumulated and produced oxygen concentration as higher amounts escaped into the cap rock.

Fig. 6.49 shows that the oil drainage pattern in the THAI process is not affected by the cap rock. As a result, quantity of oil mobilised and produced in the three models are only marginally different (i.e. varying by a maximum of 5.5%). Therefore presence or absence of cap rock while modelling the THAI process results in similar shape of oil saturation profile, over the 834 days studied. However, there is a difference in oil saturation, depending on the model, at the same reservoir location. Observing the viscosity of the cold oil zone (i.e. the unaffected oil zone downstream of the combustion zone) indicated a dramatic decrease in viscosity compared to when no cap rock is included while modelling the THAI process. This can be seen in Fig. 6.49a, b, c, & d where the oil saturation becomes richer (i.e. 88 to 100%) compared to the initial saturation of 80%. From the temperature distribution, the decrease in viscosity is found to be caused by an increase in heat distribution. This is because the heat conducted (i.e. in the case of C2 and C3) to the cap rock from around the combustion zone is rapidly transported downstream, towards the heel end of the HP well. This is the reason why the oil saturation in the top horizontal oil layer, just below the oil-cap rock interface, is substantially reduced to $\leq 50\%$ (Fig. 6.49a, b, c, & d). It, therefore, implies that there is top-down oil drainage from zones not directly affected by the ‘‘bulldozing effect’’ of the combustion front as indicated by the oil flux vectors superimposed on the oil saturation profiles (Fig. 6.49a, b, c, & d). Comparing the temperature distribution of C1, C2, and C3, it is found that

the minimum temperatures of the cold oil layer, at 834 days, are approximately 20, 42, and 45 ^{o}C for models C1, C2, and C3 respectively. This shows that the tripling of the Kv value (i.e. from that in C2 to that in C3) enhance the heat transfer in the cold oil zone, most probably by convection. From these observations, it can be infer that the inclusion of cap rock while modelling the THAI process reveals it is usefulness in aiding heat distribution into the oil zone of the reservoir.

As both the permeability (Kv and Kh) and the porosity of the cap rock are increased by a factor of 10 as in model C4, the effectiveness of cap rock in aiding heat distribution into the oil reservoir is reduced. This is because convection is now the dominant mechanism through which heat is distributed as the larger pore volume is easily accessible by the combustion gases. Additionally, the contact surface between the rock particles is reduced with increase in porosity thereby reducing the effectiveness of heat transfer via conduction. That is why there is no top-down oil drainage from the top horizontal oil layer below the cold oil zone as depicted by the absence of oil flux vectors (Fig. 6.49e, & f). This can be noted by observing that the oil saturation there has a value of $\geq$ 75 % (Fig. 6.49e, & f). Also, comparing the oil saturation profiles of the three models (i.e. C2, C3, and C4), it can be seen that model C4 has the smallest rich oil bank area, which is due to absence of top-down oil drainage in the cold oil zone. The minimum temperature in the cold oil zone in C4 is found to be roughly 24 ^{o}C, which is still higher than in the absence of cap rock.

To summarise, it has been shown in this work that cap rock, depending on it is permeability and porosity, only marginally affects the oil recovery in the THAI process, within the operation period studied. Future work would look into

whether longer operation period has adverse effect on the stability of the combustion front, and thus on the overall performance of the THAI process. It would also investigate the maximum cap rock permeability or porosity or both beyond which THAI should not be implemented in it is conventional form.

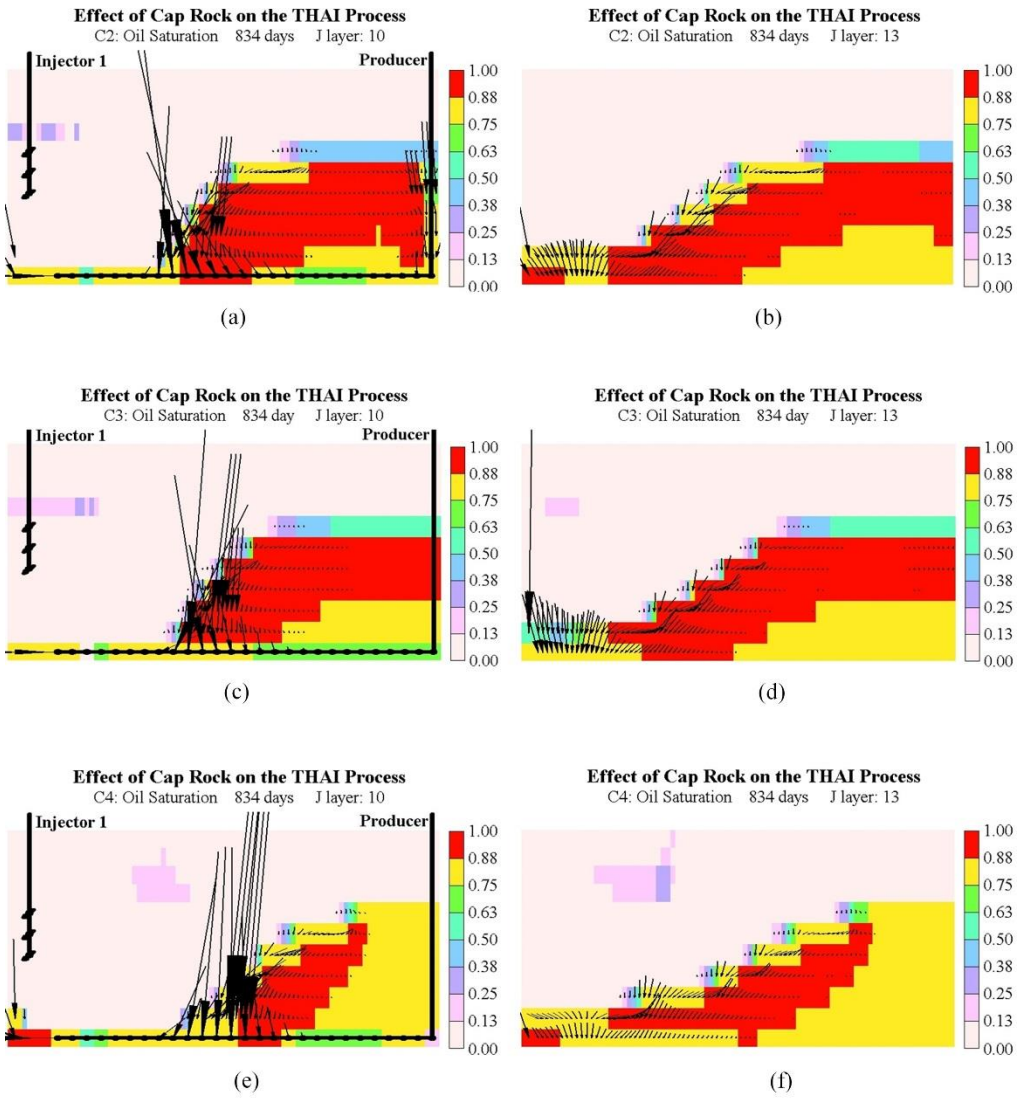

Fig. 6.49: Oil saturation profiles along the vertical mid-plane and adjacent vertical mid-planes for models (a) C2 and (b) C2, and (c) C3 and (d) C3, and (e) C4 and (f) C4 respectively

6.4 Summary

The study has shown that at constant Kv/Kh ratio of 0.3, oil recovery in the THAI process increases with the increase in oil mobilisation rate, which

increases with the increase in absolute permeability. However, this is at the expense of oxygen utilisation which is found to decrease with the increase in absolute permeability.

In the presence of random reservoir heterogeneity, it is found that the level of heterogeneity studied here has negligible effect on the THAI process. Also, it is shown that when the mean value of the absolute permeability of the heterogeneous model is the same as that used in the homogeneous model, then the cumulative oil recovery is roughly the same.

For the two phase permeability reservoir, it is concluded that the shape of the combustion front and, thus, the volume of reservoir swept, depends on the dominant phase (i.e. low or high fraction of low permeability zones). Oxygen utilisation efficiency is found to be low in a channelized reservoir (i.e. high presence of low permeability zones). However, the presence of the discontinuous low permeability zones does not adversely affect the performance of the THAI process except where a long continuous low permeability zone is formed. This, then inhibits the flow of mobilised oil, thereby decreasing the oil recovery.

In the shaly reservoir (PS_{30}), the combustion propagates along the permeable zone only and has fairly similar shape as in P_{30} but covers larger distance axially since the areal sweep is restricted. It is also found that the oxygen utilisation is lower due to both lower fuel availability and the ease with which O_2 channels compared to in P_{30}. The simulation also shows that the combustion front is skewed towards the side less populated by shales. Overall, the THAI process is

found to have larger AOR in reservoir containing discontinuous distribution of shale lenses compared to the base case.

For the layered reservoir, the THAI process has highest oil recovery in the HPC model with the LPC having the lowest recovery due to restricted oil flow. This shows that when drilling the HP well, careful study must be carried out in order not locate it along the low permeability axis as in LPC. This study has also found that THAI is only noticeably affected in terms of the smaller fraction of oil coked in TPI compared to that in TPD. Otherwise, the two latter models have negligible differences in terms of cumulative oil recovery and AOR.

In the presence of static aquifer, the oil recovery is affected by how large the thickness of BW zone is. No oxygen bypasses the combustion front to exit the reservoir via the BW zone. This study also shows that there is a period of low oil production rate which corresponds to oil displacement into the BW zone and a surge in water production rate. It is also reveals that the height of the mobilised displaced oil into the BW equates to that of the replaced water. It is also observed that when the BW thickness is 50% that of the OL, less than 50% of the mobilised drained oil will be recovered when the entire reservoir is swept by the combustion front. As a result, new strategy is needed to enhance the oil production and hence recovery rates.

When the location of the HP well is changed at constant BW to OL thickness ratio of 1:2, it is found that highest oil recovery is achieved with the HP well located below the oil-water interface. The further below the oil-water interface, the higher the oil recovery. The study reveals that implementing the THAI process, in it is conventional form, in the BW reservoir results in a period of

sudden drop in oil production regardless of where the HP well is located vertically. It is also concluded that the times of sudden drop in oil production rates are determined by how deep down into the BW reservoir the HP well is located. It is found that a 'basal gas layer' is only formed, just below the oil-water contact, when the HP well is located below the oil-water interface. Conclusively, the oil recovery and cumulative water production from BW reservoir, in which the conventional THAI process is implemented, are affected by the location of the HP well. Therefore, locating the HP well as far above the oil-water interface results in an uneconomical oil recovery rate and potentially would result in early oxygen breakthrough.

The current study has also shown that there is a limit to BW thickness above which the performance of the THAI process is severely affected even though the combustion front can be stably propagated. The oil production is heavily delayed to the extent that no oil is produced in all the models over the 834 days except in model 1A. It is found that the thickness of the 'basal gas layer' (BGL) depends on how further down into the BW zone the HP well is located. From the study, it is found that the critical BW thickness, when the THAI process is implemented in any heavy oil BW reservoir with the wells arranged in an SLD pattern, should lie in the range of 50% OL < BW < 100% OL. However, future work is required to establish this.

The comparative study between the active and non-active aquifer models show that the same cumulative volume of water is produced and that over the 715 days of the process, only negligible amount of oil is produced from BWN. It is found that in neither of the models does oxygen bypass the combustion front and as in the previous studies, both fronts are restricted to the upper part of the reservoir,

within the oil zone. Therefore, it follows that even in the presence of active aquifer, the THAI process still operates stably in terms of combustion front propagation and sustenance.

For the combustion initiated at the oil-water interface, it is found that controlled gravity override resulted in a high rate of advancement of combustion front at the top of the reservoir. The combustion is observed to not propagate along the 'basal gas layer', rather, it propagates as though it is initiated at the top of the reservoir. It is shown that the 'basal gas layer' is only formed during the early period of air injection as the combustion gases could not reach the HP well without displacing the bottom water to create an initial gas flow pathway into the HP well. It is also observed that initiating the combustion at the oil-water interface results in an improved oil recovery rates, most especially when implemented in the DLD pattern.

It has also been shown in this chapter that cap rock, depending on it is permeability and porosity, only marginally affects the oil recovery in the THAI process, within the operation period studied. It is found that the cap rock aids in heat distribution to the extent that most of the upper oil layer is mobilised. However, the effect is observed to be less pronounced with increase in permeability and porosity as in model C4.

7. Chapter Seven: Conclusion and Future Work

7.1 Conclusion

The laboratory scale model offered an insight into the mechanism through which oxygen production begins. It revealed that oxygen production was as a result of the combustion front propagating along the horizontal producer (HP). It also showed that presence of coke inside the horizontal producer is an essential requirement for stable combustion front propagation. The model also showed that the temperature around the mobile oil zone, where CAPRI^{TM} is envisaged, will not be sufficient to make the catalysts effective. Therefore, it is concluded that some form of external heating must be used in order to raise the temperature of the catalyst bed. To simulate the THAI-CAPRI, future experimental work is needed to determine the kinetics of the process.

Two out of the three different Arrhenius kinetics schemes that were successfully used to history-match the 3D combustion cell experiment were adjusted and implemented in the field scale simulations. This is because the kinetics parameters obtained from the laboratory scale model cannot be used directly for the field scale simulation as a result of excessive coke deposition. A comparative study between the two kinetics schemes showed that model P predicted a higher oil rate, and that a higher air rate can be injected right from the initiation of the combustion when compared to the case of model G.

Model P was then used to study the field-scale performance because it provided a more realistic representation of the physicochemical processes than model G. It revealed that even if the combustion front swept the whole reservoir length, it has to propagate along the HP well for oxygen production to take place. It was

observed that the combustion zone does not only have to cover the whole reservoir length but also has to expand laterally in order to produce the whole reservoir. In the field scale, the highest oil rate entering the HP well was observed to occur at the toe of the well. This was caused by the forward leaning, and thus stable, nature of the combustion front. Future work should determine the duration needed to recover the whole reservoir.

For heterogeneous reservoirs, the THAI process was found to have larger air-oil ratio, AOR, in a reservoir containing discontinuous distribution of shale lenses compared to the homogeneous model. However, overall, the THAI process is only marginally affected in terms of cumulative oil recovery. The combustion front is found to propagate in a stable manner just like in the homogeneous model. However, further study is needed to investigate the effect different permeability distributions would have on the THAI process. This should allow the optimum location of the wells to be determined.

For the effect of bottom water (BW) on the THAI process, the oil recovery is heavily affected by the thickness of BW zone. It was found that the location of the HP well relative to the oil-water interface significantly affected the oil production rate and hence the cumulative oil produced. More oil was recovered when the HP well is located inside the BW zone. It is found that a ‘basal gas layer’, just below the oil-water interface, is formed when the HP well is located in the BW zone. The study has shown that there is a limit to BW thickness above which the THAI process cannot be applied to a BW reservoir. However, future work is needed to determine this BW thickness.

The permeability and porosity of the reservoir cap rock only marginally affected the oil recovery in the THAI process. It was found that the cap rock aids in heat distribution to the extent that most of the upper oil layer is mobilised. However, the effect was observed to be less pronounced with increases in permeability and porosity. Future work should look into whether a longer operation period has an adverse effect on the stability of the combustion front, and thus on the overall performance of the THAI process.

7.2 Future Work

Apart from the future work suggested in section 7.1, the following processes should be studied in more detail as only preliminary study is presented here.

7.2.1 Simulation of CAPRI Process

For the details of the procedure followed to generate the input parameters and simulate the CAPRI process, please see Appendix C.

To obtain accurate and representative results, the frequency factors of the hydrotreating reactions were taken as the adjustable variables thereby varying the overall rate constant. This is carried out, via trial and error, and based on the increased average range of 4 to 7 API points catalytic upgrading, reported by Xia and Greaves (2001) and Xia et al. (2002b), until an average overall upgrading by around 6 API points was achieved. This, therefore, provides the kinetics parameters to be used to explain the the effect of parameters such as catalyst packing porosity, packing density, thickness etc. on the CAPRI process. However, before any change to the frequency factors, the original value for each reaction was used. This provided the base case model with which a comparative study is made. However, prior to this, an initial hydrogen-air ratio (HAR) of 1:4,

in parallel to the study in Shah et al. (2011) and Hart et al. (2013), was assumed. The inlet zone of the sandpack, around the HI well, was then electrically pre-heated for 30 minutes before the gas (air and H_2) was injected at the rate of 10000 cm^3 min^{-1}, which is equivalent to a gas flux of 15 m^3 $m^{-2}h^{-1}$. After 190 minutes, just like in the THAI model discussed in chapter 4, the gas flux was increased by four-third resulting in gas injection rate of 13333.3 cm^3 min^{-1}. This is maintained until 320 minutes. Below, the sensitivity of the oil rate, the cumulative oil produced, and the API gravity to the frequency factor of the reactions respectively are discussed. However, the multiplier by which the frequency factor for each model was multiplied, thereby varying the rate constant, is shown in Tab. 7.1 first.

Tab. 7.1: Frequency factor multipliers

Model	Frequency factor multiplied by
TC0 (Base case)	10^0
TC1	10^6
TC2	10^7
TC3	10^8
TC4	10^9

Despite the differences in the rate constants, all the models predicted identical peak temperature from the start of the process up to 54 minutes (Fig. 7.1). However, further into the combustion period, the peak temperatures diverge, with the model TC4 overlaying all the other models up to 240 minutes. Thereafter, it lies below all the other models up to the 320 minutes. This is due to oxygen production which began at 270 minutes. This is expected since the

change in the frequency factors of both the HDS and HDN reactions do not result in an appreciable change in the overall fuel availability, the maximum variation, at the end of the combustion period, is only 5.6 kg m^{-3}. However, the maximum variation in the temperature difference is 40 ^{o}C throughout the combustion period.

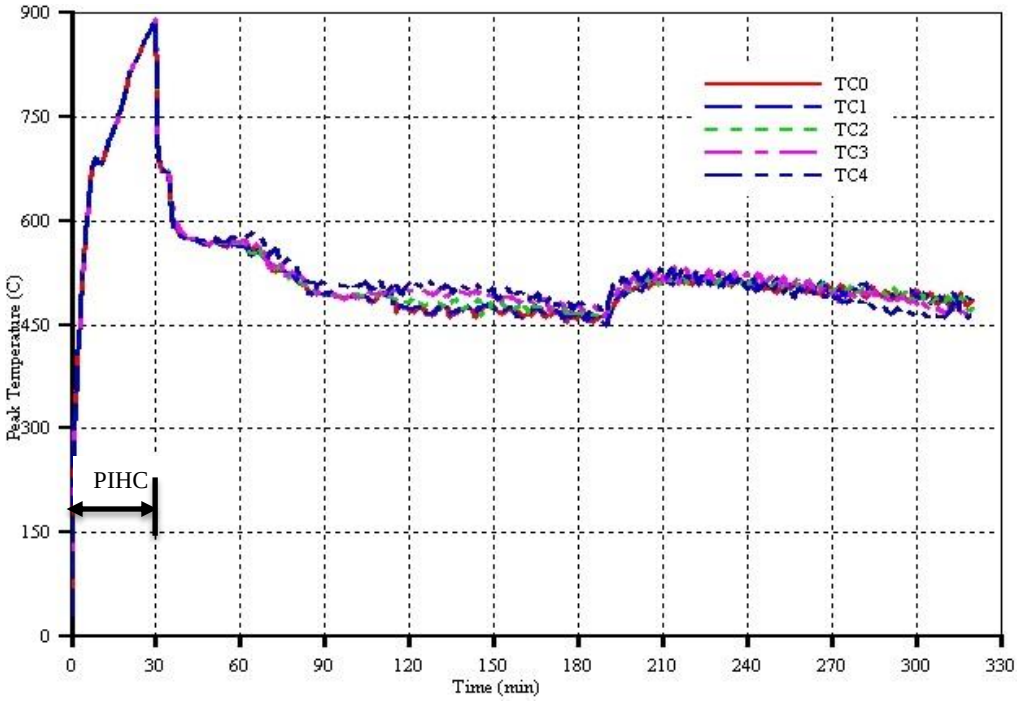

Fig. 7.1: Peak temperature

No oil was produced during the 30 minutes of electrical PIHC. The oil rate is the same over the first 6 minutes of combustion (Fig. 7.2). However, an increase in the production rate, with the increase in the multiplication factor, can be observed. This is caused by the increase in the degree of upgrading as more hydrogen is rapidly consumed by the increased hydrotreating reaction rates. Similar observations can be made from the cumulative oil production, where model TC4 lied above all the other models (Fig. 7.3). However, models TC0 to TC2 predicted nearly the same cumulative oil recovery, with a maximum

variation within the range of 19 to 71 cm^3. This is despite the difference in the rate constants between the three models of a factor of 10^6 or 10^7. A one order of magnitude increase in the frequency factor, from that in model TC2 to TC3 (Tab. 7.1), resulted in a pronounced increase in the cumulative oil recovery from 2095.51 in TC2 to 2306 cm^3 in the TC3. Similarly, a further increase by one order of magnitude caused the cumulative oil recovery to increase to 2493.58 cm^3 (Fig. 7.3). These are in accordance with the observation made by Salazar-Sotelo et al. (2004) that hydrotreatment results in an increase in product yields. It is caused by an increase in the lighter fractions, which have lower densities.

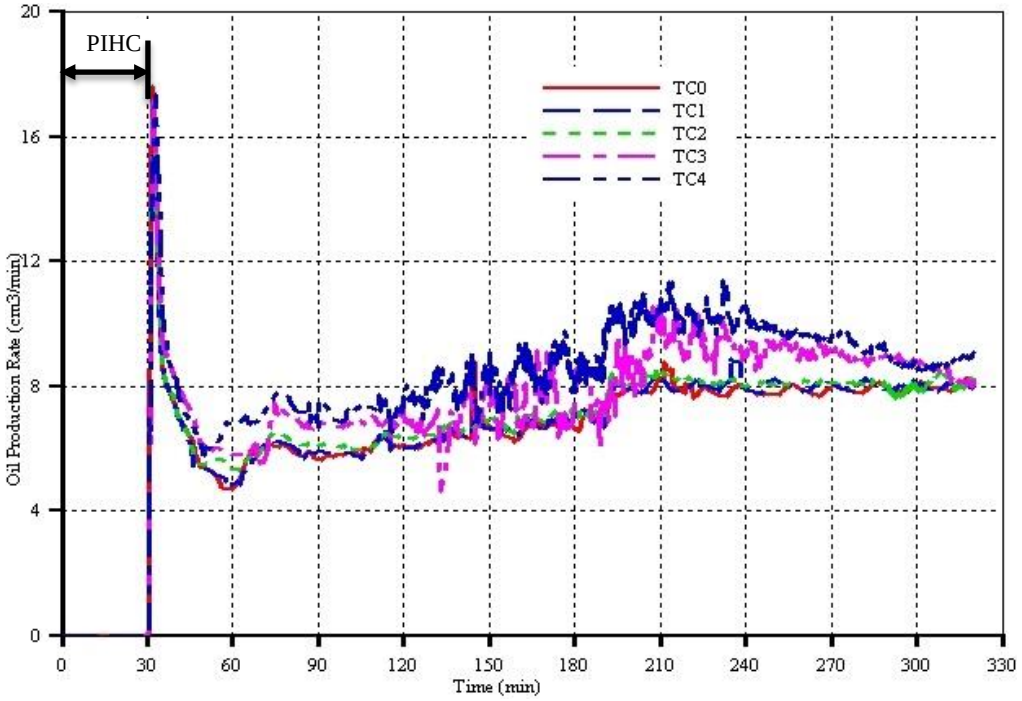

Fig. 7.2: Oil production rate

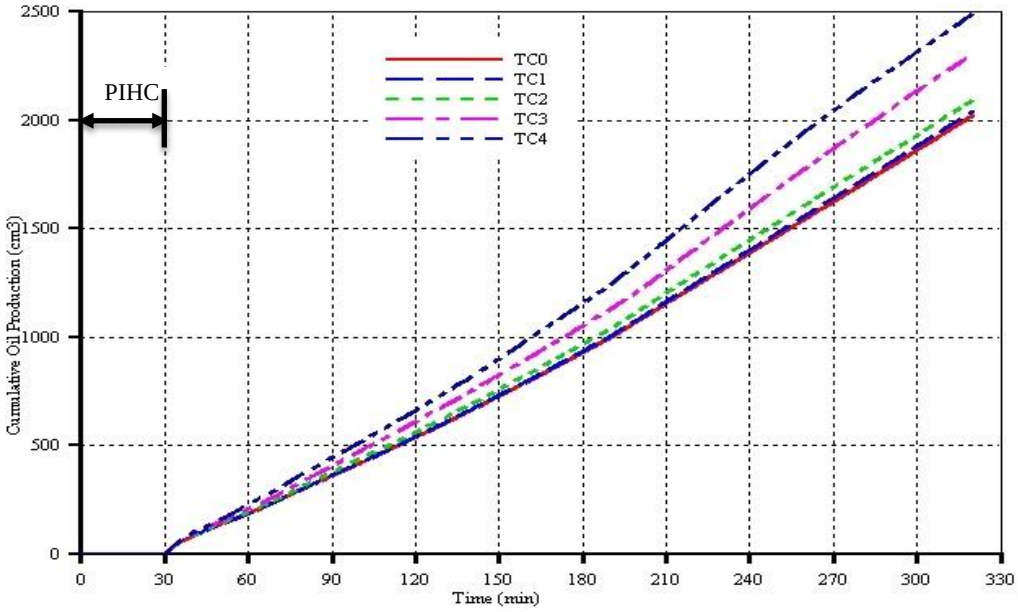

Fig. 7.3: Cumulative oil production

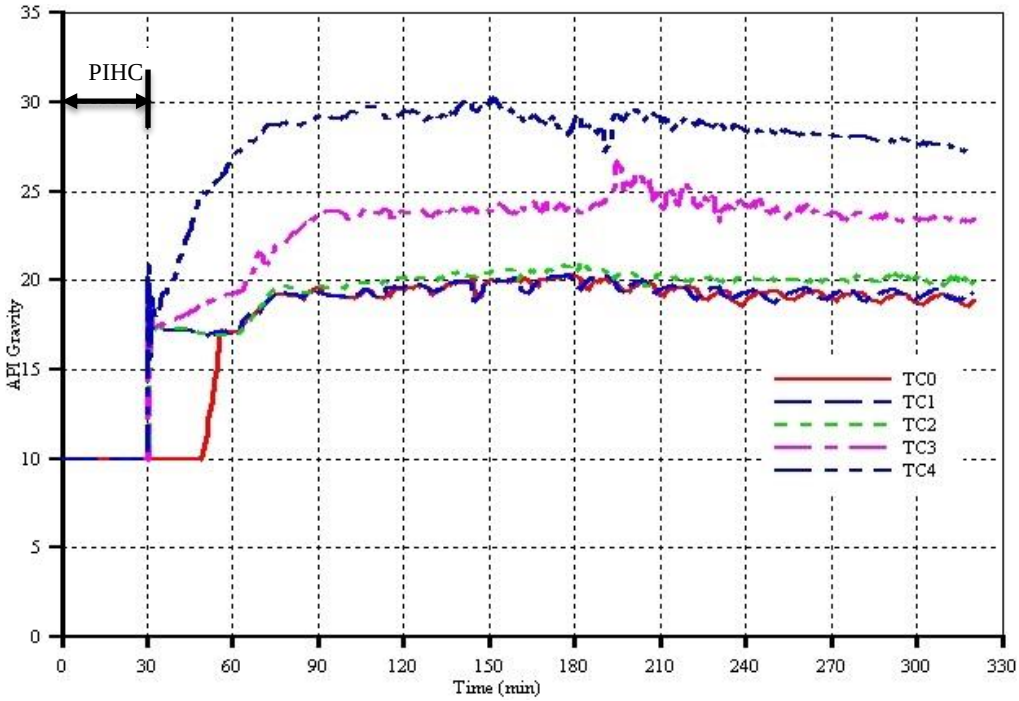

Fig. 7.4: Degree of upgrading in terms of API gravity

The degree of upgrading, based on API gravity, gives the measure of the extent of the catalytic effect on the produced THAI-CAPRI oil. In addition, it allows the selection of the correct frequency factor such that the same degree of upgrading as reported experimentally is realised. As in the case of the oil rate

and cumulative oil production, the API gravity predicted by models TC0, TC1, and TC2 are approximately the same with the later model, TC2 lying above models TC0 and TC1 by ≈ 2º API (Fig. 7.4). Models TC3 and TC4 show a substantial increase, by 5 to 7 and 10 API points respectively, in the degree of upgrading from that in the base case model, TC0. This shows that the average degree of upgrading achieved in TC3 is identical to that reported experimentally. As a result, both the HDS and HDN kinetics parameters of TC3 are used for the remainder of this study.

The sensitivity study showed that the assumptions made to construct the model are only valid to some extent since other experimentally monitored parameters, such as oil rate, produced oxygen concentration, cumulative oil recovery, etc. are need to fully validate the model. It also shows that the actual kinetics should be derived from the specific experiment. However, since this study only considered the relative order of magnitude effects of the various parameters influencing the performance of the THAI-CAPRI process then, as a consequence, the accuracy, or otherwise, of the catalytic kinetics reactions parameters, beyond the basic API gravity selection criterion, do not require further discussion in this study. Further studies, both experimental and numerical simulation, would look at this in greater detail.

The following studies should be carried out to further understand the CAPRI process:

- Investigation of the effect of the thickness of catalyst bed
- Investigation of the effect of catalyst packing porosity
- Effect of combustion cell pressure

- Effect of hydrogen to air ratio
- Comparison between dry and wet CAPRI
- Microwave heating to activate the catalyst bed to the right temperature
- Development of catalyst with the right dielectric properties from experiments
- Effect of incorporation of electrical heater to activate the catalyst bed

7.2.2 THAI with the Electrically Heated HP Well

- In each of the field scale models, the wells were arranged in a DLD pattern with the steam injected at the rate of up to 495 bbl/day (CWE) for the period of 104 days of PIHC.
- The base case model contains no electrical heaters while models AOP-1 and AOP-2 contain electrical heaters embedded along the horizontal producer (HP) well. The heating rate in AOP-1 is 1 kW/m while it is 1.5 kW/m in model AOP-2.
- Oil production began one week after the start of PIHC in the base case model whereas it started after six weeks in either of AOP-1 or AOP-2 (Fig. 7.5). The addition of electric heating along the HP well restricted the flow of the lighter mobile components (gas, water, and LC) into the producer. This resulted in pressure build-up near and above the toe of the HP well before the toe region is heated enough to establish communication between the two wells. All the three models converge toward a common oil production rate, on the commencement of air injection, for a period of 20 days (Fig. 7.5). Thereafter, the oil rate diverged, with the AOP-2 laying above the rest of the two models for the most part of the combustion period.

- Fig. 7.6 shows that the inclusion of electrical heating around the HP well enhances the cumulative oil production. Also, despite the difference in the rate of heat addition between the AOP-1 and AOP-2, the same cumulative volume of oil is recovered at the end of the two years of combustion.
- Fig. 7.7 shows that the larger the heating rate, the larger the proportion of the length of the HP well used for oil production.
- This study is only preliminary and future work should look at the improvement in terms of the fraction of the length of HP well used for oil production. It should also investigate if embedding the electrical heater along the HP well results in thermal cracking and hence coking of the well.

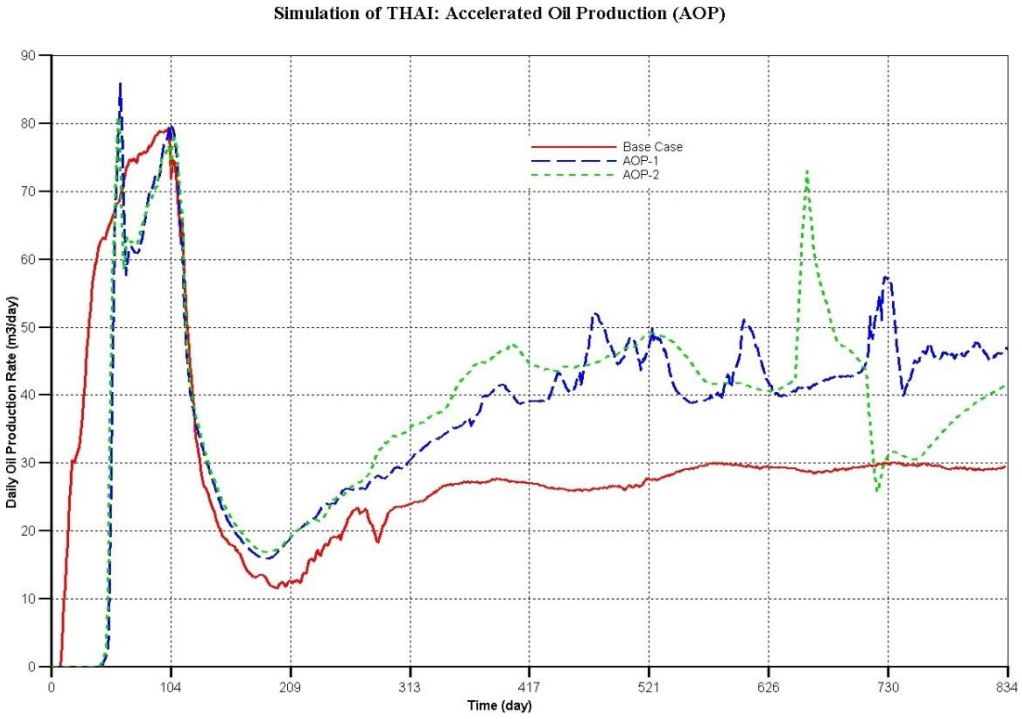

Fig. 7.5: Oil production rate

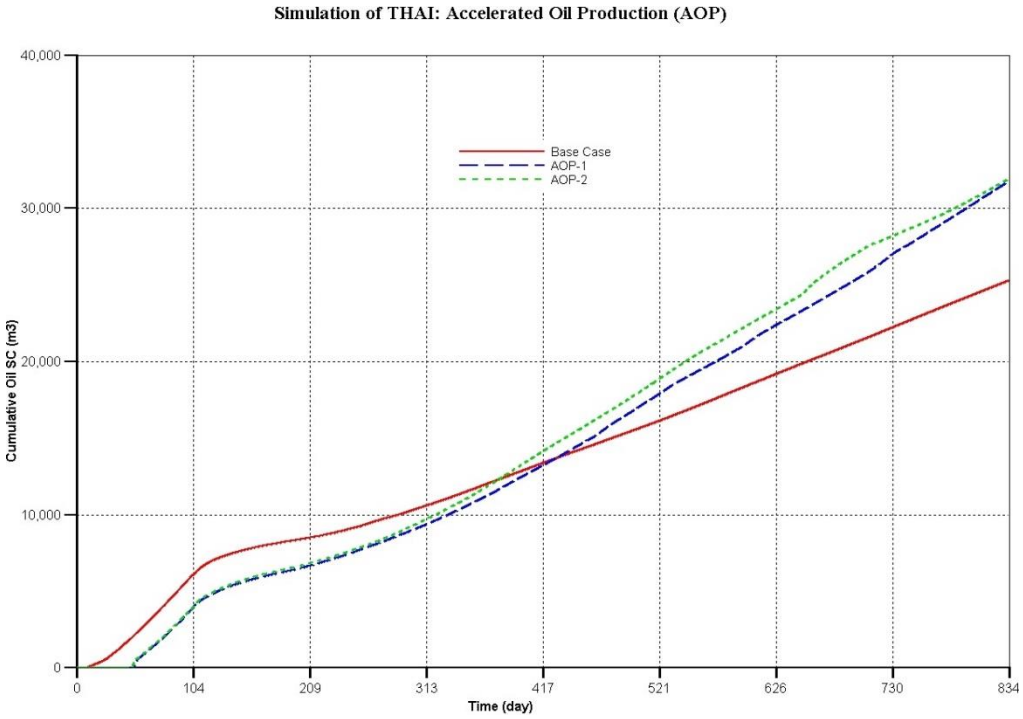

Fig. 7.6: Cumulative oil production

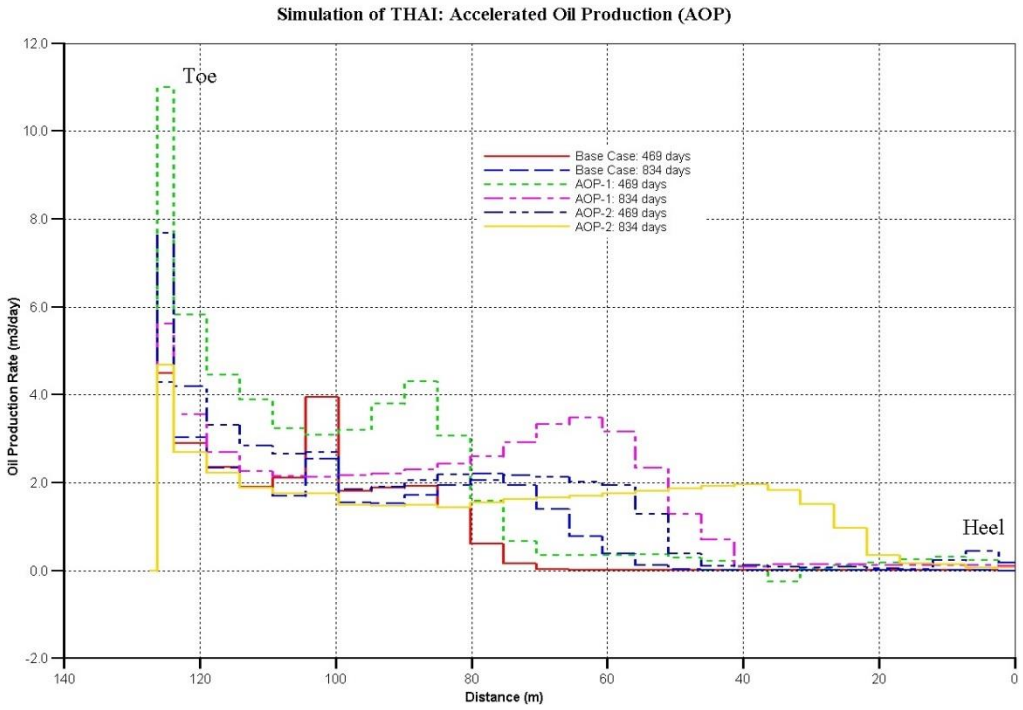

Fig. 7.7: Oil rate along the HP well and at different times

7.2.3 Effect of Oil Layer Thickness

All the models have the same field scale reservoir dimensions, and the same well arrangement (i.e. SLD) as that shown in Fig. 5.22b. The reservoir thickness,

however, was decreased from 24 m in the first model to 16 m and 8 m respectively. As can be seen in Tab. 7.2, during the 104 days of PIHC, the steam injection rate was varied based on the reservoir thickness.

Tab. 7.2: Average steam injection rate for the PIHC

Reservoir thickness (m)	Average saturated steam injection rate (bbl day^{-1}) at 5500 kPa and with quality of 0.8
24	400 max. of (495)
16	327 max. of (330)
8	165 max. of (165)

At the end of the PIHC, apart from fully establishing communication between the wells, the following oil is recovered.

Tab. 7.3: Oil recovery at the end of the 104 days of PIHC

Reservoir thickness (m)	Cumulative Oil Recovered (m^3)	%OOIP Recovery
24	2883	3.10
16	2871	4.62
8	1255	4.04

The above values of the percent oil recovery (Tab. 7.3) at the end of the PIHC are quite similar to the 4 %OOIP recovery achieved in the experiment as well as the experimental model described in chapter 4. The cumulative oil produced, however, decreased with a decrease in reservoir thickness. When the reservoir thickness was decreased by 33.3% to 16 m from the 24 m, the cumulative oil produced at the end of the PIHC decreased by only 0.42%. This is because there was high enough volume of oil around the zone of the vertical injectors and the

steam injection rate was only 18% lower than in the case when the reservoir thickness is 24 m. On further decrease of reservoir thickness by 66.7% to 8 m from 24 m, the reduction in the cumulative oil production at the end of the PIHC was quite substantial – 56.5%.

As the air injection began at 104 days and at the rate of 20,000 Sm^3 day^{-1} regardless of the reservoir thickness, the oil production rate curves overlap each other (Fig. 7.8). When the reservoir thickness is 24 m or 16 m, the production rate was maintained the same throughout the 2 years of combustion. In the case of reservoir with thickness of 8.1 m, however, over 270 to 350 days, the oil rate steadily peaked reaching a maximum of 52 m^3/day before declining back to steady state rate of 36 m^3/day. The period of 270 to 350 days corresponds to when the combustion zone reached the heel of the horizontal producer and more oil flows from either side of the producer.

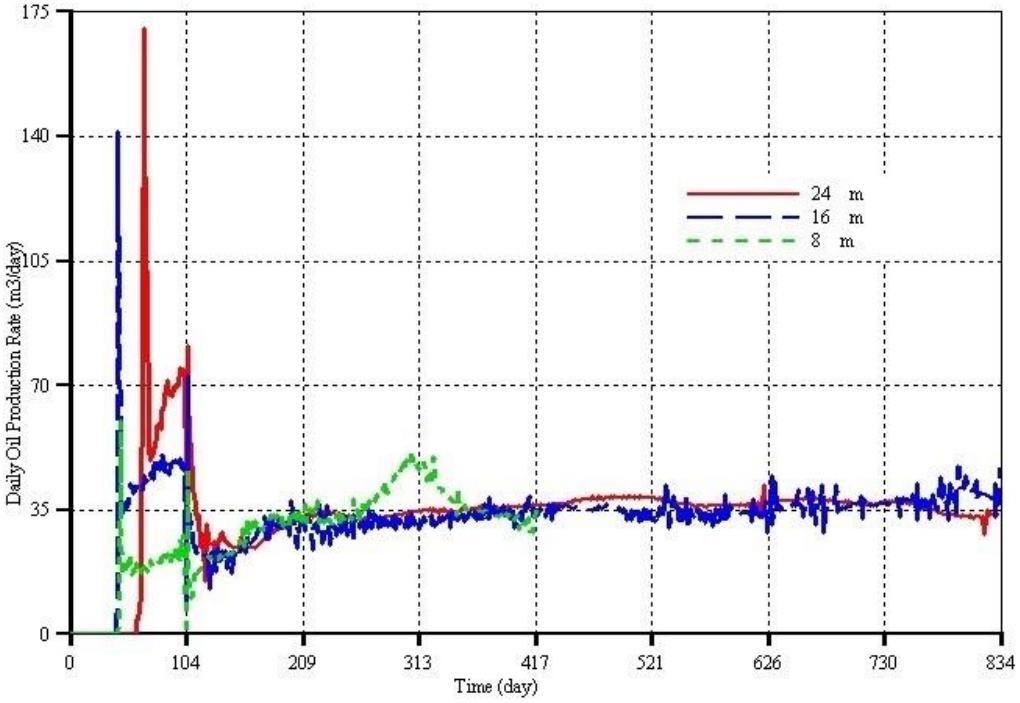

Fig. 7.8: Oil production rate for the different reservoir thickness

From Fig. 7.9, it can be seen that the reservoir thickness has negligible effect on the cumulative oil recovered. This is quite similar to the observation made by Xia et al. (2002a) when they studied the effect of oil layer thickness on oil recovery. It should be note, however, that the slight decrease in the cumulative oil production with the decrease in reservoir thickness was due to increased heat loss.

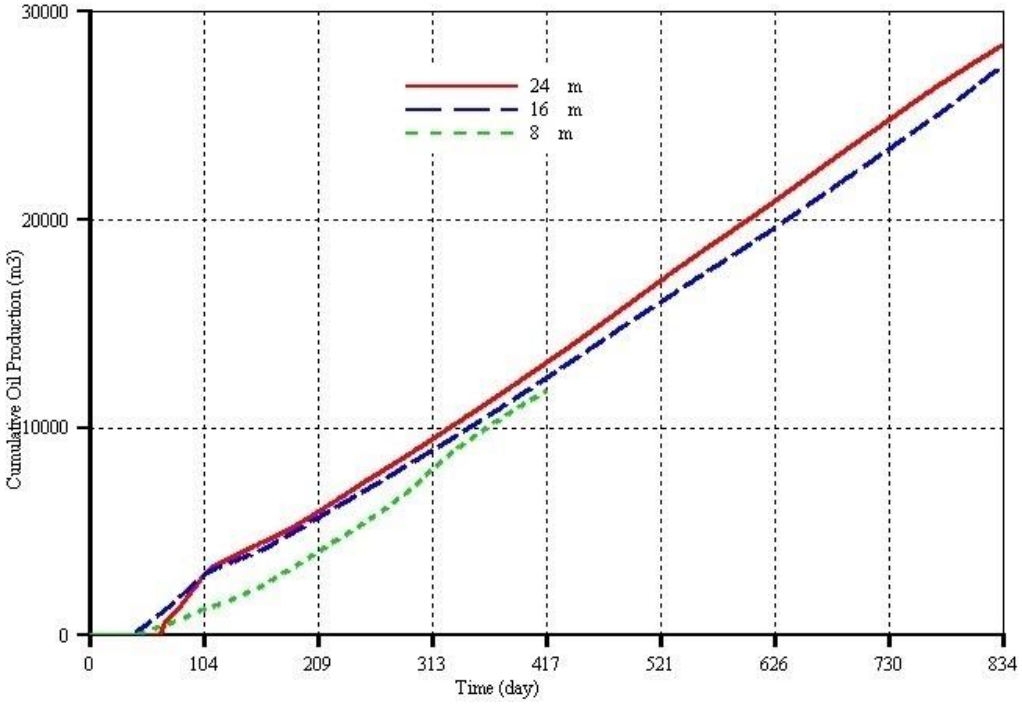

Fig. 7.9: Cumulative oil production for the different reservoir thickness

The smaller the oil layer thickness, the faster the advancement of the combustion front. This can be observed from Fig. 7.10, where the comparison is shown. The oxygen concentration profile shows that at 417 days, the combustion front covered one-third of the reservoir length when the reservoir thickness is 24 m. As the thickness is decreased by 33.3% to 16 m, the combustion covered ½ of the reservoir length at 417 days. By further decreasing the oil layer thickness to 8 m, the combustion front covered the whole reservoir length along the vertical

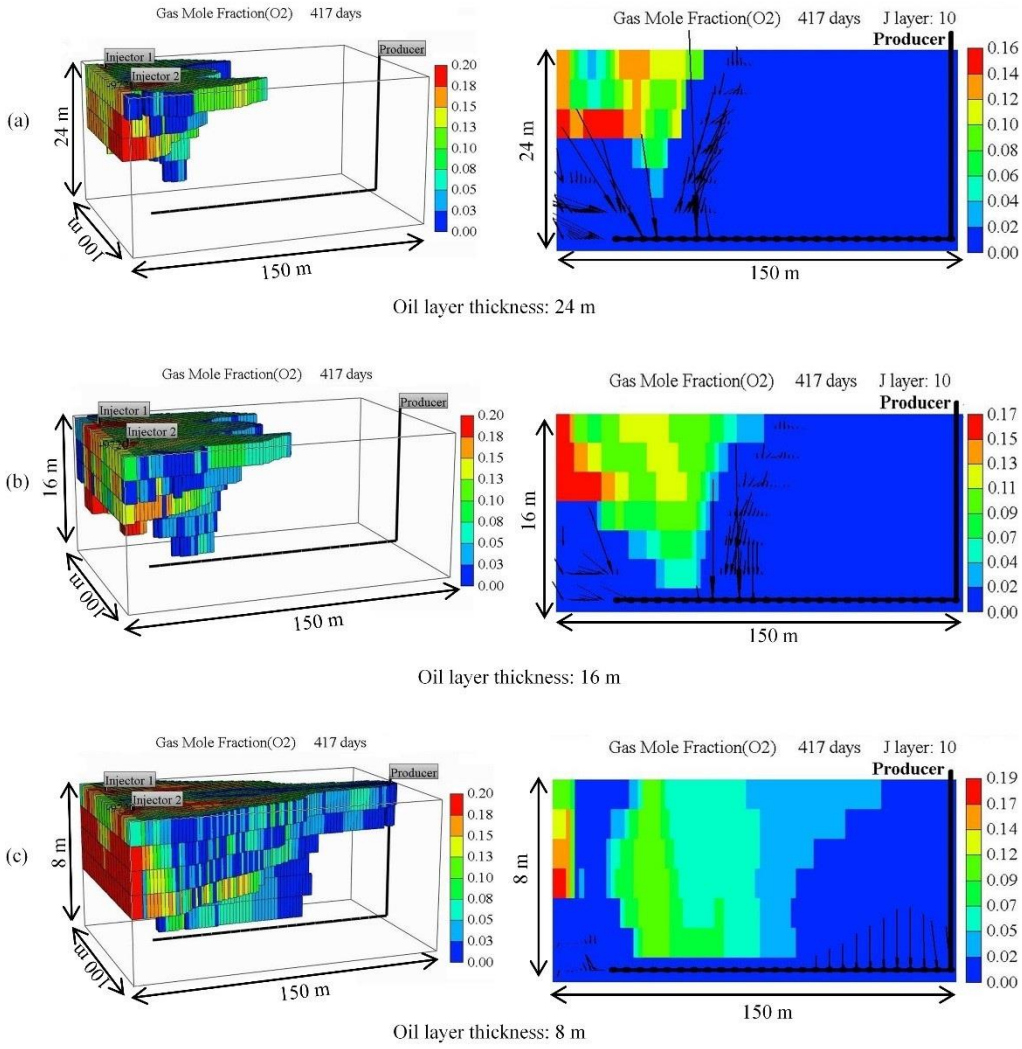

Fig. 7.10: The left side shows the 3D shape of the combustion front while on the right side, the oxygen concentration profiles along the vertical middle plane at 417 days are shown.

middle plane as can be seen from the 3D plots. Earlier, it has been shown from the experimental model that oxygen breakthrough only takes place once the combustion front propagates along the horizontal producer. From the profiles, it can be observed that as the oil layer thickness decreases, the combustion front advance quickly in all the three directions. This shows that at constant air injection rate, the lower the oil layer thickness, the earlier the oxygen production will begin take place. Further study, on an equivalent basis such as the same air flux, or running to completion, or both, is needed, however, in order to make comparisons from which decisive conclusion can be drawn.

7.2.4 Novel Well Arrangements

In order to maximise oil production compared to that obtained with the THAI process implemented in it is conventional form, different novel well configurations are explored. By using to horizontal producers with their toes located at the centre of the reservoir, it is proposed that combustion could be propagated in either direction. Here, the result of various well arrangements are compared with that of the conventional THAI process as base case. Further simulation study is needed, however, in order to compare the results at the final cut-off of oil production (i.e. when most of the reservoir is recovered and the oil production rate enters the declining rate period).

Model A01 consists of two inline horizontal producers with two vertical injectors arranged in a staggered line drive as depicted in Fig. 7.11. The injectors are located at the top of the reservoirs, 7 metres away from the toe of each horizontal producer, P2A and P2B.

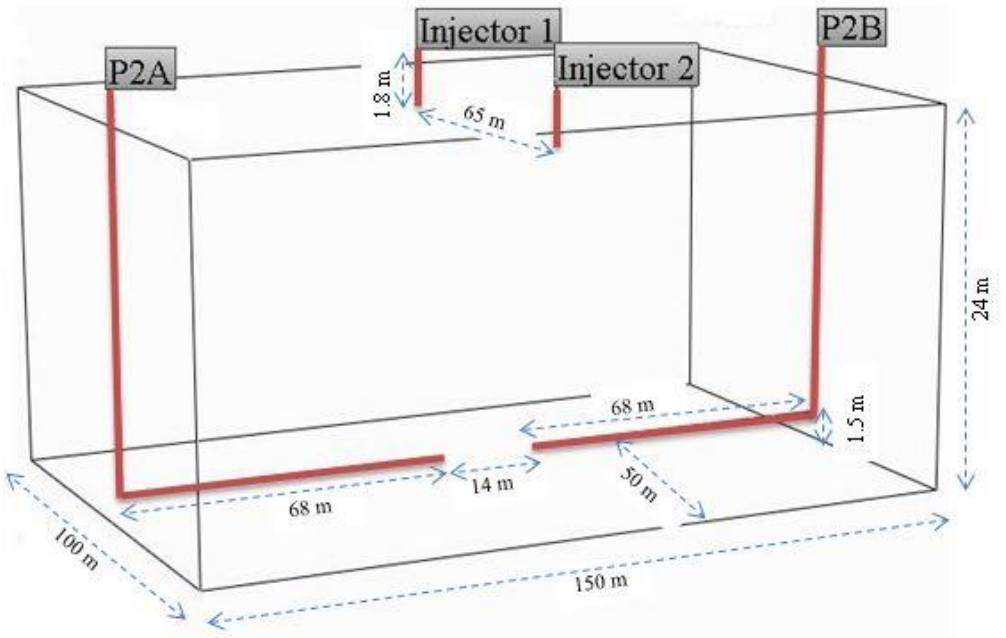

Fig. 7.11: Well arrangements in model A01

Model A02 is similar to A01 except that one short horizontal injector was used as opposed to the two vertical injectors used in A01. The horizontal injector was placed 17 metres vertically above the horizontal producers. From the toe to 8 m of each producer was directly under the horizontal injector as can be seen in Fig. 7.12 below.

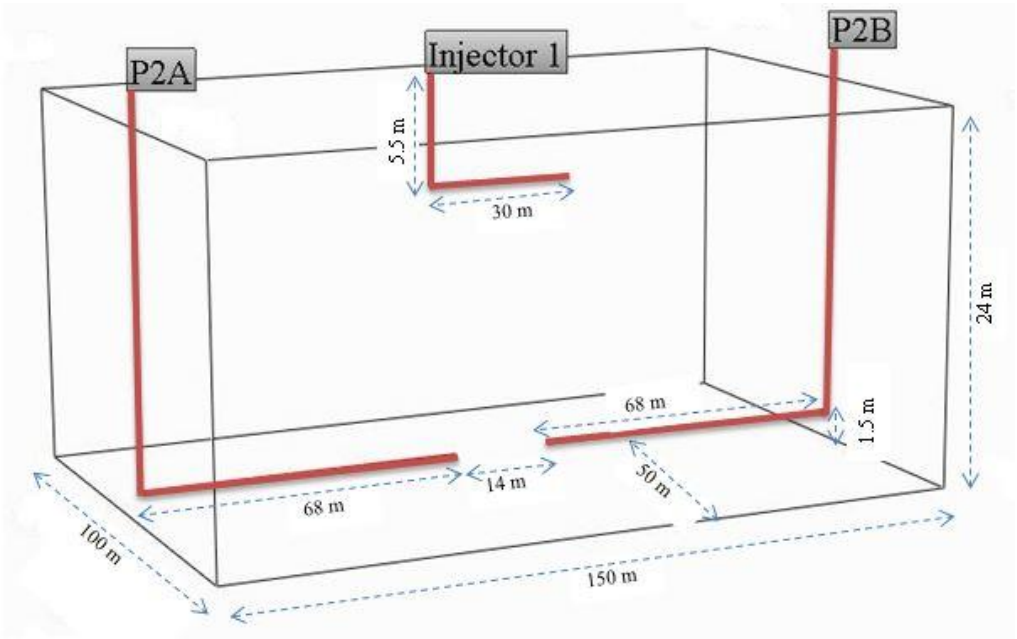

Fig. 7.12: Well arrangements in model A02

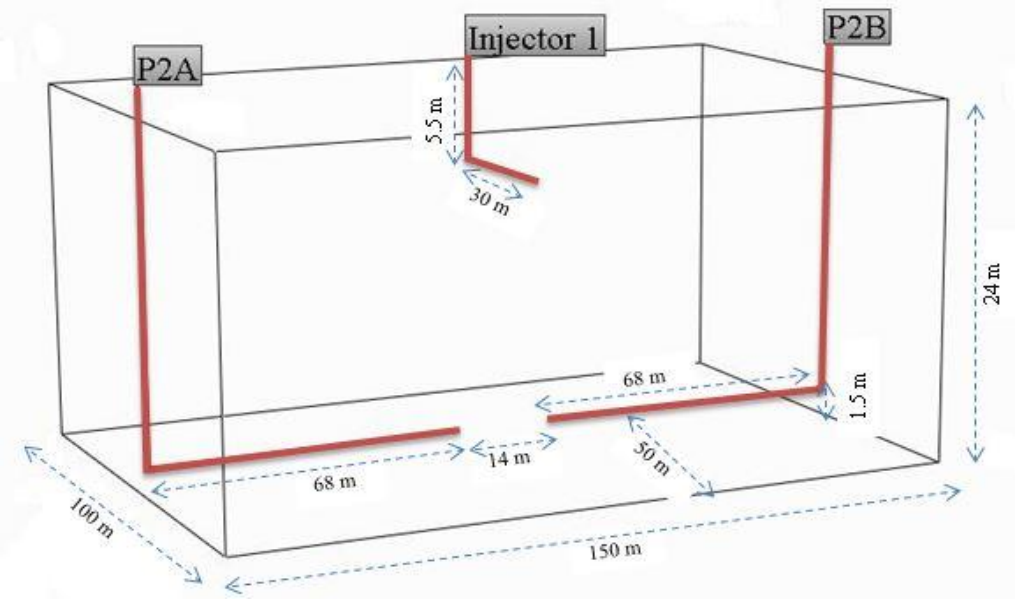

Fig. 7.13: Well arrangements in model A03

In **Model A03**, the producer wells arrangement and the length of the horizontal injector are respectively similar to those in model A02. In model A03, however, the horizontal injector is oriented perpendicularly to the axial direction of the horizontal producers as depicted below (Fig. 7.13).

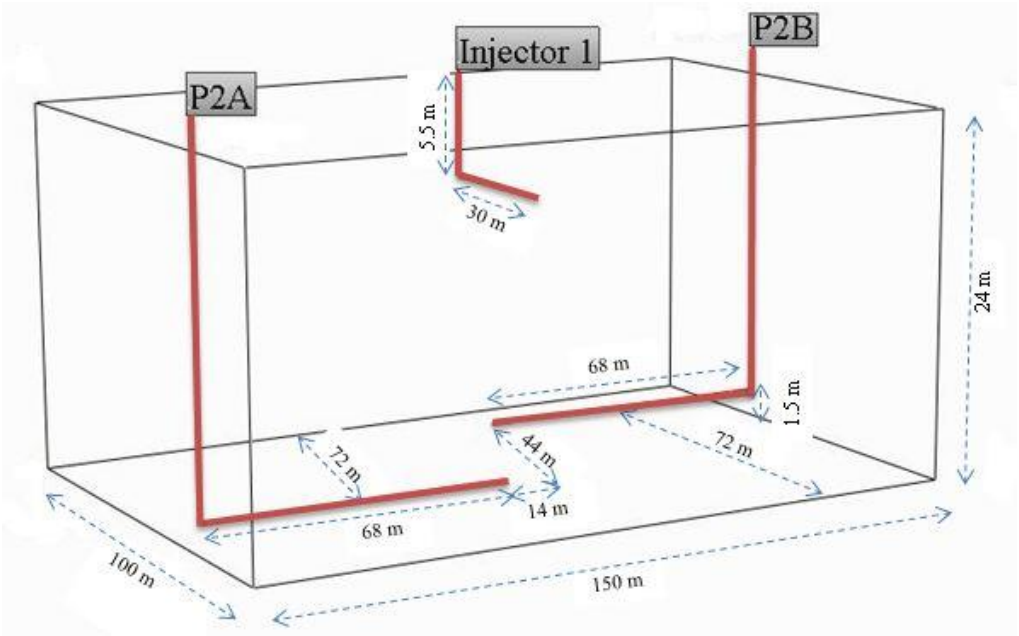

Fig. 7.14: Well arrangements in model A04

Model A04 has similar horizontal injector dimension and orientation as model A03. The horizontal producers, however, are no longer along the same plane. Producer P2A was placed 22 m to the right of the vertical mid-plane while producer P2B was placed 22 m to the left of vertical mid-plane. This means the two producers were separated by a distance of 44 m laterally as shown above (Fig. 7.14).

Model A05 is very similar to model A02 except that vertical injector in a direct line drive is used in model A05 as shown above (Fig. 7.15).

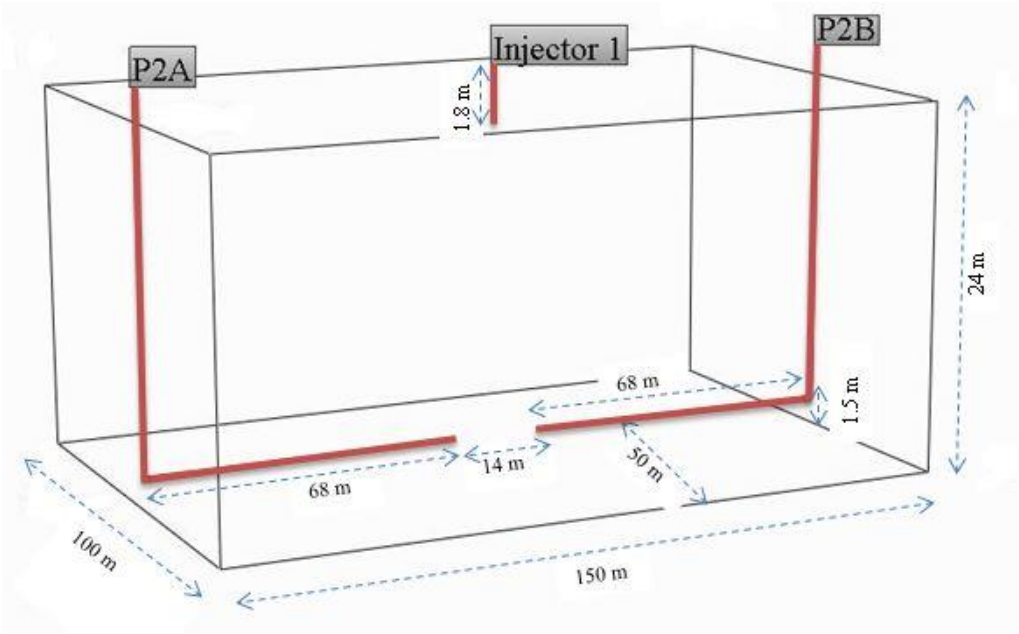

Fig. 7.15: Well arrangements in model A05

In each model, steam was injected at the rate of 495 bbl day^{-1} (CWE) for 104 days prior to the commencement of air injection, which was at combined rate of 20,000 Sm^3 day. In model A01, once air injection was started, the combined oil production rate declined gradually to a lowest value of 15 m^3 day^{-1} before increasing steadily and stabilising at around 46 m^3 day^{-1} after 374 days (Fig. 7.16). As the combustion front continued to expand and heat was further distributed into the reservoir, more mobilised oil was displaced towards the toe of producer P2B. This resulted in a further steady increase in the combined oil production rate at 620 days (Fig. 7.16). The small increase was sustained up to the end of the 2 years of combustion period while the oil rate stabilises at around 55 m^3 day^{-1}. For the two years of combustion only, Fig. 7.17 shows that the combined cumulative oil recovery was 30.78 %OOIP.

In model A02, as the air injection was started, the combined oil production rate declined steadily before reaching a lowest value of around 10 m^3 day^{-1} at 220

days (Fig. 7.16). As the combustion front expanded and heat was distributed into the reservoir, more oil was mobilised which resulted in a gradual increase in oil production rate before reaching a maximum value of 46 m^3 day^{-1} at 270 days after the start of air injection (Fig. 7.16). The combined oil production rate then decreased before it stabilised at 36 m^3 day^{-1} at 520 days up to the end of the two years of combustion period. The cumulative percent oil recovery due to the two years of combustion only is 25.50 %OOIP (Fig. 7.17). This is lower than in A01 by 8.25 %OOIP.

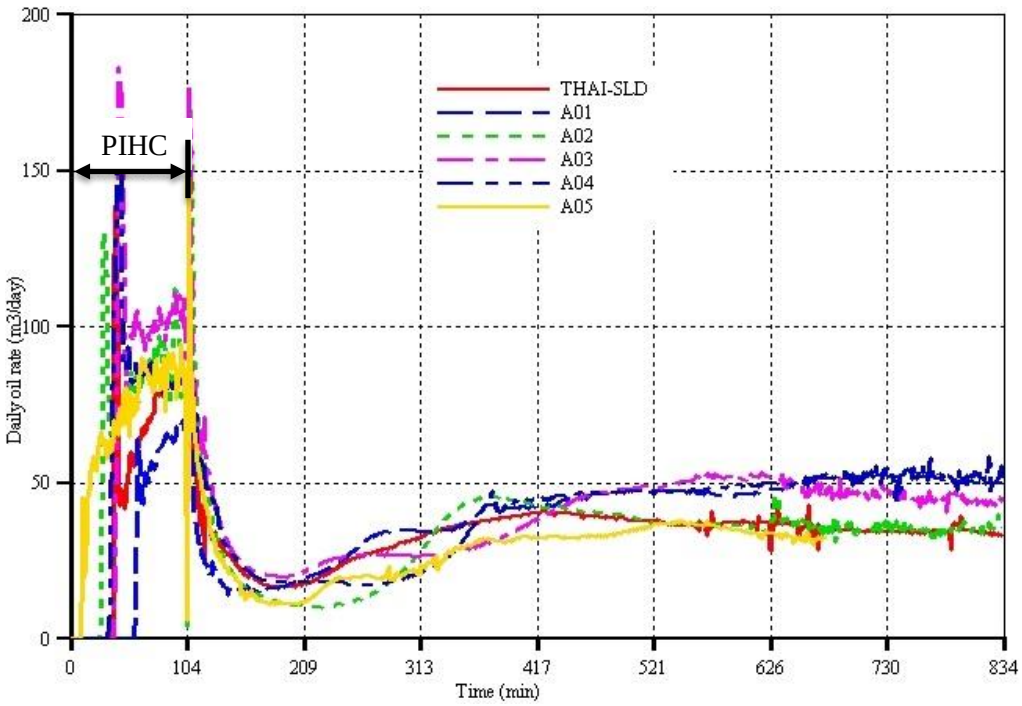

Fig. 7.16: Oil production rate for the various well arrangements

Just like in the previous two models, A01 and A02, the combined oil production rate dropped steadily to a lowest value of 20 m^3 day^{-1} 76 days after the start of air injection. The oil rate increased slowly before it stabilised to a value of around 50 m^3 day^{-1} up to the end of the combustion period (Fig. 7.16). The combined cumulative oil percent recovery due to combustion only is 30.5

%OOIP (Fig. 7.17), which is approximately the same as that achieved in model A01.

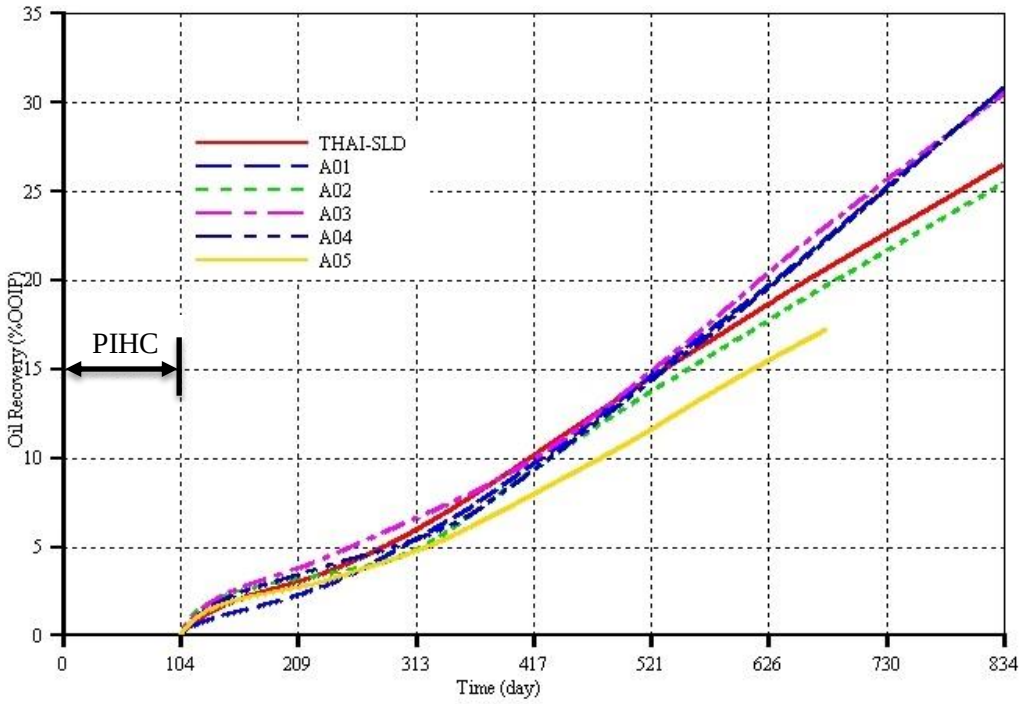

Fig. 7.17: Percent oil recovery due to two years of combustion only for the various well arrangements

As in the case of the previous models, A01, A02, and A03, the combined oil production rate, model A04 declined steadily upon air injection to a lowest value of 15 m^3 day^{-1} 36 days after the start of air injection. As the combustion heat is distributed within the reservoir, the oil production rate picked up and steadied out at around 47 m^3 day^{-1} after 520 days of combustion. The oil rate eventually became constant at around 53 m^3 day^{-1} up to the end of the two years of combustion (Fig. 7.16). The oil recovery for the two years of combustion only is 30.88 %OOIP, which is approximately the same as that achieved in model A01.

The arrangement in model A05 has the lowest oil recovery and significant oxygen production began as early as 130 days after the start of air injection. This

run was stopped after it was run for 676 days of process time as the time-step cut became too small and thus, the simulation too expensive to continue to be run.

From this preliminary study, it is found that at the end of the two years of combustion, models A01, A02, and A03 predicted larger cumulative oil recovery by 4.27, 3.99, and 4.37 %OOIP respectively compared to the original THAI process arranged in an SLD pattern. Therefore, it is concluded that further study should run each model until the most of the reservoir is produced. This would allow the overall oxygen utilisation, air-oil ratio (AOR), cumulative oil recovery, and the oil production rate to be compared and decisive conclusion to be drawn. It would also allow the stability of the combustion front in each model to be fully investigated.

7.2.5 Model Containing both the Cap rock and BW

The combined effect of the cap rock and BW on the THAI process has not be investigated in this thesis. As a consequence, the future work should look at how do the cap rock and BW affect the oil mobilisation and recovery, and the stability of the combustion front.

8. References

ABU, I. I., MOORE, R. G., MEHTA, S. A., URSENBACH, M. G., MALLORY, D. G., PEREIRA ALMAO, P. & CARBOGNANI ORTEGA, L. 2015. Upgrading of Athabasca Bitumen Using Supported Catalyst in Conjunction With In-Situ Combustion. *Journal of Canadian Petroleum Technology*.

ADEGBESAN, K., DONNELLY, J., MOORE, R. & BENNION, D. 1987. Low-Temperature Oxidation Kinetic Parameters for In-Situ Combustion Numerical Simulation. *SPE Reservoir Engineering,* 2**,** 573-582.

AKKUTLU, I. Y. & YORTSOS, Y. C. 2005. The effect of heterogeneity on in-situ combustion: Propagation of combustion fronts in layered porous media. *SPE Journal,* 10**,** 394-404.

ALBERTA-ENERGY. 2013. *Talk about Oil Sands* [Online]. Available: http://www.energy.gov.ab.ca/OilSands/pdfs/FactSheet_OilSands.pdf [Accessed 3rd January 2014].

ALEXANDER, J., MARTIN, W. L. & DEW, J. 1962. Factors affecting fuel availability and composition during in situ combustion. *Journal of Petroleum Technology,* 14**,** 1154-1164.

ALI, S. & MELDAU, R. 1979. Current steamflood technology. *Journal of Petroleum Technology,* 31**,** 1,332-1,342.

ALI, S. F. 2003. Heavy oil—evermore mobile. *Journal of Petroleum Science and Engineering,* 37**,** 5-9.

ALMEHAIDEB, R., ASHOUR, I. & EL-FATTAH, K. 2003. Improved K-value correlation for UAE crude oil components at high pressures using PVT laboratory data. *Fuel,* 82**,** 1057-1065.

ANAYA, I., LA CRUZ, R., ALVAREZ, A., GUTIERREZ, D., SKOREYKO, F. & CARD, C. Simulation Study for Designing an In-Situ Combustion Pilot in the Orinoco Belt of Venezuela: From Laboratory Studies to the Field Scale. Canadian Unconventional Resources and International Petroleum Conference, 2010.

AZIZ, K., AZIZ, K. & SETTARI, A. 1979. *Petroleum reservoir simulation*, Applied Science Publishers.

BAGCI, S. & KOK, M. V. 2004. Combustion reaction kinetics studies of Turkish crude oils. *Energy & fuels,* 18**,** 1472-1481.

BELGRAVE, J., MOORE, R. & URSENBACH, M. 1997. Comprehensive kinetic models for the aquathermolysis of heavy oils. *Journal of Canadian Petroleum Technology,* 36.

BELGRAVE, J., MOORE, R., URSENBACH, M. & BENNION, D. 1993. A comprehensive approach to in-situ combustion modeling. *SPE Advanced Technology Series,* 1**,** 98-107.

BIENTINESI, M., PETARCA, L., CERUTTI, A., BANDINELLI, M., DE SIMONI, M., MANOTTI, M. & MADDINELLI, G. 2013. A radiofrequency/microwave heating method for thermal heavy oil recovery based on a novel tight-shell conceptual design. *Journal of Petroleum Science and Engineering,* 107**,** 18-30.

BRANDT, A. R. 2008. Converting Oil Shale to Liquid Fuels: Energy Inputs and Greenhouse Gas Emissions of the Shell in Situ Conversion Process. *Environmental Science & Technology,* 42**,** 7489-7495.

BURGER, J., SOURIEAU, P. & COMBARNOUS, M. 1985. *Thermal methods of oil recovery*, Gulf Publishing Company, Book Division.

CAPP. 2015. *The Facts on Oil Sand* [Online]. Canada: Canadian Association of Petroleum Producers. Available: http://www.capp.ca/publications-and-statistics/publications/270274 [Accessed 01 July 2016].

CAVALLARO, A., GALLIANO, G., MOORE, R., MEHTA, S., URSENBACH, M., ZALEWSKI, E. & PEREIRA, P. 2008. In situ upgrading of Llancanelo heavy oil using in situ combustion and a downhole catalyst bed. *Journal of Canadian Petroleum Technology,* 47**,** 23-31.

CENOVUS-ENERGY. 2014. *Seam Assisted Gravity Drainage (SAGD)* [Online]. Available: http://www.cenovus.com/operations/technology/sagd.html [Accessed 05 January 2014].

CHEN, J. X., COATES, R. M., OLDAKOWSKI, K. & WIWCHAR, B. In Situ Combustion as a Followup Process to CHOPS. SPE Heavy Oil Conference Canada, 2012. Society of Petroleum Engineers.

CHEN, Q. 2009. *Assessing and improving steam-assisted gravity drainage: Reservoir heterogeneities, hydraulic fractures, and mobility control foams*.

CHHETRI, A. B. & ISLAM, M. R. 2008. A Critical Review of Electromagnetic Heating for Enhanced Oil Recovery. *Petroleum Science and Technology,* 26**,** 1619-1631.

CHUEH, P. & PRAUSNITZ, J. 1968. Calculation of high-pressure vapor-liquid equilibria. *Industrial & Engineering Chemistry,* 60**,** 34-52.

CINAR, M., CASTANIER, L. M. & KOVSCEK, A. R. 2011. Combustion Kinetics of Heavy Oils in Porous Media. *Energy & Fuels,* 25**,** 4438-4451.

CMG 2012. *Advanced Process and Thermal Reservoir Simulator,* Calgary, Alberta Canada, Computer Modelling Group Ltd.

COATES, R., LORIMER, S. & IVORY, J. Experimental and numerical simulations of a novel Top Down in-situ combustion process. SPE International Heavy Oil Symposium, 1995. Society of Petroleum Engineers.

COATS, K. Some observations on field-scale simulation of the in-situ combustion process. SPE Reservoir Simulation Symposium, 1983. Society of Petroleum Engineers.

CROOKSTON, R., CULHAM, W. & CHEN, W. 1979. A numerical simulation model for thermal recovery processes. *Society of Petroleum Engineers Journal,* 19**,** 37-58.

DESCHAMPS, R., GUY, N., PREUX, C. & LERAT, O. 2012. Analysis of Heavy Oil Recovery by Thermal EOR in a Meander Belt: From Geological to Reservoir Modeling. *Oil Gas Sci. Technol. – Rev. IFP Energies nouvelles,* 67**,** 999-1018.

DIM, P., HART, A., WOOD, J., MACNAUGHTAN, B. & RIGBY, S. P. 2015. Characterization of pore coking in catalyst for thermal down-hole upgrading of heavy oil. *Chemical Engineering Science,* 131**,** 138-145.

FATEMI, S., GHOTBI, C. & KHARRAT, R. 2009. Effect of wells arrangement on the performance of toe-to-heel air injection. *Brazilian Journal of Petroleum and Gas,* 3.

FATEMI, S. M. 2012. The Effect of Geometrical Properties of Reservoir Shale Barriers on the Performance of Steam-assisted Gravity Drainage (SAGD). *Energy Sources, Part A: Recovery, Utilization, and Environmental Effects,* 34**,** 2178-2191.

FERDOUS, D., DALAI, A. & ADJAYE, J. 2006. Hydrodenitrogenation and hydrodesulfurization of heavy gas oil using NiMo/Al2O3 catalyst containing

boron: Experimental and kinetic studies. *Industrial & engineering chemistry research,* 45**,** 544-552.

FERZIGER, J. H. & PERIC, M. 2001. *Computational Methods for Fluid Dynamics*, Springer Berlin Heidelberg.

FOGLER, H. S. 2006. *Elements of Chemical Reaction Engineering*, Prentice Hall PTR.

FROMENT, G. F., BISCHOFF, K. B. & DE WILDE, J. 2010. *Chemical Reactor Analysis and Design, 3rd Edition*, John Wiley & Sons, Incorporated.

GATES, I. D. & LARTER, S. R. 2014. Energy efficiency and emissions intensity of SAGD. *Fuel,* 115**,** 706-713.

GRAY, M. R., MCCAFFREY, W. C., HUQ, I. & LE, T. 2004. Kinetics of Cracking and Devolatilization during Coking of Athabasca Residues. *Industrial & Engineering Chemistry Research,* 43**,** 5438-5445.

GREAVES, M. & BENTAHER, A. 2007. Exothermicity characteristics of Wolf Lake heavy oil, Athabasca tar sand and medium heavy Clair oil. *J. Can. Pet. Technol,* 46**,** 1-4.

GREAVES, M., DONG, L. & RIGBY, S. 2012a. Simulation study of the toe-to-heel air injection three-dimensional combustion cell experiment and effects in the mobile oil zone. *Energy & Fuels,* 26**,** 1656-1669.

GREAVES, M., DONG, L. & RIGBY, S. 2012b. Validation of Toe-to-Heel air-injection bitumen recovery using 3D combustion-cell results. *SPE Reservoir Evaluation & Engineering,* 15**,** 72-85.

GREAVES, M., DONG, L. L. & RIGBY, S. P. Determination of Limits to Production in THAI. SPE Heavy Oil Conference Canada, 2012c. Society of Petroleum Engineers.

GREAVES, M., XIA, T., IMBUS, S. & NERO, V. THAI-CAPRI Process: Tracing Downhole Upgrading of Heavy Oil. Canadian International Petroleum Conference, 2004. Petroleum Society of Canada.

GREAVES, M., XIA, T. X. & TURTA, A. T. 2008. Stability of THAI (TM) process - Theoretical and experimental observations. *Journal of Canadian Petroleum Technology,* 47**,** 65-73.

GUTIERREZ, D., SKOREYKO, F., MOORE, R., MEHTA, S. & URSENBACH, M. 2009. The challenge of predicting field performance of air injection projects based on laboratory and numerical modelling. *Journal of Canadian Petroleum Technology,* 48**,** 23-33.

GUTIERREZ, D., URSENBACH, M. G., MOORE, R. G. & MEHTA, S. A. Oil Recovery from Thin Heavy Oil Reservoirs: The Case of the Combined Thermal Drive Pilot in the Morgan Field. SPE Heavy Oil Conference and Exhibition, 2011. Society of Petroleum Engineers.

HART, A., GREAVES, M. & WOOD, J. 2015. A comparative study of fixed-bed and dispersed catalytic upgrading of heavy crude oil using-CAPRI. *Chemical Engineering Journal,* 282**,** 213-223.

HART, A., LEEKE, G., GREAVES, M. & WOOD, J. 2014a. Down-hole heavy crude oil upgrading by CAPRI: Effect of hydrogen and methane gases upon upgrading and coke formation. *Fuel,* 119**,** 226-235.

HART, A., LEEKE, G., GREAVES, M. & WOOD, J. 2014b. Downhole heavy crude oil upgrading using CAPRI: effect of steam upon upgrading and coke formation. *Energy & Fuels,* 28**,** 1811-1819.

HART, A., SHAH, A., LEEKE, G., GREAVES, M. & WOOD, J. 2013. Optimization of the CAPRI process for heavy oil upgrading: effect of

hydrogen and guard bed. *Industrial & Engineering Chemistry Research*, 52**,** 15394-15406.

HASCAKIR, B., BABADAGLI, T. & AKIN, S. 2010. Field-Scale Analysis of Heavy-Oil Recovery by Electrical Heating. *SPE Reservoir Evaluation & Engineering*, 13**,** 131-142.

HAYASHITANI, M., BENNION, D., DONNELLY, J. & MOORE, R. Thermal cracking models for Athabasca oil sands oil. SPE Annual Fall Technical Conference and Exhibition, 1978.

HWANG, M., JINES, W. & ODEH, A. 1982. An In-Situ Combustion Process Simulator With a Moving-Front Representation. *Society of Petroleum Engineers Journal*, 22**,** 271-279.

HYNE, N. J. 2001. *Nontechnical Guide to Petroleum Geology, Exploration, Drilling, and Production*, Penn Well Corporation.

HYNE, N. J. 2012. *Nontechnical Guide to Petroleum Geology, Exploration, Drilling, and Production*, PennWell Corporation.

HYSYS. 2016. *A Property Methods and Calculations* [Online]. Available: http://people.clarkson.edu/~wwilcox/Design/HYSYSpropSelect.pdf [Accessed 10 August 2016].

IEA. 2013a. *Key World Energy Statistics* [Online]. Available: http://www.iea.org/ [Accessed 22 Dec 2013].

IEA. 2013b. *World Energy Outlook 2013 Factsheet* [Online]. Available: http://www.worldenergyoutlook.org/ [Accessed 22 Dec 2013].

ITO, Y. & CHOW, A. K.-Y. 1988. A field scale in-situ combustion simulator with channeling considerations. *SPE reservoir engineering*, 3**,** 419-430.

JHA, K. & CHAKMA, A. 1999. Heavy-oil recovery from thin pay zones by electromagnetic heating. *Energy sources,* 21**,** 63-73.

JIA, N., MOORE, R., MEHTA, S. & URSENBACH, M. 2006. Kinetic modelling of thermal cracking and low temperature oxidation reactions. *Journal of Canadian Petroleum Technology,* 45.

KALOGERAKIS, N. & LUUS, R. 1983. Improvement of Gauss-Newton method for parameter estimation through the use of information index. *Industrial & engineering chemistry fundamentals,* 22**,** 436-445.

KAPADIA, P. R., KALLOS, M. S. & GATES, I. D. 2013. A new kinetic model for pyrolysis of Athabasca bitumen. *The Canadian Journal of Chemical Engineering,* 91**,** 889-901.

KAPADIA, P. R., KALLOS, M. S. & GATES, I. D. 2015. A review of pyrolysis, aquathermolysis, and oxidation of Athabasca bitumen. *Fuel Processing Technology,* 131**,** 270-289.

KHANSARI, Z., GATES, I. D. & MAHINPEY, N. 2012. Detailed study of low-temperature oxidation of an Alaska heavy oil. *Energy & Fuels,* 26**,** 1592-1597.

KOVSCEK, A., CASTANIER, L. & GERRITSEN, M. 2013. Improved Predictability of In-Situ-Combustion Enhanced Oil Recovery. *SPE Reservoir Evaluation & Engineering,* 16**,** 172-182.

LAU, E. 2001. Basal combustion-A recovery technology for heavy oil reservoirs underlain by bottom water. *Journal of Canadian Petroleum Technology,* 40.

LE RAVALEC, M., MORLOT, C., MARMIER, R. & FOULON, D. 2009. Heterogeneity impact on SAGD process performance in mobile heavy oil reservoirs. *Oil & Gas Science and Technology-Revue de l'IFP,* 64**,** 469-476.

LEE, B. I. & EDMISTER, W. C. 1971. A generalized method for predicting vapor-liquid equilibrium. *AIChE Journal,* 17**,** 1412-1418.

LEE, S., SPEIGHT, J. G. & LOYALKA, S. K. 2007. *Handbook of Alternative Fuel Technologies*, Taylor & Francis.

LEVINTER, M. E., MEDVEDEVA, M. I., PANCHENKOV, G. M., ASEEV, Y. G., NEDOSHIVIN, Y. N., FINKEL'SHTEIN, G. B. & GALIAKBAROV, M. F. 1966. Mechanism of coke formation in the cracking of component groups in petroleum residues. *Chemistry and Technology of Fuels and Oils,* 2**,** 628-632.

LIANG, J., GUAN, W., JIANG, Y., XI, C., WANG, B. & LI, X. 2012. Propagation and control of fire front in the combustion assisted gravity drainage using horizontal wells. *Petroleum Exploration and Development,* 39**,** 764-772.

LIM, G., COATES, R. & IVORY, J. 2008. Gravity stable combustion processes for Athabasca oil sand reservoirs.

LIN, C., CHEN, W., LEE, S. & CULHAM, W. 1984. Numerical simulation of combustion tube experiments and the associated kinetics of in-situ combustion processes. *Old SPE Journal,* 24**,** 657-666.

LIU, H., FANG, X., ZHANG, G., ZHANG, Z., LU, C. & DONG, X. Feasibility of the Steam-Assisted-Gravity-Drainage Process in Offshore Heavy Oil Reservoirs with Bottom Water. Offshore Technology Conference-Asia, 2014. Offshore Technology Conference.

MAHINPEY, N., AMBALAE, A. & ASGHARI, K. 2007. In situ combustion in enhanced oil recovery (EOR): A review. *Chemical Engineering Communications,* 194**,** 995-1021.

MARJERRISON, D. & FASSIHI, M. A procedure for scaling heavy-oil combustion tube results to a field model. SPE/DOE Enhanced Oil Recovery Symposium, 1992. Society of Petroleum Engineers.

MARTIN, W. L., ALEXANDER, J. D. & DEW, J. N. 1958. Process variables of in situ combustion. *Petroleum Transactions, AIME,* 213**,** 28-35.

MILLOUR, J., MOORE, R., BENNION, D., URSENBACH, M. & GIE, D. 1987. An Expanded Compositional Model For Lowtemperature Oxidation Of Athabasca Bitumen. *Journal of Canadian Petroleum Technology,* 26.

MOJARAB, M., HARDING, T. & MAINI, B. 2011. Improving the SAGD Performance by Introducing a New Well Configuration. *Journal of Canadian Petroleum Technology,* 50**,** 9-18.

MOORE, R. G., LAURESHEN, C. J., BELGRAVE, J. D., URSENBACH, M. G. & MEHTA, S. R. 1995. In situ combustion in Canadian heavy oil reservoirs. *Fuel,* 74**,** 1169-1175.

MOSSOP, G. D. 1980. Geology of the Athabasca oil sands. *Science,* 207**,** 145-152.

NATIONAL-ENERGY-BOARD. 2013. *Canada's Energy Future 2013 - Energy Supply and Demand Projections to 2035 - An Energy Market Assessment* [Online]. Available: http://www.neb-one.gc.ca/clf-nsi/rnrgynfmtn/nrgyrprt/nrgyftr/2013/nrgftr2013-eng.html#s5 [Accessed 3rd January 2014].

NISSEN, A., ZHU, Z., KOVSCEK, A., CASTANIER, L. & GERRITSEN, M. 2015. Upscaling Kinetics for Field-Scale In-Situ-Combustion Simulation. *SPE Reservoir Evaluation & Engineering,* 18**,** 158-170.

OVALLES, C. & RODRIGUEZ, H. 2008. Extra Heavy Crude Oil Downhole Upgrading Using Hydrogen Donors Under Cyclic Steam Injection Conditions: Physical and Numerical Simulation Studies. *Journal of Canadian Petroleum Technology,* 47**,** 43-51.

PAITAKHTI OSKOUEI, S. J., MOORE, R. G., MAINI, B. & MEHTA, S. 2011. Feasibility of In-Situ Combustion in the SAGD Chamber. *Journal of Canadian Petroleum Technology,* 50**,** 31-44.

PETROBANK. 2008. *Oil Analysis* [Online]. Available: http://www.energy.alberta.ca/ [Accessed 26 August 2015].

PETROBANK 2010. Annual Progress Report (2008) for White Sands Experimental Project.

PETROBANK. 2013. *Petrobank Reports Q2 2013 Financial Results and Operational Update* [Online]. Available: http://www.petrobank.com/news [Accessed 20 May 2014].

PETROBANK. 2014a. *Petrobank and Touchstone to Combine to Create a High Growth, Fully Capitalized Oil Company* [Online]. Calgary, Alberta: Petrobank. Available: http://www.touchstoneexploration.com/files/5128.PBG-2014-March6.pdf [Accessed 09 May 2016].

PETROBANK. 2014b. *Petrobank Announces Q1 2014 Financial and Operating Results* [Online]. Available: http://www.petrobank.com/news [Accessed 20 May 2014].

PETROBANK. 2014c. *Touchstone and Petrobank Announce Court Approval of Plan of Arrangement* [Online]. Calgary, Alberta: Petrobank. Available: http://www.touchstoneexploration.com/files/5125.PBG-2014-April30.pdf [Accessed 09 May 2016].

PHILLIPS, C. R., HAIDAR, N. I. & POON, Y. C. 1985. Kinetic models for the thermal cracking of athabasca bitumen: the effect of the sand matrix. *Fuel,* 64**,** 678-691.

POOLADI-DARVISH, M. & MATTAR, L. 2002. SAGD operations in the presence of overlying gas cap and water layer-effect of shale layers. *Journal of Canadian Petroleum Technology,* 41.

PRAY, H. A., SCHWEICKERT, C. E. & MINNICH, B. H. 1952. Solubility of Hydrogen, Oxygen, Nitrogen, and Helium in Water at Elevated Temperatures. *Industrial & Engineering Chemistry,* 44**,** 1146-1151.

PROWSE, D. R., WALLACE, E. D., LOTT, R. K., DAIGNEAULT, L. E., SHELLY, N., IVORY, J., KUMAR, D., FRAUENFELD, T. & SINGH, B. 1983. Some Physical Properties of Bitumen and Oil Sand. *In:* DEPARTMENT, O. S. R. (ed.). Edmonton, Alberta: Alberta Research Council.

RADMANESH, R., CHAN, E. & GRAY, M. R. 2008. Modeling of mass transfer and thermal cracking during the coking of Athabasca residues. *Chemical Engineering Science,* 63**,** 1683-1691.

RANGEL-GERMAN, E. R., SCHEMBRE, J., SANDBERG, C. & KOVSCEK, A. R. 2004. Electrical-heating-assisted recovery for heavy oil. *Journal of Petroleum Science and Engineering,* 45**,** 213-231.

RAZZAGHI, S., KHARRAT, R., VOSSOUGHI, S. & RASHTCHIAN, D. 2008. Feasibility Study of Auto Ignition in In-situ Combustion Process. *Journal of the Japan Petroleum Institute,* 51**,** 287-297287.

ROJAS, J., RUIZ, J. & VARGAS, J. Numerical Simulation of an EOR Process of Toe to Heel Air Injection (THAI)-Finding the Best Well Pattern. SPE EOR Conference at Oil & Gas West Asia, 2010.

SAHNI, A., KUMAR, M., KNAPP, R. B. & LIVERMORE, L. 2000. Electromagnetic heating methods for heavy oil reservoirs. *paper SPE,* 62550.

SALAZAR-SOTELO, D., MAYA-YESCAS, R., MARIACA-DOMÍNGUEZ, E., RODRÍGUEZ-SALOMÓN, S. & AGUILERA-LÓPEZ, M. 2004. Effect of hydrotreating FCC feedstock on product distribution. *Catalysis today,* 98**,** 273-280.

SANDS, G. O. 2014. *May River* [Online]. Available: http://www.grizzlyoilsands.com/operations/may-river [Accessed 22 May 2014].

SHAH, A., FISHWICK, R., LEEKE, G., WOOD, J., RIGBY, S. & GREAVES, M. 2011. Experimental optimization of catalytic process in situ for heavy-oil and bitumen upgrading. *Journal of Canadian Petroleum Technology,* 50**,** 33-47.

SHAH, A., FISHWICK, R., WOOD, J., LEEKE, G., RIGBY, S. & GREAVES, M. 2010. A review of novel techniques for heavy oil and bitumen extraction and upgrading. *Energy & Environmental Science,* 3**,** 700-714.

SHELL 2006. Plan of Operations: Shell Frontier Oil and Gas Inc. Oil Shale Test Project. Shell Frontier Oil and Gas Inc.

SHELL. 2014. *Technology - Mahogony Oil Shale Project* [Online]. Available: http://www.shell.us/aboutshell/projects-locations/mahogany/technology.html [Accessed 23 May 2014].

STITT, H., MARIGO, M. & WILKINSON, S. 2015. How Good is Your Model? *Johnson Matthey Technology Review,* 59**,** 74-89.

SUGIANTO, S. & BUTLER, R. 1990. The production of conventional heavy oil reservoirs with bottom water using steam-assisted gravity drainage. *Journal of Canadian Petroleum Technology,* 29.

THOMAS, F., MOORE, R. & BENNION, D. 1985. Kinetic parameters for the high-temperature oxidation of in-situ combustion coke. *Journal of Canadian Petroleum Technology,* 24.

TOUCHSTONE. 2014. *Touchstone Provides Operational Update* [Online]. Calgary, Alberta: Touchstone. Available: http://www.touchstoneexploration.com/files/5327.Q3-2014-Operational-Update-FINAL.pdf [Accessed 09 May 2016].

TOUCHSTONE. 2015a. *Touchstone Announces 2015 Third Quarter Results and Elimination of Net Debt; Updates Trinidad Acquisition* [Online]. Calgary, Alberta: Touchstone. Available: http://www.touchstoneexploration.com/files/6136.November%2013%202015%20-%20Q3%202015%20Results%20-%20FINAL%20-%20Formatted%20(002).pdf [Accessed 09 May 2016].

TOUCHSTONE. 2015b. *Touchstone Announces Dawson Disposition and Confirms Credit Facility Borrowing Base* [Online]. Calgary, Alberta: Touchstone. Available: http://www.touchstoneexploration.com/files/6122.July%2022,%202015%20

-%20Dawson%20Disposition%20&%20Credit%20Facility.pdf [Accessed 09 May 2016].

TOUCHSTONE. 2016. *Touchstone Announces Kerrobert Saskatchewan Disposition* [Online]. Calgary, Alberta: Touchstone. Available: http://www.touchstoneexploration.com/files/6149.January%2020,%202016%20-%20Kerrobert%20Disposition%20-%20FINAL.pdf [Accessed 09 May 2016].

TURTA, A. 2014. *Conventional ISC* [Online]. Available: http://insitucombustion.ca/conventional.htm [Accessed 05 January 2014].

TURTA, A., COATES, R. & GREAVES, M. In-Situ Combustion in the Oil Reservoirs Underlain by Bottom Water. Review of the Field and Laboratory Tests. Canadian International Petroleum Conference, 2009. Petroleum Society of Canada.

TURTA, A. & SINGHAL, A. 2004. Overview of short-distance oil displacement processes. *Journal of Canadian Petroleum Technology,* 43.

VERMEULEN, F. & CHUTE, F. 1983. Electromagnetic techniques in the in-situ recovery of heavy oils. *journal of microwave power,* 18**,** 1.

VERMEULEN, F. & MCGEE, B. 2000. In situ electromagnetic heating for hydrocarbon recovery and environmental remediation. *Journal of Canadian Petroleum Technology,* 39**,** 24-28.

WEISSMAN, J., KESSLER, R., SAWICKI, R., BELGRAVE, J., LAURESHEN, C., MEHTA, S., MOORE, R. & URSENBACH, M. 1996. Down-hole catalytic upgrading of heavy crude oil. *Energy & fuels,* 10**,** 883-889.

WEISSMAN, J. G. 1997. Review of processes for downhole catalytic upgrading of heavy crude oil. *Fuel Processing Technology,* 50**,** 199-213.

WIEHE, I. A. 1993. A phase-separation kinetic model for coke formation. *Industrial & Engineering Chemistry Research,* 32**,** 2447-2454.

XIA, T., GREAVES, B., WERFILLI, M. & RATHBONE, R. THAI Process-Effect of Oil Layer Thickness on Heavy Oil Recovery. Canadian International Petroleum Conference, 2002a.

XIA, T. & GREAVES, M. 3-D physical model studies of downhole catalytic upgrading of Wolf Lake heavy oil using THAI. Canadian International Petroleum Conference, 2001.

XIA, T. & GREAVES, M. 2002. Upgrading Athabasca tar sand using toe-to-heel air injection. *Journal of Canadian Petroleum Technology,* 41.

XIA, T., GREAVES, M. & TURTA, A. 2005. Main mechanism for stability of THAI-Toe-to-Heel Air Injection. *Journal of Canadian Petroleum Technology,* 44.

XIA, T., GREAVES, M., WERFILLI, W. & RATHBONE, R. Downhole conversion of Lloydminster heavy oil using THAI-CAPRI process. SPE International Thermal Operations and Heavy Oil Symposium and International Horizontal Well Technology Conference, 2002b.

YANG, X. & GATES, I. 2009. Combustion Kinetics of Athabasca Bitumen from 1D Combustion Tube Experiments. *Natural Resources Research,* 18**,** 193-211.

YOUNGREN, G. K. 1980. Development and application of an in-situ combustion reservoir simulator. *Society of Petroleum Engineers Journal,* 20**,** 39-51.

YUI, S. M. & SANFORD, E. C. 1989. Mild hydrocracking of bitumen-derived coker and hydrocracker heavy gas oils: kinetics, product yields, and product properties. *Industrial & engineering chemistry research,* 28**,** 1278-1284.

ZHAO, R., CHEN, Y., HUAN, R., CASTANIER, L. M. & KOVSCEK, A. R. 2015. An experimental investigation of the in-situ combustion behavior of Karamay crude oil. *Journal of Petroleum Science and Engineering,* 127**,** 82-92.

ZHU, Z., GERRITSEN, M. G., KOVSCEK, A. R. & THIELE, M. R. 2011. *Efficient simulation of thermal enhanced oil recovery processes,* Stanford University.

ZHU, Z., ZENG, F., ZHAO, G. & LAFORGE, P. 2013. Evaluation of the hybrid process of electrical resistive heating and solvent injection through numerical simulations. *Fuel,* 105**,** 119-127.

9. Appendices

Appendix A: Validation of lab scale models

Here, the results from four different models based on different kinetics schemes are compared.

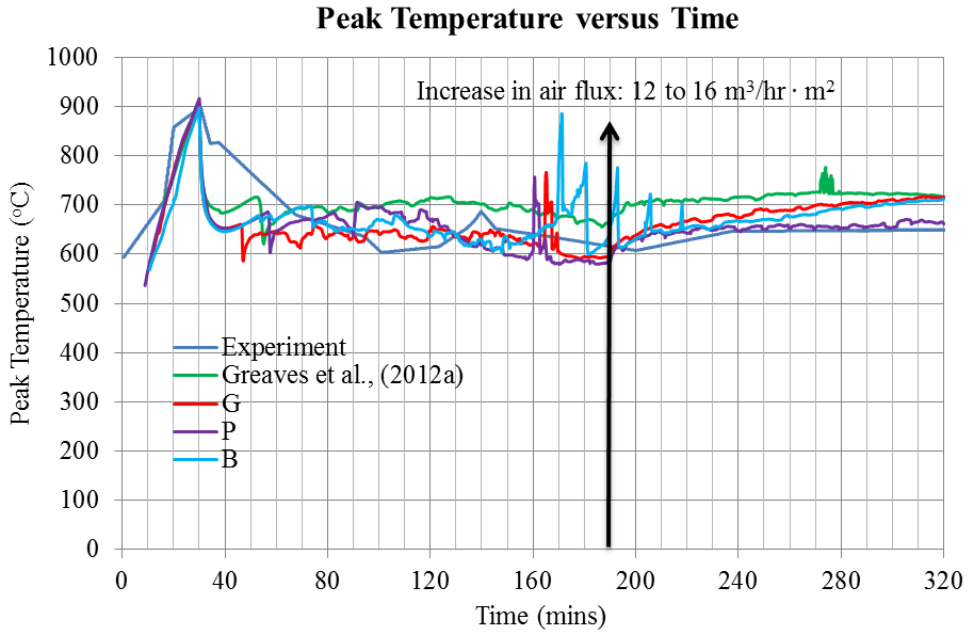

Fig. 9.1: Peak temperature

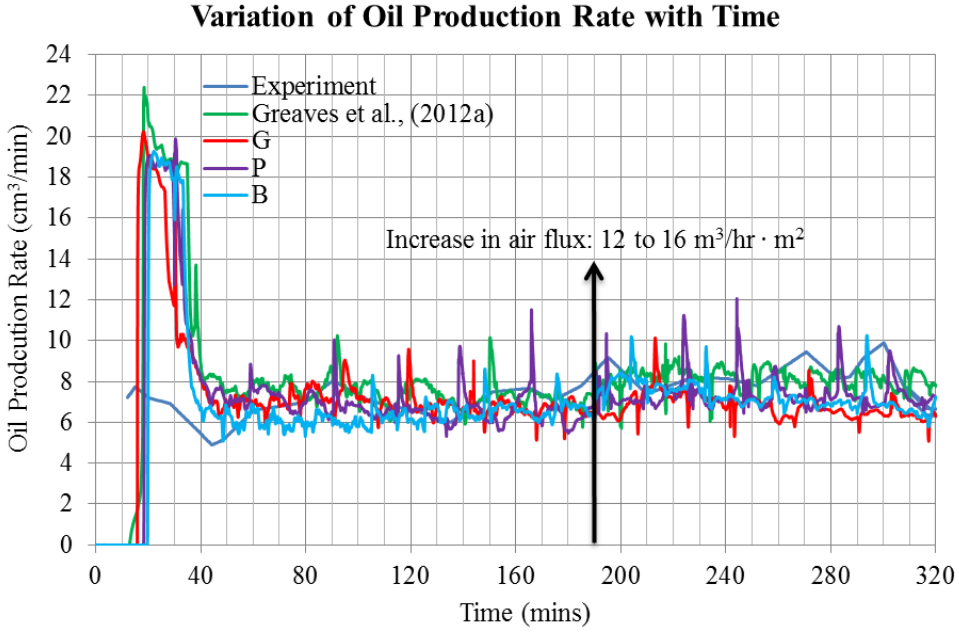

Fig. 9.2: Oil production rate

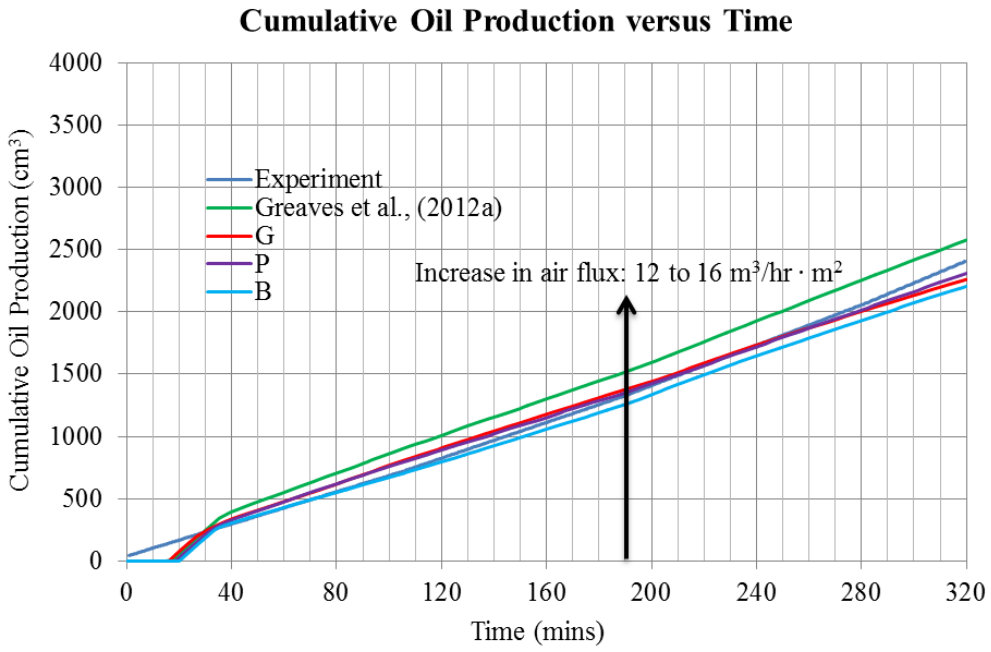

Fig. 9.3: Cumulative oil production

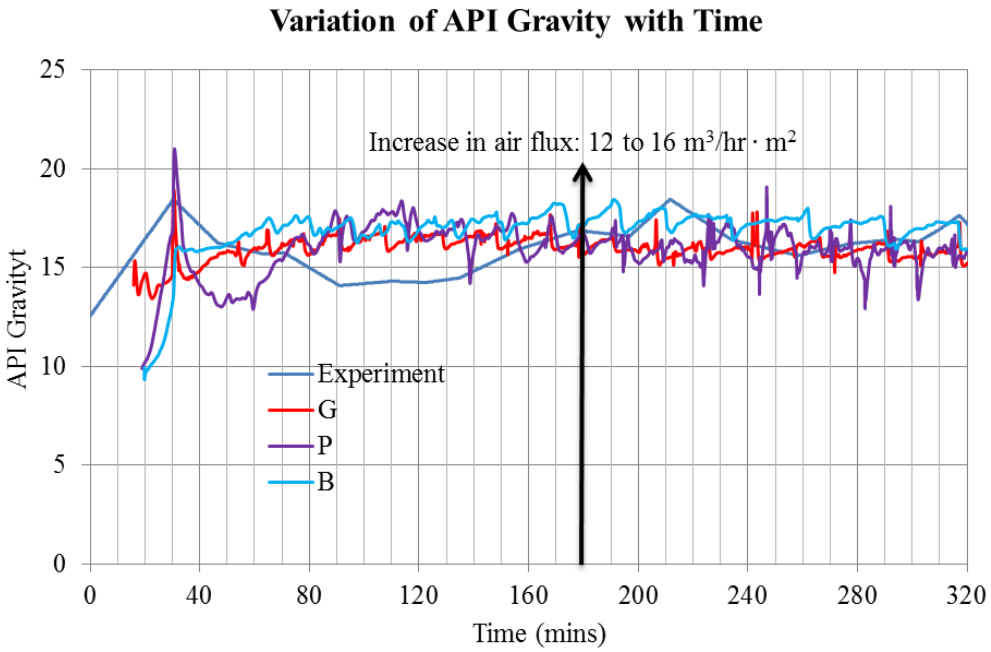

Fig. 9.4: API gravity

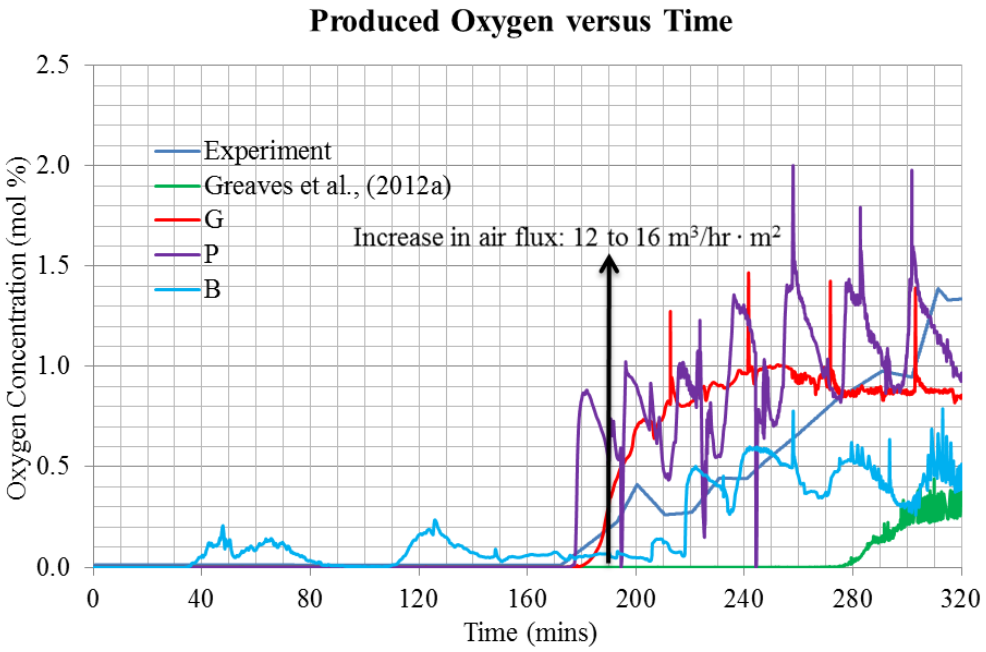

Fig. 9.5: Produced oxygen mole percent

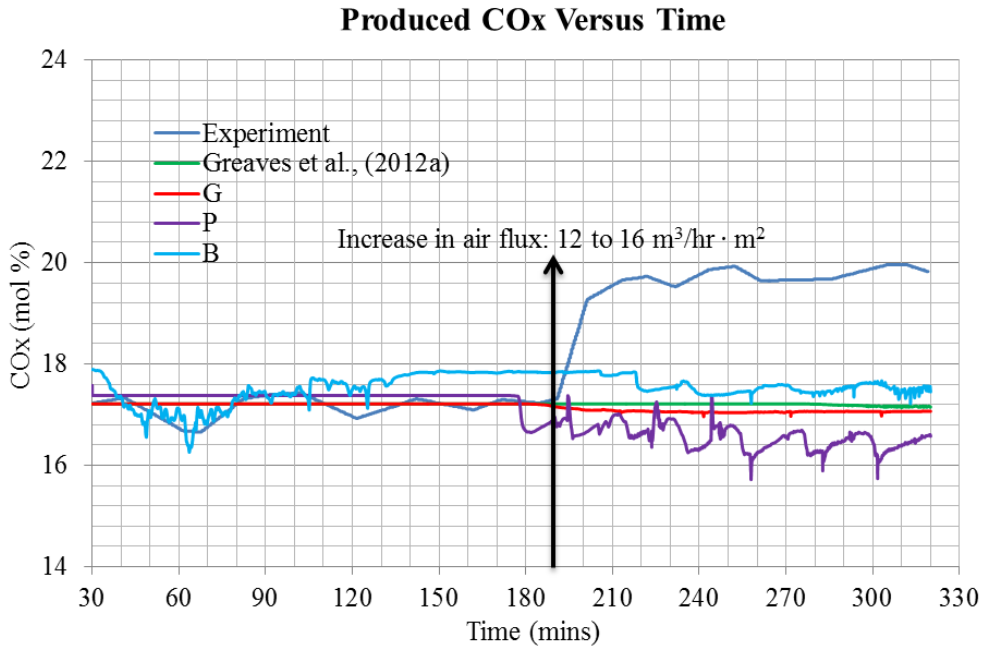

Fig. 9.6: Produced CO_X mole percent

Appendix B: Effect of PIHC Method Based on Model G

Effect of pre-ignition heating cycle (PIHC) method on the THAI process based on model G.

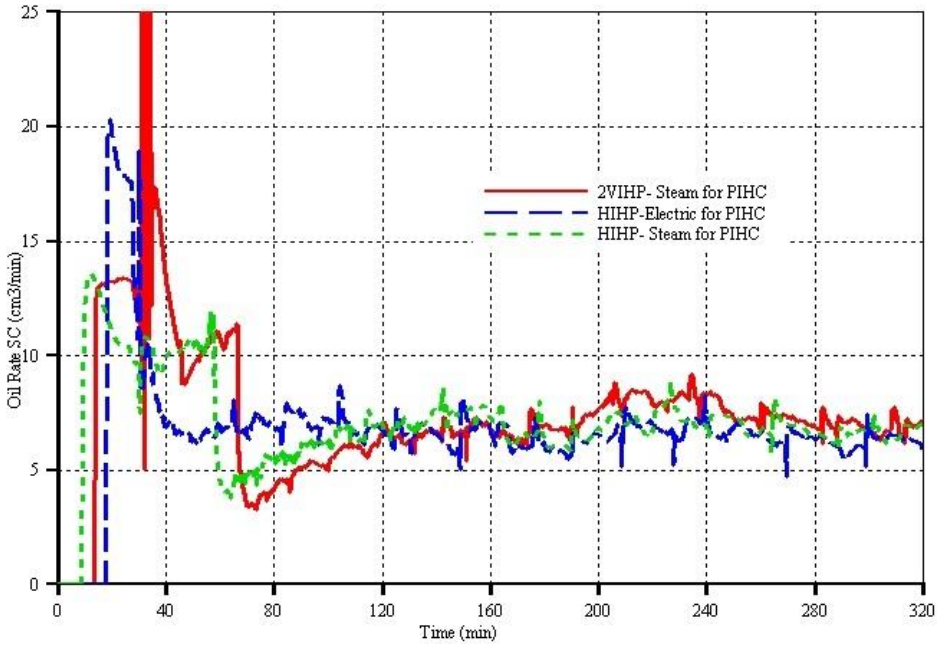

Fig. 9.7: Oil production rate

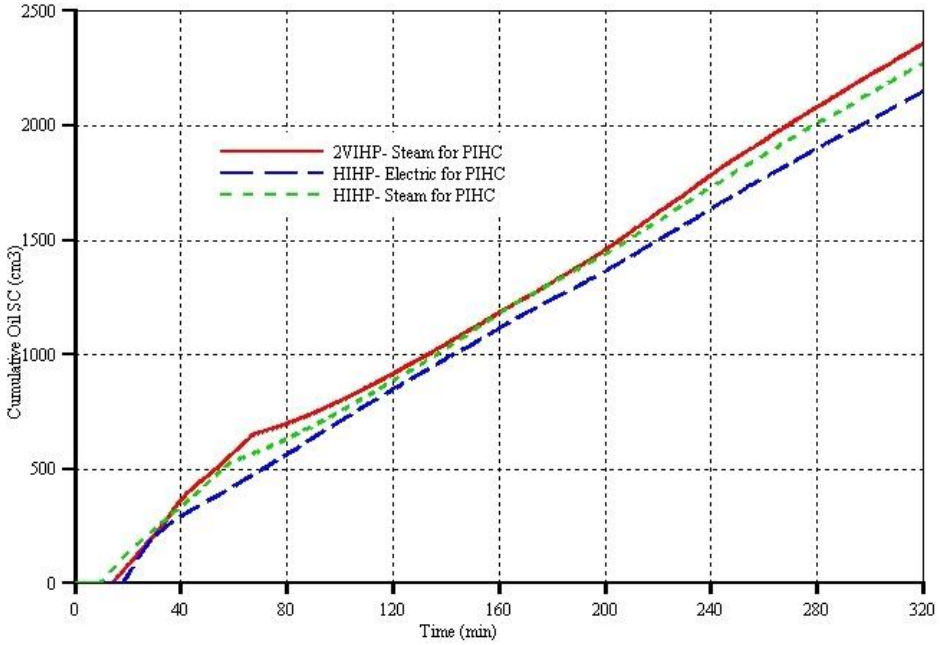

Fig. 9.8: Cumulative oil production

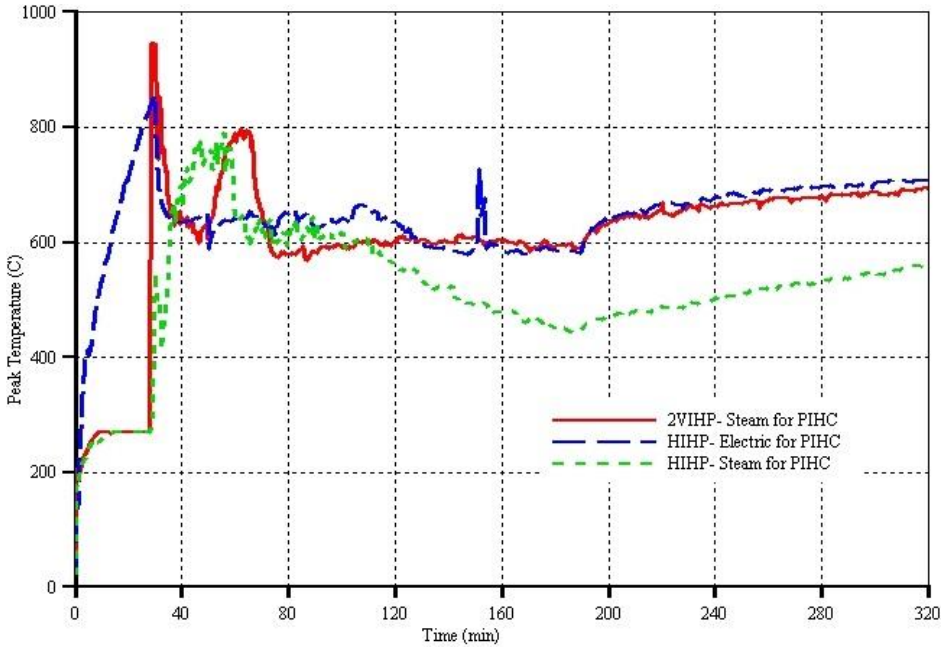

Fig. 9.9: Peak temperature

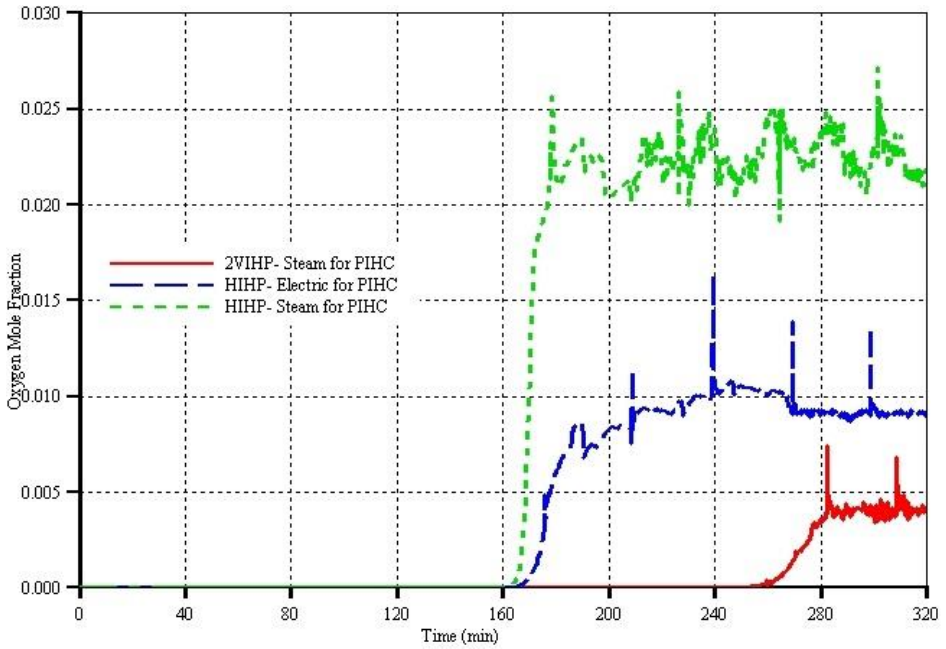

Fig. 9.10: Produced oxygen mole fraction

Appendix C: Simulation of CAPRI™

Introduction

In-situ catalysis is the reverse of the current industrial practice in which crude oil is taken to the processing facilities. Instead, the processing facilities are deployed in the native oil location for catalytic upgrading. This is succinctly captured by Weissman, (1997) as ‘‘bringing processing to the oil, rather than bringing oil to a process’’. As discussed in section 2.2.3 of chapter 2, downhole catalytic upgrading has the advantages of locking heavy oil impurities underground, providing high quality and easily transportable feed oil to refineries, minimising the need for surface upgrading facilities, and providing an environmentally friendly alternative means of achieving high value petroleum products. These have been demonstrated successfully at laboratory scale. However, no numerical model, either at laboratory or field scale, was developed to investigate the upgrading mechanism given that numerical simulation of THAI has shown that the mobile oil zone (MOZ), where the catalytic upgrading is envisaged, has temperatures of less than 300 ^{o}C. This is below what is require for the industrial hydro-treating catalysts to be effective and, thus, catalytic upgrading to take place.

Models Development

The THAI-CAPRI model is of the same dimensions as that of the experimental scale THAI model discussed in chapter 4 as can be seen in Fig. 9.11. It contains horizontal-injector (HI) and horizontal producer (HP) wells arranged in a staggered line drive (SLD). In addition, the THAI-CAPRI model has an annular catalyst layer emplaced around the HP well as indicated by the thick yellow

lines in Fig. 9.11. The model is discretised into 30 × 19 × 9 (i, j, k) gridblocks with the variable thickness in the latter two directions. Since the thickness of the combustion front is around 1 inch, to better capture it is dynamics, each gridblock is further refined into 3 sub-grids in **i** direction. This makes the total number of gridblocks, including those of the discretised wellbore, to be 19900.

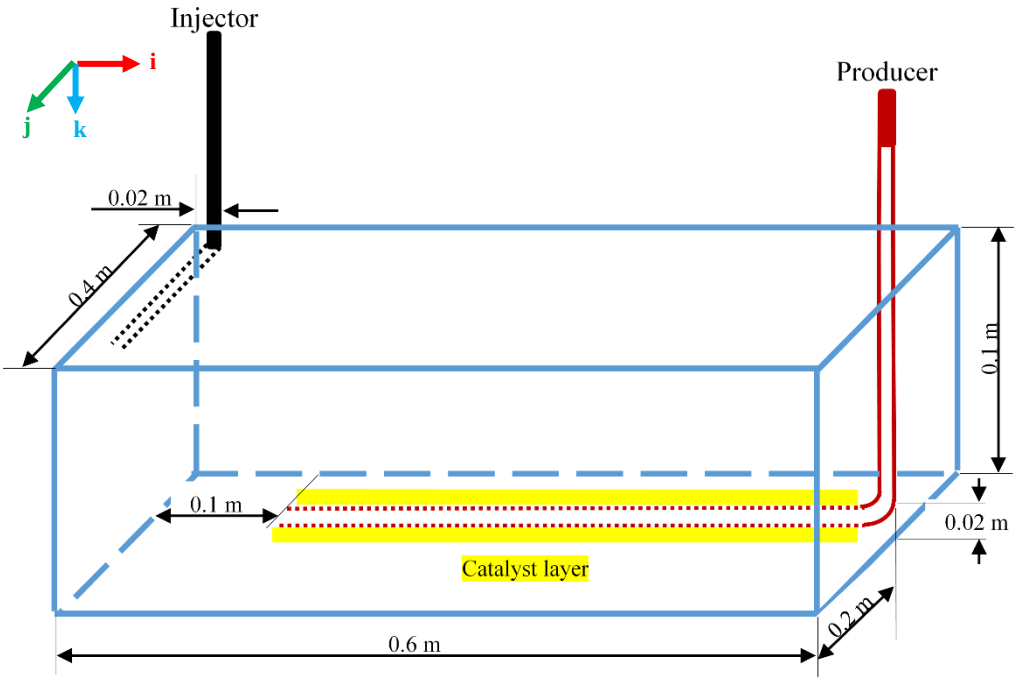

Fig. 9.11: 3D diagram of THAI-CAPRI with the annular catalyst layer shown by thick yellow line

PVT Data Generation for the CAPRI Produced Oil

In order to include the catalytic reactions in the numerical model, Hart et al., (2014a) provided the simulated distillation data for the THAI oil upgraded using CAPRI under nitrogen atmosphere and at process conditions of 425 ^{o}C and 20 bar. They employed the ASTM-D2887 method to obtain the boiling point distribution of the catalytically upgraded oil. To obtain the PVT data of the upgraded oil, the experimental distillation curve was inputted into Aspen HYSYS software and the Peng-Robinson Equation of State (PR-EOS) was used to fit a calculated distillation curve (Fig. 9.12). The calculated curve closely

matches the experimental curve except below 5 wt%. The deviation is because the model was set to split the upgraded oil into two pseudo-components which means large portion of heavier fractions, and thus more weight is given to their PVT data, in fitting the curve. However, it was observed that when the number of pseudo-components (i.e. the number of cuts) is increased, the deviation between the experimental and the calculated curves disappeared. As a result, the small deviation has been observed to not result in any noticeable error in the PVT data of the upgraded oil shown in Tab. 9.1.

Tab. 9.1: PVT data for light upgraded oil (LUO) and heavy upgraded oil (HUO)

Components	Split (mol%)	RMM (g/mol)	ρ (kgm^{-3})	T_c (^oC)	P_c (kPa)	Eccentricity
LUO	20.31	128.01	776.53	353.12	2448.61	0.39
HUO	79.69	252.50	850.48	502.19	1523.46	0.70

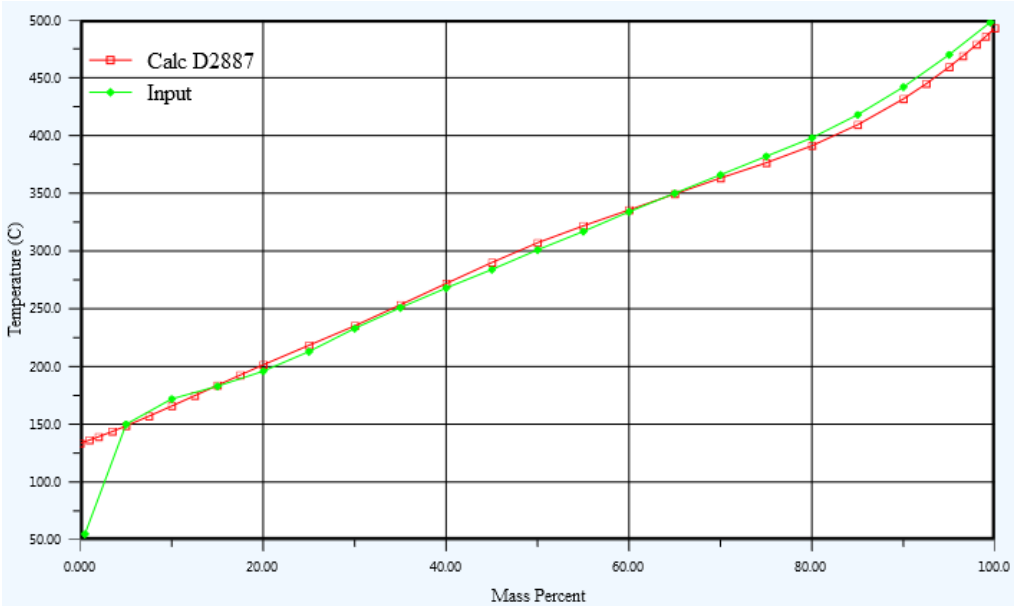

Fig. 9.12: Experimental and Calculated Distillation Curves for CAPRI Upgraded Oil

The split is achieved by considering that catalytic upgrading results in a substantial decrease in oil density. Therefore, the RMM, and, hence, the density of the respective CAPRI pseudo-components must be less than those of the THAI pseudo-components. The light upgraded oil (LUO) contains any hydrocarbon with boing point of at most 187 ^{o}C while the heavy upgraded oil (HUO) is the cut with hydrocarbons having boiling point of greater than 187 ^{o}C.

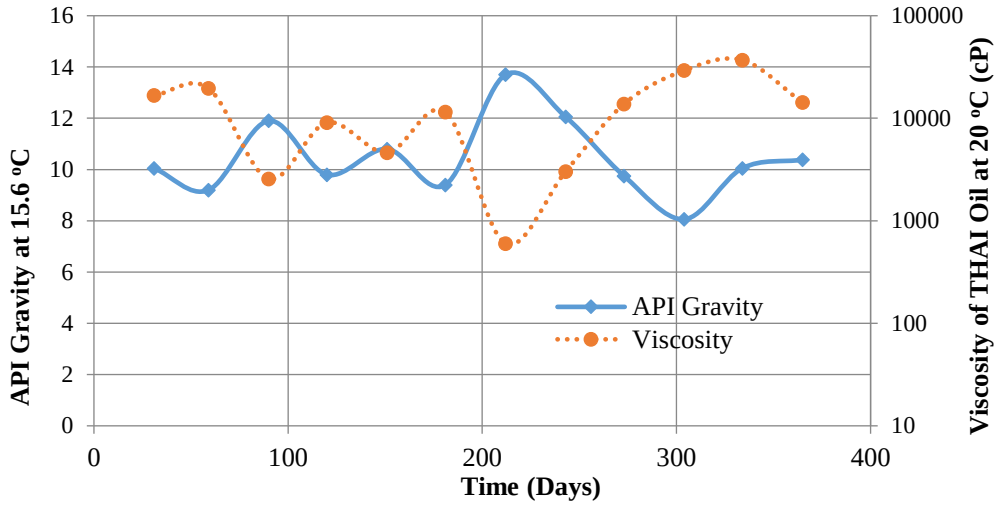

Fig. 9.13: API Gravity and Viscosity of THAI Oil from Producer P2 (Petrobank, 2008)

As shown in Fig. 9.13, the viscosity of the produced THAI oil from the horizontal producer, P2, in the Petrobank's Kerrobert field project is lower than that of the original bitumen by at least 79.6% (Petrobank, 2008). Therefore, to carry out the CAPRI study, Hart et al., (2014a) used THAI oil with viscosity of 1091 cP at 20 ^{o}C. They observed a further viscosity reduction of 92.8% when the THAI oil was CAPRI-processed under hydrogen atmosphere. It follows that around 99.96% reduction in viscosity could be achieved with THAI-CAPRI. This is very close to the 99.98% reduction in viscosity recorded by Abu et al., (2015) from the their dry combustion tube catalytic upgrading of Athabasca bitumen. Therefore, the CAPRI oil viscosity is taken as 0.0431% of the original

Athabasca bitumen viscosity. Similarly, the viscosity of the LUO is taken as 0.0431% of that of LC pseudo-component. This is justified given that their properties are quite close and that LUO is present in a lower fraction compared to LC. The viscosity of the HUO is then calculated using the logarithmic mixing rule (Fig. 9.14).

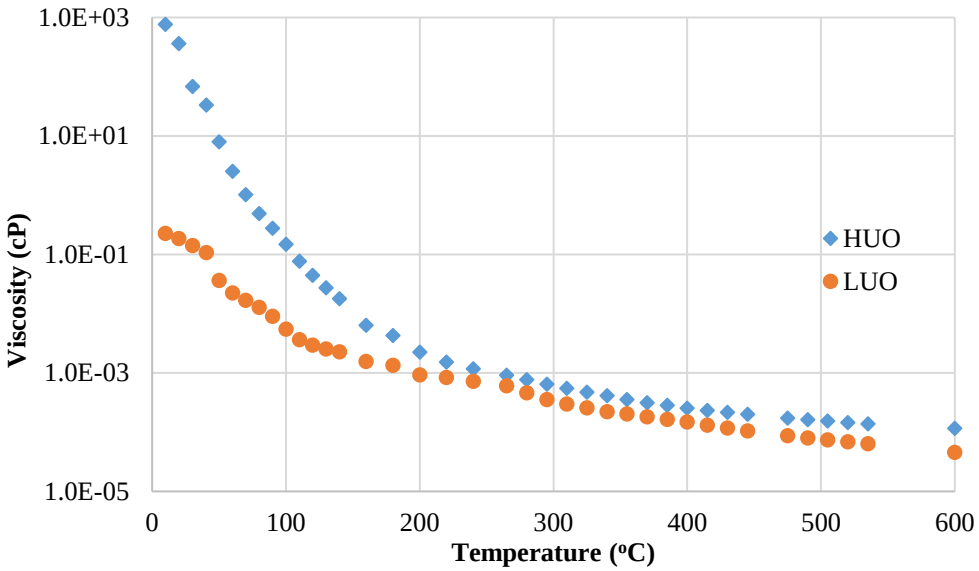

Fig. 9.14: Viscosities of the CAPRI Oil Pseudo-components

As during the modelling of THAI, which is presented in Chapter 4, the phase equilibrium K-values of the CAPRI oil pseudo-components are respectively estimated using Wilson equation (Almehaideb et al., 2003) and are presented in Fig. 9.15. These are included in the CAPRI model to account for phase change.

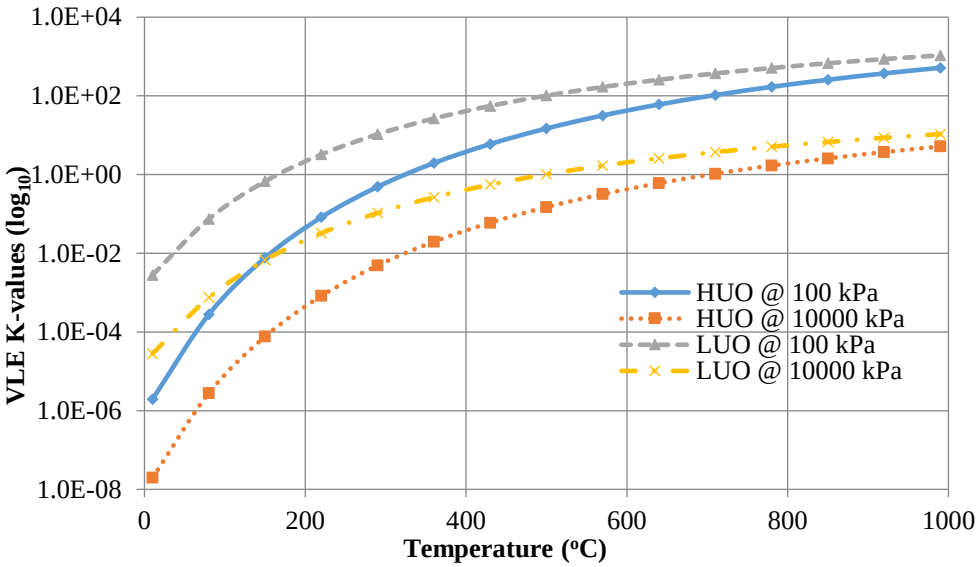

Fig. 9.15: VLE K-values for the CAPRI Oil Pseudo-components

Kinetics Scheme and Implementation

When CAPRI is coupled to the THAI process (i.e. THAI-CAPRI), catalytic reactions, in addition to the thermal cracking and combustion reactions, described in section 4.2.2.3 of Chapter 4, also take place. These catalytic reactions, that take place in the presence of hydrotreating catalyst under sufficient temperature and pressure, are mainly hydrodesulphurisation (HDS) and hydrodenitrogenation (HDN). However, they only take place in the presence of the main co-reactant, hydrogen, which experimental studies (Abu et al., 2015) showed to be generated during air injection enhanced heavy oil recovery. The generation of water vapour, and carbon monoxide from the combustion zone, the presence of hydrotreating catalyst, and, importantly, that of gaseous hydrocarbons, were observed to result in hydrogen generation via water-gas shift (WGS) and steam gasification (SG) reactions (Weissman et al., 1996; Weissman, 1997; Cavallaro et al., 2008; Hart et al., 2014b; Abu et al., 2015). The generalised form of the WGS and SG reactions is:

WGS: $CO + H_2O \leftrightarrow CO_2 + H_2$

SG: $C_xH_b + 2xH_2O \rightarrow xCO_2 + (2x + b/2)H_2$

However, the above reactions are not included in the model because of the unavailability of kinetics data which is obtained under the in-situ combustion. Instead, the hydrogen is injected together with the air. By varying the hydrogen-air ratio (HAR) from model to model, the effect of the concentration of the in-situ generated hydrogen is investigated. This is parallel to the study carried out by Shah et al.,(2011) and Hart et al., (2013), where hydrogen and flue gas mixture and pure hydrogen were injected into a microreactor to respectively simulate the effect of combustion gases on the THAI-CAPRI process.

The thermal cracking and combustion reactions, used in this model, are based on the modified Greaves et al., (2012a) scheme. Therefore, the HDS and HDN reactions are based on the HEAV and LITE pseudo-components making up the original THAI upgraded oil. For the catalytic reactions, the carbon-sulphur, and carbon-nitrogen bonds are respectively cleaved, thereby resulting in the formation of new carbon-hydrogen bond in either case. The substituted heteroatoms, hydrogen and nitrogen, combine with the hydrogen to form hydrogen sulphide and ammonia respectively. The reaction orders of the HDN and HDS, for the Athabasca bitumen-derived heavy gas oil, and with the respective to each oil pseudo-component, are first and three-half respectively (Yui and Sanford, 1989; Ferdous et al., 2006). Since there are two oil pseudo-components, and the HDS and HDN have different reaction orders, the catalytic reactions are represented by four balanced chemical reactions (Tab. 9.2).

Tab. 9.2: Balanced HDS and HDN reactions with their kinetics parameters

HDS and HDN reactions	Activation Energy (kJ/mol)	Frequency Factor (min^{-1})
HEAV + 19.932 H_2 ➔ 3.477 HUO + 0.585 H_2S	87	2.7×10^7
LITE + 3.286 H_2 ➔ 1.328 LUO + 0.194 H_2S	87	2.7×10^7
HEAV + 1.593 H_2 ➔ 3.477 HUO + 0.189 NH_3	75	1.0×10^6
LITE + 0.095 H_2 ➔ 1.328 HUO + 0.011 NH_3	75	1.0×10^6

The activation energy and frequency factor of the HDS, and HDN reactions are taken from Ferdous et al. (2006) and can be seen in Tab. 9.2. In each case, the same kinetics parameters are assigned to both the HEAV and LITE pseudo-components. The justification being only overall kinetics parameters are available, and therefore, the stoichiometry of each reaction will determine the extent of heteroatom removal.

To determine the stoichiometric coefficients of each reaction so that a chemically balanced equation is specified in STARS, the fractions of each of the two heteroatoms, sulphur and nitrogen, removed due to the catalytic action is used. This entails estimating the initial elemental composition of each pseudo-component based on the original elemental composition of Athabasca bitumen found in Prowse et al. (1983). Abu et al. (2015) found that, after catalytically upgrading Athabasca bitumen using dry in-situ combustion, a total of 35 % and 60 % sulphur and nitrogen respectively were removed from the original bitumen. As a result, this study assumes the same degree of heteroatoms removal

to allow for the product's stoichiometric coefficients to be calculated. First the weight fractions of sulphur and nitrogen in the LITE pseudo-component are taken from Yui and Sanford, (1989) and it is assigned the atomic hydrogen to carbon ratio of 1.87 which is similar to that of saturate fraction of the Athabasca bitumen (Prowse et al., 1983). These were then used to calculate the weight fraction of carbon atoms in the LITE pseudo-component (Tab. 9.3). The elemental compositions of the bitumen and that of LITE pseudo-component, together with the component split are used to obtain the elemental composition of the HEAV pseudo-component.

Tab. 9.3: Elemental compositions

Element	Bitumen	HEAV	LITE	LUO	HUO
H (wt%)	10.687	10.430	13.005	16.764	12.866
C (wt%)	84.075	84.210	82.859	82.859	84.210
N (wt%)	0.414	0.447	0.112	0.019	0.147
S (wt%)	4.824	4.913	4.025	0.359	2.777

Since the HDS and HDN reactions involve sulphur and nitrogen removal, and respective replacement by hydrogen, it follows that the number of carbon atoms in each pseudo-component will not change with the catalytic upgrading. Therefore, by using the pseudo-component split (Tab. 9.1), fractional sulphur and nitrogen removal of 35% and 60% respectively, and the weight fraction of carbon in each pseudo-component, the elemental compositions of the upgraded pseudo-components were calculated (Tab. 9.3). These calculations showed that there is an increase in the hydrogen to carbon atomic ratio from 1.48 in the HEAV to 1.82 in the HUO and 1.87 in the LITE to 2.41 in the LUO. However,

it is noted that since all the four pseudo-components are produced as a certain fraction, the overall atomic hydrogen to carbon ratio will be higher than the 1.53 in the original bitumen but less than that in the LUO.

The balanced reactions, together with the kinetics parameters, are then added to the thermal cracking and combustion reactions into the THAI-CAPRI model. However, STARS will treat the catalyst just like reservoir rock unless the catalyst is specified as both part of the reactants, and products as exemplified by the following reaction:

$$HEAV + 19.932\ H_2 + CAT \rightarrow 3.477\ HUO + 0.585\ H_2S + CAT$$

This means that the HUO and H_2S are only produced when HEAV and H_2 contact the catalyst under the right temperature and pressure. Under this circumstance, the reaction is first-order with respect to the catalyst, CAT. Recalling that the results of the THAI model, presented in chapter 4, have shown that the maximum temperature around the mobile oil zone (MOZ), where the catalytic upgrading is envisaged, is only 265 ^oC and not enough to activate the catalyst and hence to achieve any catalytic upgrading. In the light of this, it becomes necessary to either externally heat the catalyst or set the model to compensate for this.

In this study, the concept of activation temperature, first introduced by Coats, (1983) to correct for the effect of large field scale gridblock sizes, is used to account for the inadequacy of temperature around the MOZ. A minimum activation temperature, T_a, of 400 ^oC was set into the model. That is, if the catalyst temperature in the MOZ is less than T_a, then the temperature-dependent HDS and HDN reaction rates in that zone are respectively calculated using T_a.

When the catalyst temperature is more T_a, then the actual temperature is used. That means, under this situation, the wrapped catalyst around the HP is simulated as a sort of already heated porous cylindrical wall via which when mobilised oil flows, it becomes further upgraded. However, this method of activating the catalyst has the downside of considering the catalytic reaction to take place along the entire length of HP well wrapped by catalyst layer. As a result, the predicted degree could be much more than that would have been achieved if the heating is localised. This might not necessarily be the case since in at least the two THAI-CAPRI experiments (Xia and Greaves, 2001; Xia et al., 2002b), neither used an external heater to activate the catalyst despite the upgrading achieved by up to 6 API points.

Catalyst Properties and Wrapping

To emplace the annular catalyst layer around the HP well, so that the mobilised oil has to contact it first before flowing into the HP well, the thickness of the catalyst annulus must be specified such that the gridblocks, surrounding the HP well, correspond to the same size. In Xia and Greaves, (2001), a 0.5 or 1 inch OD tube was used to place the catalyst. However, they did not specify the thickness of the catalyst layer. In view of this, this study assumed an initial catalyst annular thickness of 0.5 cm (Fig. 9.16) to start with. In addition to that, the catalyst properties must be used to determine both the packing porosity and the solid concentration. As a result, the properties of cobalt oxide-molybdenum oxide (CoMo) hydrotreating catalyst supported on alumina are used. This is because CoMo is widely used industrially and has been used to study THAI-CAPRI (Xia and Greaves, 2001; Xia et al., 2002b). Also, other studies of the

catalytic upgrading in conjunction with the in-situ combustion used alumina supported NiMo catalyst (Cavallaro et al., 2008; Abu et al., 2015).

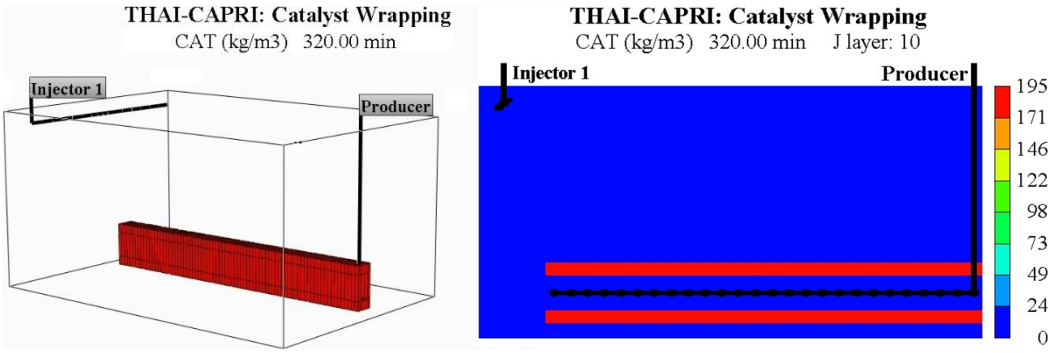

(a) (b)

Fig. 9.16: Shows the catalyst wrapped around the HP well (a) in 3D, and (b) as side view

The constituents, and their respective fractions, of the CoMo catalyst taken from MSDS can be seen in Tab. 9.4. The catalyst bulk density, 1053.1 kg m^{-3}, is taken from Salazar-Sotelo et al., (2004) and is used in conjunction with the void volume, and packing porosities to calculate the catalyst loading, using equation 3-7 presented in section 3.2 of chapter 3. As a result, a catalyst packing porosity of 45% has been initially used in this work, and it lies between the 44 and 45.1% used by Abu et al. (2015). It should be noted that the effect of the packing porosity on the THAI-CAPRI process has been investigated as will be shown subsequently.

The solid catalyst concentration to be placed to surround the entire HP well is 0.005485 mol cm^{-3} (574.4 kg m^{-3}) of pore volume (Tab. 9.5). This is specified as an initial condition in the STARS simulator, and by specifying the CAT as both reactant and product in the HDS and HDN reactions, the CAT concentration at every point is preserved up to the end of the combustion period (the 320 minutes) (Fig. 9.16b).

Tab. 9.4: CoMo catalyst constituents

Constituents	RMM (g/mol)	wt%
CoO	74.93	4.00
MoO_3	143.96	14.00
Al_2O_3	101.96	82.00
Total	104.73	100.00

Tab. 9.5: Calculated catalyst loading based on 45% fluid porosity

Void porosity	Packing porosity	Catalyst bulk density (kg m^{-3})	CAT loading (kg m^{-3} pore volume)	CAT loading (mol cm^{-3} pore volume)
0.99	0.45	1053.1	574.4	0.005484882

The specific heat capacity of the catalyst, CAT, is assumed to be identical to that of the reservoir rock, 0.753 J $g^{-1}K^{-1}$. This is justified given that 82 % by weight of the catalyst is made up of alumina.

Overall then, the above data is enough to numerically simulate the THAI-CAPRI and obtain preliminary results that will provide further insight as to the parameters influencing the process. However, the approximate kinetics parameters must be used.

Appendix D: THAI Data File

Example of the STARS data input file is presented below:

```
RESULTS SIMULATOR STARS 201401
TITLE1 'SIMULATION OF TOE-TO-HEEL AIR INJECTION'

**  ====================  INPUT/OUTPUT  CONTROL
=======================
```

```
INTERRUPT STOP

INUNIT LAB

OUTUNIT LAB


OUTPRN ITER NEWTON

OUTPRN GRID OBHLOSS PRES SG SO SOLCONC SW TEMP VISO VISW
X Y


OUTPRN WELL ALL

WRST 400

WPRN GRID 300

WPRN ITER 300

OUTSRF GRID CCHLOSS CMPDENO CMPDENW CMPVISG CMPVISO
CMPVISW FLUXRC FLUXSC FPOROS KRG KRO

     KRW KVALYW KVALYX MASDENG MASDENO MASDENW
OBHLOSS PCOG PCOW PERMI PERMJ

     PERMK PRES SG SO MASS SOLCONC SW TEMP VISG VISO
VISW VPOROS

     W X Y

OUTSRF WELL MASS COMPONENT ALL

OUTSRF WELL MOLE COMPONENT ALL

OUTSRF SPECIAL MAXVAR MASDENO

        MAXVAR VISO

        MAXVAR PRES

        MAXVAR MASS SOLCONC 'COKE'

        MAXVAR TEMP

        MINVAR MASDENO

        MINVAR VISO

        MINVAR PRES

        MINVAR MASS SOLCONC 'COKE'

        MINVAR TEMP

        AVGVAR MASDENO
```

```
AVGVAR VISO
AVGVAR PRES
AVGVAR MASS SOLCONC 'COKE'
AVGVAR TEMP
MOLEFRAC  'Producer' 'CO2' GAS
MOLEFRAC  'Producer' 'CO' GAS
MOLEFRAC  'Producer' 'N2' GAS
MOLEFRAC  'Producer' 'O2' GAS
MOLEFRAC  'Producer' 'STEAM' GAS
MOLEFRAC  'Producer' 'LC' OIL
MOLEFRAC  'Producer' 'MC' OIL
MOLEFRAC  'Producer' 'IC' OIL
MATBAL  GASEOUS 'STEAM'
MATBAL  AQUEOUS 'STEAM'
MATBAL  GASEOUS 'LC'
MATBAL  GASEOUS 'MC'
MATBAL  OLEIC 'IC'
MATBAL  OLEIC 'LC'
MATBAL  OLEIC 'MC'
MATBAL  CURRENT 'COKE'
MATBAL  CURRENT 'O2'
MATBAL  CURRENT 'CO2'
MATBAL  CURRENT 'N2'
MATBAL  CURRENT 'CO'
MATBAL  CURRENT 'IC'
MATBAL  CURRENT 'LC'
MATBAL  CURRENT 'MC'
MATBAL  REACTION 'STEAM'
MATBAL  REACTION 'CO2'
MATBAL  REACTION 'CO'
MATBAL  REACTION 'O2'
MATBAL  REACTION 'IC'
```

```
            MATBAL  REACTION 'LC'
            MATBAL  REACTION 'MC'
            MATBAL  REACTION 'COKE'
            DELP  'Injector 1' 'Producer'
            OBHLOSSCUM
            CCHLOSSCUM
            OBHLOSSRATE
            CCHLOSSRATE
OUTSRF WELL LAYER ALL
OUTSRF WELL DOWNHOLE

REWIND 150
INTERRUPT RESTART-STOP

RESULTS XOFFSET         0.0000
RESULTS YOFFSET         0.0000
RESULTS ROTATION          0.0000

**$
**********************************************************************
**********
**$ Definition of fundamental cartesian grid
**$
**********************************************************************
**********

GRID CART 30 19 7
KDIR DOWN
*DI *IVAR
30*2.0
DJ *JVAR
19*2.10526
DK *KVAR
```

```
6*1.466667 1.2

WELLBORE  0.2
RELROUGH 0.0000005
RANGE  5:30 10 6

REFINE 2:30 1:19 2:5 INTO 3 3 1
REFINE 2:30 1:19 7 INTO 3 3 1
REFINE 3:30 1:19 1 INTO 3 3 1
REFINE 2:4 1:19 6 INTO 3 3 1
REFINE 5:30 1:9 6 INTO 3 3 1
REFINE 5:30 11:19 6 INTO 3 3 1

NULL CON          1

POR CON       0.34
POR WELLBORE 5:30 10 6 CON 0.34

PERMI CON  11500
PERMJ CON 11500
PERMK CON 3450

PINCHOUTARRAY CON          1
*end-grid

ROCKTYPE 1
ROCKCP 0.753
THCONR 5.0
THCONW 0.34
THCONO 0.2
THCONG 0.065
THCONS 3.12
```

```
THCONMIX COMPLEX
HLOSSPROP OVERBUR 0.095020147 0.0950829
          UNDERBUR 0.095020147 0.0950829
ROCKTYPE 2
ROCKCP 0.753
THCONR 5.0
THCONW 0.34
THCONO 0.2
THCONG 0.065
THCONS 3.12
THCONMIX SIMPLE

THTYPE CON 1
THTYPE WELLBORE 5:30 10 6 CON 2
** ================= FLUID DEFINITIONS ==================
** Model and number of components
MODEL 9 8 4 1
COMPNAME 'STEAM' 'IC' 'MC' 'LC' 'CO2' 'CO' 'N2' 'O2' 'COKE'
CMM
0.018 1.0170 0.4968 0.2108 0.04401 0.02801 0.028013 0.031999 0.01313
PCRIT
22048 729.22 1038.46 1682.88 7376 3496 3394 5046
TCRIT
374.25 940.36 698.53 464.68 31.05 -140.25 -146.95 -118.55
KV1
1.1860e+7 0 0 0
KV2
0 0 0 0
KV3
0 0 0 0
KV4
-3816.44 0 0 0
```

KV5

-227.02 0 0 0

KVTABLIM 100 2000 10 990

**$ Gas-liquid K Value tables

KVTABLE 'IC'

1.56545E-18 7.82724E-20
1.04992E-13 5.24958E-15
1.78160E-10 8.90798E-12
3.66099E-08 1.83050E-09
2.00182E-06 1.00091E-07
4.51845E-05 2.25923E-06
5.48345E-04 2.74173E-05
4.23466E-03 2.11733E-04
2.32903E-02 1.16452E-03
9.86333E-02 4.93167E-03
3.40102E-01 1.70051E-02
9.94790E-01 4.97395E-02
2.54537E+00 1.27269E-01
5.83305E+00 2.91653E-01
1.21934E+01 6.09669E-01

**$ Gas-liquid K Value tables

KVTABLE 'MC'

4.53768E-12 2.26884E-13
1.30069E-08 6.50346E-10
2.67699E-06 1.33849E-07
1.21436E-04 6.07182E-06
2.13399E-03 1.06699E-04
1.98966E-02 9.94832E-04
1.18938E-01 5.94688E-03

```
    5.14333E-01  2.57166E-02
    1.74413E+00  8.72063E-02
    4.90460E+00  2.45230E-01
    1.19039E+01  5.95193E-01
    2.56792E+01  1.28396E+00
    5.03332E+01  2.51666E+00
    9.11663E+01  4.55832E+00
    1.54604E+02  7.73020E+00

**$ Gas-liquid K Value tables
KVTABLE 'LC'
    1.40504E-05  7.02519E-07
    1.26714E-03  6.33571E-05
    2.57692E-02  1.28846E-03
    2.22829E-01  1.11415E-02
    1.12703E+00  5.63515E-02
    3.98328E+00  1.99164E-01
    1.09490E+01  5.47452E-01
    2.50607E+01  1.25304E+00
    4.99919E+01  2.49959E+00
    8.97067E+01  4.48533E+00
    1.48112E+02  7.40562E+00
    2.28775E+02  1.14388E+01
    3.34727E+02  1.67364E+01
    4.68359E+02  2.34180E+01
    6.31390E+02  3.15695E+01
PRSR 101.325
TEMR 25.0
CPG1
38.182 2510 -27.13598793 -7.913 19.795 30.869 31.15 28.106
CPG2
-0.0175 0 3.294427341 0.9609 7.34E-02 -1.29E-02 -1.36E-02 -3.68E-06
```

CPG3

5e-05 0 -0.001814495 -5.288e-4 5.60E-05 2.79E-05 2.68E-05 1.75E-05

CPG4

-3e-08 0 3.58291E-06 1.131e-7 1.72E-08 -1.27E-08 -1.17E-08 -1.07E-08

HVR

4820. 8569. 7485.0032 5579.

EV

0.38 0.38 0.38 0.38

SOLID_DEN 'COKE' 0.00138 0 0

SOLID_CP 'COKE' 12 0.0

MASSDEN

0.000999 0.001088039 0.000961663 0.000828242

CP

5.8e-7 2.5E-07 4.0E-07 6.91E-07

CT1

-1.9095e-3 1.08E-05 2.0E-05 2.02E-05

CT2

7.296e-6 4.58E-07 8E-07 1.58E-06

AVG

1.7e-5 0 7.565e-6 4.174e-6 4.098e-6 4.098e-6 4.098e-6 4.232e-6

BVG

1.116 0 1.102 0.943 0.702 0.702 0.702 0.702

GVISCOR

VISCTABLE

** temp

20.00 0.000E+00 9.4675E+06 4.5502E+06 1.2900E+03

30.26 0.000E+00 1.3039E+06 3.6829E+05 9.8700E+02

40.51 0.000E+00 5.6798E+05 1.3510E+05 7.4700E+02

50.03 0.000E+00 1.2547E+05 2.5996E+04 2.5500E+02

60.03 0.000E+00 3.4819E+04 5.6394E+03 1.5600E+02

70.03 0.000E+00 1.1965E+04 1.5469E+03 1.1700E+02

80.03 0.000E+00 6.4719E+03 4.1222E+02 8.9700E+01

90.03	0.000E+00	2.6772E+03	2.9996E+02	6.3000E+01
100.03	0.000E+00	1.3883E+03	1.4808E+02	3.8100E+01
110.03	0.000E+00	8.3427E+02	4.9035E+01	2.5380E+01
120.03	0.000E+00	4.9990E+02	2.7447E+01	1.7200E+01
130.03	0.000E+00	2.2881E+02	1.8403E+01	1.4825E+01
140.03	0.000E+00	9.7768E+01	1.6566E+01	1.3250E+01
150.03	0.000E+00	7.4334E+01	1.3338E+01	1.0340E+01
160.03	0.000E+00	3.6117E+01	7.7441E+00	5.4450E+00
180.03	0.000E+00	2.4103E+01	5.9724E+00	3.7560E+00
200.03	0.000E+00	1.0787E+01	3.1093E+00	2.5800E+00
220.03	0.000E+00	7.4356E+00	2.2042E+00	1.9600E+00
240.03	0.000E+00	4.3614E+00	2.2490E+00	1.6800E+00
265.00	0.000E+00	3.1460E+00	1.8052E+00	1.4135E+00
280.00	0.000E+00	2.8756E+00	1.4465E+00	1.0689E+00
295.00	0.000E+00	2.6597E+00	1.1820E+00	8.2704E-01
310.00	0.000E+00	2.2846E+00	9.9723E-01	6.9224E-01
325.00	0.000E+00	1.9405E+00	8.5724E-01	5.9821E-01
340.00	0.000E+00	1.7205E+00	7.4235E-01	5.1269E-01
355.00	0.000E+00	1.4194E+00	6.5966E-01	4.7073E-01
370.00	0.000E+00	1.2334E+00	5.8779E-01	4.2410E-01
385.00	0.000E+00	1.0994E+00	5.2696E-01	3.8119E-01
400.00	0.000E+00	9.9540E-01	4.7564E-01	3.4360E-01
415.00	0.000E+00	9.3960E-01	4.2987E-01	3.0464E-01
430.00	0.000E+00	8.9060E-01	3.9124E-01	2.7235E-01
445.00	0.000E+00	8.4720E-01	3.5837E-01	2.4535E-01
460.00	0.000E+00	8.0870E-01	3.3016E-01	2.2254E-01
475.00	0.000E+00	7.7430E-01	3.0579E-01	2.0311E-01
490.00	0.000E+00	7.4340E-01	2.8458E-01	1.8645E-01
505.00	0.000E+00	7.1550E-01	2.6602E-01	1.7206E-01
520.00	0.000E+00	6.9030E-01	2.4968E-01	1.5955E-01
535.00	0.000E+00	6.6730E-01	2.3522E-01	1.4861E-01
600.00	0.000E+00	6.5320E-01	1.8495E-01	1.0611E-01

900.00 0.000E+00 3.5000E-01 1.0888E-01 6.5111E-02

**$ Reaction specification 1- Asphaltene = > Heavy Oil

STOREAC

0 1 0 0 0 0 0 0 0

STOPROD

0 0 2.0471 0 0 0 0 0 0

FREQFAC 3.822e20

EACT 239.01e3

**$ Reaction specification 2- Heavy Oil = > Asphaltene

STOREAC

0 0 1 0 0 0 0 0 0

STOPROD

0 0.488496 0 0 0 0 0 0 0

FREQFAC 3.366e18

EACT 215.82e3

**$ Reaction specification 3- Heavy Oil = > Light Oil

STOREAC

0 0 1 0 0 0 0 0 0

STOPROD

0 0 0 2.35674 0 0 0 0 0

FREQFAC 1.132e15

EACT 184.88e3

**$ Reaction specification 4- Light Oil = > Heavy Oil

STOREAC

0 0 0 1 0 0 0 0 0

STOPROD

0 0 0.424315 0 0 0 0 0 0

FREQFAC 1.524e15

EACT 180.45e3

**$ Reaction specification 5- Asphaltene = > Coke

STOREAC

0 1 0 0 0 0 0 0 0

STOPROD

0 0 0 0 0 0 0 0 77.4563

FREQFAC 2.32e15

EACT 180.88e3

**$ Reaction specification 6- IC + Oxygen = > H2O + CO2 + CO

STOREAC

0 1 0 0 0 0 0 106.684 0

STOPROD

46.904 0 0 0 78.85 4.153 0 0 0

FREQFAC 1.812e8

RENTH 4.00e7

EACT 1.38e5

**$ Reaction specification 7- MC + Oxygen = > H2O + CO2 + CO

STOREAC

0 0 1 0 0 0 0 37.0695 0

STOPROD

22.365 0 0 0 28.1334 1.509 0 0 0

FREQFAC 1.812e9

RENTH 1.600e7

EACT 1.38e5

**$ Reaction specification 8- LC + Oxygen = > H2O + CO2 + CO

STOREAC

0 0 0 1 0 0 0 17.4649 0

STOPROD

14.5 0 0 0 11.17597 0.6 0 0 0

FREQFAC 1.812e10

RENTH 4.913e5

EACT 1.38e5

**$ Reaction specification 9- Coke + Oxygen = > H2O + CO2 + CO

STOREAC

0 0 0 0 0 0 0 1.22 1

STOPROD

0.565 0 0 0 0.9352 0.03001 0 0 0

FREQFAC 1e10

RENTH 3.90e5

EACT 1.23e5

** ========== Rock-FLUID PROPERTIES ==========

ROCKFLUID

RPT 1 WATWET

SWT

**$ Sw krw krow

0.1 0.0 0.9

0.25 0.004 0.6

0.44 0.024 0.28

0.56 0.072 0.144

0.672 0.168 0.048

0.752 0.256 0.0

SLT

**$ Sl krg krog

0.10 0.9 0.000

0.1200 0.5650 0.0100

0.2500 0.4100 0.0520

0.4720 0.2880 0.1000

0.5800 0.1560 0.2100

0.6800 0.0670 0.3400

0.7200 0.0340 0.4100

0.8320 0.0120 0.6200

0.9500 0.0060 0.8200

0.9900 0.0000 0.9000

RPT 2

SWT

**$ Sw krw krow

```
        0.0       0.0       1.0
        1.0       1.0       0.0

SLT
**$       Sl       krg       krog
        0.0       1.0     0.000
        1.0       0.0     1.0
KRTYPE CON 1
*KRTYPE *WELLBORE 5:30 10 6 *CON 2

**              ==============              INITIAL              CONDITIONS
==================================
INITIAL
VERTICAL OFF

INITREGION 1

PRES CON         290
TEMP CON          27
SW CON          0.15
SO IJK 1:30 1:19 1:7    0.85
      5:30 10 6         0
SG IJK 5:30 10 6 1.0
MFRAC_OIL 'MC' CON     0.239143
MFRAC_OIL 'LC' CON     0.424971
MFRAC_OIL 'IC' CON     0.335886
MFRAC_GAS 'STEAM' CON           0
MFRAC_GAS 'O2' CON           0
MFRAC_GAS 'N2' CON           0
MFRAC_GAS 'CO2' CON           0
MFRAC_GAS 'CO' CON           0
CONC_SLD 'COKE' CON           0
```

```
**              ==============         NUMERICAL         CONTROL
================================
NUMERICAL
DTMIN 0.0000000000001
MAXSTEPS 100000000
MATBALTOL 0.00001
NEWTONCYC 30
NORTH 180
NCUTS 15
ITERMAX 280
SOLVER PARASOL
DPLANES 12
PNTHRDS 8
PPATTERN AUTOPSLAB 4
MINPRES 100.0
MAXTEMP 946.85
MAXPRES 2000.0

RUN
TIME 0
DTWELL 0.001

WELL  'Producer'

TRANSI WELLBORE 5:30 10 6 CON 0.05
PRODUCER 'Producer'
OPERATE  MIN  BHP  170  CONT REPEAT
OPERATE  MAX  STL  25.  CONT REPEAT
MONITOR  MAX  TEMP  927.  STOP
**          rad  geofac  wfrac  skin
GEOMETRY  I  0.2  0.2488  1.0  0.0
```

```
PERF  GEO  'Producer'
** UBA             ff    Status  Connection
   30 10 6 / 1 1 1  12.5  OPEN    FLOW-TO  'SURFACE'

HEATR IJK
2:2    2:18    1:1  2115
DYNAGRID-TSINT 121
DYNAGRID DEREFINE    GMOLAR 0.03 OMOFRC 0.02 PRESS 20
TEMPER 30 2:30 1:19 2:5
DYNAGRID DEREFINE    GMOLAR 0.03 OMOFRC 0.02 PRESS 20
TEMPER 30 2:30 1:19 7

DYNAGRID DEREFINE    GMOLAR 0.03 OMOFRC 0.02 PRESS 20
TEMPER 30 3:30 1:19 1

DYNAGRID DEREFINE    GMOLAR 0.03 OMOFRC 0.02 PRESS 20
TEMPER 30 2:4 1:19 6

DYNAGRID DEREFINE    GMOLAR 0.03 OMOFRC 0.02 PRESS 20
TEMPER 30 5:30 1:9 6
DYNAGRID DEREFINE    GMOLAR 0.03 OMOFRC 0.02 PRESS 20
TEMPER 30 5:30 11:19 6

TIME 10
OUTSRF GRID FLUXRC FLUXSC FPOROS PRES SG SO SOLCONC SW
TEMP W X Y
TIME 20
OUTSRF GRID REMOVE
TIME 30
OUTSRF GRID REMOVE

WELL  'Injector 1'
INJECTOR UNWEIGHT 'Injector 1'
INCOMP  GAS  0.  0.  0.  0.  0. 0. 0.79  0.21
```

```
TINJW  25.
OPERATE  MAX  STG  8000.  CONT REPEAT
GEOMETRY J 0.2 0.2488 1.0 0
**$ UBA     wi    Status  Connection
PERF  WI  'Injector 1'
** UBA      wi    Status  Connection
   2 18 1  1.25  OPEN    FLOW-FROM  'SURFACE'  REFLAYER
   2 17 1  1.25  OPEN    FLOW-FROM  1
   2 16 1  1.25  OPEN    FLOW-FROM  2
   2 15 1  1.25  OPEN    FLOW-FROM  3
   2 14 1  1.25  OPEN    FLOW-FROM  4
   2 13 1  1.25  OPEN    FLOW-FROM  5
   2 12 1  1.25  OPEN    FLOW-FROM  6
   2 11 1  1.25  OPEN    FLOW-FROM  7
   2 10 1  1.25  OPEN    FLOW-FROM  8
   2 9 1   1.25  OPEN    FLOW-FROM  9
   2 8 1   1.25  OPEN    FLOW-FROM  10
   2 7 1   1.25  OPEN    FLOW-FROM  11
   2 6 1   1.25  OPEN    FLOW-FROM  12
   2 5 1   1.25  OPEN    FLOW-FROM  13
   2 4 1   1.25  OPEN    FLOW-FROM  14
   2 3 1   1.25  OPEN    FLOW-FROM  15
   2 2 1   1.25  OPEN    FLOW-FROM  16

HEATR CON 0

TIME 40
OUTSRF GRID REMOVE
TIME 50
OUTSRF GRID REMOVE
TIME 60
OUTSRF GRID REMOVE
```

```
TIME 70
OUTSRF GRID REMOVE
TIME 80
OUTSRF GRID REMOVE
TIME 90
OUTSRF GRID REMOVE
TIME 100
OUTSRF GRID REMOVE
TIME 110
OUTSRF GRID REMOVE
TIME 120
OUTSRF GRID REMOVE
TIME 130
OUTSRF GRID REMOVE
TIME 140
OUTSRF GRID REMOVE
TIME 150
OUTSRF GRID REMOVE
TIME 160
OUTSRF GRID REMOVE
TIME 170
OUTSRF GRID REMOVE
TIME 180
OUTSRF GRID REMOVE
TIME 190
OUTSRF GRID REMOVE

WELL  'Injector 1'
INJECTOR UNWEIGHT 'Injector 1'
INCOMP  GAS  0.  0.  0.  0.  0. 0. 0.79  0.21
TINJW  25.
OPERATE  MAX  STG  10667.  CONT REPEAT
```

```
GEOMETRY J 0.2 0.2488 1.0 0
**$ UBA     wi    Status  Connection
PERF  WI  'Injector 1'
** UBA      wi    Status  Connection
   2 18 1  1.25  OPEN    FLOW-FROM  'SURFACE'  REFLAYER
   2 17 1  1.25  OPEN    FLOW-FROM  1
   2 16 1  1.25  OPEN    FLOW-FROM  2
   2 15 1  1.25  OPEN    FLOW-FROM  3
   2 14 1  1.25  OPEN    FLOW-FROM  4
   2 13 1  1.25  OPEN    FLOW-FROM  5
   2 12 1  1.25  OPEN    FLOW-FROM  6
   2 11 1  1.25  OPEN    FLOW-FROM  7
   2 10 1  1.25  OPEN    FLOW-FROM  8
   2 9 1   1.25  OPEN    FLOW-FROM  9
   2 8 1   1.25  OPEN    FLOW-FROM  10
   2 7 1   1.25  OPEN    FLOW-FROM  11
   2 6 1   1.25  OPEN    FLOW-FROM  12
   2 5 1   1.25  OPEN    FLOW-FROM  13
   2 4 1   1.25  OPEN    FLOW-FROM  14
   2 3 1   1.25  OPEN    FLOW-FROM  15
   2 2 1   1.25  OPEN    FLOW-FROM  16

TIME 200
OUTSRF GRID REMOVE
TIME 210
OUTSRF GRID REMOVE
TIME 220
OUTSRF GRID REMOVE
TIME 230
OUTSRF GRID REMOVE
TIME 240
OUTSRF GRID REMOVE
```

TIME 250

OUTSRF GRID REMOVE

TIME 260

OUTSRF GRID REMOVE

TIME 270

OUTSRF GRID REMOVE

TIME 280

OUTSRF GRID REMOVE

TIME 290

OUTSRF GRID REMOVE

TIME 300

OUTSRF GRID REMOVE

TIME 310

OUTSRF GRID REMOVE

TIME 320

STOP

Appendix E: CAPRI Data File

Example of the STARS data input file for the CAPRI model is presented below:

RESULTS SIMULATOR STARS 201401

**----------Comments----------

** This did not consider external means of heating.

** The same as in the main folder except that the air injection rate has been increased.

** Catalyst packing porosity of 45%

** Called model TC3 in the future work section

TITLE1 'THAI-CAPRI SIMULATION'

INTERRUPT STOP

INUNIT LAB

EXCEPT 2 0

OUTUNIT LAB

```
** ------ Output file (.irf): Grid and wells -------

OUTPRN ITER NEWTON

OUTPRN GRID OBHLOSS PRES SG SO SOLCONC FPOROS SW TEMP
VISO VISW X Y

OUTPRN WELL ALL

WRST 400

WPRN GRID 300

WPRN ITER 300

OUTSRF GRID CCHLOSS CMPDENO CMPDENW CMPVISG CMPVISO
CMPVISW FLUXRC FLUXSC FPOROS KRG KRO

     KRW KVALYW KVALYX MASDENG MASDENO MASDENW
OBHLOSS PCOG PCOW PERMI PERMJ

     PERMK PRES SG SO MASS SOLCONC SW TEMP VELOCSC
VISCVELG VISCVELO VISCVELW

     VISG VISO VISW VPOROS W X Y Z

OUTSRF WELL MASS COMPONENT ALL

OUTSRF WELL MOLE COMPONENT ALL

OUTSRF SPECIAL MAXVAR MASDENO

        MAXVAR VISO

        MAXVAR PRES

        MAXVAR MASS SOLCONC 'COKE'

        MAXVAR TEMP

        MINVAR MASDENO

        MINVAR VISO

        MINVAR PRES

        MINVAR MASS SOLCONC 'COKE'

        MINVAR TEMP

        AVGVAR MASDENO

        AVGVAR VISO

        AVGVAR PRES

        AVGVAR MASS SOLCONC 'COKE'

        AVGVAR TEMP

        MASSFRAC  'Producer' 'LITE' OIL
```

```
MASSFRAC  'Producer' 'HEAV' OIL
MOLEFRAC  'Producer' 'NH3' GAS
MOLEFRAC  'Producer' 'H2' GAS
MOLEFRAC  'Producer' 'H2S' GAS
MOLEFRAC  'Producer' 'O2' GAS
MOLEFRAC  'Producer' 'WATER' GAS
MOLEFRAC  'Producer' 'CO2/CO' GAS
MOLEFRAC  'Producer' 'LITE' OIL
MOLEFRAC  'Producer' 'HEAV' OIL
MOLEFRAC  'Producer' 'LUO' OIL
MOLEFRAC  'Producer' 'HUO' OIL
MATBAL  WELL 'NH3'
MATBAL  WELL 'H2'
MATBAL  WELL 'O2'
MATBAL  WELL 'H2S'
MATBAL  GASEOUS 'WATER'
MATBAL  AQUEOUS 'WATER'
MATBAL  GASEOUS 'LITE'
MATBAL  GASEOUS 'HEAV'
MATBAL  OLEIC 'LITE'
MATBAL  OLEIC 'HEAV'
MATBAL  OLEIC 'LUO'
MATBAL  OLEIC 'HUO'
MATBAL  CURRENT 'COKE'
MATBAL  CURRENT 'WATER'
MATBAL  CURRENT 'CO2/CO'
MATBAL  CURRENT 'NH3'
MATBAL  CURRENT 'H2'
MATBAL  CURRENT 'H2S'
MATBAL  CURRENT 'O2'
MATBAL  CURRENT 'LITE'
MATBAL  CURRENT 'HEAV'
```

```
            MATBAL  CURRENT 'LUO'
            MATBAL  CURRENT 'HUO'
            MATBAL  REACTION 'WATER'
            MATBAL  REACTION 'CO2/CO'
            MATBAL  REACTION 'NH3'
            MATBAL  REACTION 'H2'
            MATBAL  REACTION 'H2S'
            MATBAL  REACTION 'O2'
            MATBAL  REACTION 'LITE'
            MATBAL  REACTION 'HEAV'
            MATBAL  REACTION 'LUO'
            MATBAL  REACTION 'HUO'
            MATBAL  REACTION 'COKE'
            DELP  'Injector 1' 'Producer'
            OBHLOSSCUM
            OBHLOSSRATE
OUTSRF WELL LAYER ALL
OUTSRF WELL DOWNHOLE
REWIND 150
INTERRUPT RESTART-STOP

RESULTS XOFFSET         0.0000
RESULTS YOFFSET         0.0000
RESULTS ROTATION         0.0000

**$
**********************************************************************
************
**$ Definition of fundamental cartesian grid
**$
**********************************************************************
************
```

```
GRID CART 30 19 9
KDIR DOWN
*DI *IVAR
30*2.0
DJ *JVAR
8*2.3125 0.5 2 0.5 8*2.3125
DK *KVAR
5*1.4 0.5 1.4 0.5 0.6

WELLBORE  0.2
RELROUGH 0.0000005
RANGE  5:30 10 7

REFINE 2:30 1:19 2:6 INTO 3 1 1
REFINE 2:30 1:19 8:9 INTO 3 1 1

REFINE 3:30 1:19 1 INTO 3 1 1

REFINE 2:4 1:19 7 INTO 3 1 1

REFINE 5:30 1:9 7 INTO 3 1 1
REFINE 5:30 11:19 7 INTO 3 1 1

NULL CON           1

POR CON    0.34
    MOD  5:30 9:11 6  = 0.99
5:30 9:11 8  = 0.99
5:30 9 7  = 0.99
5:30 11 7  = 0.99

PERMI CON  11500
```

```
PERMJ CON 11500
PERMK CON 3450

PINCHOUTARRAY CON          1
*end-grid

ROCKTYPE 1
ROCKCP 0.753
THCONR 5.0
THCONW 0.34
THCONO 0.2
THCONG 0.065
THCONS 3.12
THCONMIX COMPLEX
HLOSSPROP OVERBUR 0.095020147 0.0950829
          UNDERBUR 0.095020147 0.0950829
ROCKTYPE 2
ROCKCP 0.753
THCONR 5.0
THCONW 0.34
THCONO 0.2
THCONG 0.065
THCONS 3.12
THCONMIX SIMPLE

THTYPE CON 1
THTYPE WELLBORE 5:30 10 7 CON 2
** ================= FLUID DEFINITIONS ==================
** Model and number of components
MODEL 12 10 5 1
COMPNAME 'WATER' 'HEAV' 'LITE' 'HUO' 'LUO' 'CO2/CO' 'H2' 'NH3'
'H2S' 'O2' 'COKE' 'CAT'
```

CMM

0.018 0.878 0.17 0.2525 0.12801 0.04304 0.002016 0.017029 0.034086 0.032 0.013 0.10473

PCRIT

22048 1031.29 2305.95 1523.46 2448.61 3447.38 1315.50 11276.9 8937 5033.17

TCRIT

647.4 1053.15 698.31 775.34 626.27 121.4 33.44 405.55 373.2 154.82

KVTABLIM 100 10000 298.15 1318.98

**$ Gas-liquid K Value tables

KVTABLE 'HEAV'

2.18000E-06 2.64000E-07

9.00000E-05 1.09000E-05

1.39500E-03 1.69000E-04

1.15000E-02 1.39000E-03

6.05000E-02 7.36000E-03

2.34500E-01 2.84000E-02

7.16000E-01 8.68000E-02

1.83150E+00 2.22000E-01

4.09200E+00 4.96000E-01

8.18400E+00 9.92000E-01

1.49655E+01 1.81400E+00

2.54605E+01 3.08610E+00

4.07665E+01 4.94140E+00

6.52672E+01 7.91118E+00

1.04493E+02 1.26658E+01

**$ Gas-liquid K Value tables

KVTABLE 'LITE'

1.57000E-02 1.90000E-03

1.21300E-01 1.47000E-02

5.40350E-01 6.55000E-02

```
    1.70610E+00  2.06800E-01
    4.23650E+00  5.13500E-01
    8.86300E+00  1.07430E+00
    1.63268E+01  1.97900E+00
    2.72950E+01  3.30850E+00
    4.23100E+01  5.12850E+00
    6.17650E+01  7.48650E+00
    8.58950E+01  1.04115E+01
    1.14798E+02  1.39150E+01
    1.48453E+02  1.79945E+01
    1.91949E+02  2.32669E+01
    2.48190E+02  3.00841E+01

**$ Gas-liquid K Value tables
KVTABLE 'HUO'
    1.961E-06  1.961E-08
    2.780E-04  2.780E-06
    7.650E-03  7.650E-05
    8.215E-02  8.215E-04
    4.889E-01  4.889E-03
    1.962E+00  1.962E-02
    5.969E+00  5.969E-02
    1.485E+01  1.485E-01
    3.174E+01  3.174E-01
    6.040E+01  6.040E-01
    1.049E+02  1.049E+00
    1.692E+02  1.692E+00
    2.572E+02  2.572E+00
    3.723E+02  3.723E+00
    5.172E+02  5.172E+00

**$ Gas-liquid K Value tables
```

KVTABLE 'LUO'

2.796E-03 2.796E-05

7.462E-02 7.462E-04

6.718E-01 6.718E-03

3.241E+00 3.241E-02

1.057E+01 1.057E-01

2.656E+01 2.656E-01

5.554E+01 5.554E-01

1.016E+02 1.016E+00

1.682E+02 1.682E+00

2.576E+02 2.576E+00

3.714E+02 3.714E+00

5.100E+02 5.100E+00

6.732E+02 6.732E+00

8.601E+02 8.601E+00

1.070E+03 1.070E+01

PRSR 101.325

TEMR 298.15

CPG1

38.182 -34.081 -7.913 -34.081 -7.913 31.150 27.804 27.3 30.24 28.106

CPG2

-0.0175 4.1375 0.9609 4.1375 0.9609 -1.357e-2 0.003402 0.02646 0.01512 -3.680e-6

CPG3

5e-05 -2.279e-3 -5.288e-4 -2.279e-3 -5.288e-4 2.680e-5 0 0 0 1.746e-5

CPG4

-3e-08 4.8365e-6 1.131e-7 4.8365e-6 1.131e-7 1.168e-8 0 0 0 -1.065e-8

HVR

4820. 9999. 6220. 9999. 6220.

EV

0.38 0.38 0.38 0.38 0.38

SOLID_DEN 'COKE' 0.0013 0 0

SOLID_DEN 'CAT' 0.0010531 0 0

SOLID_CP 'COKE' 12 0

SOLID_CP 'CAT' 74.8835 0

MASSDEN

0.000999 0.001012073 0.0009038 0.000850481 0.000776532

CP

5.8e-7 2.03E-07 6.91E-07 2.03E-07 6.91E-07

CT1

-1.909e-3 1.08E-05 2.02E-05 1.08E-05 2.02E-05

CT2

7.296e-7 4.58E-07 1.58E-06 4.58E-07 1.58E-06

AVG

1.7e-5 7.565e-6 4.174e-6 7.565e-6 4.174e-6 4.098e-6 4.232e-6 4.232e-6 4.232e-6 4.232e-6

BVG

1.116 1.102 0.943 1.102 0.943 0.702 0.702 0.702 0.702 0.702

GVISCOR

VISCTABLE

** temp

293.15 0.00E+00 5.8025E+06 4.3000E+02 7.6485E+02 2.2791E-01

303.406 0.00E+00 7.6980E+05 3.2900E+02 3.6388E+02 1.8544E-01

313.663 0.00E+00 3.3123E+05 2.4900E+02 6.8866E+01 1.4189E-01

323.175 0.00E+00 7.2396E+04 8.5000E+01 3.3227E+01 1.0738E-01

333.176 0.00E+00 1.9738E+04 5.2000E+01 7.9493E+00 3.6657E-02

343.175 0.00E+00 6.7097E+03 3.9000E+01 2.5532E+00 2.2426E-02

353.175 0.00E+00 2.8739E+03 2.9900E+01 1.0190E+00 1.6819E-02

363.175 0.00E+00 1.5462E+03 2.1000E+01 4.9113E-01 1.2895E-02

373.175 0.00E+00 7.9864E+02 1.2700E+01 2.7890E-01 9.0565E-03

383.175 0.00E+00 3.8726E+02 8.4600E+00 1.4874E-01 5.4770E-03

393.175 0.00E+00 2.0609E+02 6.8800E+00 7.6921E-02 3.6485E-03

403.175 0.00E+00 1.1565E+02 5.9300E+00 4.4610E-02 2.9671E-03

413.175	0.00E+00	7.0158E+01	5.3000E+00	2.7310E-02	2.5574E-03
423.175	0.00E+00	5.0774E+01	4.7000E+00	1.7921E-02	2.2857E-03
433.175	0.00E+00	2.1336E+01	3.6300E+00	6.4253E-03	1.5655E-03
453.175	0.00E+00	1.3269E+01	3.1300E+00	4.2698E-03	1.3499E-03
473.175	0.00E+00	6.5473E+00	2.1500E+00	2.2529E-03	9.2722E-04
493.175	0.00E+00	4.1458E+00	1.9600E+00	1.5360E-03	8.4528E-04
513.175	0.00E+00	3.1049E+00	1.6800E+00	1.1822E-03	7.2452E-04
538.1500	0.00E+00	2.3659E+00	1.4135E+00	9.1913E-04	6.0959E-04
553.1500	0.00E+00	2.0213E+00	1.0689E+00	7.6606E-04	4.6098E-04
568.1500	0.00E+00	1.7544E+00	8.2704E-01	6.4961E-04	3.5667E-04
583.1500	0.00E+00	1.4931E+00	6.9224E-01	5.5100E-04	2.9854E-04
598.1500	0.00E+00	1.2761E+00	5.9821E-01	4.7196E-04	2.5799E-04
613.1500	0.00E+00	1.1178E+00	5.1269E-01	4.1159E-04	2.2110E-04
628.1500	0.00E+00	9.5799E-01	4.7073E-01	3.5771E-04	2.0301E-04
643.1500	0.00E+00	8.4324E-01	4.2410E-01	3.1636E-04	1.8290E-04
658.1500	0.00E+00	7.5386E-01	3.8119E-01	2.8313E-04	1.6439E-04
673.1500	0.00E+00	6.8147E-01	3.4360E-01	2.5579E-04	1.4818E-04
688.1500	0.00E+00	6.2907E-01	3.0464E-01	2.3420E-04	1.3138E-04
703.1500	0.00E+00	5.8398E-01	2.7235E-01	2.1576E-04	1.1745E-04
718.1500	0.00E+00	5.4485E-01	2.4535E-01	1.9988E-04	1.0581E-04
733.1500	0.00E+00	5.1071E-01	2.2254E-01	1.7409E-04	8.7594E-05
748.1500	0.00E+00	4.8072E-01	2.0311E-01	1.6353E-04	8.0409E-05
763.1500	0.00E+00	4.5422E-01	1.8645E-01	1.5421E-04	7.4203E-05
778.1500	0.00E+00	4.3067E-01	1.7206E-01	1.4593E-04	6.8808E-05
793.1500	0.00E+00	4.0967E-01	1.5955E-01	1.3854E-04	6.4090E-05
808.1500	0.00E+00	3.9082E-01	1.4861E-01	1.1631E-04	4.5761E-05
873.1500	0.00E+00	3.4189E-01	1.0611E-01	6.6571E-05	2.8080E-05
1173.15	0.00E+00	1.9226E-01	6.5111E-02	5.8815E-05	2.5319E-05

**$ Reaction specification

STOREAC

0 1 0 0 0 0 0 0 0 0 0 0

STOPROD

0 0 1.6 0 0 0 0 0 0 0 46.61538 0

FREQFAC 1.50E9

RENTH 0.0

EACT 0.99e5

**$ Reaction specification

STOREAC

0 0 1 0 0 0 0 0 0 18.6488333 0 0

STOPROD

14.5 0 0 0 0 11.75 0 0 0 0 0 0

FREQFAC 1.812e12

RENTH 4.913e5

EACT 1.38e5

**$ Reaction specification

STOREAC

0 1 0 0 0 0 0 0 0 80.0325 0 0

STOPROD

26.72 0 0 0 0 68.7 0 0 0 0 0 0

FREQFAC 1.812e11

RENTH 5.913e5

EACT 1.38e5

**$ Reaction specification

STOREAC

0 0 0 0 0 0 0 0 0 1.22 1 0

STOPROD

0.5 0 0 0 0 1 0 0 0 0 0 0

FREQFAC 8.6e7

RENTH 3.65e5

EACT 1.23e5

********** HDS & HDN REACTIONS **********

**$ Reaction specification

STOREAC

0 1 0 0 0 0 9.887128 0 0 0 0 1

STOPROD

0 0 0 3.477228 0 0 0 0 0.584769 0 0 1

RORDER

0 1.5 0 0 0 0 1.1 0 0 0 0 1

FREQFAC 2.7e15

RENTH 0.0

EACT 87e3

RTEMLOWR 673.15

**$ Reaction specification

STOREAC

0 0 1 0 0 0 3.285899 0 0 0 0 1

STOPROD

0 0 0 0 1.328021 0 0 0 0.194343 0 0 1

RORDER

0 0 1.5 0 0 0 1.1 0 0 0 0 1

FREQFAC 2.7e15

RENTH 0.0

EACT 87e3

RTEMLOWR 673.15

** Reaction specification

STOREAC

0 1 0 0 0 0 1.592688 0 0 0 0 1

STOPROD

0 0 0 3.477228 0 0 0 0 0.188552 0 0 0 1

RORDER

0 1 0 0 0 0 1.8 0 0 0 0 1

FREQFAC 1e14

RENTH 0.0

EACT 75e3

RTEMLOWR 673.15

```
** Reaction specification
STOREAC
0 0 1 0 0 0 0.095215 0 0 0 0 1
STOPROD
0 0 0 0 1.328021 0 0 0.011272 0 0 0 1
RORDER
0 0 1 0 0 0 1.8 0 0 0 0 1
FREQFAC 1e14
RENTH 0.0
EACT 75e3
RTEMLOWR 673.15

** ============== Rock-FLUID PROPERTIES ==============================
ROCKFLUID
RPT 1 WATWET
**$     Sw              Krw             Krow
SWT
       0.1            0   0.9938207434
      0.25        0.004   0.6864535032
      0.44  0.03015463918   0.3701213851
      0.56  0.08466494845   0.1908238283
     0.672   0.1890463918  0.07940320373
     0.752   0.3457881453  0.03201742086
       0.8         0.45  0.01792975568
       0.9         0.69            0

**$      Sl          krg          krog
SLT
      0.10   0.9925301443             0
    0.1200   0.9144175397  0.003704216112
    0.2500   0.6195414577   0.03711340206
```

```
      0.4720   0.2539948454    0.1229381443
      0.5800   0.1580465541    0.2148445345
      0.6800  0.08766644798    0.3457268371
      0.7200  0.06791062871    0.4124027271
      0.8320   0.0243556701           0.62
      0.9500          0.006    0.8721545441
      0.9900              0    0.9938207434

RPT 2
SWT
**$       Sw       krw      krow
        0.0       0.0       1.0
        1.0       1.0       0.0

SLT
**$       Sl       krg      krog
        0.0       1.0     0.000
        1.0       0.0     1.0

KRTYPE CON 1
KRTYPE WELLBORE 5:30 10 7 CON 2

**              ==============              INITIAL              CONDITIONS
==================================
INITIAL
VERTICAL OFF

INITREGION 1

PRES CON         8000
TEMP CON       300.15
SW CON          0.15
```

```
SO CON    0.85
    MOD  5:30 9:11 6:8     =    0
SG IJK 5:30 10 6:8        1.0
MFRAC_OIL 'LUO' CON           0
MFRAC_OIL 'LITE' CON       0.3647
MFRAC_OIL 'HUO' CON           0
MFRAC_OIL 'HEAV' CON       0.6353
MFRAC_GAS 'NH3' CON           0
MFRAC_GAS 'CO2/CO' CON            1
CONC_SLD 'COKE' CON           0
CONC_SLD 'CAT' IJK 1:30 1:19 1:9  0
MOD 5:30 9:11 6  = 0.005484882
   5:30 9:11 8  = 0.005484882
   5:30 9 7  = 0.005484882
   5:30 11 7  = 0.005484882

**              ==============              NUMERICAL              CONTROL
==================================
NUMERICAL
NORM PRESS 2000
DTMIN 1e-12
MAXSTEPS 100000000
MATBALTOL 1e-6
NEWTONCYC 30
NORTH 150
ITERMAX 250
**
**********************************************************************
**********
SOLVER PARASOL
DPLANES 12
PNTHRDS 8
PPATTERN AUTOPSLAB 4
```

```
MINPRES 100.0
MAXTEMP 1220.0
NCUTS 15
MAXPRES 10000.0

RUN
TIME 0
DTWELL 0.01

WELL  'Producer'
PRODUCER 'Producer'
OPERATE  MIN  BHP  8000.0  CONT REPEAT
OPERATE  MAX  STL  25.0  CONT REPEAT
MONITOR  MAX  TEMP  1200.0  STOP

TRANSI WELLBORE 5:30 10 7 CON 0.05
** UBA                    ff         Status  Connection
**         rad  geofac  wfrac  skin
GEOMETRY  I  0.2  0.2488  1.0  0.0
PERF  GEO  'Producer'
** UBA              ff    Status  Connection
   30 10 7 / 1 1 1  12.5  OPEN    FLOW-TO  'SURFACE'

HEATR IJK
2:2     2:18    1:1  1600

TIME 10
OUTSRF GRID FLUXRC FLUXSC FPOROS PRES SG SO SOLCONC SW
TEMP VELOCSC VISCVELG
        VISCVELO VISCVELW W X Y Z
TIME 20
OUTSRF GRID REMOVE
```

```
TIME 30
OUTSRF GRID REMOVE

WELL  'Injector 1'
INJECTOR UNWEIGHT 'Injector 1'
INCOMP  GAS  0.0  0.0  0.0  0.0  0.0  0.632  0.2  0.0  0.0  0.168
TINJW  298.15
OPERATE  MAX  STG  10000.0  CONT REPEAT
GEOMETRY J 0.2 0.2488 1.0 0
**$ UBA     wi    Status  Connection
** UBA             wi          Status  Connection
PERF  WI  'Injector 1'
** UBA      wi      Status  Connection
   2 18 1  0.0463  OPEN    FLOW-FROM  'SURFACE'  REFLAYER
   2 17 1  0.0463  OPEN    FLOW-FROM  1
   2 16 1  0.0463  OPEN    FLOW-FROM  2
   2 15 1  0.0463  OPEN    FLOW-FROM  3
   2 14 1  0.0463  OPEN    FLOW-FROM  4
   2 13 1  0.0463  OPEN    FLOW-FROM  5
   2 12 1  0.0463  OPEN    FLOW-FROM  6
   2 11 1  0.0463  OPEN    FLOW-FROM  7
   2 10 1  0.0463  OPEN    FLOW-FROM  8
   2 9 1   0.0463  OPEN    FLOW-FROM  9
   2 8 1   0.0463  OPEN    FLOW-FROM  10
   2 7 1   0.0463  OPEN    FLOW-FROM  11
   2 6 1   0.0463  OPEN    FLOW-FROM  12
   2 5 1   0.0463  OPEN    FLOW-FROM  13
   2 4 1   0.0463  OPEN    FLOW-FROM  14
   2 3 1   0.0463  OPEN    FLOW-FROM  15
   2 2 1   0.0463  OPEN    FLOW-FROM  16

HEATR CON 0
```

```
TIME 40
OUTSRF GRID REMOVE
TIME 50
OUTSRF GRID REMOVE
TIME 60
OUTSRF GRID REMOVE
TIME 70
OUTSRF GRID REMOVE
TIME 80
OUTSRF GRID REMOVE
TIME 90
OUTSRF GRID REMOVE
TIME 100
OUTSRF GRID REMOVE
TIME 110
OUTSRF GRID REMOVE
TIME 120
OUTSRF GRID REMOVE
TIME 130
OUTSRF GRID REMOVE
TIME 140
OUTSRF GRID REMOVE
TIME 150
OUTSRF GRID REMOVE
TIME 160
OUTSRF GRID REMOVE
TIME 170
OUTSRF GRID REMOVE
TIME 180
OUTSRF GRID REMOVE
TIME 190
OUTSRF GRID REMOVE
```

```
WELL  'Injector 1'
INJECTOR UNWEIGHT 'Injector 1'
INCOMP  GAS  0.0  0.0  0.0  0.0  0.0  0.632  0.2  0.0  0.0  0.168
TINJW  298.15
OPERATE  MAX  STG  13333.333  CONT REPEAT
GEOMETRY J 0.2 0.2488 1.0 0
**$ UBA     wi      Status  Connection
** UBA             wi          Status  Connection
PERF  WI  'Injector 1'
** UBA      wi      Status  Connection
   2 18 1  0.0463  OPEN    FLOW-FROM  'SURFACE'  REFLAYER
   2 17 1  0.0463  OPEN    FLOW-FROM  1
   2 16 1  0.0463  OPEN    FLOW-FROM  2
   2 15 1  0.0463  OPEN    FLOW-FROM  3
   2 14 1  0.0463  OPEN    FLOW-FROM  4
   2 13 1  0.0463  OPEN    FLOW-FROM  5
   2 12 1  0.0463  OPEN    FLOW-FROM  6
   2 11 1  0.0463  OPEN    FLOW-FROM  7
   2 10 1  0.0463  OPEN    FLOW-FROM  8
   2 9 1   0.0463  OPEN    FLOW-FROM  9
   2 8 1   0.0463  OPEN    FLOW-FROM  10
   2 7 1   0.0463  OPEN    FLOW-FROM  11
   2 6 1   0.0463  OPEN    FLOW-FROM  12
   2 5 1   0.0463  OPEN    FLOW-FROM  13
   2 4 1   0.0463  OPEN    FLOW-FROM  14
   2 3 1   0.0463  OPEN    FLOW-FROM  15
   2 2 1   0.0463  OPEN    FLOW-FROM  16

TIME 200
OUTSRF GRID REMOVE
TIME 210
```

```
OUTSRF GRID REMOVE
TIME 220
OUTSRF GRID REMOVE
TIME 230
OUTSRF GRID REMOVE
TIME 240
OUTSRF GRID REMOVE
TIME 250
OUTSRF GRID REMOVE
TIME 260
OUTSRF GRID REMOVE
TIME 270
OUTSRF GRID REMOVE
TIME 280
OUTSRF GRID REMOVE
TIME 290
OUTSRF GRID REMOVE
TIME 300
OUTSRF GRID REMOVE
TIME 310
OUTSRF GRID REMOVE
TIME 320
STOP
```